Technical Report Documentation Page

1. Report No.	2. Government Accession No.	3. Recipient's Catalog No.
SWUTC/14/600451-00028-1		

4. Title and Subtitle	5. Report Date
SUSTAINABILITY OF BRIDGE FOUNDATIONS USING ELECTRICAL RESISTIVITY IMAGING AND INDUCED POLARIZATION TO SUPPORT TRANSPORTATION SAFETY	April 2014
	6. Performing Organization Code

7. Author(s)	8. Performing Organization Report No.
Stefan Hurlebaus, Jean-Louis Briaud, and Stacey Tucker	SWUTC 600451-00028-1

9. Performing Organization Name and Address	10. Work Unit No. (TRAIS)
Texas A&M Transportation Institute The Texas A&M University System College Station, Texas 77843-3135	11. Contract or Grant No. DTRT12-G-UTC06

12. Sponsoring Agency Name and Address	13. Type of Report and Period Covered
Southwest Region University Transportation Center Texas A&M Transportation Institute The Texas A&M University System College Station, Texas 77843-3135	Research Report: January 2013–January 2014
	14. Sponsoring Agency Code

15. Supplementary Notes

Supported by a grant from the U.S. Department of Transportation, University Transportation Centers Program

16. Abstract

As of September 2007, there were 67,240 U.S. bridges in the National Bridge Inventory classified as having unknown foundations (FHWA 2008). The bridges spanning rivers are of critical importance due to the risks of potential scour. In fact, it is estimated that 60 percent of all bridge collapses are due to scour (Parola et al. 1997). Not only are these failures costly, they can be deadly for the traveling public. On April 5, 1987, 10 people were killed in New York when a pier collapsed on the Schoharie Creek Bridge causing two spans of the deck to fall into the creek. Several other fatal collapses have occurred since the Schoharie Creek Bridge failure. Detecting scour is only part of the assessment that must take place to determine risk of failure and knowing the foundation depth is a critical component of the assessment.

This research explored the feasibility and effectiveness of induced polarization (IP) and electrical resistivity imaging (ERI), near surface geophysical methods, for determining the depth of unknown foundations. With budget cuts and deteriorating infrastructure, there is a need to seek alternative solutions for nondestructive structural integrity testing that are more robust to limit bridge failures that hinder transportation safety. The existing methods for unknown bridge foundations in the literature are often hindered by the type of foundation or require the use of a borehole, making them very costly. As a result, only a few states are working to identify the depth of unknown bridge foundations around them. In order to solve this national problem, a new and effective method needs to be investigated with full scale bridge testing and disseminated nationwide. In this work, an experimental study was conducted at a National Geotechnical Experimentation Site (NGES) to identify key parameters for the testing design and setup in order to obtain optimal surveys of bridge foundations. The conclusions of the NGES investigations were used to plan the field surveys on four bridges with known foundations. The outcomes of the four bridges showed that IP and ERI can be used in concert with one another to estimate the type and depth of bridge foundations. The results of the field surveys were used to create a probability of non-exceedance curve for future predictions of unknown bridge foundations using the methods described in this research. Finally, the probability of exceedance curve was used to validate the method with testing on a foundation unknown at the time of testing, and the use of IP and ERI were extended to other subsurface infrastructure when a gas line was imaged.

17. Key Words	18. Distribution Statement
Unknown Bridge Foundations, Scour, Electrical Resistivity, Induced Polarization, Probability of Exceedance	No restrictions. This document is available to the public through NTIS: National Technical Information Service Alexandria, Virginia 22312 http://www.ntis.gov

19. Security Classif.(of this report)	20. Security Classif.(of this page)	21. No. of Pages	22. Price
Unclassified	Unclassified	161	

Form DOT F 1700.7 (8-72) **Reproduction of completed page authorized**

SUSTAINABILITY OF BRIDGE FOUNDATIONS USING ELECTRICAL RESISTIVITY IMAGING AND INDUCED POLARIZATION TO SUPPORT TRANSPORTATION SAFETY

by

Stefan Hurlebaus
Associate Professor, Texas A&M University

Jean-Louis Briaud
Research Engineer, Texas A&M University

Stacey Tucker
Graduate Student, Texas A&M University

Report SWUTC/14/600451-00028-1
Project 600451-00028
Project Title: Sustainability of Bridge Foundations using Electrical Resistivity Imaging and Induced Polarization to Support Transportation Safety

Southwest Region University Transportation Center
Texas A&M Transportation Institute
The Texas A&M University System
College Station, Texas 77843-3135

April 2014

DISCLAIMER

The contents of this report reflect the views of the authors, who are responsible for the facts and the accuracy of the data presented herein. This document is disseminated under sponsorship of the Department of Transportation, University Transportation Centers Program in the interest of information exchange. The U.S. Government assumes no liability for the contents or use thereof.

ACKNOWLEDGMENTS

The authors recognize the support for this research was provided by a grant from the U.S. Department of Transportation, University Transportation Centers Program to the Southwest Region University Transportation Center.

TABLE OF CONTENTS

LIST OF FIGURES

LIST OF TABLES

EXECUTIVE SUMMARY

As of September 2007, there were 67,240 U.S. bridges in the National Bridge Inventory classified as having unknown foundations (FHWA 2008). The bridges spanning rivers are of critical importance due to the risks of potential scour. In fact, it is estimated that 60 percent of all bridge collapses are due to scour (Parola et al. 1997). Not only are these failures costly, they can be deadly for the traveling public. On April 5, 1987, 10 people were killed in New York when a pier collapsed on the Schoharie Creek Bridge causing two spans of the deck to fall into the creek. Several other fatal collapses have occurred since the Schoharie Creek Bridge failure. Detecting scour is only part of the assessment that must take place to determine risk of failure and knowing the foundation depth is a critical component of the assessment.

This research explored the feasibility and effectiveness of induced polarization (IP) and electrical resistivity imaging (ERI), near surface geophysical methods, for determining the depth of unknown foundations. With budget cuts and deteriorating infrastructure, there is a need to seek alternative solutions for nondestructive structural integrity testing that are more robust to limit bridge failures that hinder transportation safety. The existing methods for unknown bridge foundations in the literature are often hindered by the type of foundation or require the use of a borehole, making them very costly. As a result, only a few states are working to identify the depth of unknown bridge foundations around them. In order to solve this national problem, a new and effective method needs to be investigated with full scale bridge testing and disseminated nationwide.

In this work, an experimental study was conducted at a National Geotechnical Experimentation Site (NGES) to identify key parameters for the testing design and setup in order to obtain optimal surveys of bridge foundations. The conclusions of the NGES investigations were used to plan the field surveys on four bridges with known foundations. The outcomes of the four bridges showed that IP and ERI can be used in concert with one another to estimate the type and depth of bridge foundations. The results of the field surveys were used to create a probability of non-exceedance curve for future predictions of unknown bridge foundations using the methods described in this research. Finally, the probability of non-exceedance curve was used to validate the method with testing on a foundation unknown at the time of testing, and the use of IP and ERI were extended to other subsurface infrastructure when a gas line was imaged.

1. INTRODUCTION

MOTIVATION

On Sunday morning, April 5, 1987, during a 50-year flood event a pier on the New York Thruway (I-90) bridge over Schoharie Creek collapsed. The collapse caused the third and fourth spans (of five total) to fall approximately 20 m into the creek along with a tractor-trailer and one car. Three more cars that were unable to stop also drove into gap, falling into the creek before the bridge was closed. Ten people were killed. Fig. 1.1 shows the aftermath.

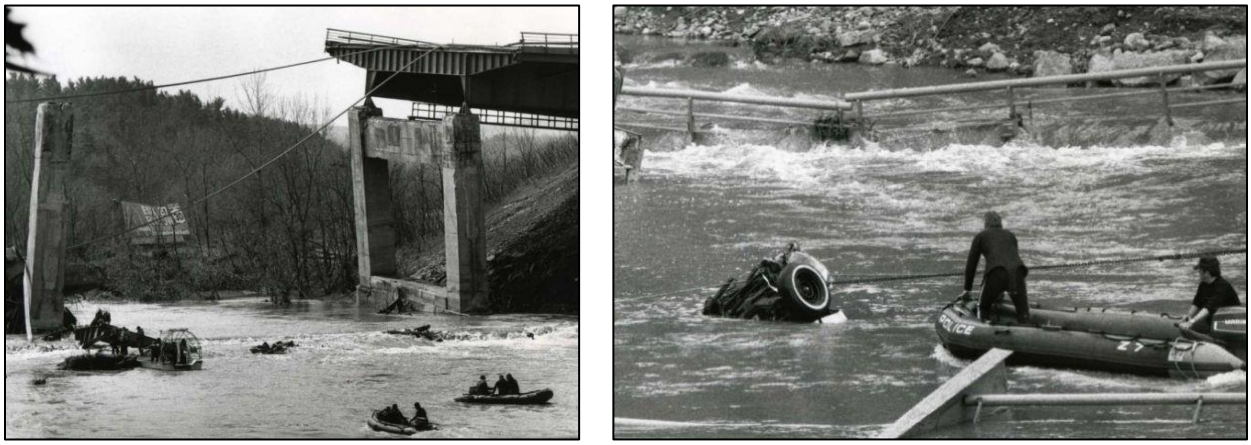

(a) Police searching the river (b) An exposed section of one of the fallen vehicles

Fig. 1.1. On April 9, 1987, police search for bodies, four days after the collapse of the Schoharie Creek (McKinney 2012)

Upon later inspection, investigators determined that excessive scour caused the pier to collapse. In response to the failure, the Federal Highway Administration (FHWA) published the "Interim Procedures for Evaluating Scour at Bridges" (FHWA 1988), which included for the first time scour assessment at bridges. The 1988 FHWA publication marked the beginning of the national bridge scour evaluation program.

Despite the new interim guidelines for nationwide scour assessment, on April 1, 1989, bents 70 and 71 of the northbound lanes of US 51 over the Hatchie River in Tennessee collapsed. Three spans of the roadway and five cars also plunged into the river as a result of the collapse, killing eight. Like the Schoharie Creek bridge, the Hatchie River bridge failed due to localized scour. Several other bridge collapses due to scour have occurred since; some were fatal.

As the scour and bridge collapse problem became more apparent across the nation, the FHWA took several steps toward mitigation. The "Procedures for Evaluating Scour at Bridges" has been updated five times (FHWA 2012) and as of 2008 the FHWA addressed the issue of unknown foundations. The "Technical Guidance for Bridges over Waterways with Unknown Foundations" (FHWA 2008) was directed specifically toward the process "to reduce or eliminate the population of bridges over waterways identified as having unknown foundations, which in turn would allow bridge owners to evaluate these bridges for their scour vulnerability." This report stated that in 2008 each state was required to identify the bridges in their database coded as '113' or as missing information related to foundations details in scour vulnerable waterways.

If a state was unable to identify all of its unknown foundations by 2010, it was required to have a plan of action.

BACKGROUND

Chapter 2 includes a full review of the existing methods for determining unknown bridge foundations and a review of the two proposed methods.

Unknown Foundations

A bridge with an unknown foundation is a bridge where details pertaining to the type and/or depth of the foundation are missing in the National Bridge Inventory (NBI). As-built details of a foundation, particularly the depth of embedment of a foundation, are critical when bridges are evaluated for scour vulnerability. Fig. 1.2 shows an example of different elements of a bridge.

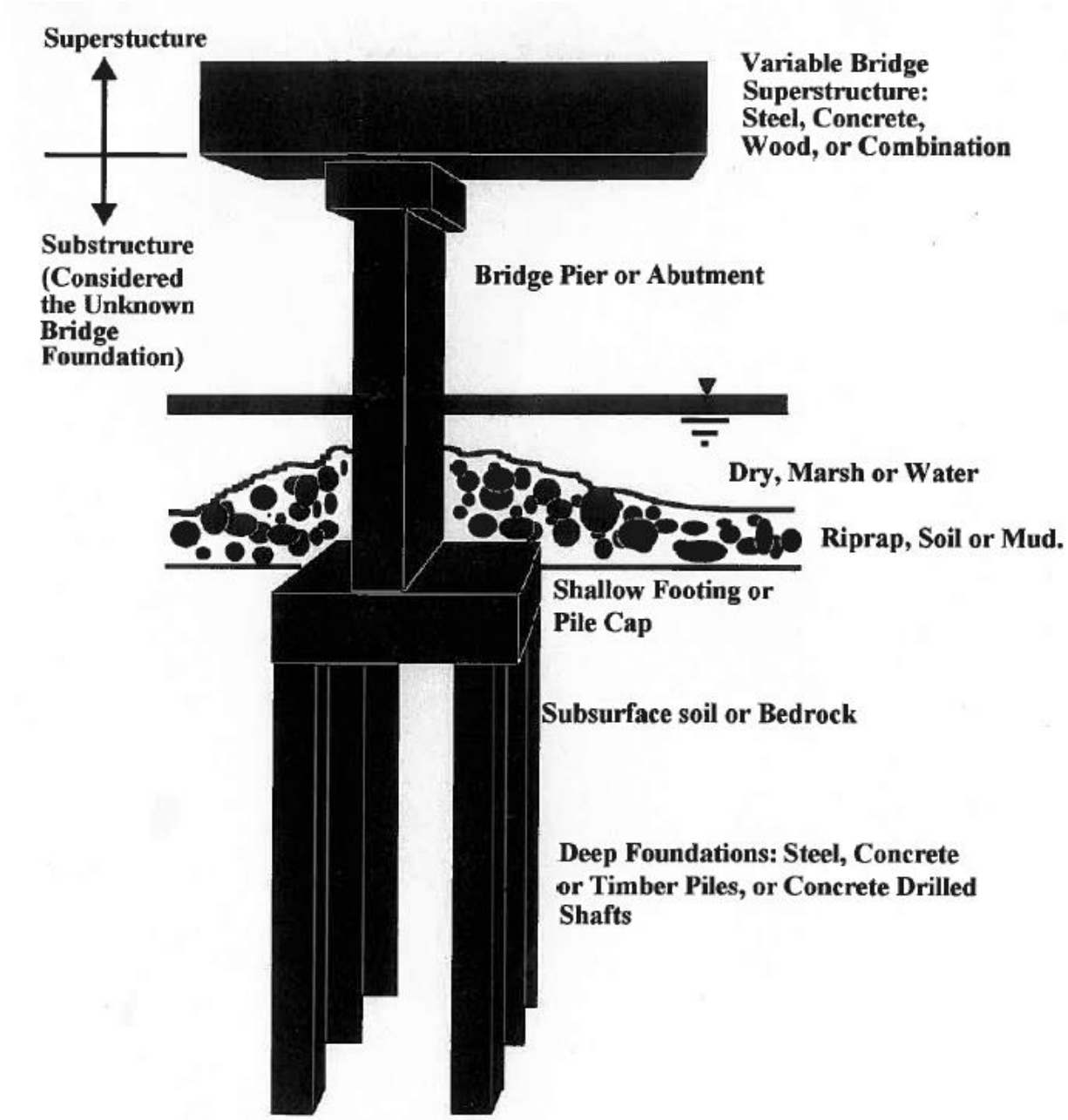

Fig. 1.2. Variables of an unknown bridge foundation (Olson et al. 1998)

The elements related to the substructure as shown in Fig. 1.2 are considered the pertinent information for scour evaluation, in particular, those elements below the surface. Fig. 1.2 shows piles beneath a pile cap. Piles can be driven and made of reinforced concrete, steel, or timber or reinforced concrete drilled shafts. Piles may also exist without a pile cap, with a column connecting the superstructure to the pile or foundations can be shallow footings that look like pile caps without piles beneath.

Bridge Scour

Approximately 60 percent of all bridge collapses are due to scour (Parola et al. 1997). Fig. 1.3 shows a schematic of a bridge as it was originally built and after scour has occurred.

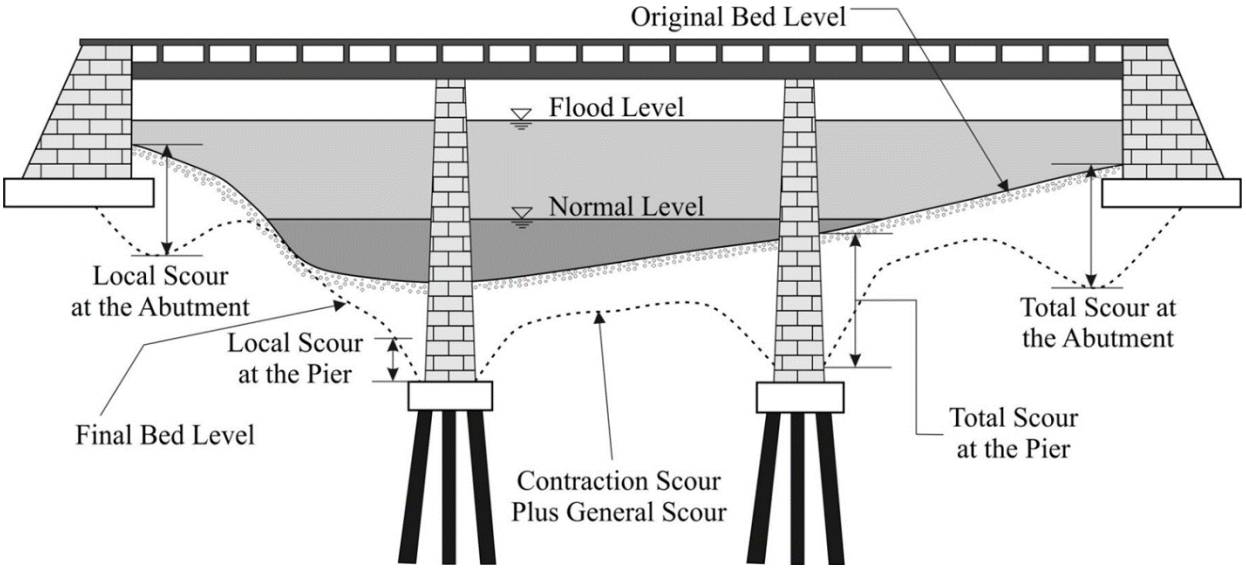

Fig. 1.3. Potential scour around bridge foundations (Melville and Coleman 2000)

In Fig. 1.3, the original riverbed is shown with the abutments and piers embedded to safely support the bridge for the traveling public. As shown in the figure scour can occur around both the abutments and piers as well as between the piers. General scour, local scour, and contraction scour are the three types of scour that may occur. These types can occur individually or simultaneously (Fig. 1.3). General scour refers to scour that naturally occurs over time regardless of the presence of a bridge. Local scour and contraction scour, on the other hand, are due to the bridge elements that have been constructed through the river. Local scour is caused by the pier or abutment being in the riverbed, forcing water to flow around it versus an unobstructed path as it did before the bridge. Contraction scour is due to the accelerated flow of a river between piers, such as shown in Fig. 1.3.

Scour can be very deep. The Schoharie Creek Bridge failed because the third pier was undermined by scour. Approximately 7.5 to 9 m along the length of the third pier fell into a scour hole that was approximately 9 m deep (National Transportation Safety Board 1988).

TECHNICAL NEED

Ultimately, one universal method is not feasible for determining the depth of unknown bridge foundations. Each bridge is a unique combination of the structure and its surrounding environment. Different bridges require different levels of confidence in the foundation estimation and certain approaches to determine the foundation depth may or may not be feasible. For this reason, there is a technical need for a variety of methods for determining the depth of unknown foundations. Induced polarization (IP) and electrical resistivity imaging (ERI) are electrical methods in the field of near surface geophysics that image the subsurface using spatial distributions of the response of the ground. The two methods are very similar, requiring an extra electrode line to collect IP data to ensure minimal noise. ERI has already been used for bridge

foundations (Arjwech 2011; Hossain et al. 2011) but collecting ERI data does not increase IP survey time. IP is better at imaging long slender piles; however, because IP is fundamentally based on the measurements collected in an ERI study, the ERI data are a good representative of the quality of the IP data. Using ERI and IP in conjunction with each other is a unique tool to add to the unknown bridge foundation testing method database.

OBJECTIVES

The primary objective of this research was to establish that foundations as well as other infrastructure elements possess measurable IP responses in the field. The objectives of this research were accomplished in several phases, beginning with foundation measurements on known infrastructure elements near Texas A&M University (TAMU) using ERI and IP. Next, actual bridge foundations where the as-built plans were available were tested. After the method was used on assorted bridges, the data were used to assess the reliability of the method. The objectives of this research were to:

1. Establish that bridge foundations possess a measurable IP response on known foundations at the control site.
2. Establish the range of applications for IP and ERI in the field to detect known foundations.
3. Develop a post processing algorithm for predicting the depth of bridge foundations.
4. Develop a probability of non-exceedance curve for estimating unknown foundation depths with collected data from known foundations.
5. Evaluate the method for applications to other subsurface civil engineering infrastructure.

ORGANIZATION OF THE REPORT

This report is organized into seven chapters. Following this introduction is a literature review of existing methods for determining unknown bridge foundation depths as well as an overview of the ERI and IP methods. The bulk of the information is in Chapter 3, which includes tests at the control site, representing a laboratory study, and tests at four bridge sites. The post processing method for estimating the foundation depth and a probability of non-exceedance curve are developed and described in the next chapter. Next, the developed non-exceedance curve is used for a prediction of an unknown foundation in Chapter 5 where a blind study is conducted. The following chapter discusses the use of ERI and IP for another subsurface infrastructure, a buried gas line. The report is finalized with conclusions and recommendations.

2. LITERATURE REVIEW

INTRODUCTION

The unknown foundations problem in the United States has been studied for decades. Over time, many deterministic methods have been developed for estimating the depth of bridge foundations. In 1996, a National Cooperative Highway Research Program (NCHRP) project was granted to an Engineering firm to investigate the current field testing of bridge foundations (Olson et al. 1998). The testing methods discussed in this report are still being used today, along with a few that have been established after the NCHRP report. Unfortunately, while it has been known for several years that there is an unknown foundation issue and despite the fact that many states are investigating unknown foundations and updating the NBI, the number of unknown foundations is still growing. The problem still needs to be addressed after bridge construction, when as-built construction plans must be submitted to the NBI and to the State Transportation Department.

EXISTING EXPERIMENTAL METHODS

There are over 9,000 bridges in Texas alone with unknown foundations. The bridges spanning water are of critical importance due to the risk of potential scour. States nationwide are identifying their unknown foundations to update bridge databases; however, current techniques are typically invasive and costly. Many reports with extensive research have been published on current surface and subsurface tests (Maser et al. 1998; Mercado and O'Neil 2003; Olson et al. 1998; Olson 2005; Robinson and Webster 2008). Some of the capabilities and limitations of these methods are presented in this section. While there are many components of a foundation that are important for its stability, the depth of embedment is the most pertinent when evaluating the bridge for scour potential and safety. The most effective method for successfully identifying the type and depth of a foundation is conventional excavation, exposing a portion of the bridge foundation for visual conformation. As can be expected, this is not typically done. First, it is extremely expensive, especially when the bridge is over water, requiring the area to be sheeted and dewatered. If the bridge is large, excavations may also be difficult due to a lack of access, and if the bridge is over water, costly barges may be necessary. Also, excavation can be very dangerous and difficult for workers. Precautions have to be taken so that the foundation is not undermined and the bridge does not collapse. These reasons as well as others have emphasized the need for nondestructive testing methods.

Surface Methods

In general, surface methods are preferred over subsurface methods if possible. They are more economical, without the upfront cost of a borehole; however, they are often dependent on access to bridge foundations. The simplest nondestructive testing method is a driving rod test.

Driving Rod Test

The driving rod test was used to determine if the foundation is shallow or deep. Robinson and Webster (2008) used a 1.27 cm diameter steel rod driven with a 6.8 kg hammer dropped 0.61 m near the bridge foundation. Blow counts per 0.3 m were recorded until the rod cannot be

driven farther. This test can provide the depth to weathered rock, dense sand layers, or soft layers. Shallow foundations were presumed if the results indicate a strong material or rock near the surface.

Sonic Echo Test

The sonic echo test was developed to evaluate the integrity and length of newly constructed piles. For new piles, the source and receiver are placed on the top of the pile. The source generates a compression wave of known magnitude. The velocity of the wave can be estimated with the impulse magnitude. Using the known velocity and the known dimensions of the recently constructed pile, defects in the pile can be detected. Sonic echo can determine the depth of bridge foundations by placing a receiver on the top or side of an exposed pile underneath a bridge. If the top is not exposed, at least two receivers are placed on the side of the structure. Compression waves are generated with a handheld hammer. The depth of the foundation is determined using the arrival time of the reflected compression wave to the receiver. The method is very effective for columnar substructures. Unfortunately, it is limited because the compression waves generated by the impulse are often diffused into other components, like the pile cap (Fig. 1.2). Also, it has been determined, as a rule of thumb, that when embedded length to diameter ratios are greater than 20:1 or 30:1 in stiffer soils, there will be no identifiable bottom echoes due to excessive damping of the compression wave energy in the sonic echo (Olson et al. 1998).

Bending Wave Test

The bending wave test is similar to the sonic echo test; however, it uses flexural (bending) waves instead of compression waves. Pioneered by Darrin Holt in the early 1990s, bending waves had not yet been investigated for foundation testing prior to this research (Holt and Douglas 1994). For a bending wave test, at least two horizontal receivers are placed on the same side of the pile as where it will be impacted, noted by “The Strike” in Fig. 2.1.

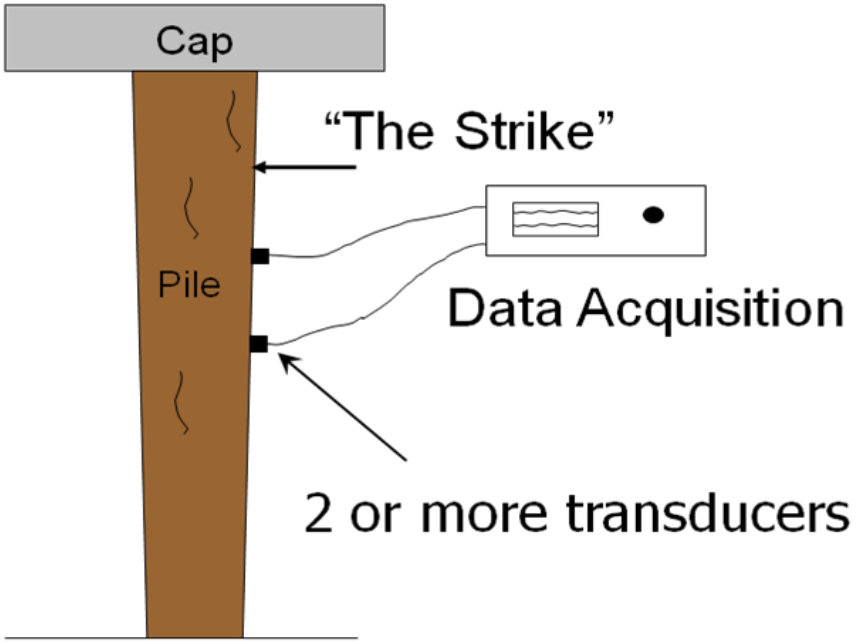

Fig. 2.1. Bending wave testing principle (Holt and Douglas 1994)

Once the bending wave is initiated, the time of arrival of the echoes of the wave is measured. The wave velocity, which is dependent on the material of the foundation and the force of the impact can be calculated. The depth of the foundation can then be calculated based on the arrival time of the wave. Unlike compressional waves, bending waves are highly dispersive. This dispersive nature sometimes hinders the use of the bending wave method because the impulse must be a certain amplitude. Another constraint of the bending wave method is the length of the pile that must be exposed above the ground surface for the two transducers. The transducers must be spaced over 1 m apart, and there must still be space available over the uppermost transducer for the strike impact. The bending wave test is also only effective for columnar substructures.

Ultraseismic Test

Ultraseismic (US) is another wave propagation test; it uses geophysical digital data processing to analyze the propagation of the waves. Unlike the sonic echo test, multiple channels of data are used, so the test requires access to at least 1.5 m of the surface of the substructure. US was investigated to address the issues that sonic echo and bending wave have on non-columnar foundations. US again uses a handheld hammer to generate the waves, but the arrivals and the reflections of both the compression and bending waves are analyzed using seismic processing. The compression waves are generated by striking the foundation vertically, and the bending waves are generated by striking it horizontally. Olson et al. (1998) determined that the US method has the broadest applications in determining unknown foundations of all the surface methods investigated the NCHRP study. While US has proved to be more successful at testing more complex substructures than the previously described methods, the waves are still not able to travel through pile caps or other components on top of piles as shown in Fig. 2.2.

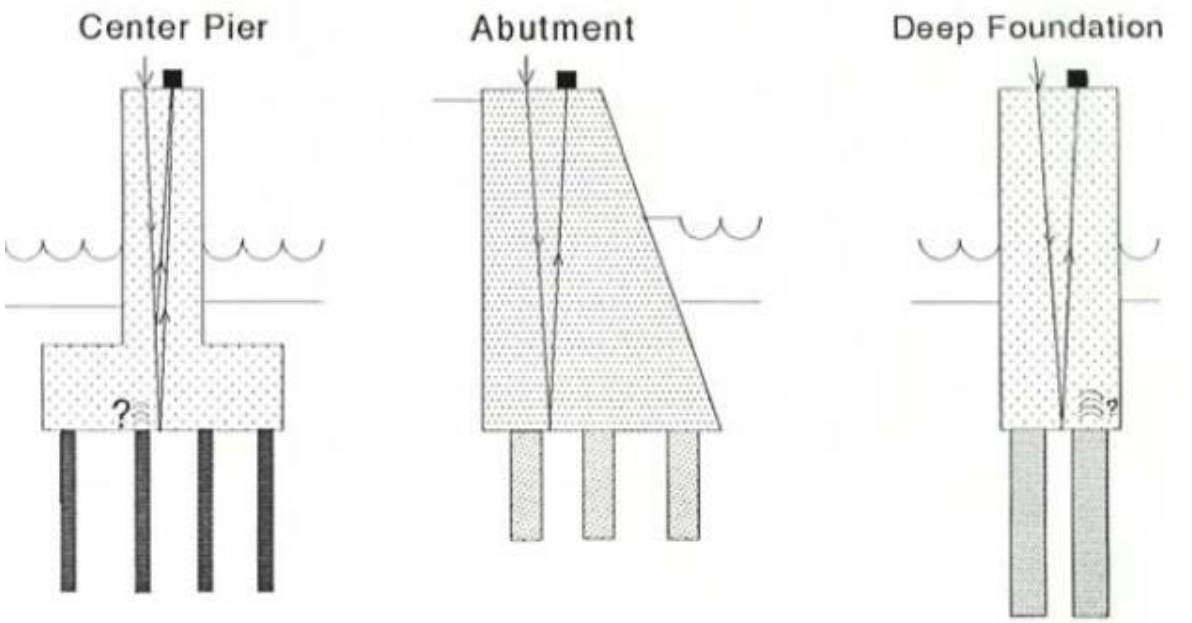

Fig. 2.2. Impedance of wave propagation by complex foundations (Olson et al. 1998)

Dynamic Foundation Response Method

Waves impeded by piles caps may lead to false results that indicate shallower foundations than exist, as Fig. 2.2 shows. Another surface method, the Dynamic Foundation Response Method (Olson et al. 1998), uses an impulse hammer with a built in force transducer to excite the bridge in the vertical and horizontal directions along the frame of the substructure as a form of modal analysis. It was created to differentiate between shallow and deep foundations, as other surface methods are unable to detect piles beneath a pile cap. In the Dynamic Foundation Response Method, the substructure is struck with a known force and the accelerometers measure the resulting vibrations. Using these data, the transfer function is calculated and plots of the transfer function versus the frequency of the structure are created. This is done under the principle that, all other components of the structure being the same, a shallow foundation will exhibit a lower resonance frequency than a deep foundation. The researchers have noted, however, that they need more powerful vibrations to excite the bridge to low frequencies comparable to the natural frequencies identified in numerical modeling. They have suggested using other methods to excite the bridge because of this observation. In a later study, Olson (2005) again attempted to excite bridges using handheld devices. Researchers used a 1.36 kg impulse hammer, a 45.4 kg vibrator, and a 5.45 kg impulse sledge hammer; again these did not generate enough energy to excite the bridge.

Ultimately, Olson (2005) used the Vibroseis truck to excite the substructure from the bridge deck level because of its ability to generate a low frequency output. While the bridge was excited to necessary frequencies, modeling the data was not yet successful. Olson attempted to use parameter estimation for finding a solution to different pile cases, but results were consistently incorrect. Also, parameter estimation was used to solve for the first vertical mode of vibration of the structure to measure damage. Researchers concluded that this method is not feasible for estimating foundation damage because the effects of the damage are too small to model.

Structural Response Method

Maser et al. (1998) believed that the approaches such as dynamic and seismic testing were too complex, requiring specialized knowledge and equipment that were not readily available making some projects not feasible. Researchers desired to implement a simple and low-cost approach using a stiffness matrix created from measurements taken during loading from dump trucks. Axle loads were continuously measured while driving slowly across a bridge. Because the excitation must go through the deck and all the way down the foundation, much more energy must be generated to be effective. The team generated six models to find stiffness matrices for different foundation types and conducted field tests on two bridges with different known foundations. Unfortunately, the measured stiffness matrices did not show similarities to the models. The team did find that for both the measured and field tests, the stiffness matrices had distinctly different patterns of coefficients for spread footings versus pile foundations.

Maser et al. (1998) hypothesized that each foundation type has a unique pattern of stiffness coefficients. Because the bridge was loaded with a truck that has known properties, they assumed the loading and certain known displacements to generate a stiffness matrix. While they had not determined the coefficients at the time of publishing, they showed that the pattern of the coefficients is different for shallow versus deep foundations, and these differences were similar to those predicted by theory. Similarly, Suzuki et al. (2007) used the ratios of a theoretical stiffness to indicate scour on bridge piers. Accelerometers were attached to the top of bridge piers to measure the vertical and horizontal accelerations of a pier noting that a change in the horizontal stiffness occurs when scour removes the soil from one side of a foundation. This unbalance of stiffness is being used as a monitoring system for bridges over water.

Subsurface Methods

In some bridge foundation predictions it is possible to drill a borehole for different testing. Brief overviews of four subsurface methods are now described: parallel seismic, borehole sonic, borehole radar, and the induction method.

Parallel Seismic Test

Another way to determine the depth of an unknown foundation of a bridge is by investigating it using a subsurface method after drilling a borehole. Parallel seismic is one of the subsurface methods that is commonly used. Once the hole is drilled, a hydrophone or geophone is lowered at set intervals as the exposed foundation substructure is impacted with an impulse hammer. The compression waves that travel down the substructure are refracted into the soil, and the arrival of the waves is tracked through the receiver (Fig. 2.3).

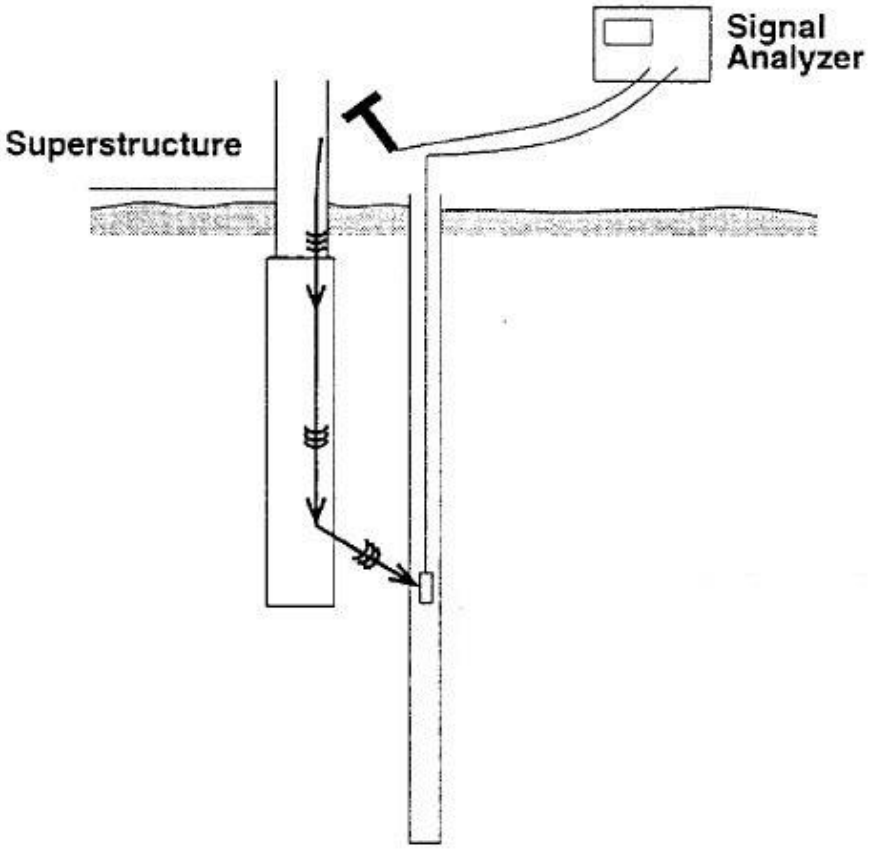

Fig. 2.3. Parallel seismic (Olson et al. 1998)

When the receiver notes an apparent change in the waves, the bottom of the foundation is noted. Olson et al. (1998) noted that the parallel seismic method has the broadest application for determining unknown foundations of the 10 that were investigated. Parallel seismic can not only be used for identifying the depth of bridge foundations, but it can also determine the depth of the scour zone (Mercado and O'Neil 2003).

Borehole Sonic, Borehole Radar, and the Induction Method Tests

The borehole sonic test is similar to parallel seismic, measuring the reflection of waves from alongside the structure. Borehole radar is similar to borehole sonic, but it relies on the dielectric constants that cause reflections instead of differences in stiffness. The induction method, which was used in North Carolina (Robinson and Webster 2008), is performed by lowering an induction sensor in a borehole. The induction sensor creates a magnetic field. The field is interrupted by metal objects, such as rebar in a foundation. This disruption allows for the rebar in the foundation to generate its own magnetic field, which is detected by the induction sensor in the borehole. The received voltages read by the induction sensor are measured at a minimum of every 0.31 m. The depth at which the receiver no longer indicates a voltage reading is the estimated foundation length. This method is highly dependent on metal within the substructure.

Existing Methods Summary

Of all the methods reviewed, vibration based methods are most common due to the ease of instrumenting the bridge and interpreting the results. Unfortunately, many researchers have noted that it is difficult to excite a bridge to the desired frequency for determining unknown foundations (Maser et al. 1998; Olson et al. 1998; Olson 2005). The Dynamic Foundation Response Method (Olson et al. 1998) uses a 5.44 kg hammer with a built in force transducer to excite the bridge in the vertical and horizontal directions along the frame of the substructure. However, more powerful vibrations are needed to excite the bridge to frequencies comparable to the natural frequencies identified in numerical modeling. The researchers suggested using other methods to excite the bridge. Other researchers have unsuccessfully tried to excite a bridge using heavy traffic, such as loaded dump trucks (Maser et al. 1998).

Methods are often hindered by the assumptions researchers make based on typical foundation construction practices. Unfortunately, some of the bridges with unknown foundations may not have been built with standard construction methods. For example, a few years ago, a group of engineers were able to go into a partially collapsed salt mine discovered beneath a bridge to investigate the foundation. While beneath the surface, it was discovered that the concrete substructure contained no reinforcing steel. These methods that depend on certain components of a substructure that are assumed to always be present could hinder the results for cases when they are not included. ERI and IP do not depend on the structure in any way so they are not hindered like most surface methods. Also, they do not rely on common construction practices for estimating the depth of foundations so adding them to the testing database will complement the issues of many of the current methods.

ELECTRICAL METHODS

IP and ERI are reviewed in this section. The use of IP and ERI for Geotechnical Engineering is not new. ERI is used for characterizing shallow subsurface ground conditions to see between bore holes (Hiltunen and Roth 2003; Wisen et al. 2005; Groves et al. 2011). ERI testing is also used for landfill mapping (Bernstone et al. 2000). Moreover, the electrical resistivity of reinforced concrete is used to evaluate corrosion of the rebar (Su et al. 2002). The electrical resistivity of reinforced concrete varies depending on the degree of corrosion in the rebar, the moisture content, and the material composition (Tuuti 2001). In conjunction with parallel seismic and sonic echo testing, ERI has been successfully employed for determining the depth of bridge foundations (Hossain et al. 2011).

IP has also been used to measure the corrosion of reinforcing bars in concrete. Hubbard et al. (2003) placed electrodes on a concrete surface and successfully measured a change in the IP response as corrosion occurred in the reinforcement. IP is used for archaeological surveys when searching for buried artifacts (Meyer et al. 2007) and for distinguishing between coarse and fine-grained materials in landfill explorations (Leroux et al. 2007). IP is also used for differentiating between waste and reinforced concrete at the bottom of waste dumps (Bavusi et al. 2006). It is used for aquifer explorations, locating unexploded ordnances and land mines (Pellerin 2002), and is increasingly used for contaminant-plume mapping (Sogade et al. 2006).

Electrical Resistivity Imaging

ERI and IP field data collection are very similar, requiring an extra electrode line to collect IP data to ensure minimal noise. In this report, IP is better at imaging long slender piles. IP data are dependent on ERI data so ERI is included to show the quality of the IP surveys. In order to fully understand IP principles, a basic understanding of ERI is necessary. ERI is derived from Ohm's law in an isotropic homogeneous medium:

$$\vec{J} = \sigma \vec{E} \tag{1.1}$$

where $\vec{J}$ is the current density vector in A/m^2, σ is the conductivity in S/m (where S is Siemens, the reciprocal of 1 Ω), and $\vec{E}$ is the electric field vector in V/m. Equation 2.2 is the general equation for the more well-known circuit law:

$$V = IR \tag{1.2}$$

where V is voltage, I is current, and R is resistance. Resistance should not be confused with resistivity. If current is injected into a homogeneous half-space, as in Fig. 2.4, the electric field is parallel to the current flow and perpendicular to the equipotential lines (shown as a hemispherical surface of radius r in Fig. 2.4).

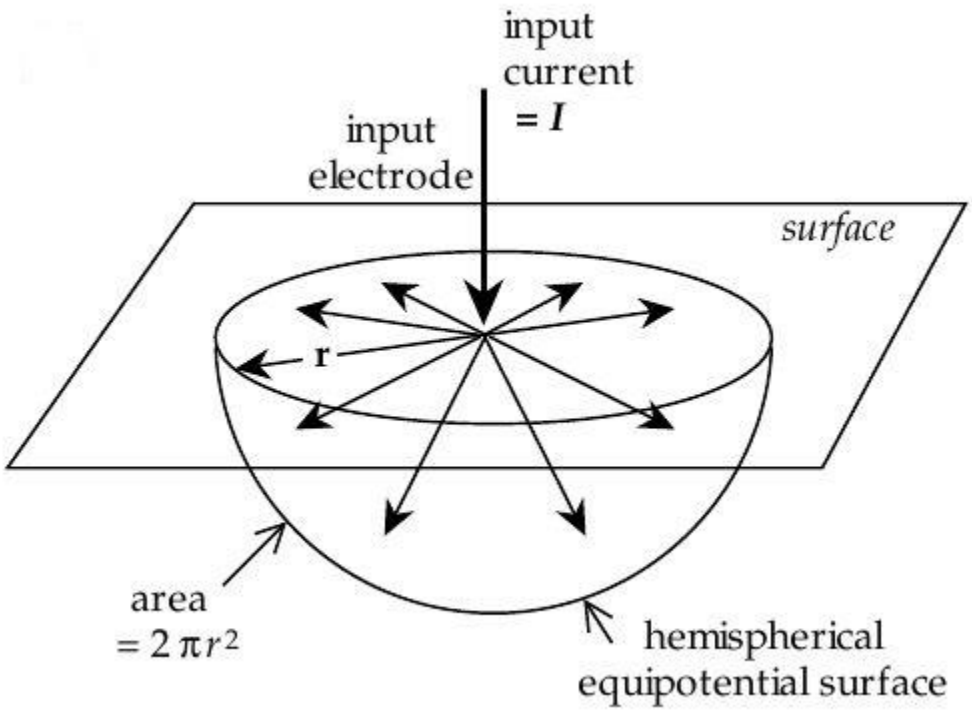

Fig. 2.4. Current injected into a homogeneous half-space (Lowrie 2007)

Using this model, the current density, $\vec{J}$, is the current, I, divided by the assumed surface area, $2\pi r^2$. Note that conductivity, σ is the reciprocal of resistivity, ρ. From Equation 2.1, the electric field, $\vec{E}$, at a distance r is:

$$\vec{E} = \rho \vec{J} = \rho \frac{I}{2\pi r^2} \tag{1.3}$$

where all variables have previously been introduced.

The voltage measured at a point, P, on surface within the radius r, is equal to the work done by a vector field to move a test charge from infinity to P. Work is fundamentally the product of force and distance, where the force experienced by a test charge is proportional to the electric field, $\vec{E}$. Using these fundamental definitions, the voltage at P is defined as the integral:

$$V_{\mathrm{p}} = \int_r^{\infty} \vec{E} \cdot \mathrm{d}r = \int_r^{\infty} \frac{I\rho}{2\pi r^2} \mathrm{d}r = \frac{I\rho}{2\pi r} \tag{1.4}$$

where all variables have been defined. This is the basic equation of electrical resistivity.

Fig. 2.5 is the same as Fig. 2.4 but two additional electrodes are added to the surface for measuring the voltage. The voltage measured across the terminals P and Q is the difference between the two voltages.

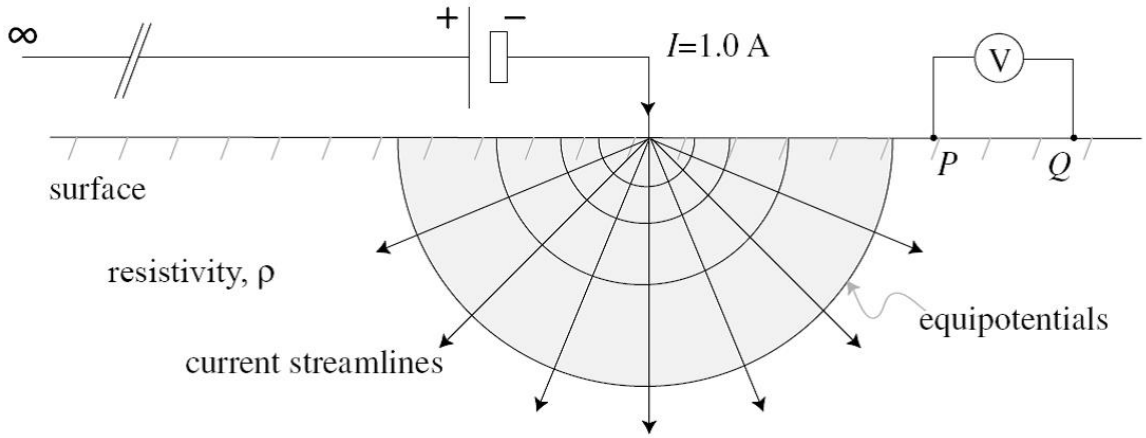

Fig. 2.5. Voltage measured between points P and Q for a point source of electric current injected into a half-space of uniform resistivity, ρ (Briaud et al. 2012)

Using Equation 2.4, the voltage potential measured across terminals P and Q is:

$$V_{\mathrm{PQ}} = V_{\mathrm{P}} - V_{\mathrm{Q}} = \frac{I\rho}{2\pi} \left\{ \frac{1}{r_{\mathrm{P}}} - \frac{1}{r_{\mathrm{Q}}} \right\} \tag{1.5}$$

where r_{P} is the distance from the current source to the potential electrode P, and r_{Q} is the distance to potential electrode Q.

All derivations so far have been made assuming that the subsurface is homogeneous, but in reality the spatial resistivity of the Earth is heterogeneous. Apparent resistivity, ρ_{a}, is the resistivity that would have been measured if the Earth was, in fact, homogeneous. Apparent resistivity is found by rearranging Equation 2.5 so that:

$$\rho_{\mathrm{a}} = \frac{2\pi V}{I} \left\{ \frac{1}{r_{\mathrm{P}}} - \frac{1}{r_{\mathrm{Q}}} \right\}^{-1} \tag{1.6}$$

which is how the measured apparent resistivity data for this research are estimated should the electrode configuration in Fig. 2.5 be used. For this research, instead a four electrode configuration is used as in Fig. 2.6.

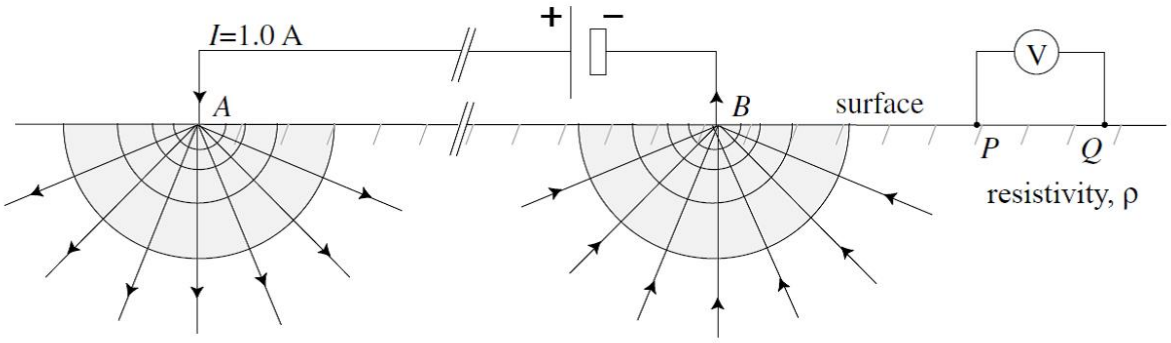

Fig. 2.6. Voltage measured between points P and Q for a point source A and point sink B of electric current (Briaud et al. 2012)

With both a current source and current sink the apparent resistivity is:

$$\rho_a = \frac{2\pi V}{I}\left\{\frac{1}{r_{AP}} - \frac{1}{r_{AQ}} - \frac{1}{r_{BP}} + \frac{1}{r_{BQ}}\right\}^{-1} \tag{1.7}$$

which is the general equation for all arrays that use four electrodes. Equation 2.7 can be simplified for established array types where the distances are specified between current and potential electrodes.

The current and potential electrodes in Fig. 2.6 can be arranged in many different combinations, but there are traditional four-electrode configurations. The array in Fig. 2.7 is the dipole-dipole array.

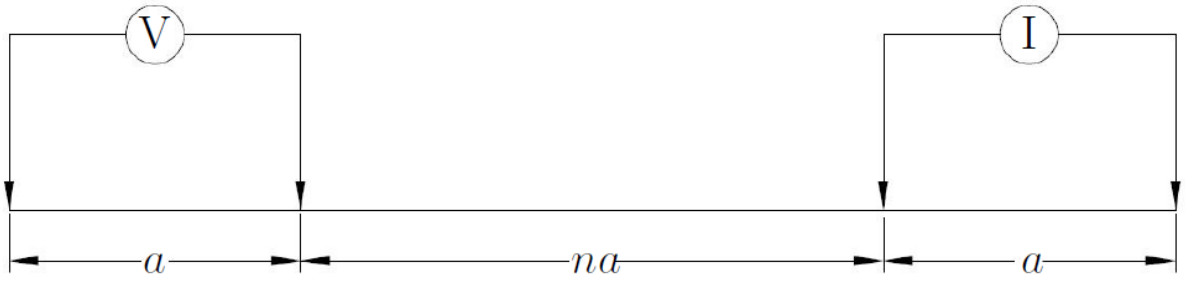

Fig. 2.7. Dipole-dipole array

Arrays vary by the spacing between the two sets of electrodes and the spacing in between the sets. Each array has advantages; some are capable of gathering deeper data, some are better at lateral changes, etc. Similarly, every array has disadvantages. The dipole-dipole array is used exclusively in this research as it is shown to yield the highest quality results for foundations using IP (Chapter 3). In the dipole-dipole array the spacing between the current electrodes and

the potential electrodes remains constant; the two sets of electrodes are separated by a factor of this spacing, n.

Induced Polarization Imaging

IP is a near surface geophysical imaging technique that is similar to electrical resistivity testing. Conrad Schlumberger first observed this in the early 1900s while he was using resistivity equipment in the field (Schlumberger 1920). The use of IP for infrastructure has not been widely documented other than considering the infrastructure a nuisance. Seigel (1959) stated that "strong (nonsulphide) IP responses were almost invariably found in the vicinity of man-made metal structures, such as grounded metal fences, pipelines, and railway tracks," which was seen as a burden that lead to erroneous conclusions.

Similar to ERI, IP also uses four electrodes consisting of two current and two voltage potential reading electrodes. For IP measurements, the current is introduced into the subsurface for a predetermine time window (2 s in this research) and then turned off. After this sudden stop, the voltage measured across the potential electrodes does not immediately drop to zero. Instead, Fig. 2.8 shows that the primary voltage, V_p, drops significantly to the secondary voltage, V_s, followed by an approximately logarithmic voltage decay (or transient voltage), $V(t)$. This behavior can be loosely considered analogous to the charging and discharging of a capacitor.

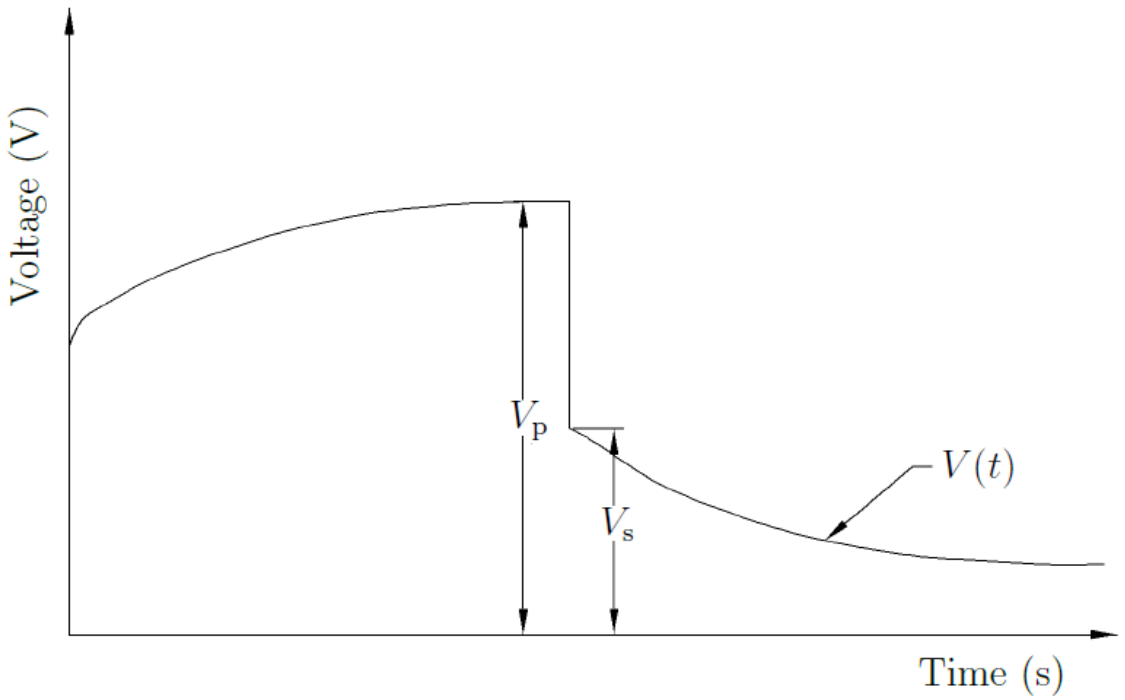

Fig. 2.8. IP decay curve

When current is turned on the voltage jumps to an initial increase followed by a similar build-up of current until the original amplitude is reached. According to Sumner (1976) the IP effect is due to electrochemical effects. When current is introduced into the ground, the current flow can cause chemical reactions with certain minerals. The chemical reaction in turn causes energy to be stored as chemical energy. When the current flow is disrupted, the chemical

reactions reverse while returning some of the stored energy as current, which decays in time. These chemical reactions are composed of two effects: electrode and membrane polarization (Deceuster and Kaufmann 2012).

Electrode polarization occurs when the soil matrix has metallic components in its pores. When current is applied, electrolyte ions concentrate at the interface between the metallic grains and electrolytes. When the current is turned off, these ions relax and return to their undisturbed distribution. The response shown on the inversions for this research is considered to be an effect of strong electrode polarization due to the steel in reinforced concrete acting as a metallic component in the concrete matrix of the foundation. Membrane polarization occurs when there is no metal, but instead ions in the electrolyte move through electrically open and restricted pores. Membrane polarization is found in clay rich environments. In order to determine which mechanism controls, an unreinforced foundation was tested in a sand rich environment and it showed little IP response indicating that electrode polarization is the controlling measurement for reinforced concrete.

The IP effect lies in measuring the decay and growth curves of voltages measured at the surface. These decay and growth curves are approximately logarithmic. This was determined by Scott and West (1969) using synthetic low porosity samples and an oscilloscope to visualize the curves. Prior to their work, it was thought that decay curves were exponential. Even today, visualizing these decay curves can be a useful tool for quality control of data.

The fundamental law of IP relates the polarization, $\vec{P}$, with current density, $\vec{J}$:

$$\vec{P} = -M\vec{J} \tag{1.8}$$

where $\vec{J}$ is current density in A/m^2. The chargeability, M, is dimensionless. From Equation 2.8, $\vec{P}$ is proportional to the negative of the secondary voltage, V_s, and $\vec{J}$ is proportional to V_p, the primary voltage, so that:

$$M = \frac{V_s}{V_p} \tag{1.9}$$

which is the fundamental, and theoretically, observable measurement of the IP effect. Even though chargeability is a dimensionless quantity, it is often defined in terms of millivolts per volt (mV/V). According to Sumner (1976), while the fundamental law holds true for ideal and theoretical measurements, in practice chargeability is measured as an area under the decay curve rather than by Equation 2.8. The equipment used for this research, the Advanced Geosciences, Inc. (AGI) SuperSting™R8/IP multi-channel imaging system, estimates the chargeability by measuring the transient curve and projecting the curve to zero time so V_s can be estimated and Equation 2.9 is used.

Chargeability is also presented as Sumner (1976) suggested; the integrated area under the transient decay curve in Fig. 2.8 normalized by V_p. Equation 2.10 more easily shows the relationship of chargeability with a capacitor as mentioned earlier:

$$M = \frac{1}{V_p}\int_{t_1}^{t_2} V(t)\mathrm{d}t \tag{1.10}$$

where V_p is the measured voltage when the current is turned on, and $V(t)$ is the transient voltage integrated over a time window between t_1 and t_2. The integrated chargeability is in ms. Equations 2.9 and 2.10 are considered equal due to the Newmont M331 standard. The standard is derived from a standard pulsed square wave and the integration time of the secondary voltage (Dolan and McLaughlin 1967). Using the Newmont Standard the two units of measurement are interchangeable; however, mV/V are used exclusively for this study. Note that IP can be measured in both the time domain and the frequency domain; time domain is used exclusively in this research.

Depth of Investigation

A common source of confusion for geophysical methods is the depth of investigation. As a rule of thumb, the penetrating depth for ERI and IP surveys is 15–25 percent of the longest array length for a four electrode array. The actual depth of penetration also depends on the subsurface resistivity distribution. The maximum depth of the inverted section using Advanced Geosciences, Inc.'s (AGI's) EarthImager 2D™ is determined by the median depth defined by Edwards (1977):

$$n(n+1)(n+2)\{[n^2+u]^{-1/2}-2[(n+1)^2+u]^{-1/2}+[(n+2)^2+u]^{-1/2}\}=1 \qquad (1.11)$$

where

$$u=4(z_{\text{med}}/a)^2 \qquad (1.12)$$

in which n and a are the electrode spacing variables from Fig. 2.7. This depth of investigation equation was found by empirically deriving depth coefficients and applying them to both theoretical and actual field cases. The depth of investigation was applied to field cases where there were multiple data sets with different dipole lengths. This formula was used so the data sets could be combined to make one complete set. Initially, the full depth where the elementary volume of earth contributed the max at the surface was used but discrepancies from the ideal dipole occurred at low values of n. This issue was resolved by instead using z_{med}, the depth where exactly half of the total signal originates from above and below the point.

3. EXPERIMENTATION

INTRODUCTION

This chapter is broken into four sections: an introduction to the equipment, the testing procedure, testing at a National Geotechnical Experimentation Site (NGES), and testing at bridges in the Bryan TxDOT District. The NGES testing was analogous to laboratory testing; it was used for planning full scale surveys and for determining the proper testing procedures. The bridges in the Bryan TxDOT District were the full scale tests that are also used for finalizing the full scale survey protocol and for calculating the probability of non-exceedance curve.

EQUIPMENT

The AGI SuperSting™ R8/IP multi-channel imaging system was used exclusively for data collection. The SuperSting™ was capable of simultaneously measuring in eight channels for potential readings with each current injection, which decreases survey time. Four sets of cable were available at TAMU, each with 14 electrode take-outs at 2 m spacing. The field setup for IP was slightly different than normal resistivity surveys, requiring a line of non-polarizable (NP) electrodes parallel to each stainless steel (SS) electrode. This means that two cables were used for the SS electrodes and two for the NP electrodes with a maximum line length of 54 m (28 electrodes, spaced the maximum 2 m). While this limited length affected the depth of investigation, the system was capable of handling larger arrays if more cables and electrodes were available. Fig. 3.1a depicts the appearance of the field set up.

The current injecting SS electrodes were 45 cm long, 1 cm diameter stainless steel rods that connect directly to the cable take-outs. The NP electrodes had a porous tip with a plastic casing that contained a copper rod surrounded by a copper sulfate solution in contact with the porous stone, which was buried in the ground. The NP electrodes (Fig. 3.1b) were used because polarization voltages at the contact between the SS electrodes and the ground can cause debilitating noise to the survey. As previously mentioned, IP was a phenomenon captured during resistivity surveys, so the NP electrodes were not required but the more sensitive NP electrodes collected higher quality data so they were used for bridge foundation surveys.

(a) Field setup

(b) NP electrode

Fig. 3.1. SuperSting™ equipment

The SuperSting™ was powered by a 12V deep cycle marine battery. Command files can be written in the office and then uploaded to the SuperSting™ in the field using a laptop. An advantage of the SuperSting™ was that once data were collected, they were instantly saved to the equipment so if power was lost or if the system froze the entire survey did not have to be redone. Once the survey was complete, the data were extracted from the SuperSting™ and then uploaded into a data processing system such as AGI EarthImager™. A full data acquisition protocol manual for ERI and IP surveys of bridge foundations is included in Appendix B.

TESTING PROCEDURE

To collect quality ERI and IP data simultaneously two sets of electrodes were necessary. The SS electrodes were pushed or driven straight into the ground until the cross bar was approximately 2 cm above the ground surface in a straight line at set intervals. The NP electrodes were buried approximately 0.3 m from each stainless steel electrode so that the entire porous stone tip was in the ground. The stone had good contact with the ground. If the ground was soft, the soil was slightly loosened and the NP electrode pushed into the soil. If the ground was very stiff, a hole was dug deep enough so the stone could be buried and the soil was mixed with water and back filled so the electrode could be pushed in without damaging it. If the porous stone did not have good contact with the soil (i.e., there were voids around the tip caused by soil clumping after the hole was dug) the IP decay curves appeared jagged and were removed from the data set.

The electrode cables were numbered for each electrode take-out where an electrode was connected. Each NP electrode was connected to the cable take-out using alligator clips so that the copper rod exposed above the chamber was in contact with the takeout or using alligator to

alligator cables (Fig. 3.2a). The SS electrode crossbars were in contact with the cable take-out. Each electrode had a spring attached to it so that the cable was held in place on the crossbar during the survey. The spring over the cable holding it in place is seen in Fig. 3.2b along with the installed electrodes.

(a) Non-polarizable electrode connection (b) Electrode installation

Fig. 3.2. Electrode connections

Two of the four cables were numbered 1–14 and two were numbered 15–28. For a typical ERI/IP data set, one of each cable section was connected to another so that two long cable sections were numbered 1–28. For bridge foundations, the electrodes were spaced equal to or less than the width of the foundation tested. As depicted in Fig. 3.3, the electrodes were installed so that the SS electrodes were on one side of the foundation and the NP electrodes were on the other side of the foundation for a pile, with the pile in the center of the array. If an abutment was tested, the line of SS electrodes was as close to the abutment as possible and straight along the side of the abutment. The line of NP electrodes was offset from the SS line with approximately 0.3 m space between the two lines.

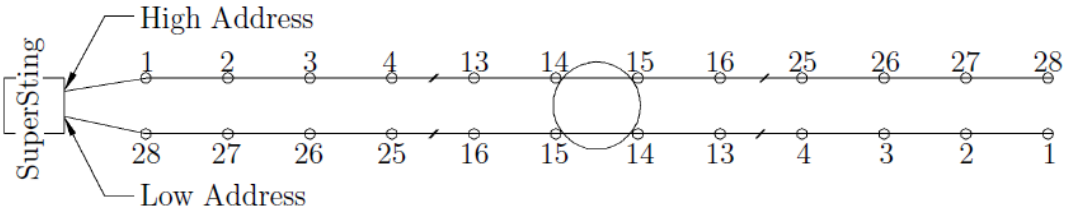

Fig. 3.3. Field setup of SuperSting™ with 28 take-outs

Fig. 3.3 shows a schematic of the field set up including the cable layout. Note that sections of the cables were removed for space in the schematic but the continuous string of electrodes was necessary in the field. The connector after the 28th takeout with the NP electrodes was connected to the low address port and the connector before the first takeout with the SS electrodes was connected to the high address port on the SuperSting™. The free ends of the cables away from the test box were *not* be connected. The cable sections was laid out as shown to use the command file and settings on the SuperSting™ described in Appendix B.

THE INVERSION PROCESS

The inversions shown in this chapter used the commercial software AGI EarthImager 2D™ (AGI 2007). The inversion process is a three step process: measured apparent resistivity, calculated apparent resistivity, and inverted resistivity. Fig. 3.4 shows the three steps.

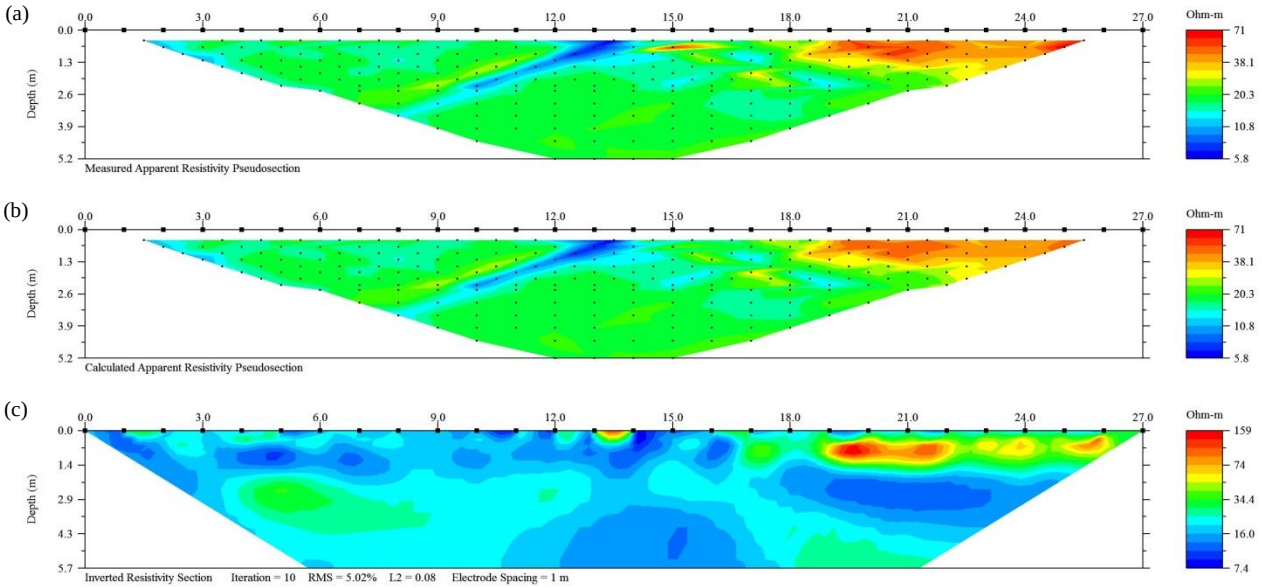

Fig. 3.4. Example of the inversion process: (a) measured apparent resistivity pseudosection; (b) calculated apparent resistivity pseudosection; (c) inverted resistivity section

The top image is the measured apparent resistivity from which a 2.5D forward model is created. The model is considered 2.5D because the model is 2D but the electrical field created to gather the data is 3D. The governing 2D partial differential equation was solved to get the forward solution:

$$\frac{\partial}{\partial x}\left(\sigma\frac{\partial V}{\partial x}\right)+\frac{\partial}{\partial z}\left(\sigma\frac{\partial V}{\partial z}\right)-k^2\sigma V=-I\cdot\partial(x)\cdot\partial(z) \qquad (2.1)$$

where σ is electrical conductivity (the inverse of electrical resistivity) as a function of x and z, V is scalar electric potential, k is the wave number, and I is electric current. Next, the inverse simulation was created from the forward model to reconstruct the subsurface resistivity and IP distributions. Fig. 3.4 shows the three step process for an ERI survey: displaying the measured apparent resistivity pseudosection, the calculated apparent resistivity, and the inverse simulation. ERI and IP simulations are processed simultaneously.

The data points (measured and calculated) were represented by the black dots in the top and middle image of Fig. 3.4. The plotting depth and location for each of these data points were approximated and displayed on the pseudosections. As shown in Fig. 3.4, the measured apparent resistivity associated with a pair of current electrodes and a pair of potential electrodes was plotted at the intersection of two lines originating from the middle of the electrode pairs that were rotated 45° from the surface.

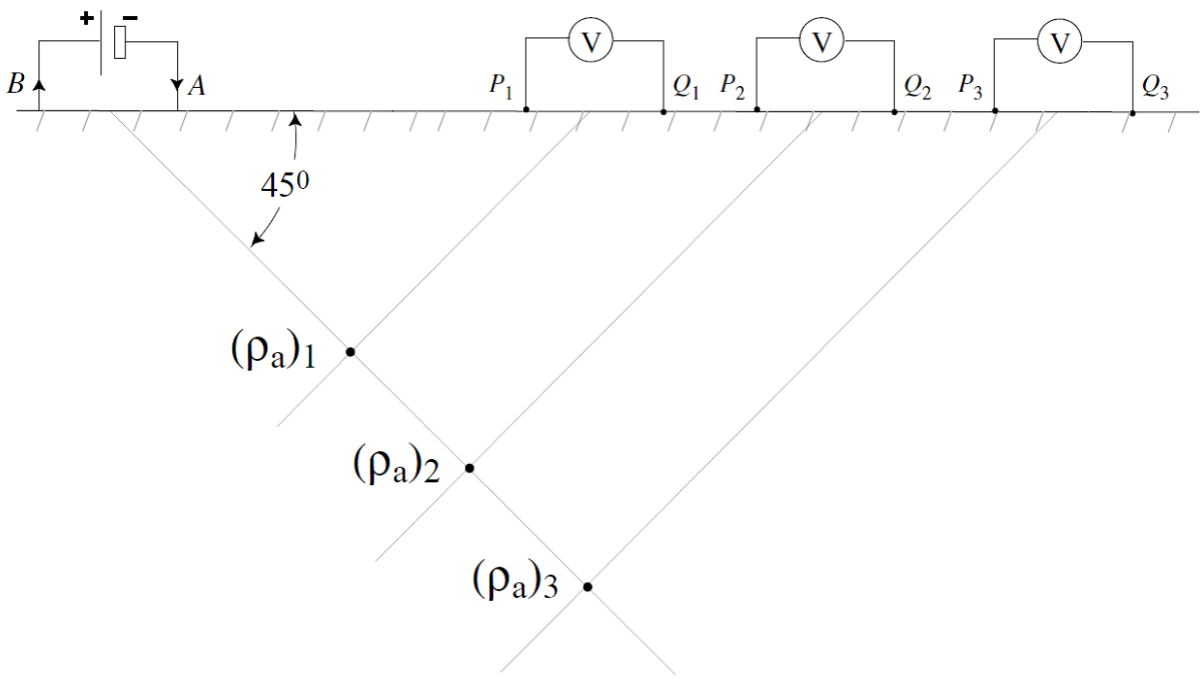

Fig. 3.5. Dipole-dipole array apparent resistivity pseudosection (Briaud et al. 2012)

The point plotted was where the two 45° lines intersect. The actual depth of penetration also depended on the subsurface resistivity distribution. For example, a conductive overburden decreased the penetrating depth dramatically. This was an approximate representation of the bulk resistivity of the subsurface. An apparent resistivity measurement was regarded as a weighted sum of the resistivity distribution of the entire earth. The pseudosection was displayed by color contouring the apparent resistivity data. Also, note that the shape of the apparent resistivity shaded contours was triangular. The triangular shape was related to the shape of Fig. 3.5, showing that the measured data had the greatest sensitivity to the ground bound by the triangular region in Fig. 3.5. The outer blank regions in Fig. 3.4 were the regions where the data were minimally affected.

Once the forward model was created, the elements in the model were compared to the measured data or the synthetic data. The goodness of fit of the calculated data was characterized by the Root Mean Square (RMS) error:

$$RMS = \sqrt{\frac{\sum_{i=1}^{N}\left(\frac{d_i^{\text{Pred}} - d_i^{\text{Meas}}}{d_i^{\text{Meas}}}\right)^2}{N}} \times 100\% \qquad (2.2)$$

where d_i^{Pred} is the calculated data, d_i^{Meas} is the measured data, and N is the total number of data points. The RMS is the average misfit over all the data points. As a rule of thumb an RMS less than 3 percent is considered an excellent fit, 3–5 percent is a good fit, 6–10 percent is an okay fit but should be interpreted with caution, and greater than 10 percent is a low quality model for the gathered data. After calculating the RMS, the inverted resistivity section was updated with the latest forward model pseudosection. The inverted section transformed the earth's response to the user defined injection of an electric field to the true resistivity subsurface distribution. The

maximum depth of the inverted resistivity section was determined by the median depth defined by Edwards (Edwards 1977) and a user defined depth factor. The median depth was discussed in Chapter 2.

The inversion in Fig. 3.4 converged to an RMS of 5.02 percent in 10 iterations. Thus the calculated data were compared to the measured data, the RMS was higher than the stop criteria of an RMS of 5 percent set before the process was started, and the calculated data were updated for the second inversion after which the RMS was still higher. This process repeated until the calculated RMS was less than the stop criteria RMS. The IP simulation was very similar except the forward model was not calculated based on the measured IP data, it was calculated using the forward model from the resistivity data. The resistivity model was used to significantly reduce the numerical errors in the IP inversion process. This was why, upon inspection, the RMS for the inverted IP section had units of mV/V.

Additionally, in the following sections it was shown that ERI was not successful at imaging slender foundations like those typically used in the Bryan TxDOT District. ERI was included for these surveys to provide additional information pertaining to the quality of the IP model. IP data that were correlated with ERI data with a low RMS were better than IP data correlated with ERI data with a high RMS, even if the IP RMS was less than the ideal 3 percent previously mentioned.

NATIONAL GEOTECHNICAL EXPERIMENTATION SITE

The NGES was located on the Texas A&M Riverside Campus approximately 16 km west of College Station, Texas. There were two soil sites on Riverside Campus available for testing: a sand site on the East side of the campus and a clay site on the west side of the campus. The sand site was used exclusively in this research. The stratigraphy at the sand site consisted of a medium dense tan silty fine sand to 3.5 m below the surface, medium dense silty sand with clay and gravel from 3.5 to 7 m, medium dense silty sand to sandy clay with gravel from 7 to 11 m, and very hard dark gray clay from 11 to 33 m. The water table at the sand site was located 4.9 m below the surface (Gibbens 1995). The overall soil characterization at the sand site was a medium dense, silty, fine, siliceous sand (Ballouz et al. 1991).

The sand site had both shallow and deep foundations. Five of the shallow foundations were founded at 0.76 m in the sand. Two of these footings were $3 \times 3 \times 1.2$ m^3, one was $2.5 \times 2.5 \times 1.2$ m^3, one was $1.5 \times 1.5 \times 1.2$ m^3, and one was $1 \times 1 \times 1.2$ m^3. These footings were built in the mid-nineties (Gibbens 1995). There was also a $3 \times 3 \times 1$ m^3 fully embedded footing that was constructed in 2010 (Dunn 2010) as well as other undocumented foundations surrounding the footings. Fig. 3.6 shows the overall topography of the sand site. The survey lines shown on Fig. 3.6 were ERI surveys from a previous study (Arjwech 2011).

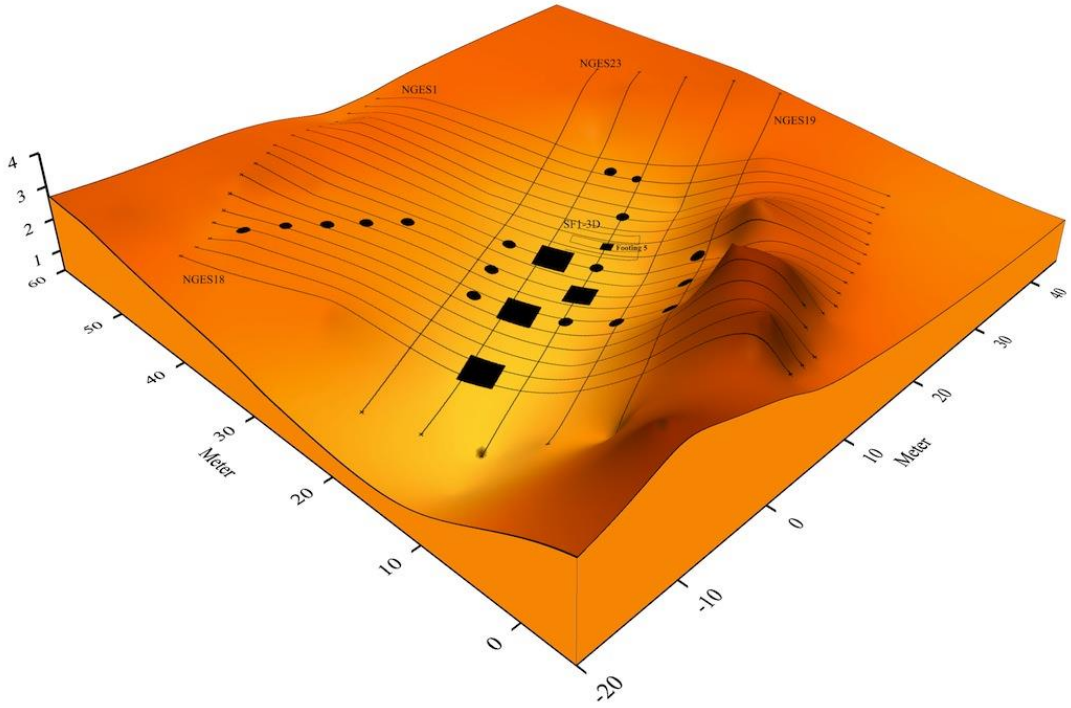

Fig. 3.6. Topography and foundation layout at the sand site (Arjwech 2011)

The deep foundations were drilled at the sand site in November 1990 for a FHWA project. Five drilled shafts were drilled wet at the sand site with planned defects (Fig. 3.7). The five shafts on the right were at the sand site. Fig. 3.7 shows the planned defects: necking, a bulb, a cave-in, and a tremie defect. The shaft with necking labeled RS #1 also had a traffic signal mounted on it.

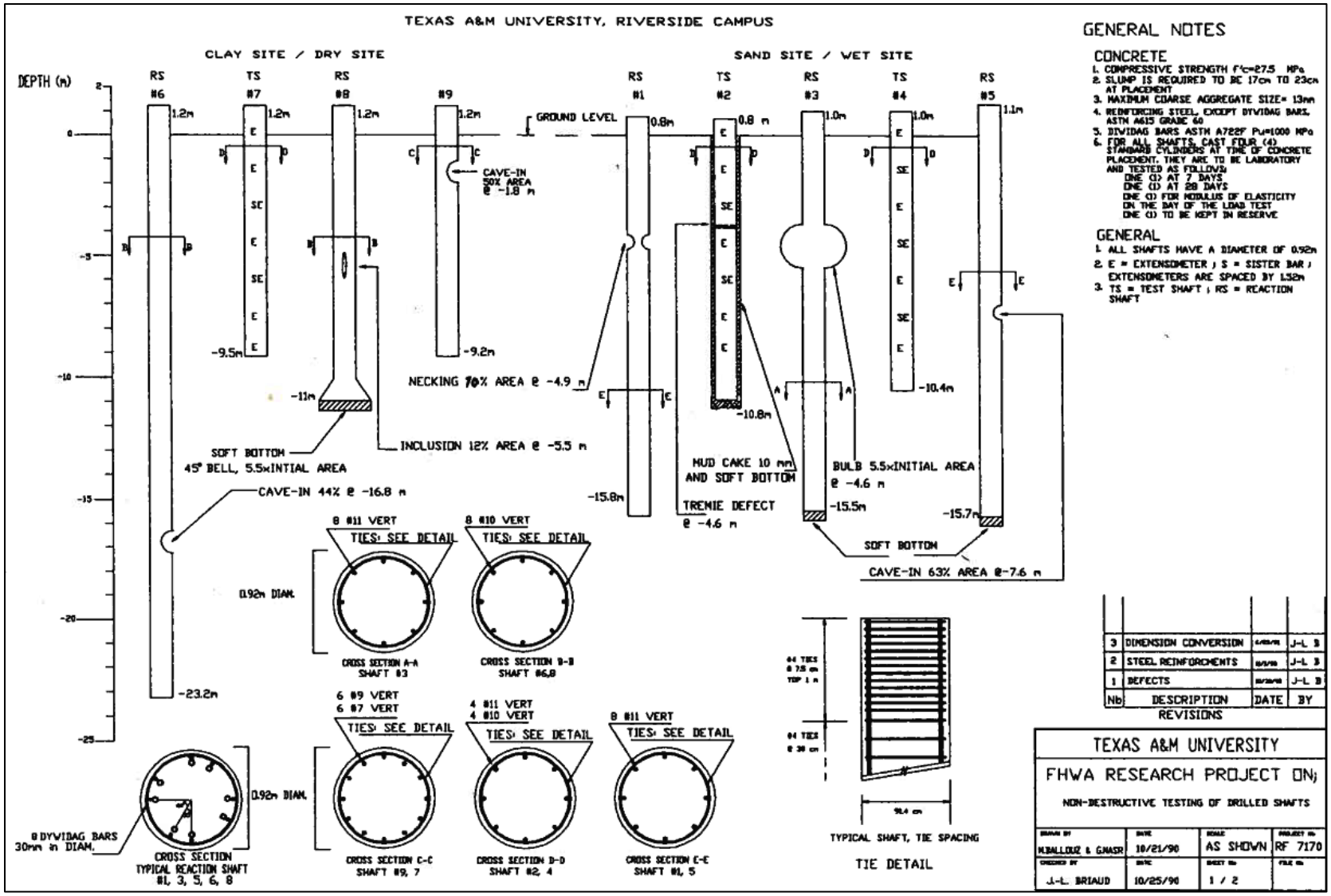

Fig. 3.7. Construction plan for the drilled shafts (Ballouz et al. 1991)

Shallow Foundations

Two shallow foundations at the NGES were tested and discussed in this section. The first was the 1 × 1 × 1.2 m^3 foundation. This foundation was used for investigating three field parameters for optimal results: the effect of electrode location relative to the foundation, the effect of the IP cycle time, and the effect of the array type used.

Electrode Locations

The first NGES test was the 1 × 1 × 1.2 m^3 foundation that was embedded 0.76 m (Gibbens 1995). This foundation was tested several times before larger foundations were investigated. Using the 1 × 1 × 1.2 m^3 foundation, different electrode configurations were investigated, specifically regarding the location of the foundation with respect to the electrode line.

The control test was a 13 m long array with electrodes spaced at 1 m. The foundation was located between the 7th and 8th electrodes as drawn on the image in Fig. 3.8. The SS electrodes and NP electrodes were parallel to each other with 0.3 m between the two lines. For the control test, the dipole-dipole array was used with a 2 s delay time on the IP survey. These settings were chosen based on recommendations from the literature.

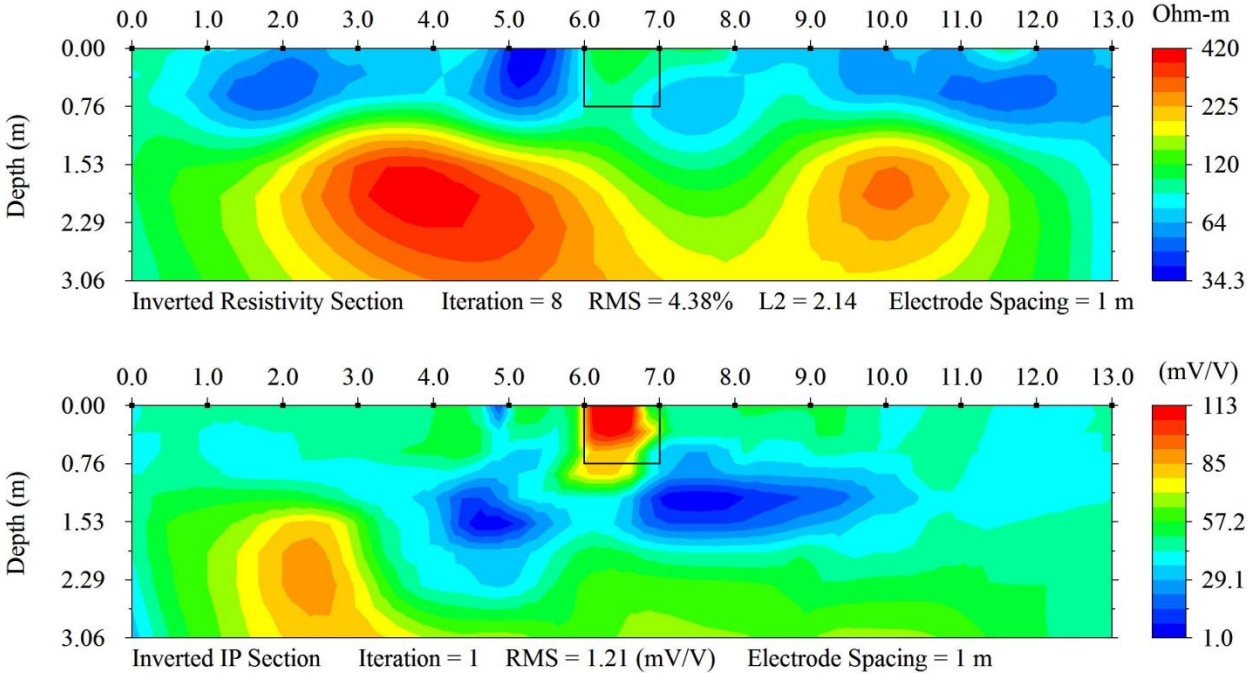

Fig. 3.8. Control test at the NGES: inverted resistivity section (*top*); inverted IP section (*bottom*)

The inverted resistivity section converged within eight iterations with an RMS of 4.38 percent. Note that an RMS of less than 5 percent was considered good quality data. The IP data were only inverted once with an RMS of 1.21 mV/V. No definitive foundation was seen on the inverted resistivity section, most likely because there was not a large contrast between the

soil below and the foundation at this site. The inverted IP section showed a strong IP response within the boundaries of the foundation.

Fig. 3.8 shows the foundation directly in the center of the electrode line, with the 7th NP and SS electrodes on one side of the foundation and the 8th NP and SS electrodes on the other side. The electrodes were shifted to the side of the foundation so the foundation no longer directly bisects the line but instead was side scanned. Fig. 3.9 shows the electrode line side scanning the $1 \times 1 \times 1.2$ m^3 foundation with the SS electrodes next to the foundation.

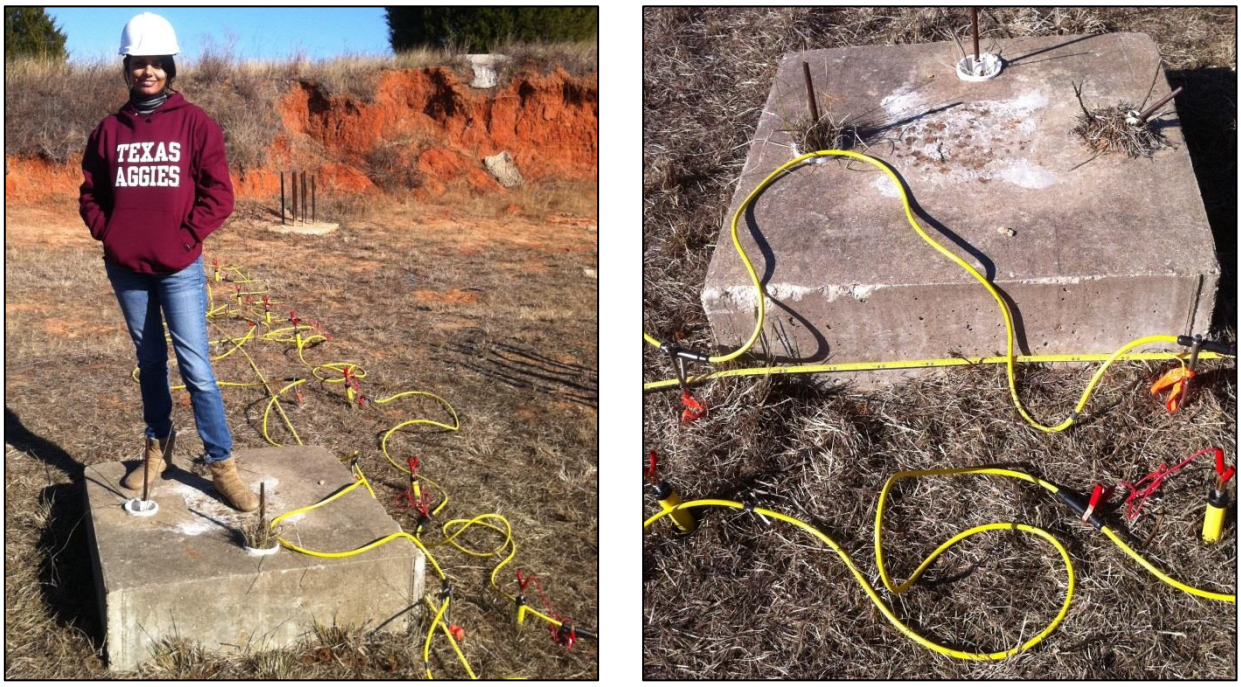

(a) Test site (b) Experimental setup

Fig. 3.9. Side scan with SS electrodes next to the foundation

Fig. 3.10 depicts the inversion of the test in Fig. 3.9. The resistivity section converged in eight iterations with an RMS of 2.64 percent. Despite the low RMS of the model, no clear resistivity response was shown in the top profile, similar to Fig. 3.8. The large highly resistive anomalies at the bottom of Fig. 3.10 were also seen in Fig. 3.8 as well as in other tests on this foundation.

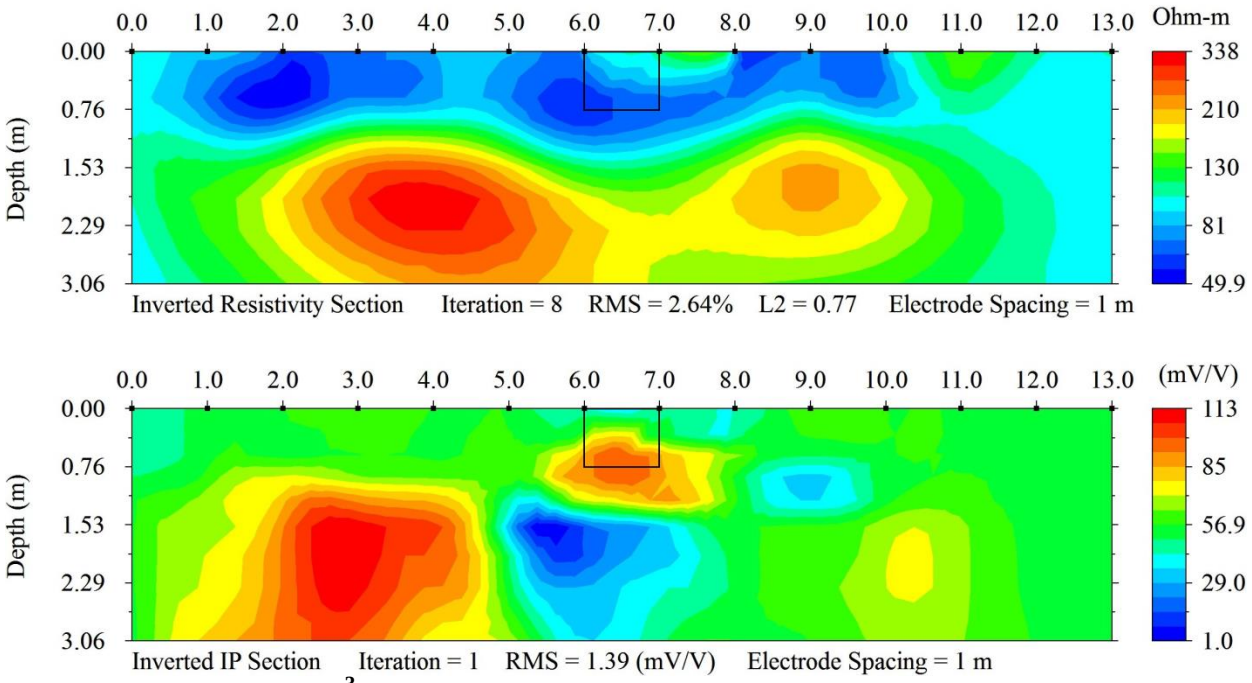

Fig. 3.10. 1 × 1 × 1.2 m^3 foundation side scan with SS electrodes next to the foundation: inverted resistivity section (*top*); inverted IP section (*bottom*)

The IP inversion showed an IP response at the bottom of the foundation, but it was a large anomaly deeper and wider than the foundation. Comparing this to Fig. 3.8 the interpretation of the foundation depth was less definitive. Again, the RMS (1.39 mV/V) showed that the model was a good fit to the data.

Similarly, in Fig. 3.11 the foundation was side scanned, but with the NP electrodes next to the foundation and the SS electrodes offset. Again, there was a significant loss in the ability to identify the foundation compared to Fig. 3.8. Comparing the results from Fig. 3.8, Fig. 3.10, and Fig. 3.11 the advantage of aligning the array so that the foundation bisects the array was clear. The same foundation was easily discernible when the foundation bisects the array as compared to a side scan. If a side scan array was used because a foundation was too large to bisect the array, the SS electrodes were placed next to the foundation with the NP electrodes parallel.

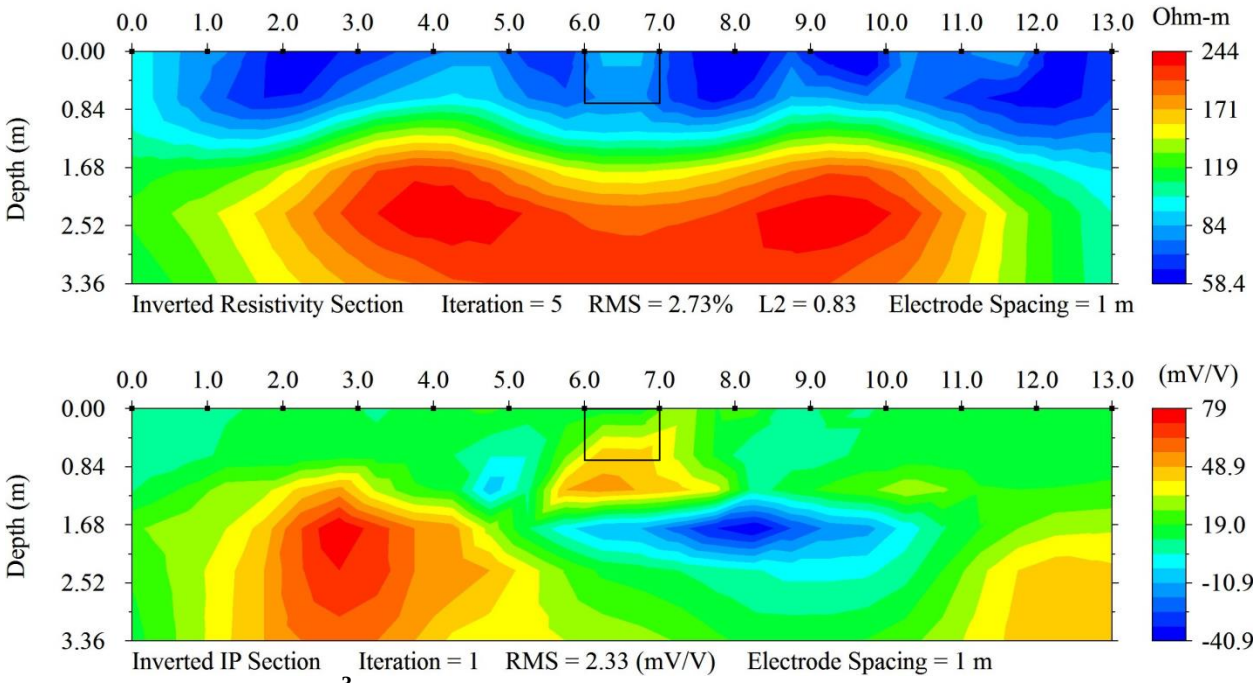

Fig. 3.11. 1 × 1 × 1.2 m^3 foundation side scan with NP electrodes next to the foundation: inverted resistivity section (*top*); inverted IP section (*bottom*)

IP Cycle Time

Once the optimal electrode setup was established, the effect of the IP delay time was investigated. Previous experiments had been run with a 2 s cycle time. This means that a positive current transmission was turned on for 2 s, off for 2 s, a negative current transmission was turned on for 2 s, and again off for 2 s. The SuperSting™ had five different cycle times: 0.5 s, 1 s, 2 s, 4 s, and 8 s. A dipole-dipole array was used with 28 NP and 28 SS electrodes spaced every 0.5 m (Fig. 3.12) using 1 s and 4 s to see if the results vary from the control test (Fig. 3.8). A smaller electrode spacing yielded higher resolution, so 28 electrodes were used instead of 14 to provide more detailed inversions with approximately the same array length (13.5 m instead of 13 m).

(a) Test site (b) Experimental setup

Fig. 3.12. IP delay test and array type test

Beginning with 1 s cycle time, no discernible foundation was seen in the resistivity section in Fig. 3.13, as expected. Additionally, the ERI section in Fig. 3.13 did not converge to an RMS of less than 5 percent within eight iterations as the 2 s cycle inversion (Fig. 3.8). The IP section in Fig. 3.13 showed a slight chargeable response, but the high response did not cover most of the foundation or penetrate to the full foundation depth as the 2 s cycle. Because these results were not as sharp as the 2 s cycle time, the 0.5 s cycle was not tested.

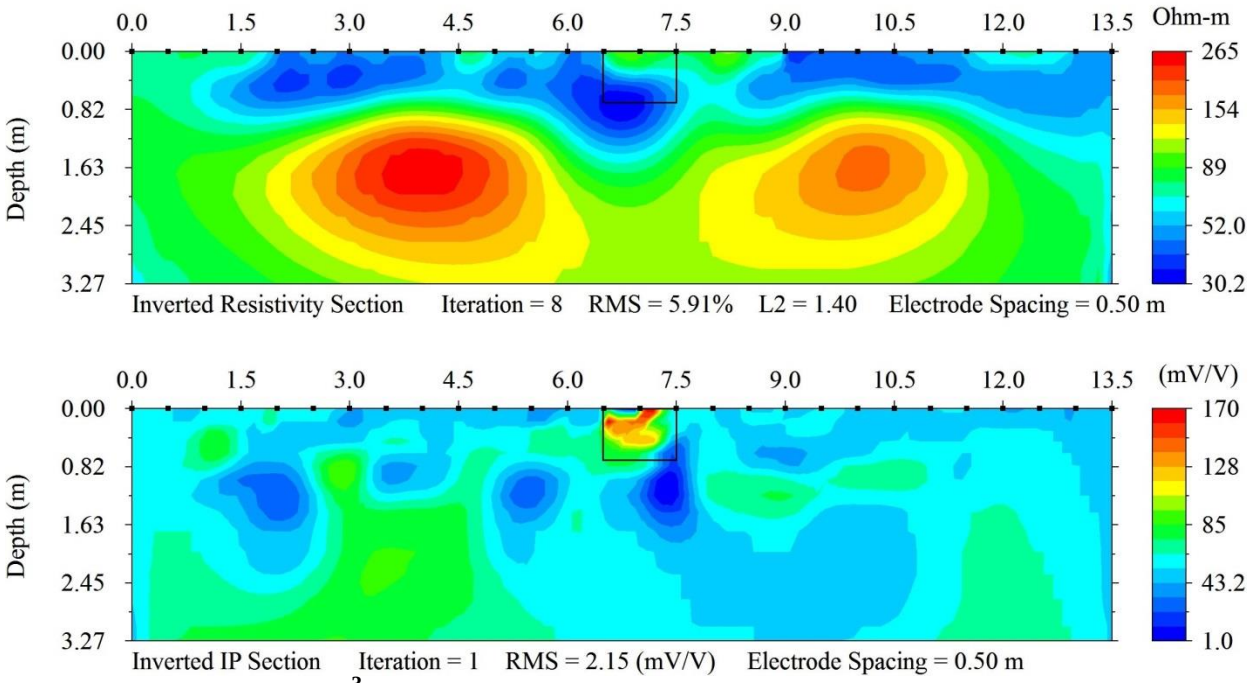

Fig. 3.13. 1 × 1 × 1.2 m^3 foundation with 0.5 m electrode spacing and 1 s IP cycle time: inverted resistivity section (*top*); inverted IP section (*bottom*)

Next, the 4 s cycle time was tested without moving the electrodes. While nothing was changed as far as installation from the 1 s test to the 4 s test, the number of negative apparent resistivity data greatly increased. There were seven negative apparent resistivity readings from the 1 s test and 31 in the 4 s cycle time test. Often, apparent resistivity was measured as negative when the surface voltage was too small to be measured accurately. These negative apparent resistivity values lower the number of data that was used in the numerical model and led to a survey with a higher RMS than in the 2 s survey.

The ERI profile in Fig. 3.14 showed little information about the foundation, but the IP section provided some details. Two zones of high chargeability (>360 mV/V) were noted on the surface of the foundation as well as a zone of over 180 mV/V within the boundaries of the foundation. Recall that the chargeability of the foundation was dependent on the amount of applied current as well as the cycle time so proceed with caution when comparing the 4 s cycle time to the 2 s cycle. Upon visual inspection there was no advantage of a 4 s cycle time over the 2 s, and the survey time was doubled. For this reason, the 8 s cycle time was not investigated. All surveys herein used 2 s cycle time unless specifically noted in this section.

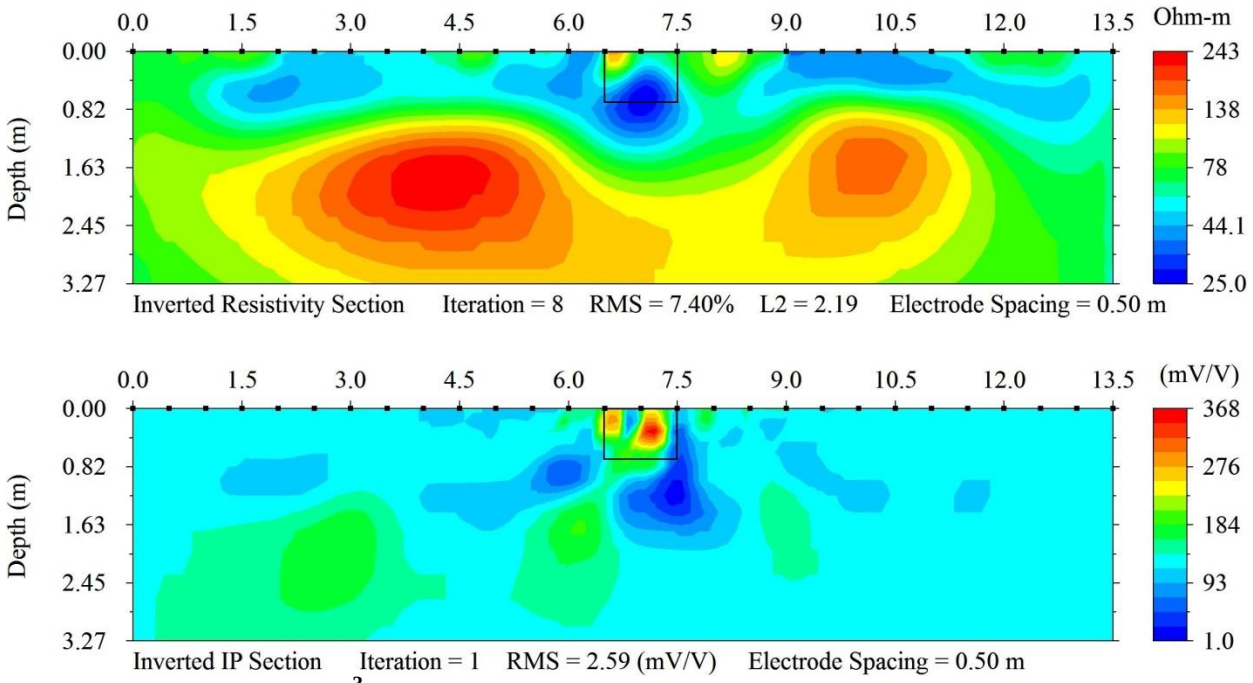

Fig. 3.14. 1 × 1 × 1.2 m^3 foundation with 0.5 m electrode spacing and 4 s IP cycle time: inverted resistivity section (*top*); inverted IP section (*bottom*)

Array Type

In addition to investigating the optimal electrode location and length of the IP cycle time, the optimal array type was examined. The dipole-dipole array was noted for its high resolution in imaging vertical structures (Deceuster and Kaufmann 2012) and it was used exclusively for all bridge surveys. Because IP had not been used for investigating bridge foundations prior to this research, the Wenner and Schlumberger arrays were given a trial run on the shallow footing and compared to the dipole-dipole results from Fig. 3.8.

The Wenner array was used first. Shown in Fig. 3.15, in the Wenner array the distance between the electrodes was constant and the voltage potential was measured between the current sources. The apparent resistivity using the geometric factor for the Wenner array was:

$$\rho_a = 2\pi a \frac{\Delta V}{I} \tag{2.3}$$

where ρ_a is the apparent resistivity, a is the spacing depicted by Fig. 3.15, ΔV is the voltage potential, and I is the electric current. The Wenner array had the highest signal to noise ratio and had good vertical resolution. The disadvantages of the Wenner array were its poor lateral resolution and that only a single channel was used for each measurement so surveys took longer.

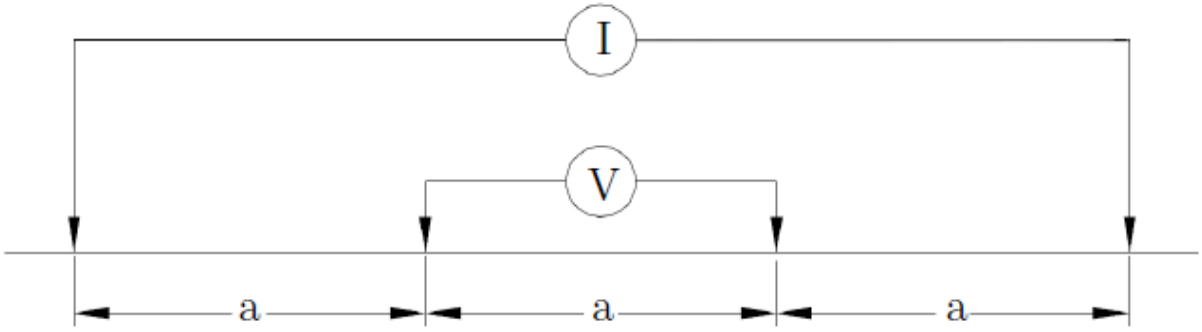

Fig. 3.15. Wenner array

Similar results were noted between Fig. 3.8 and Fig. 3.16 in terms of the inverted IP sections. Both showed a strong IP response penetrating over half the depth of the foundation. The significant difference between the two tests was the RMS of the ERI data. The RMS of the control test was 4.38 percent, which was accepted as a publishable RMS.

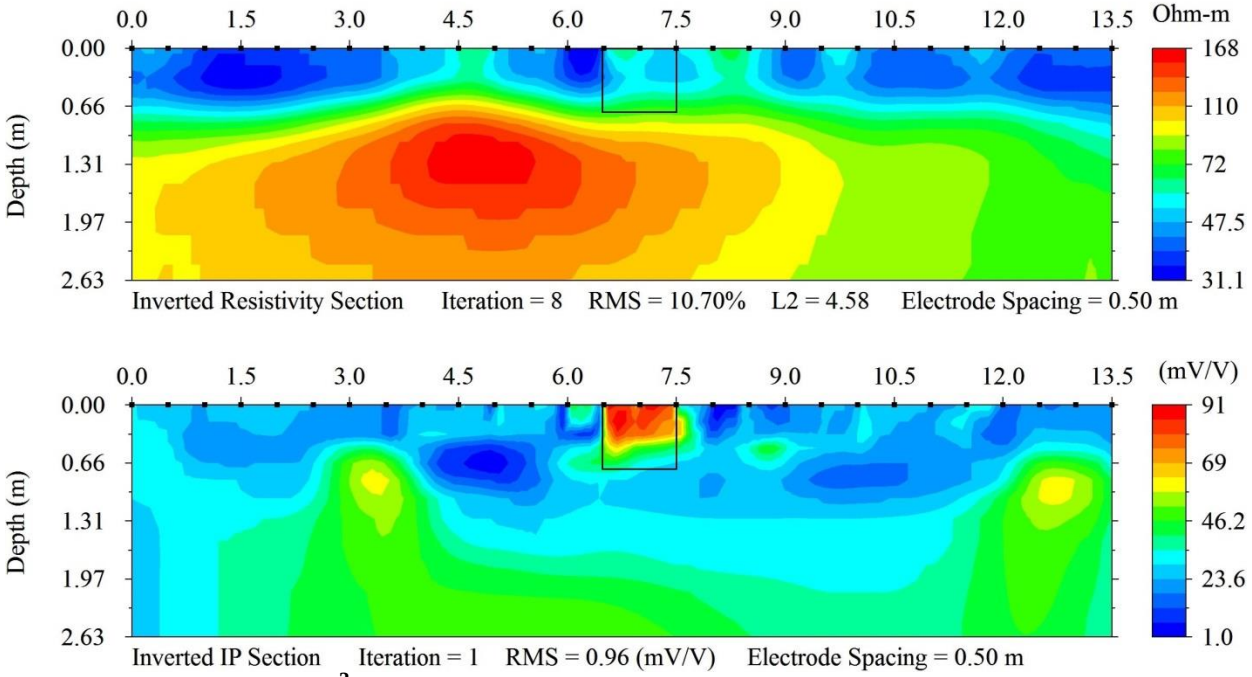

Fig. 3.16. 1 × 1 × 1.2 m^3 foundation with 0.5 m electrode spacing and the Wenner array: inverted resistivity section (*top*); inverted IP section (*bottom*)

The RMS for the Wenner test, however, was 10.70 percent so the error in the fit between the gathered data and the model had more than doubled. Similar to the Wenner array, the Schlumberger array was also only capable of using a single channel. The Schlumberger array changed the distance between electrodes. The apparent resistivity for the Schlumberger array was found by:

$$\rho_a = \frac{\pi(\frac{s^2 - a^2}{4})}{a}\frac{\Delta V}{I} \tag{2.4}$$

where s is the spacing shown on Fig. 3.17 and all other variables have been previously defined.

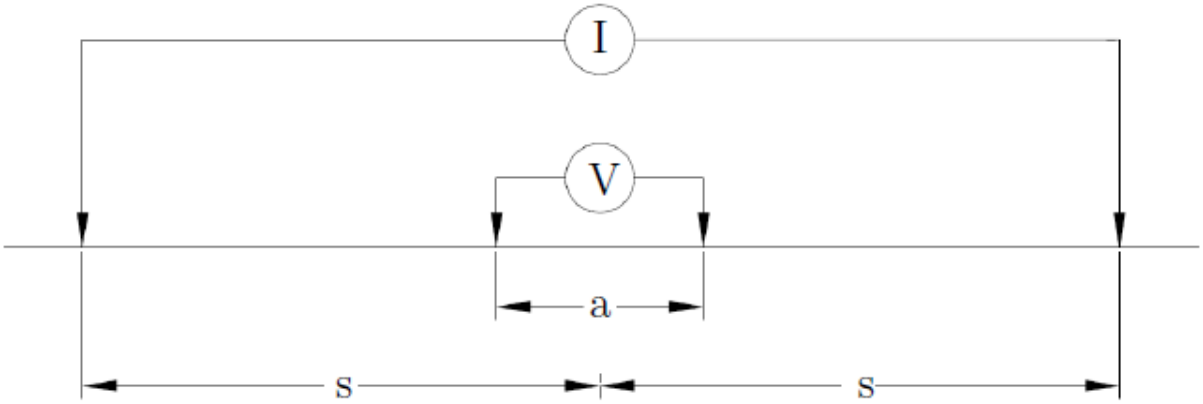

Fig. 3.17. Schlumberger array

The Schlumberger array test in Fig. 3.18 had an even higher RMS (13.53 percent) than the Wenner and dipole-dipole arrays. Additionally, the IP inversion did not show the high chargeability response surrounding the foundation that was observed in the Wenner and dipole-dipole arrays. A strong chargeability anomaly was noted at the bottom of the foundation, but it appeared deeper than the foundation and did not have the sharp resolution images of the arrays used for Fig. 3.8 and Fig. 3.18. Based on these experimental results of the same foundation, the dipole-dipole array was used exclusively in this research.

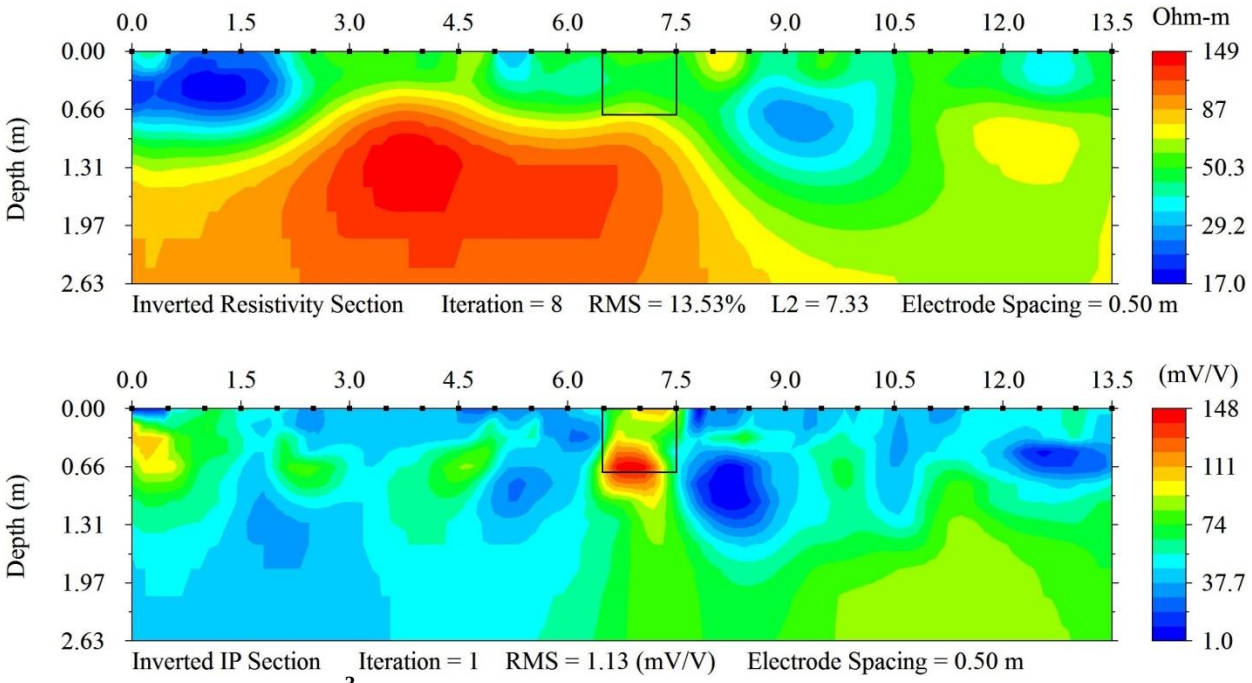

Fig. 3.18. 1 × 1 × 1.2 m^3 foundation with 0.5 m electrode spacing and the Schlumberger array: inverted resistivity section (*top*); inverted IP section (*bottom*)

The final experimental setup that was studied was whether the NP electrodes were necessary for this research. NP electrodes increased the installation time and were not necessary for collecting IP data. For reinforced concrete foundations, however, they were necessary in order to capture a measurable IP response. A 28 electrode dipole-dipole array with 0.5 m electrode spacing was used with only SS electrodes for collecting the IP data. Unfortunately, the IP decay curves showed no resemblance to the calculated IP curves and 93 percent of the data was removed based on the model criteria. If the model was forced to keep all the data, the ERI model had an RMS of 96.20 percent, and the RMS of the IP section was 4005.03 mV/V. These inversions were pure mathematical anomalies. In summary, all collected data unless otherwise noted used the dipole-dipole array with a 2 s IP cycle time and both SS and NP electrodes were used.

3 × 3 m^2 Foundation with Unknown Depth

Adjacent to the five large spread footings (Gibbens 1995) was a 3 × 3 m^2 foundation that was flush with the ground surface. The report for this foundation was not read until after the foundation was tested for a blind study (Dunn 2010). Because the foundation was 3 × 3 m^2 at the surface and the electrode take-outs on the SuperSting™ cables were spaced every 2 m, the array was set up to cross a corner of the foundation. Fig. 3.19 shows the 14 NP and 14 SS electrode line spaced every 2 m totaling 26 m.

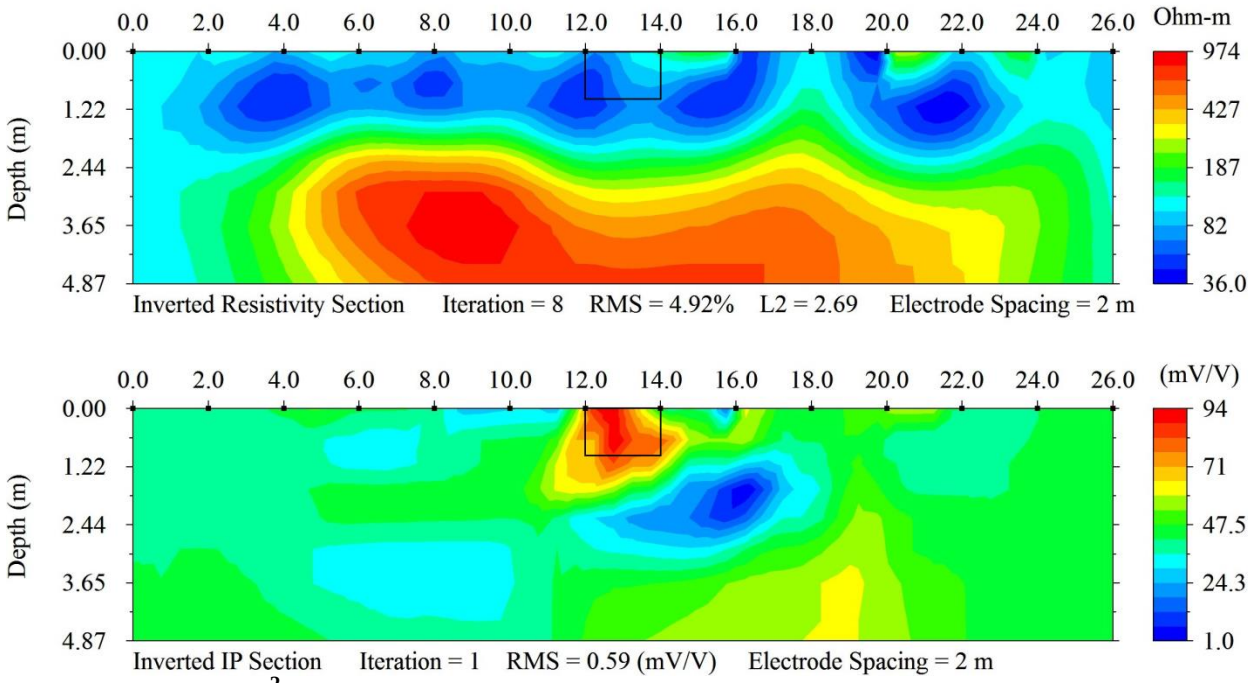

Fig. 3.19. 3 × 3 m^2 foundation with 2 m electrode spacing and unknown depth: inverted resistivity section (*top*); inverted IP section (*bottom*)

A 1.22 m thick surface layer was noted in the ERI section, which converged in 8 iterations to an RMS of 4.92 percent. No foundation was detected in the inverted resistivity section. The inverted IP section converged to an RMS of 0.59 mV/V, and an IP response of over 90 mV/V was observed in the location of the foundation. The highest response extended to approximately 1 m with a zone of over 70 mV/V extending to approximately 1.3 m. After the inversion process was complete the report for this foundation was read. The actual foundation was embedded 1 m and fully reinforced with # 6 reinforcing steel every 12.7 cm (Fig. 3.20) (Dunn 2010).

Fig. 3.20. 3 × 3 m^2 mat foundation (Dunn 2010)

If only the zone of the highest chargeability was accounted for, the foundation was predicted to the actual depth. If, instead, the zone that extended to 1.3 m was considered the foundation depth was over predicted. The decision criteria for the predicted depth of each foundation were discussed in Chapter 4. Using these criteria, the predicted depth was 1.15 m.

Deep Foundations

The NGES also contained five reinforced drilled shafts (Fig. 3.7), additional unknown foundations, and 41 steel H-piles piles. The 10.4 m embedded test shaft #4 (TS #4) from Fig. 3.7 was tested several times. The H-piles were used as a control test for testing methods on a different foundation material.

Unreinforced Foundation

Near the shallow foundations was a foundation that was believed to be 4 m deep. This assumed depth was the result of a resistivity survey (Arjwech 2011); however it has not been confirmed beyond this study. This foundation was unique because it did not appear to be reinforced and was encased in a plastic tarp, presumably to the depth of the foundation. Fig. 3.21 shows the results of this survey.

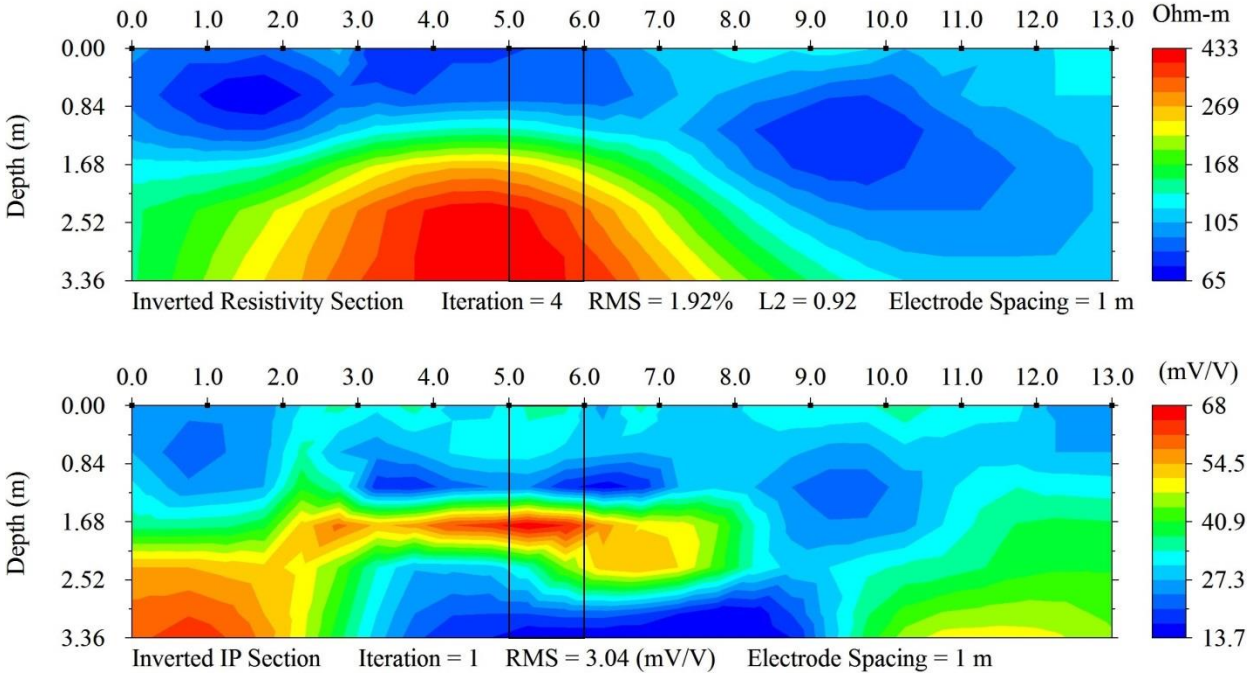

Fig. 3.21. Unknown foundation without reinforcement: inverted resistivity section (*top*); inverted IP section (*bottom*)

The RMS of the resistivity section converged to 1.92 percent in only 4 iterations and the IP to an RMS of 3.02 mV/V. Despite the low RMS, giving confidence in the numerical model, no clear foundation was seen in either section. The large highly resistivity zone did not correlate with the foundation and no unique zone of chargeability was seen in the IP section. The importance of rebar in a foundation in order to obtain a chargeable response was proved from

this test. Also, while rebar in concrete was necessary to estimate the depth of the foundation, this showed that IP can also be used to verify that a foundation in fact contains rebar.

Test Shaft #4

The deep foundation that was tested was Test Shaft (TS) #4 from Fig. 3.7 or the second closest foundation in Fig. 3.22a. This shaft extended 10.4 m into the subsurface and was built without defects. As an initial test, 14 NP and 14 SS electrodes were spaced every 1 m (Fig. 3.22b). Only 14 electrodes were used due to limited space.

(a) Test site (b) Experimental setup

Fig. 3.22. Test shaft #4

The quality of these data was very low and they were unable to converge to an acceptable RMS. This may be because the foundation was over three times deeper than the collected data. The inverted resistivity section in Fig. 4.20 stopped at 10 iterations with an RMS of 40.61 percent and from this model the IP section converged to an RMS of 8.07 mV/V. A zone of very high chargeability (over 600 mV/V) was seen at the bottom of the foundation that was deeper than the collected data, but the high RMS values made these interpretations unreliable.

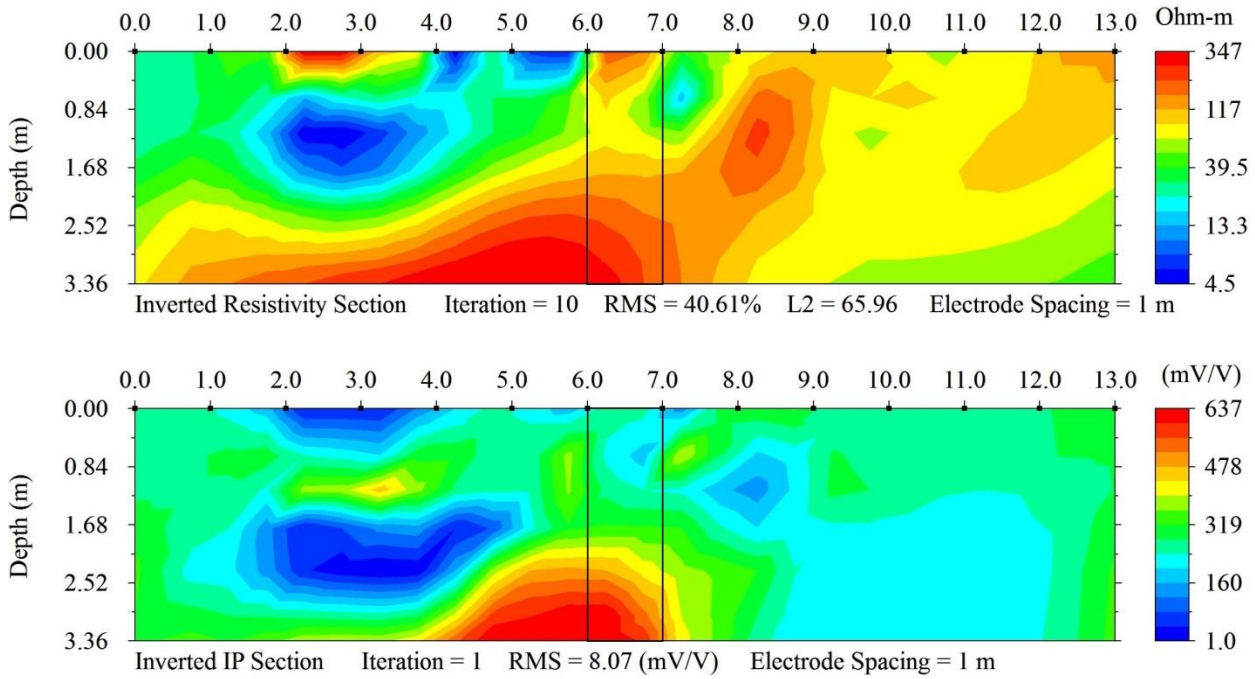

Fig. 3.23. Test shaft #4 at the sand site with 13 m long array: inverted resistivity section (*top*); inverted IP section (*bottom*)

Addressing the issue of collecting deeper data, TS #4 was next tested with 1 m spacing but using 28 electrodes. As previously mentioned, space near TS #4 was limited; there was an excavation beginning where the small trees were in the background of Fig. 3.22b, 15 m from the foundation and very tall thick brush 14 m from the foundation on the other side. For this reason, the test with 1 m spacing was angled so the foundation was side scanned (Fig. 3.24b).

(a) Test site (b) Experimental setup

Fig. 3.24. Side scan of TS #4

Again, the data collected were not as deep as the actual foundation (10.3 m), so the inversion in Fig. 3.25 showed very little in terms of the foundation depth. The inverted resistivity section had a zone of low resistivity along the middle of the pile, but it did not extend to the depth of the foundation. The IP inversion in Fig. 3.25 showed nothing relevant to the foundation depth and the RMS was very high (40.72 mV/V). The results may have been improved if it was possible to place the electrodes across the foundation as established with the shallow foundation experiment.

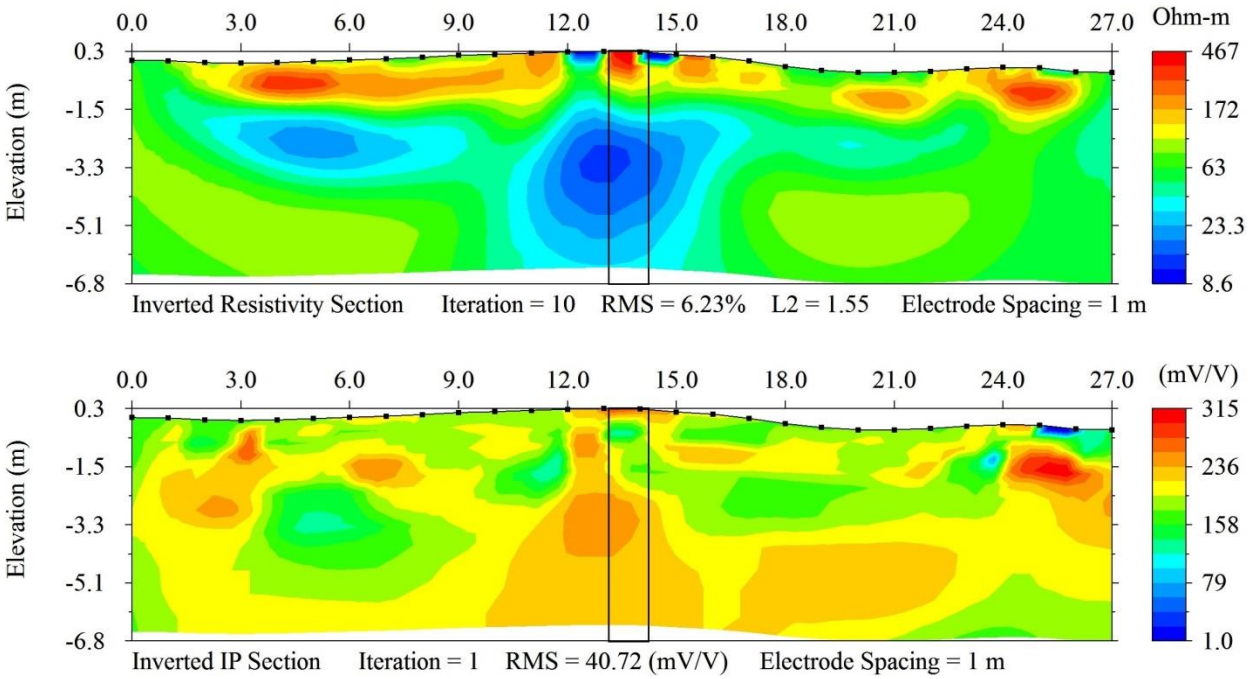

Fig. 3.25. Test shaft #4 at the sand site with 27 m long array side scan: inverted resistivity section (*top*); inverted IP section (*bottom*)

Similar results were seen in Fig. 3.26 when the electrode spacing was increased to 2 m. Increasing the spacing yielded deeper data, but the RMS for both tests were still too high to validate the results. Despite this, a very high zone of chargeability (700 mV/V) was located at the bottom of the foundation.

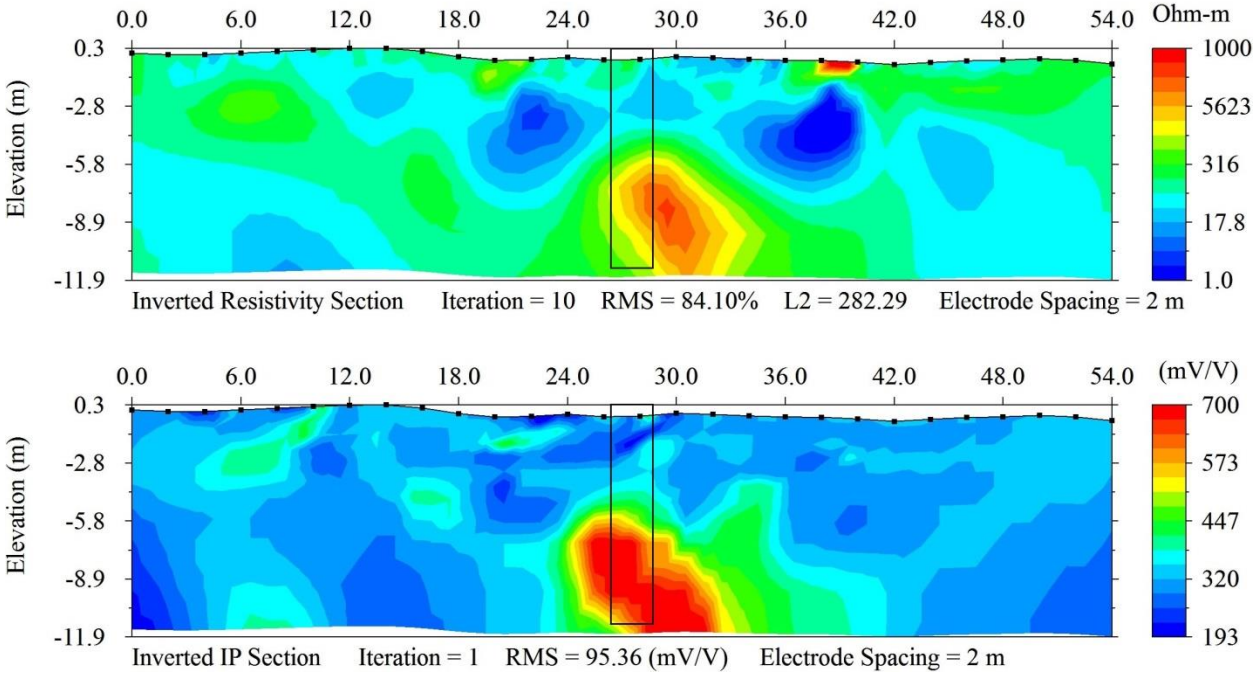

Fig. 3.26. Test shaft #4 at the sand site with 54 m long array side scan: inverted resistivity section (*top*); inverted IP section (*bottom*)

The deep foundation was also side scanned using only SS electrodes and the Wenner-Schlumberger array in Fig. 3.27. Using this array, the IP decay curves were comparable to curves that were gathered with the NP electrodes unlike the results of the shallow foundation survey with only SS electrodes. The inversions in Fig. 3.27 converged to acceptable RMS values, unlike previous deep foundation tests. Also, this test showed that it was possible to gather IP data without the more cumbersome use of the NP electrodes. Despite the high quality IP and ERI data, still no foundation was observed from either inverted section. By comparison with later tests using the dipole-dipole array and NP electrodes, the Wenner-Schlumberger test was not useful for identifying bridge foundations.

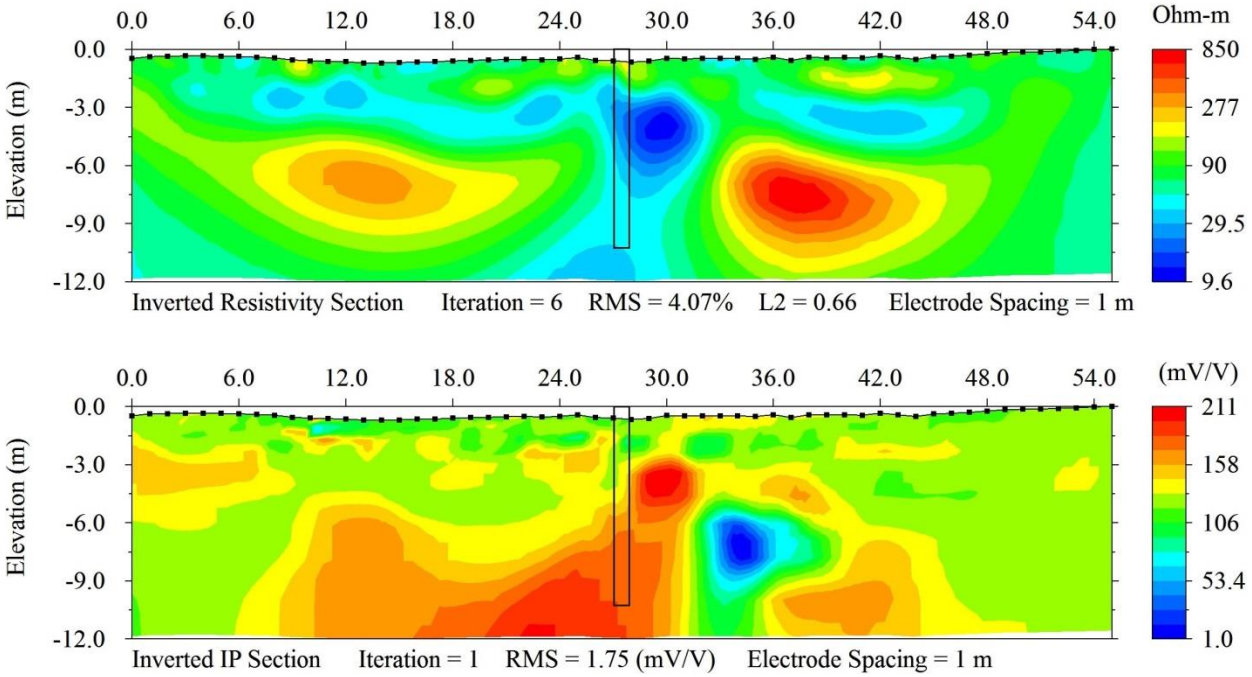

Fig. 3.27. Test shaft #4 with a 55 m array using the Wenner-Schlumberger configuration: inverted resistivity section (*top*); inverted IP section (*bottom*)

The final experimental setup considered for deep foundations was gathering two arrays of different electrode spacing and combining them. In this way, detailed data around the foundation was collected with smaller spacing (0.5 m) while still obtaining deeper data so the bottom of the foundation was estimated using 2 m electrode spacing. In Fig. 3.28, 56 SS electrodes were used for two different arrays, with the same center point. NP electrodes were not used because only 28 NP electrodes were available.

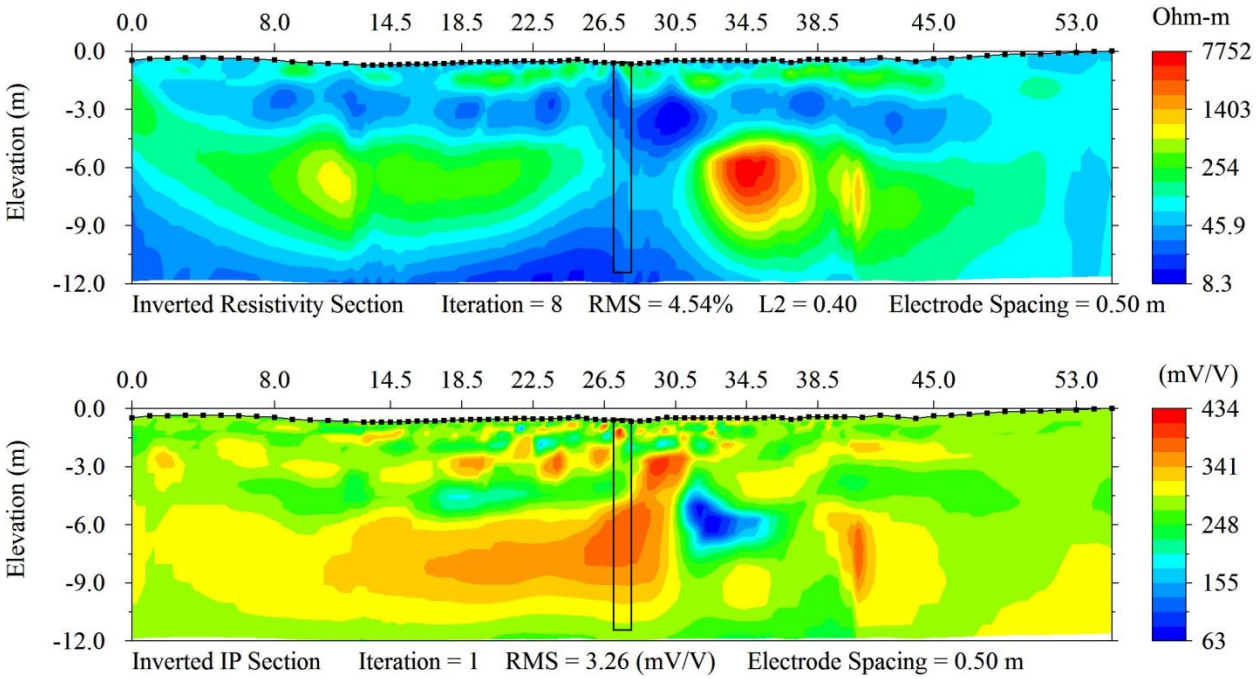

Fig. 3.28. Test shaft #4 with a combined 0.5 m and 1 m electrode spacing: inverted resistivity section (*top*); inverted IP section (*bottom*)

The first array was spaced 0.5 m and used the dipole-dipole array. The second array was spaced 1 m and used the combination Wenner-Schlumberger array. The smaller spacing and dipole-dipole array was used because of the clear inversions from the shallow foundations. The Wenner-Schlumberger array with wider electrode spacing was used because of its ability to gather deeper data. Both files converged to acceptable RMS values (4.54 percent and 3.26 mV/V), and using the known dimensions and location of the pile, a strong chargeability response was seen along a section of the pile to approximately 9 m below the surface. This response, however, was spread much larger than the foundation and did not penetrate to the full depth of the foundation. The inverted resistivity section had zones of low resistivity around the pile, but these zones were spread throughout the inversion.

The results of Fig. 3.28 did not provide more details of the pile to justify the extra time spent for this experiment. Not only was it time consuming to run two different arrays for the same pile, but the data processing afterward was more cumbersome requiring the electrodes with smaller spacing to be shifted to align with the longer array line. Again, the IP results were not as clear regarding the shape of the foundation when only SS electrodes were used instead of the combination of SS and NP electrodes.

Steel H-Piles

All foundations tested so far were concrete. But bridge foundations were also commonly supported by steel H-piles. Adjacent to the NGES sand site were 17 driven steel H-pile anchor piles, 12 vibratory driven steel pipe piles, and 12 vibratory driven steel H-piles (Fig. 3.29). Three of the steel H-piles were tested to expand the materials database. The soil profile surrounding the driven piles was stiff red sandy clay to 2.1 m, firm red-brown sand from 2.1 to 6.7 m, stiff red sandy clay from 6.7 to 8.2 m, firm tan sand from 8.2 to 11.3 m, and hard dark

gray clay to the terminated borehole depth of 12.2 m (Bosscher et al. 1998). The three piles that are shown are labeled on Fig. 3.29 as N, 6-20-A-P, and Q.

The first test of a steel pile was pile N (Fig. 3.30b) showed the issues with testing in soil with a high contact resistance. The top soil near the driven piles was a very stiff sandy clay and when the electrodes were driven into this, the soil became very loose around the stake. This caused the resistance at the electrode-soil contact to be very high (called the contact resistance). Because the IP signature was so small for foundations, in order to obtain a measurable IP response as much current as possible went into the subsurface. Ideally, maximum current came from contact resistance of less than 300 Ω. The contact resistances for this test were 700–1,500 Ω, with several from 4,000–8,000 Ω.

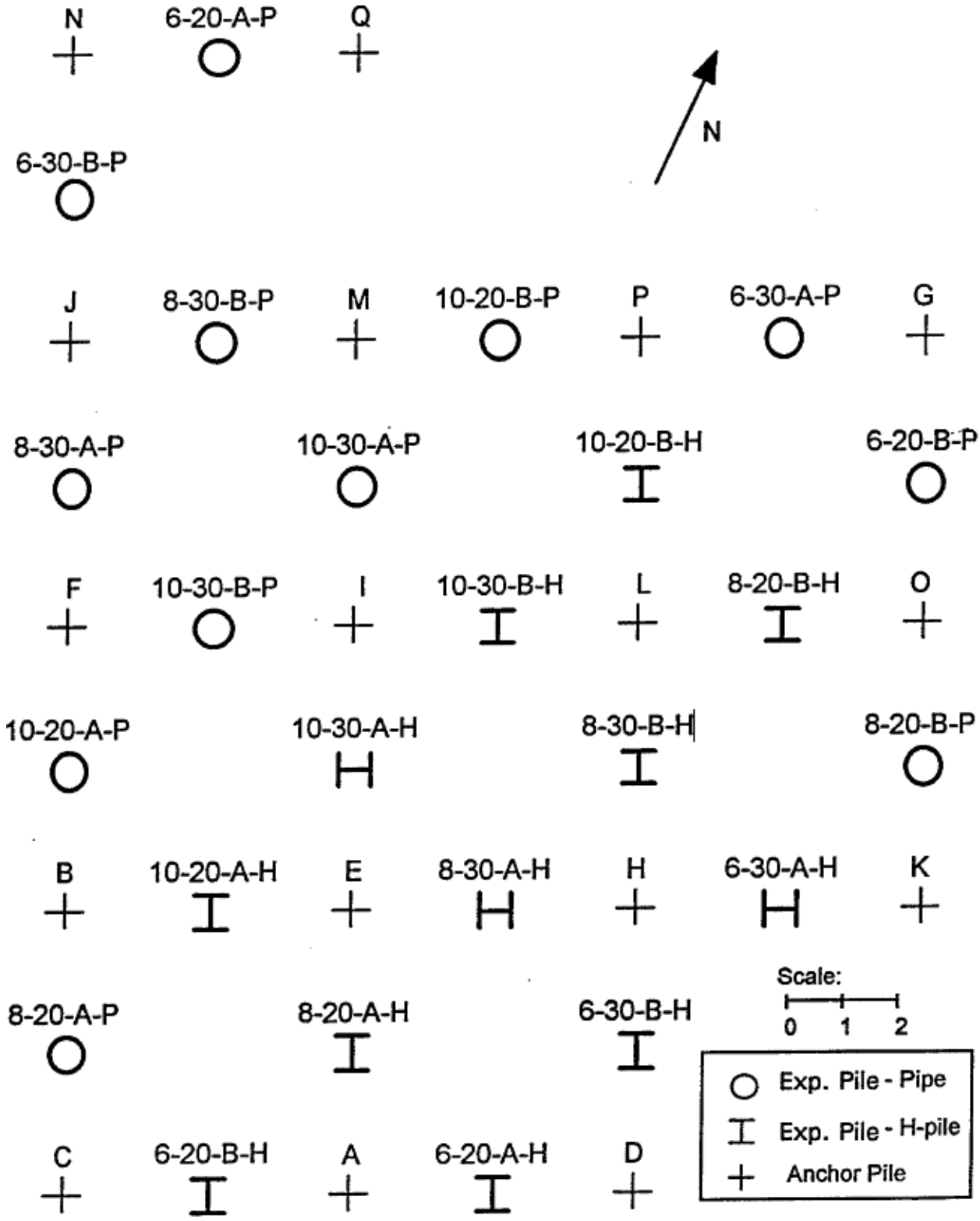

Fig. 3.29. Final layout of piles (Bosscher et al. 1998)

(a) Test site (b) Experimental setup

Fig. 3.30. Steel H-piles near the NGES

In Fig. 3.31 a very low resistivity, or alternatively high conductivity response was seen along the length of the pile. But this response was also seen to the left of the pile on the image. This was the response from the nearby steel tube, 6-30-B-P. The RMS for the resistivity section was also very high (9.75 percent) so the wide spread highly conductive zone was due to the inability of the model to correlate with the measured data.

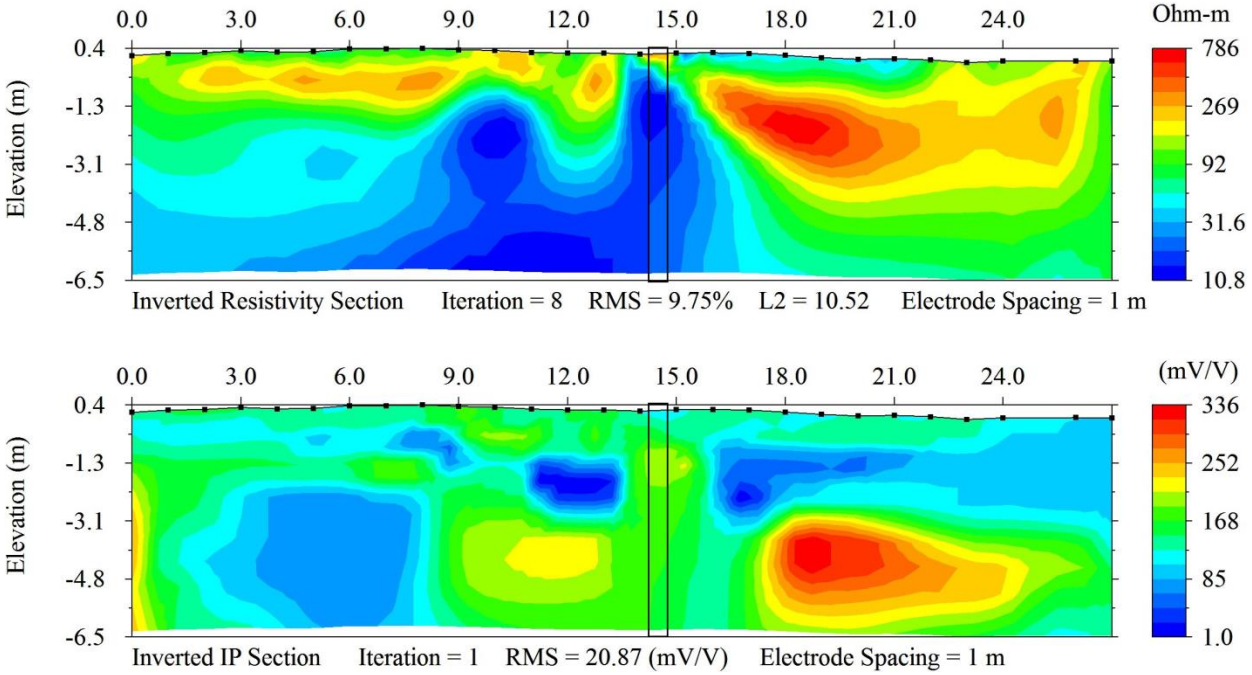

Fig. 3.31. 13.8 m long steel anchor pile with 1 m spacing: inverted resistivity section (*top*); inverted IP section (*bottom*)

Note the zone of highly resistive soil at the top of the profile, again related to the high contact resistance. The IP section showed no decipherable response of the pile, and the RMS was extremely high, 20.87 mV/V. The response in this model should not be considered accurate.

Following the Fig. 3.31 test, an array was set up along the three piles N, 6-20-A-P, and Q with the 15th electrode array centered on Q. In Fig. 3.32b, pile Q was the farthest pile on the right. Fig. 3.32b shows the first test of the three piles in a line with the electrodes spaced 0.5 m, and Fig. 3.32a shows the test with the electrodes spaced every meter.

(a) Test site (b) Experimental setup

Fig. 3.32. Three pile test

The first test run along these three piles was the array shown in Fig. 3.32a. Similar to the test from Fig. 3.31 this test had very high contact resistance (averaging 3,000 Ω with maximums near 7,500 Ω) so the inversion quality was very poor with high RMS values. The two exterior piles were 13.8 m long, and the interior pile was 6.3 m long. The exterior piles were embedded 11.5 m, and the central pile was embedded 6 m.

Fig. 3.33 shows the results from the first test. Little information was gathered from this experiment because of the high contact resistance and the number of negative apparent resistivity data measured at the surface (112 or 29 percent). This low data quality was addressed by using bentonite slurry around both the NP and SS electrodes. The bentonite slurry successfully reduced the contact resistances in half, with the average around 1,600 Ω and the maximum down to 3,300 Ω. Despite this, the negative apparent resistivity data were not resolved. The 1 m spaced test is shown in Fig. 3.34.

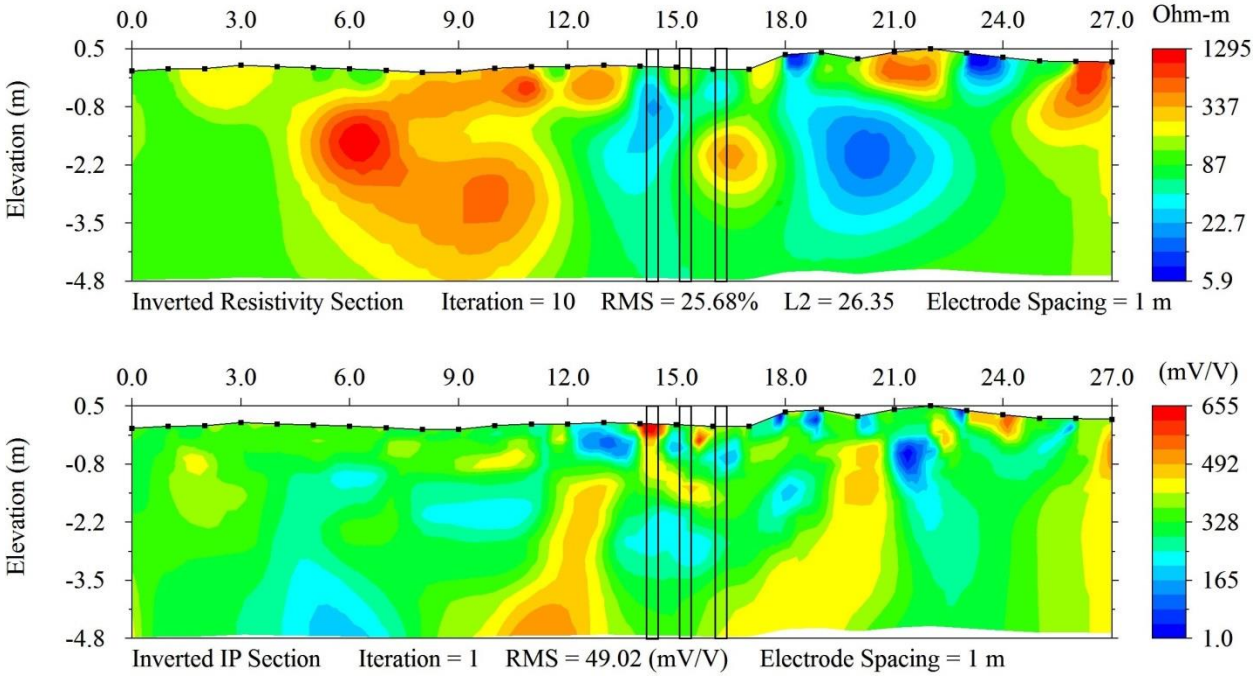

Fig. 3.33. 1 m spacing along N, 6-30-B-P, and Q; inverted resistivity section (*top*); inverted IP section (*bottom*)

The inversion quality of Fig. 3.34 was even lower than Fig. 3.33 even though the contact resistances were greatly reduced. The low data quality surrounding the H-piles was most likely due to the soil. The red-brown sand that began at 2 m until 6.7 m was classified as a poorly graded sand according to the Unified Soil Classification System with a coefficient of uniformity C_u of 1.5 and coefficient of curvature of C_c of 1.0 (Bosscher et al. 1998). Fig. 3.35 shows the gradation curve.

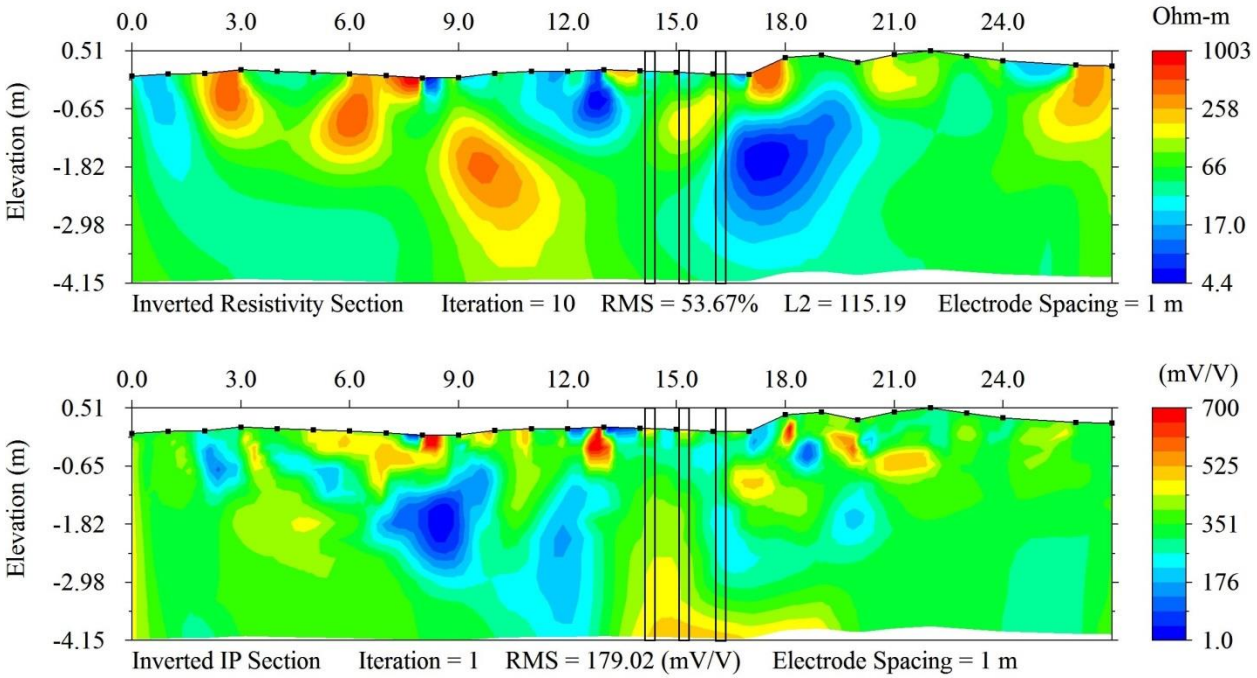

Fig. 3.34. 1 m spacing along N, 6-30-B-P, and Q with bentonite surrounding the electrodes: inverted resistivity section (*top*); inverted IP section (*bottom*)

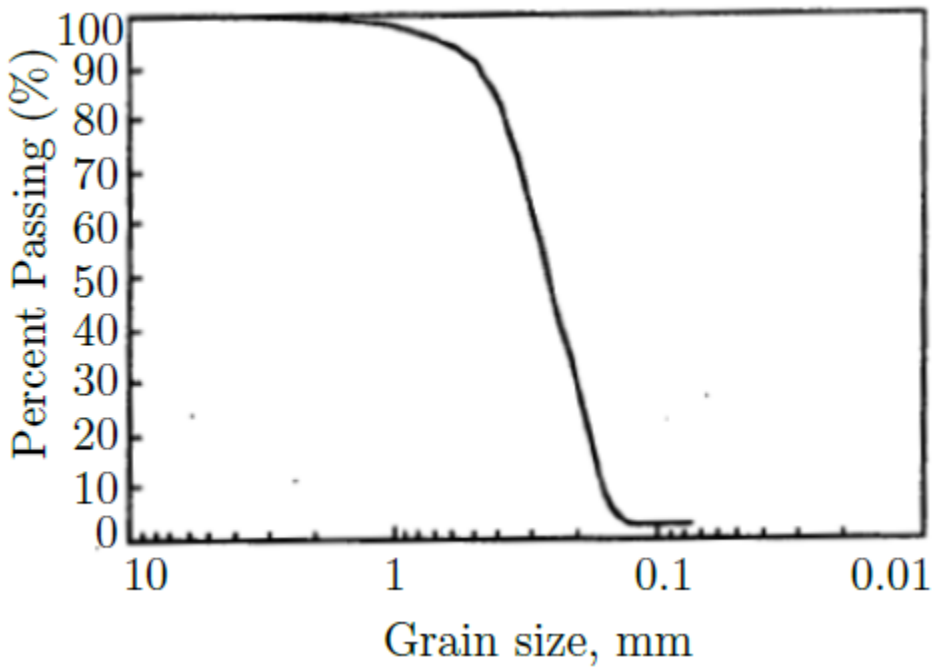

Fig. 3.35. Grain size distribution for firm red sand (Bosscher et al. 1998)

This highly uniform soil had more connectivity of pore space than a well graded sand or a sandy clay soil. This highly connected pore space greatly reduced the apparent resistivity of the ground and it also allowed the current to dissipate more easily resulting in lower quality IP curves. Also, despite the high RMS values, the chargeability in Fig. 3.33 and Fig. 3.34 was extremely high. Recall that chargeability was the ratio of the secondary to primary voltage

potentials measured at the surface (Equation 2.9). Typical values for chargeability in this research using a 2 s delay time and a maximum current of 2,000 mA were from 100–300 mV/V. In Fig. 3.34, the chargeability was 700 mV/V. Because the primary voltage did not vary greatly, this means that the secondary voltage was much higher. A higher secondary voltage indicated that the current did drop initially from the primary voltage when the current was turned off. In other words, the current was being stored in the ground instead of dissipating. Most likely, for these tests, the current was stored in the highly chargeable steel, which led to a very high IP response and also reduced the quality of the calculated IP data, thus increasing the RMS. While digging holes for the bentonite slurry, several pieces of steel near the surface were found. This scattered steel debris also affected the output, forcing current to be stored in many places in the subsurface. Because the soil and site conditions of this site was not easily overcome at the surface no more testing was conducted at around the H-piles.

FULL SCALE BRIDGE TESTING

The testing method developed at the NGES was used to plan surveys at four bridges in the Bryan TxDOT District. Each bridge was tested using 28 SS and 28 NP electrodes using the dipole-dipole array. The electrode spacing was either the width of the exposed foundation or 1 m, depending on the necessary depth of investigation. The results from each bridge were used for the reliability estimation in Chapter 4 and were used to identify the decision process for estimating the depth of an unknown foundation. Fig. 3.36 shows the locations of the four bridges discussed in this section along with the unknown bridge used for validation.

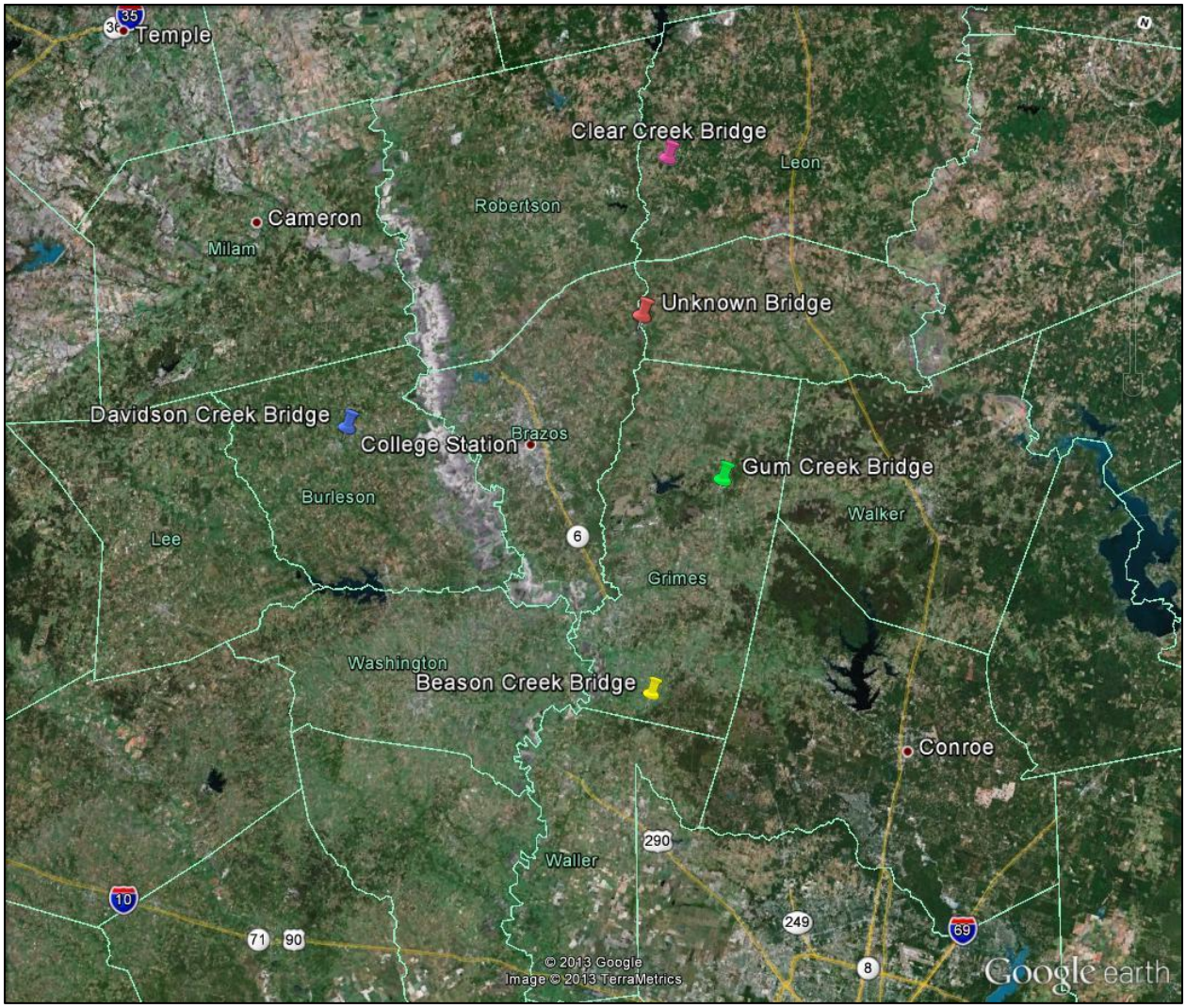

Fig. 3.36. Tested bridges in the Bryan TxDOT District

Beason Creek Bridge

The bridge on FM 362 over Beason Creek is 1.77 km south of FM 2 in Grimes County, Texas. It was constructed in 1956 and is a minor collector rural road. The total length of the bridge is 27.4 m and it is 7 m from curb to curb. The piles are 6.10 m long H 10×42 steel piles with 4.88 m embedment. Beason Creek is currently completely dry with very loose sand at the surface by visual classification (Fig. 3.37).

(a) Test site (b) Experimental setup

Fig. 3.37. Beason Creek Bridge

This very loose sand caused the contact resistance to be very high, thus leading to poor data quality. The average contact resistance in this loose sand was 2,140 Ω with a maximum resistance of 8,320 Ω.

Due to fence line encroachments and in order to isolate one pile, the foundation was located between the 10th and 11th electrodes and it was side scanned instead of placed directly in the array. Note that the first electrode was only 0.5 m from the second electrode. Again this was due to the property fence line near the first electrode. Low resistivity is seen in Fig. 3.38 around the pile as well as high chargeability but several other mathematical anomalies were also present. This was likely due to the loose soil causing a high contact resistance resulting in low current injection. Both RMS values were above the acceptable range for these data to be interpreted with confidence. The predicted depth was 2.09 m using the post processing algorithm.

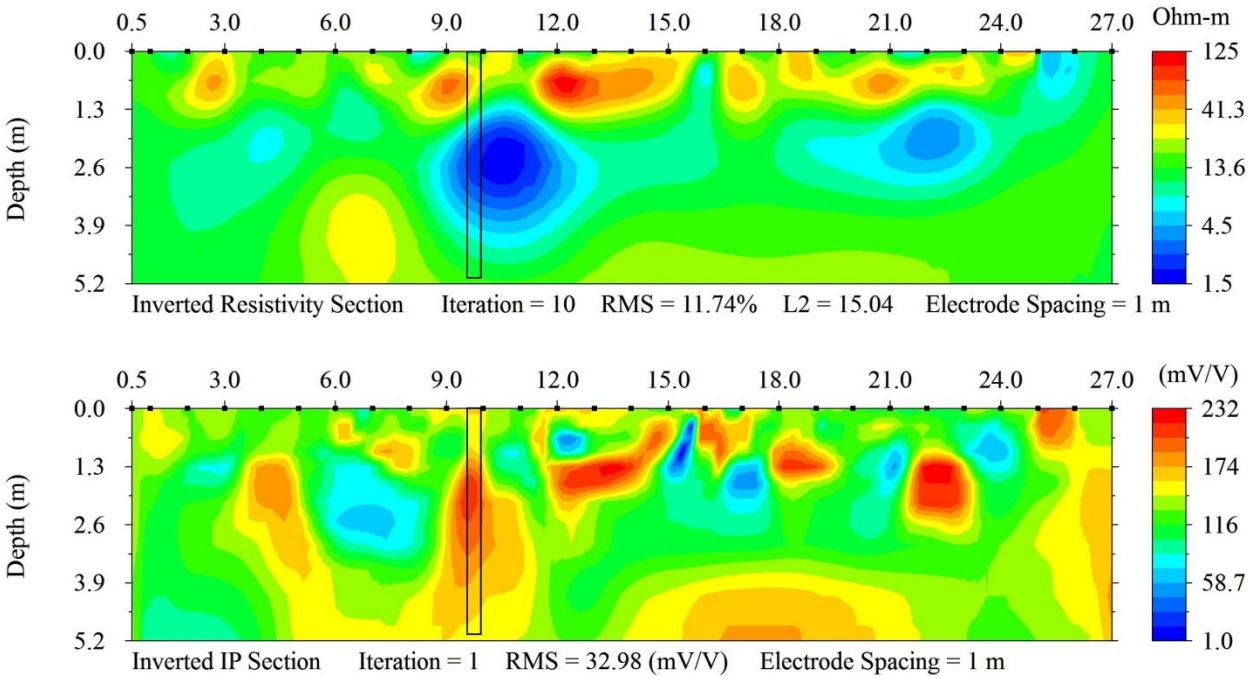

Fig. 3.38. Beason Creek Bridge with 1 m spacing: inverted resistivity section (*top*); inverted IP section (*bottom*)

Clear Creek Bridge

The Clear Creek Bridge is located in Leon County, Texas, on FM 977, 1.85 km southeast of FM 3. It is a minor collector road that was built in 1988 and is 55.5 m long and 10.5 m wide from curb to curb. It crosses the Clear Creek; however, the creek is so low that only one pile group goes through it. The dry piles along with the severe scour can be seen in Fig. 3.39a.

(a) Test site (b) Experimental setup

Fig. 3.39. Clear Creek Bridge

The line was set up with two different electrode spacing using the dipole-dipole array. First, the electrode spacing was 1 m in order to gather data deeper than the 4.6 m piles. The inverted resistivity section, shown in Fig. 3.40, converged to an RMS of 3.85 percent in 8 iterations. A zone of high resistivity was noted at the top 0.25 m of the pile, which is typical of resistivity inversions of long slender piles.

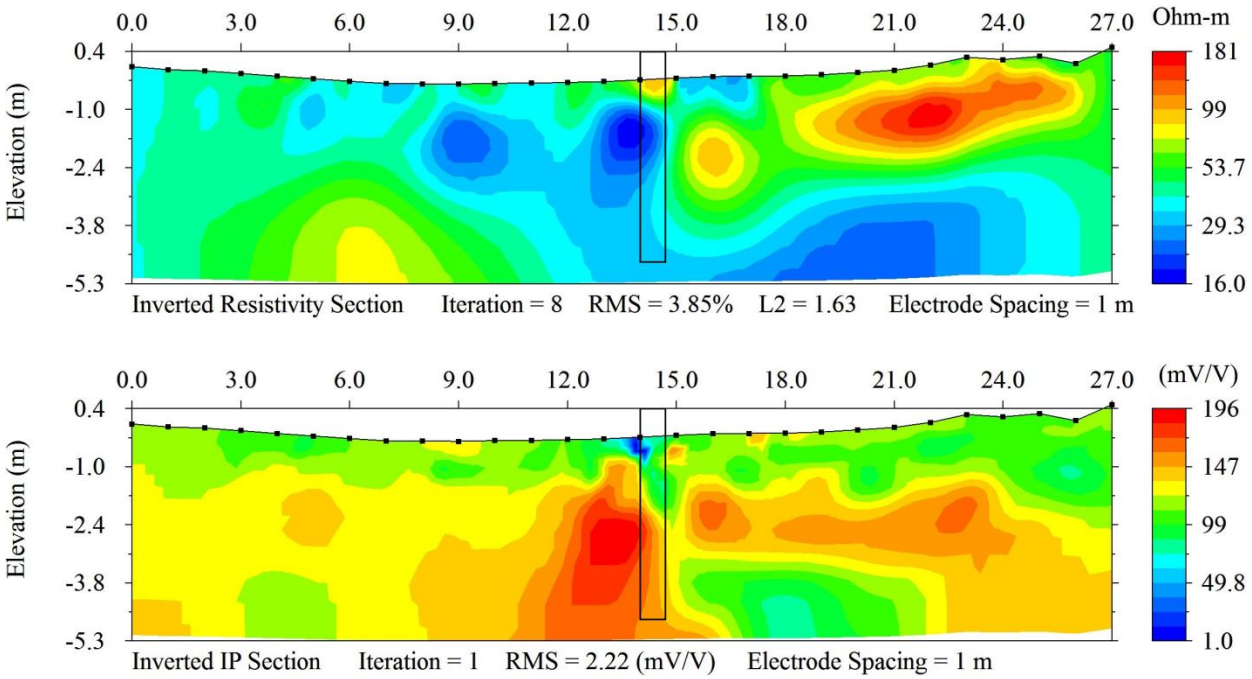

Fig. 3.40. Clear Creek Bridge with 1 m spacing: inverted resistivity section (*top*); inverted IP section (*bottom*)

Data were gathered to the full depth of the pile; however, no zone of high chargeability was seen at the top of the pile. This may be due to the fact that the current was not transmitted in the 2D plane; instead, it spread outward in a circular 3D plane that may not capture the upper portion of the foundation. Despite this, a strong chargeability was shown at the bottom half of the foundation with a chargeability much higher than that of natural objects within the ground. The chargeability of the foundation appeared to cover a much larger area than the actual foundation and it did not directly line up with the location of the foundation. The slightly skewed results may be attributed to the nature in which the array was set up. In order to isolate the exterior pile only a corner of the pile was placed within the array. This corner was less than 0.3 m wide, so much of the electrode gap typically for the foundation was free space. The predicted depth was 4.87 m. The pile was also tested with the electrode spacing equal to the width of the foundation.

Fig. 3.41 shows the same location with the electrode spacing reduced to the width of the pile, 0.57 m; no topographic data were available for this test. Again the inverted resistivity section was marked by a zone of high resistivity at the top of the pile. Note that the model required extra iterations (10) to converge to an acceptable RMS of 5.35 percent. The inverted IP response showed a zone of high chargeability in the middle of the pile that was contained to approximately the width of the foundation. This zone faded from 219 mV/V to 165 mV/V, which penetrated to the full depth of the inversion. Because of the smaller electrode spacing, data were not gathered to the depth of pile. Although the IP inversion showed a strong chargeable response on the foundation, the RMS was 16.89 mV/V, which was above the confidence level of these inversions. The predicted depth was 1.45 m.

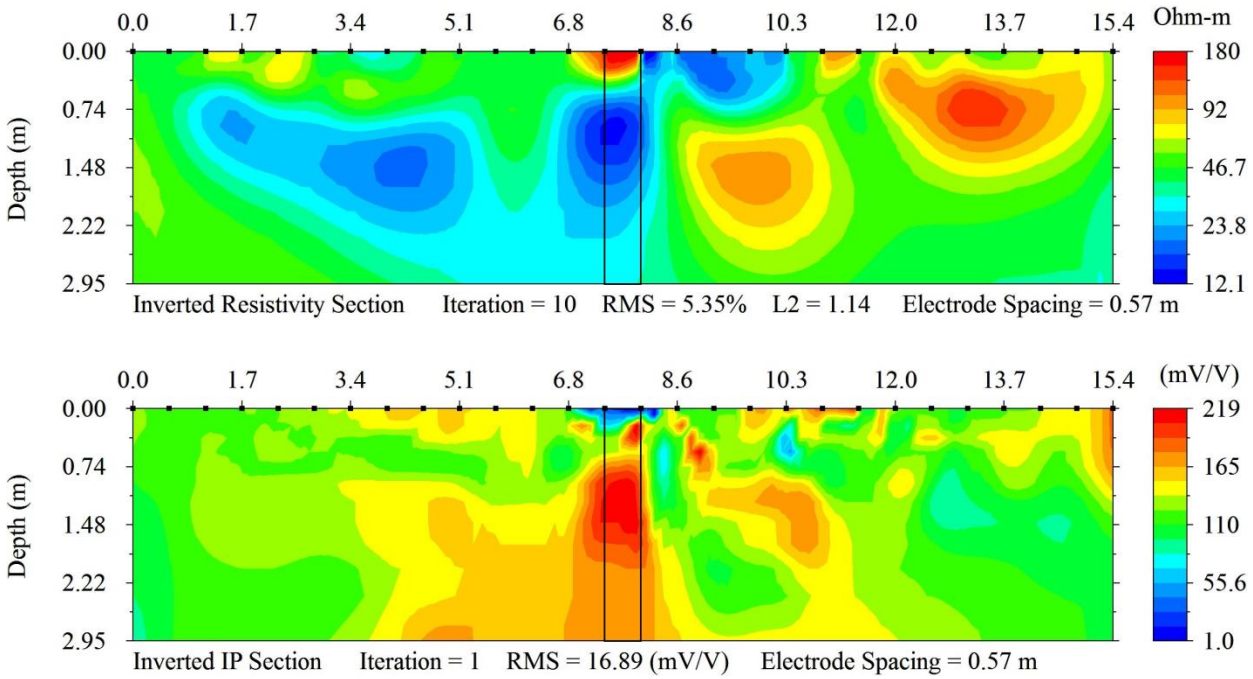

Fig. 3.41. Clear Creek Bridge with 0.57 m spacing: inverted resistivity section (*top*); inverted IP section (*bottom*)

Davidson Creek Bridge

The SH 21 over Davidson Creek Bridge is located in Burleson County on SH 21, 0.32 km northeast of SH 36 in Caldwell, Texas. It is a principal arterial road that was built in 1968 and reconstructed in 1988. The bridge is 97.5 m long and 19.9 m wide from curb to curb. The piles are a 0.4 × 0.4 m^2 straight shaft that extend approximately 6 m into the subsurface (the current depth of embedment is slightly different for each pile). The current embedment depth was approximated by measuring the length from the bridge bent to the ground surface and using the bridge drawings. This was necessary because of the scour that has occurred, as shown in Fig. 3.42a. Twenty-eight NP electrodes and 28 SS electrodes were spaced at 1 m as shown in Fig. 3.42b with the foundation 13 m from the first electrode for each of the six piles tested. Fig. 3.43 shows the layout of the piles of the Davidson Creek Bridge. The six tested piles were hatched to highlight them and numbered in the order they are presented in.

(a) Test site (b) Experimental setup

Fig. 3.42. SH 21 over Davidson Creek Bridge

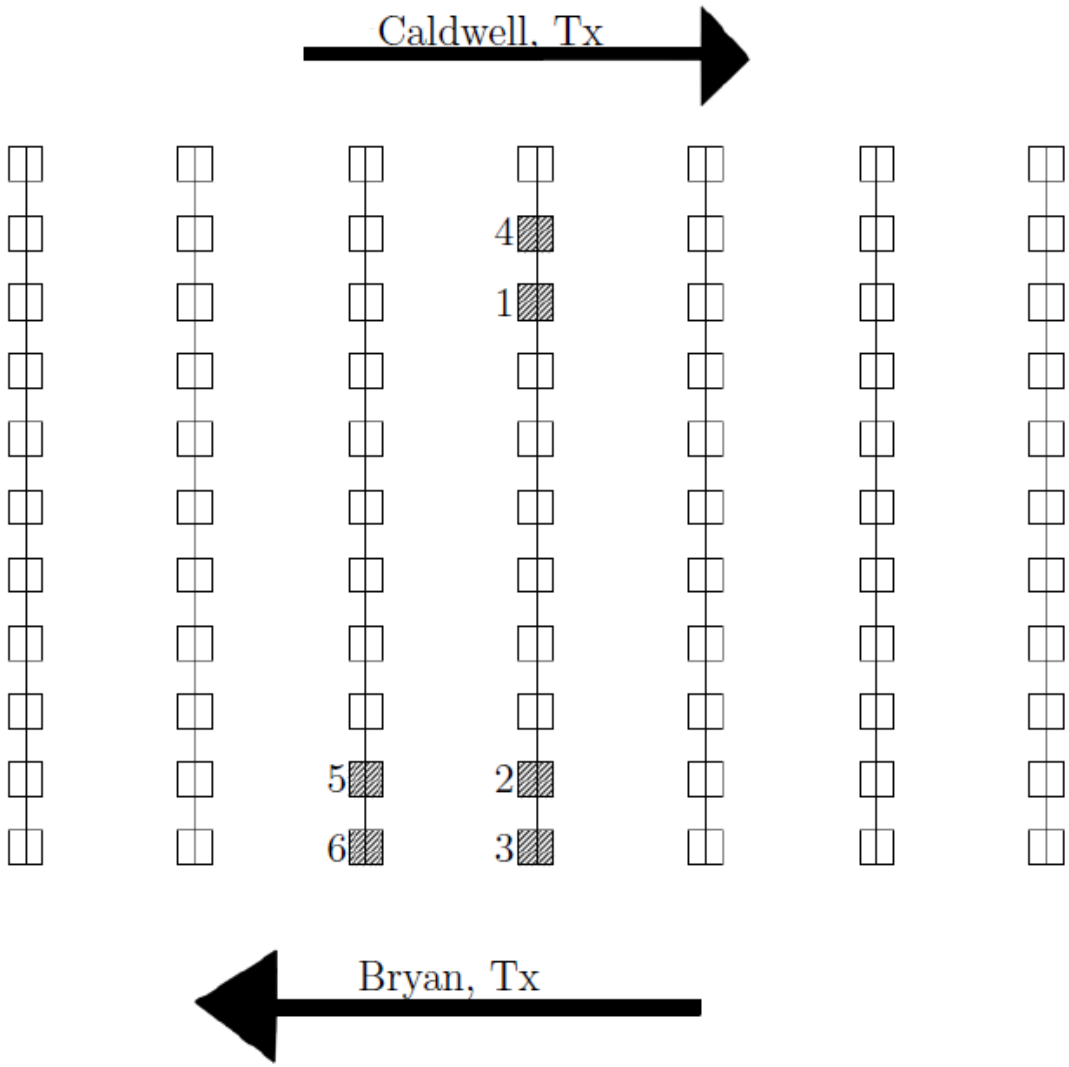

Fig. 3.43. Pile layout of the Davidson Creek Bridge

The first pile tested was the exception to the rest; the electrode spacing was set equal to the width of the pile, or 0.4 m. This only allowed for data collection to 2.07 m using the dipole-dipole array. The inverted resistivity section converged to an RMS of 4.19 percent in 10 iterations but the inverted IP section was only able to achieve an RMS of 25.95 mV/V. The results in Fig. 3.44 were similar to Fig. 3.41, in that the zone of high chargeability was confined to the area of the foundation and the IP RMS was above the accepted level. The IP inversion also did not image below 2 m of the pile, which was less than half of the 5.75 m pile embedment. The predicted depth was 1.43 m.

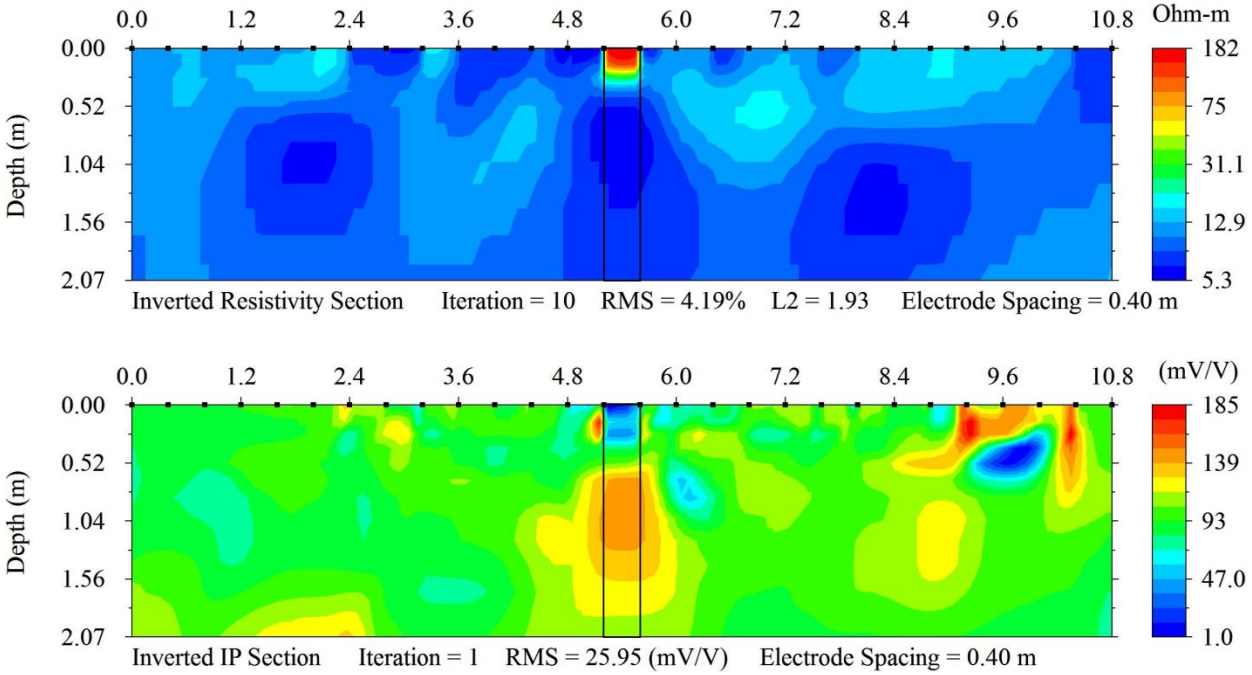

Fig. 3.44. Davidson Creek Bridge pile one with 0.4 m spacing: inverted resistivity section (*top*); inverted IP section (*bottom*)

Pile two was tested with a 27 m long array so data were collected to 5.2 m beneath the surface. After accounting for scour, this pile extended 6.08 m into the subsurface. A very strong, localized zone of high chargeability relative to the background chargeability was seen beginning halfway down the pile to the ultimate depth of the data gathered in Fig. 3.45. Again, the results in Fig. 3.45 were useful for updating the NBI by noting that the foundation was at least 5.2 m deep. Unlike Fig. 3.44, the inverted resistivity section and the inverted IP section both converged to acceptable RMS values (2.47 percent and 1.94 mV/V, respectively) so there was much more confidence in this model than from previous data. The predicted depth was 4.85 m.

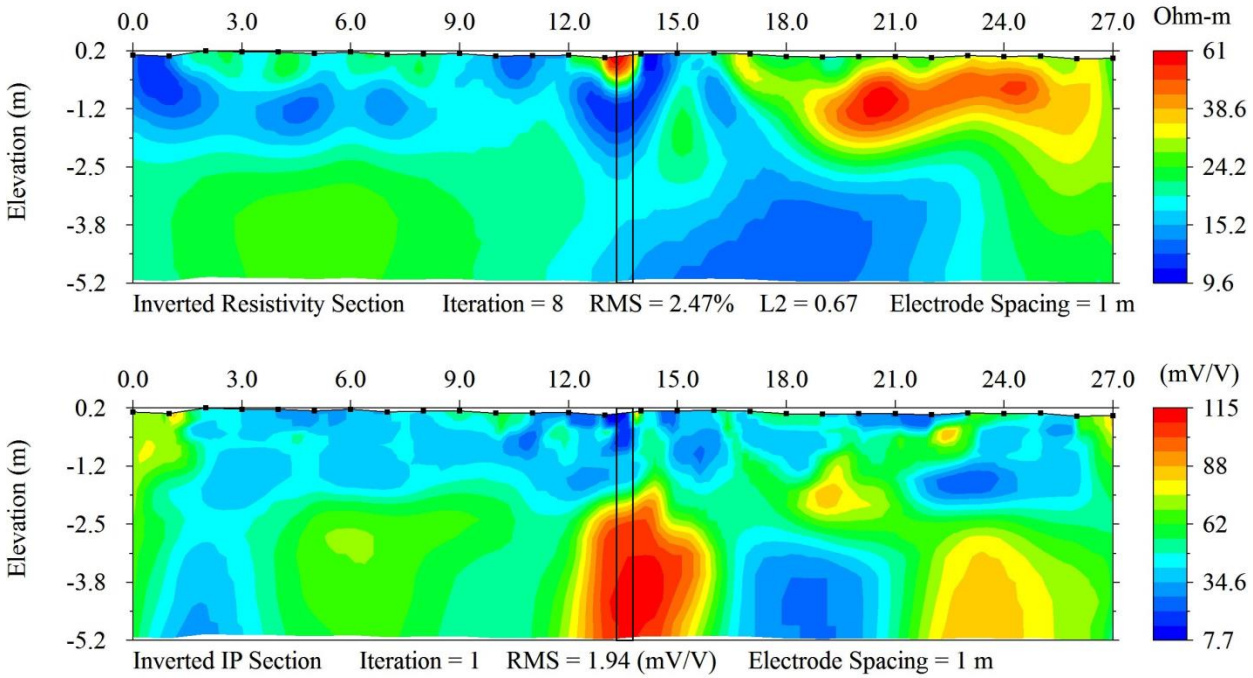

Fig. 3.45. Davidson Creek Bridge pile two with 1 m spacing: inverted resistivity section (*top*); inverted IP section (*bottom*)

The third pile was embedded 6.19 m after accounting for scour. The depth of penetration in Fig. 3.46 was 5.9 m so the pile depth was less than the depth of the data. Again, the RMS for both tests indicated that the data quality was very high. The inverted resistivity section showed no details in reference to the pile but nearly 2/3 of the pile was imaged in the IP section. Note that similar to Fig. 3.45 the foundation appeared much wider than it actually was. This was a tradeoff for gathering deeper data in order to image the entire pile. When the electrode spacing was wider than the foundation, the IP response appeared wider than the foundation in the subsurface. The predicted depth was 2.79 m.

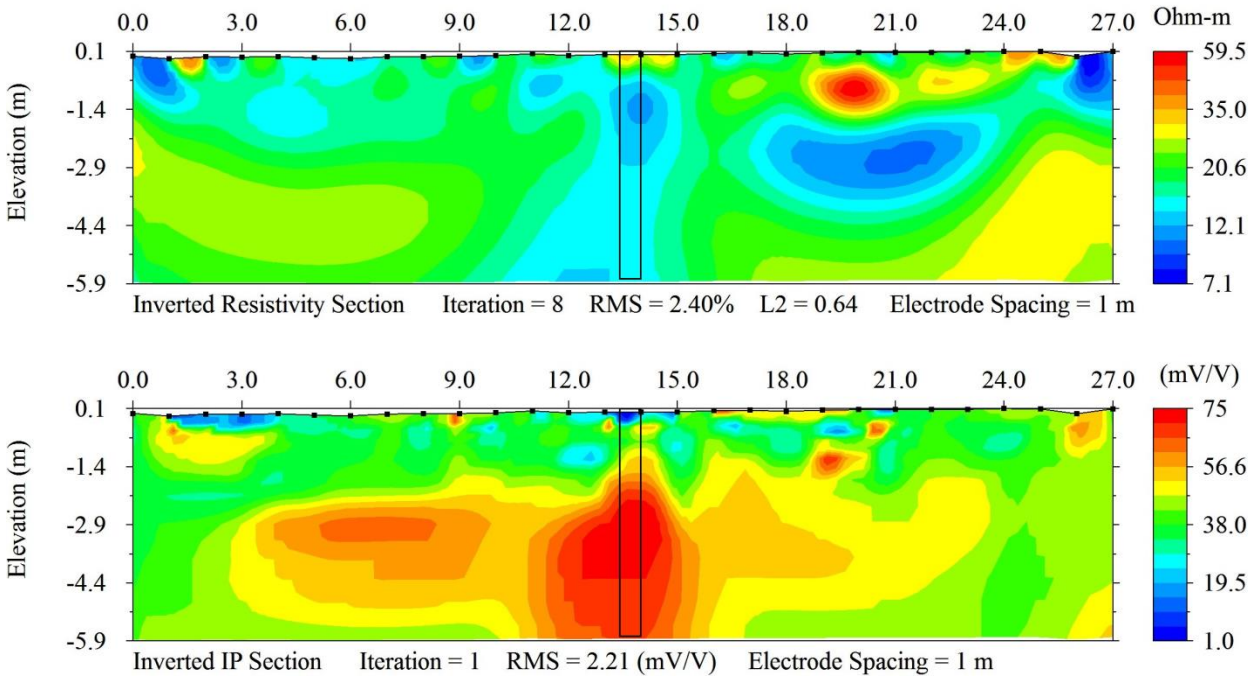

Fig. 3.46. Davidson Creek Bridge pile three with 1 m spacing: inverted resistivity section (*top*); inverted IP section (*bottom*)

Pile four was embedded 5.99 m, and the depth of investigation was 6.3 m for the 27 m long array. The inverted resistivity section in Fig. 3.47 converged to an RMS of 2.55 percent in only 7 iterations and the inverted IP section converged to an RMS of 1.90 mV/V. Looking at the inverted IP section, the localized zone of high chargeability nearly directly correlated to the depth of the foundation. This inversion highlighted the importance of the calculated decision for the foundation depth so engineers were not guessing at random as to the depth of the foundation. The calculated decision algorithm was introduced in Chapter 4. The predicted depth was 3.85 m.

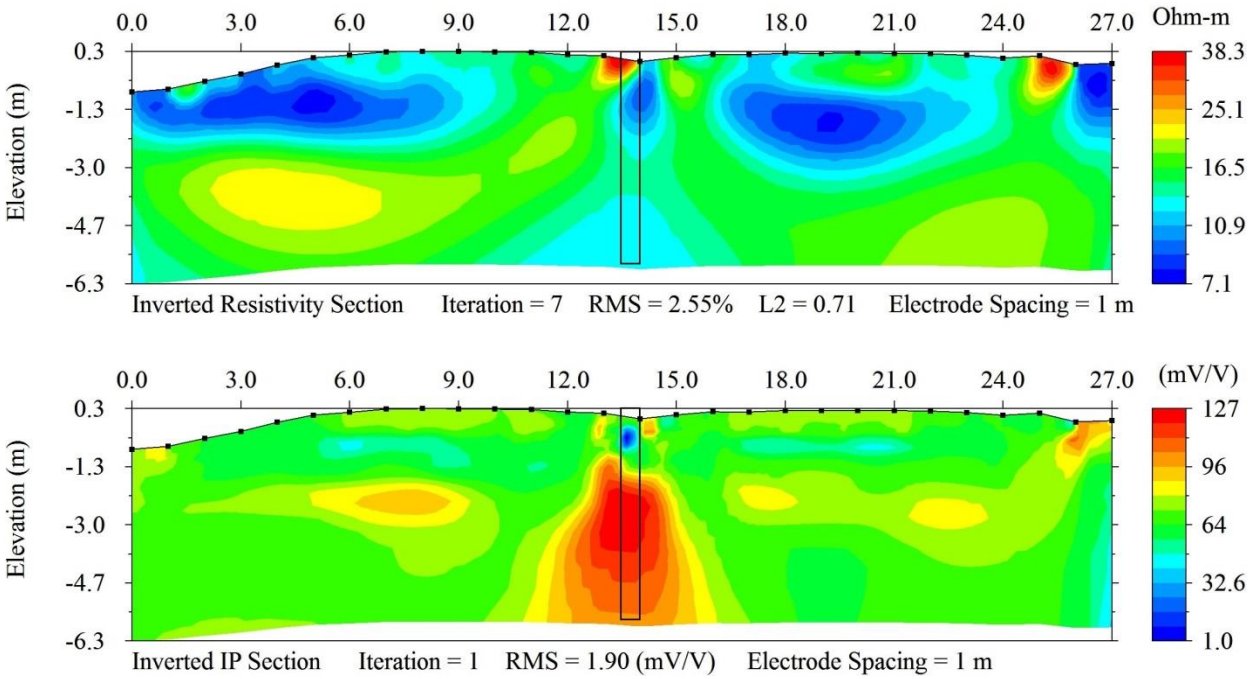

Fig. 3.47. Davidson Creek Bridge pile four with 1 m spacing: inverted resistivity section (*top*); inverted IP section (*bottom*)

Pile five (Fig. 3.48) had 2.72 m of the pile above the ground surface leaving 6.12 m below after accounting for scour. The depth of investigation for Fig. 3.48 was 6 m, nearly the depth of the pile embedment. The RMS for the inverted resistivity section was 3.58 percent after 10 iterations; with the exception of Fig. 3.44 all of the other piles on the Davidson Creek Bridge converged to an RMS of less than 3 percent in 8 or less iterations. This high ERI section generated a high RMS IP section as well—RMS of 8.95 mV/V. Looking at the IP section, the zone of high chargeability was only seen from −1.5 m to approximately −3 m. Though the zone of high chargeability stops around −3 m using visual inspection, the predicted embedment was 2.24 m using the prediction criteria described in Chapter 4.

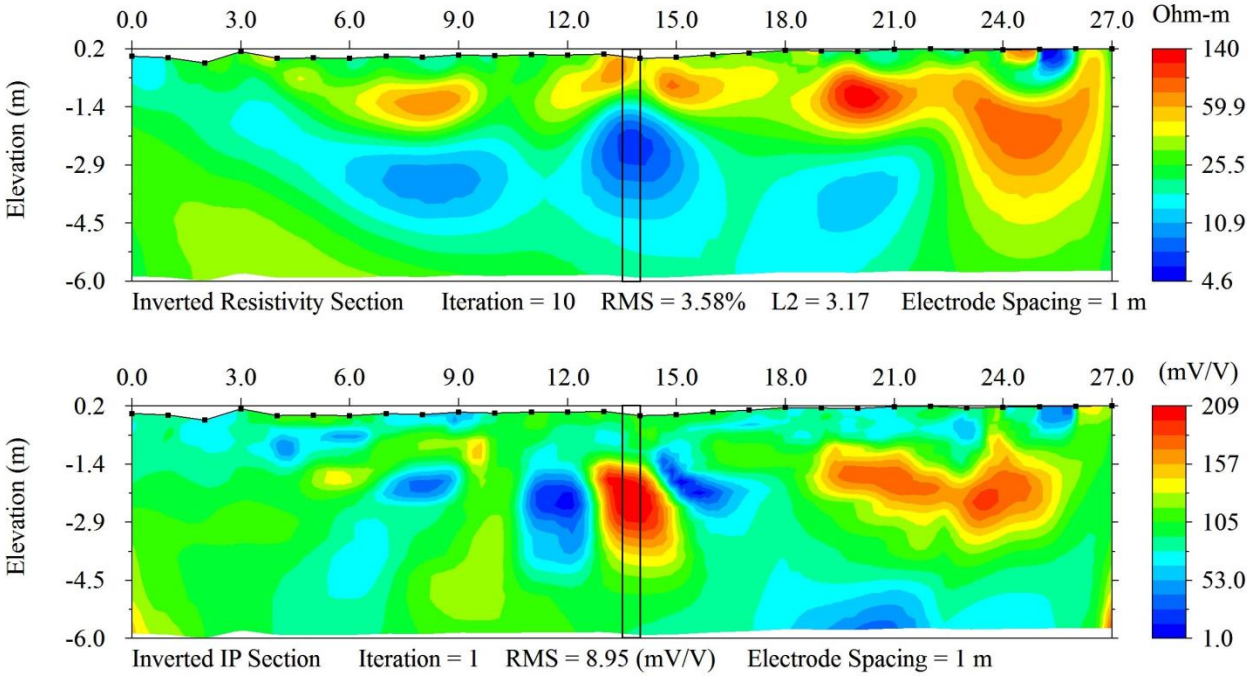

Fig. 3.48. Davidson Creek Bridge pile five with 1 m spacing: inverted resistivity section (*top*); inverted IP section (*bottom*)

Pile six was the exterior pile on the third bent. The pile in Fig. 3.49 had 2.57 m above the ground surface and 6.27 m below. The depth of investigation for the 27 m long array was 5.9 m. A zone of high resistivity was noted at the top of the pile and high chargeability from 2 m down to the depth of penetration. The predicted depth was 3.60 m.

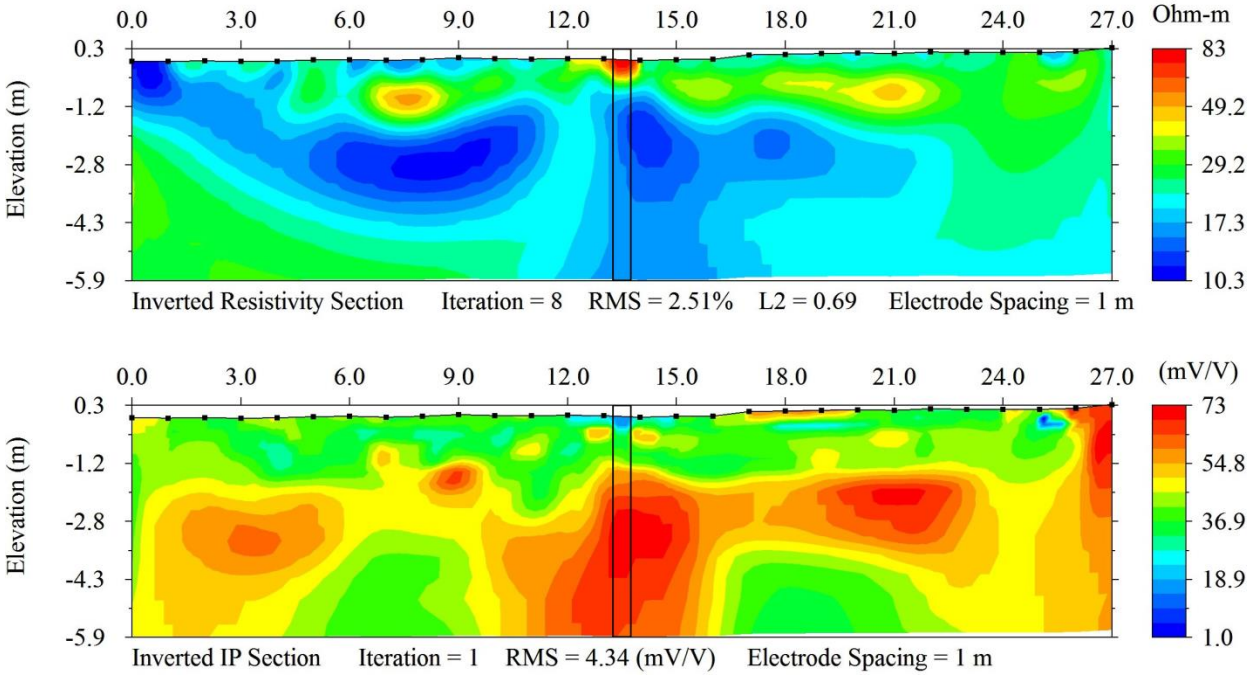

Fig. 3.49. Davidson Creek Bridge pile six with 1 m spacing: inverted resistivity section (*top*); inverted IP section (*bottom*)

Gum Creek Bridge

The final bridge is located in Grimes County, Texas, on SH 90, 6.04 km north of SH 30 outside of Roans Prairie, Texas. The bridge is on a minor arterial road. The Gum Creek Bridge was built in 1927 and reconstructed in 1960; it is 36.6 m long and 13 m wide from curb to curb. Gum Creek is flowing around two pile groups, and there is also stagnant water in a small channel in the traffic direction of the bridge. The array was set up in the traffic direction so the banks created by scour were used to keep the cables dry (Fig. 3.50).

(a) Test site (b) Experimental setup

Fig. 3.50. Gum Creek Bridge

Electrodes were spaced every 1 m again using 28 NP and 28 SS electrodes. Fig. 3.50b shows two piles were tested directly in the array path. Additionally two more were side scanned because of their close proximity to the array. Also, the first electrode was within 1 m of the bridge abutment due to limited space. The piles were located between the 6th and 7th electrodes and the 13th and 14th electrodes. Each pile was embedded approximately 3 m.

The inverted resistivity section in Fig. 3.51 converged to an RMS of 3.81 percent in 10 iterations, but again no clear foundation was seen. In the inverted resistivity section, a zone of high chargeability (over 400 mV/V) was seen around both of the piles. The response of the first pile, between the 6th and 7th electrodes, had this high chargeability along the pile that terminated at the approximate pile depth. The predicted depth was 1.36 m.

The second pile, between the 13th and 14th electrodes, had the same zone of high chargeability but the pile was only imaged to 1.5 m beneath the surface. Only the approximate depth of the foundations was available for this bridge, not the bridge plans, so the lengths of the piles were not measured and adjusted for scour. After adjusting for scour the second pile

terminated approximately 1.5 m into the subsurface. The RMS for the IP inversion was well over the acceptable bounds for a reliable model, so the pile was deeper than the inversion showed. The predicted foundation depth was 1.36 m.

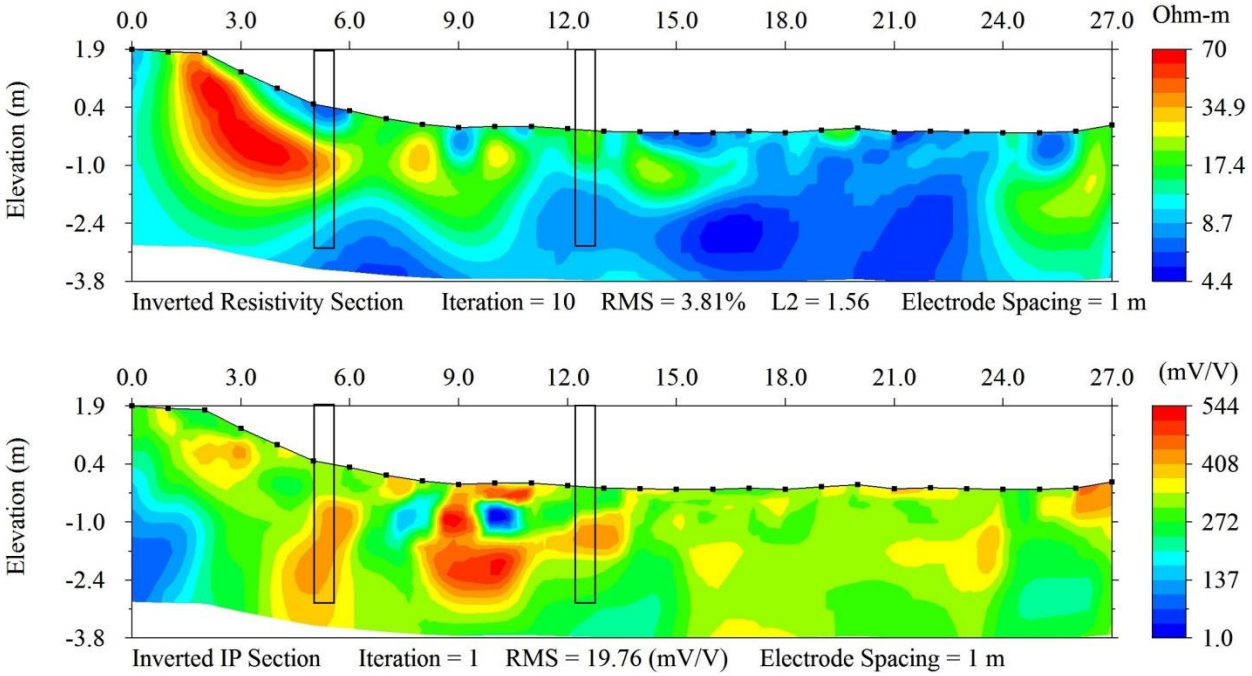

Fig. 3.51. Gum Creek Bridge with 1 m spacing: inverted resistivity section (*top*); inverted IP section (*bottom*)

Despite the high IP RMS this test showed that piles can be imaged through water, which was important because this expanded the realm of applications for this method to include both bridges with dry conditions and wet. Only one case was tested through water because the cables at the TAMU were not submersible so extra care was taken to keep them above the water line. Commercially designed submersible cables are available for bridges with piles through water.

EXPERIMENTATION SUMMARY

In this chapter the optimal experimental setup was identified by testing the different parameters possible at the NGES on reinforced concrete foundations. The optimal setup is listed below:

1. Arrange the array so that the foundation is in the middle of the electrode line.
2. The central electrodes (14th and 15th in a 28 electrode line) should be placed on either side of the foundation.
3. SS electrodes should be next to the foundation and NP electrodes offset by less than 0.3 m for a side scan survey.
4. The IP cycle time should be 2 s.
5. The dipole-dipole array should be used.
6. For concrete structures, the foundation must contain reinforcement.

Three steel H-piles were also tested. While the optimal setup was used, it was not successful on the steel H-piles. The use of a bentonite slurry for lowing the contact resistance at the surface was showed at the steel H-pile site. No discernible foundation was seen at the steel H-pile site, but the highly chargeable response indicated that the current was stored at the site and not dissipating at a typical rate for foundations. More testing is needed on steel foundations at this time.

Four full scale bridges were tested using the experimentally determined optimal setup for imaging foundations. It was shown that bridges can successfully be imaged using ERI and IP from which foundation depths can be estimated. In these tests the dependence of the soil type was shown as well as the importance of gathering data deeper than the foundation itself. Between these four bridges it was seen that ERI and IP can be used to successfully image both shallow and deep bridges in different soil types, with and without water present. The results of these bridge tests are used in Chapter 4 where a post processing bridge foundation depth estimator is developed.

4. RELIABILITY FOR UNKNOWN BRIDGE FOUNDATIONS

INTRODUCTION

Chapter 3 showed that IP was successful at imaging reinforced concrete bridge foundations and steel H-piles. ERI was not capable of successfully imaging long, slender piles like those tested here, but it can image large reinforced concrete structures. Briaud et al. (2012) noted that imaging foundations less than 1 m and deeper than 5 m is very difficult with ERI. Long, slender foundations were tested for this research because they are the common construction practice in the Bryan TxDOT District. Even though it has been shown that ERI was not capable of imaging these foundations (Arjwech 2011), the ERI data were included as an indicator of the quality of the IP data because the IP model was dependent on the ERI model. Because the ERI data were not used to estimate the bridge foundation depth, only the IP data were post processed with MATLAB®, a numerical computing environment, and used to generate the probability of non-exceedance curve. The MATLAB® post processing was performed to automate the foundation depth estimation to provide a quantitative prediction. The post processed data set and the actual dimensions of foundations were used to calculate the probability of non-exceedance curve. Each of these processes and results are described in this chapter.

INVERTED IP SECTION POST PROCESSING

The AGI EarthImager™ commercial software is very useful for processing collected data in the field. The software calculated the apparent resistivity pseudosection from a homogeneous half space model, this forward model was then compared to the measured apparent resistivity pseudosection and the data misfit between the two pseudosections was computed. Next, the linearized inverse problem was solved, the model was updated, and again the data misfit was calculated. If the data misfit was within the stop criteria the process was stopped and the inversion was complete. If the data misfit was above the stop criteria, the process was repeated. This process was similar for the IP data, but only one iteration was possible and the data misfit was calculated using the ERI model instead of the IP model. The final results were images of the spatial variations of resistivity and chargeability. These images were useful for inspecting the subsurface resistivity and chargeability distributions but they were interpreted with engineering judgment. This post processing procedure was used to automate a qualitative prediction of the estimated foundation depth so predictions did not vary from one person to the next. These automated predictions were used in conjunction with the known foundation dimensions in Chapter 3 to create the probability of non-exceedance curve.

When EarthImager™ calculated and inverted the apparent resistivity and apparent chargeability pseudosections, the calculated data and inverted data were saved in an output text file that the program used to visually display the results. This text file included the following information in the order listed below:

1. Headings.
2. Summary of data and electrodes.
3. Initial settings.
4. Surface electrode locations.
5. Commands, raw V/I, geometric factor, apparent resistivity, IP (V/V), correlation.

6. Mesh size.
7. Node location in X (m).
8. Node location in Y (m).
9. Timing.
10. Convergence.
11. IP Convergence.
12. Output of data and model of all iterations.

The inputs necessary for the post processing code were Item 6, Item 7, Item 8, and Item 12. These were copied and pasted into the MATLAB® m-file in the labeled sections. Appendix D contains the code. The following inputs were necessary from the user for the code to run: number of elements, number of elements in the *x* direction, number of elements in the *y* direction, and the range of *x*-nodes where the foundation is located. The last item was found using the known horizontal distance of the foundation at the time of testing. For example, if the foundation was located 6.5 m from the start of the line and was 1 m wide, the nodes corresponding to a horizontal distance from 6.5–7.5 m in the *x*-node section were used. The node number was first, followed by the distance in the *x* direction in m. If node 35 was at 6.5 m and node 39 was at 7.5 m, 35:39 was used as the input for the foundation. No other inputs were necessary for the code to run.

The MATLAB® code had four main sections: loading the data, organizing the elements into a numerical pseudosection, isolating the elements around the bridge foundation, and calculating the chargeability divided by the average chargeability and the normalized chargeability. The chargeability divided by the average chargeability data were used instead of the inverted chargeability values because chargeability was not an intrinsic value. The current delay time and IP measurement time were the same for all tests, so by dividing by the average chargeability the different tests were loosely compared. As an example, the data from Fig. 3.45 were used; the second pile was tested on the Davidson Creek Bridge. Recall that the depth of the data gathered for this experiment was 5.2 m below the surface, and the foundation was 6.08 m deep using the as-built bridge plans and accommodating for scour. First, chargeability data were divided by the average chargeability of the model (19 mV/V). Only the elements that coincide with the location of the foundation were plotted. Fig. 4.1 shows the chargeability plot from Davidson Creek Bridge 2.

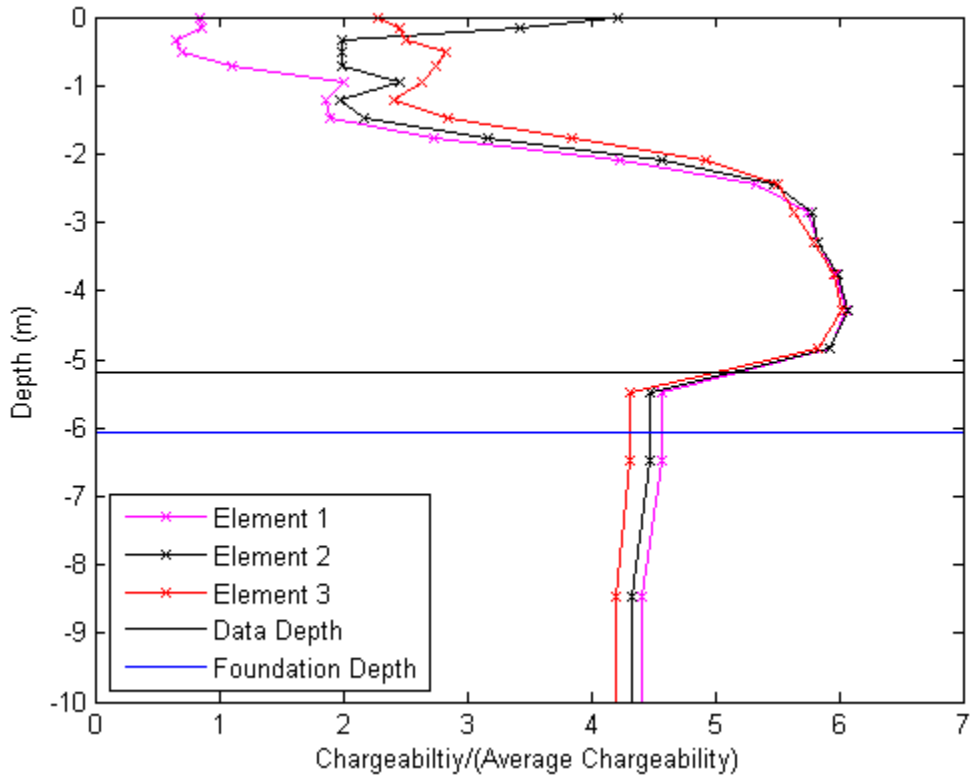

Fig. 4.1. Davidson Creek Bridge 2 chargeability around the foundation

The horizontal black line in Fig. 4.1 was the depth to which the data were collected and the horizontal blue line was the depth of the foundation. The first criterion for estimating the foundation depth was depth where the maximum ratio of the chargeability divided by the average chargeability of the model occurs, which was −4.27 m for this test.

Next, the normalized chargeability was calculated. Normalized chargeability, as defined by Slater and Lesmes (2002) is:

$$MN = \sigma'_{\text{rock}} M \tag{3.1}$$

where MN is the normalized chargeability, σ'_{rock} is the conductivity of the subsurface or the inverse of resistivity, and M is the chargeability. Again, only the data surrounding the foundation were plotted with depth in Fig. 4.2.

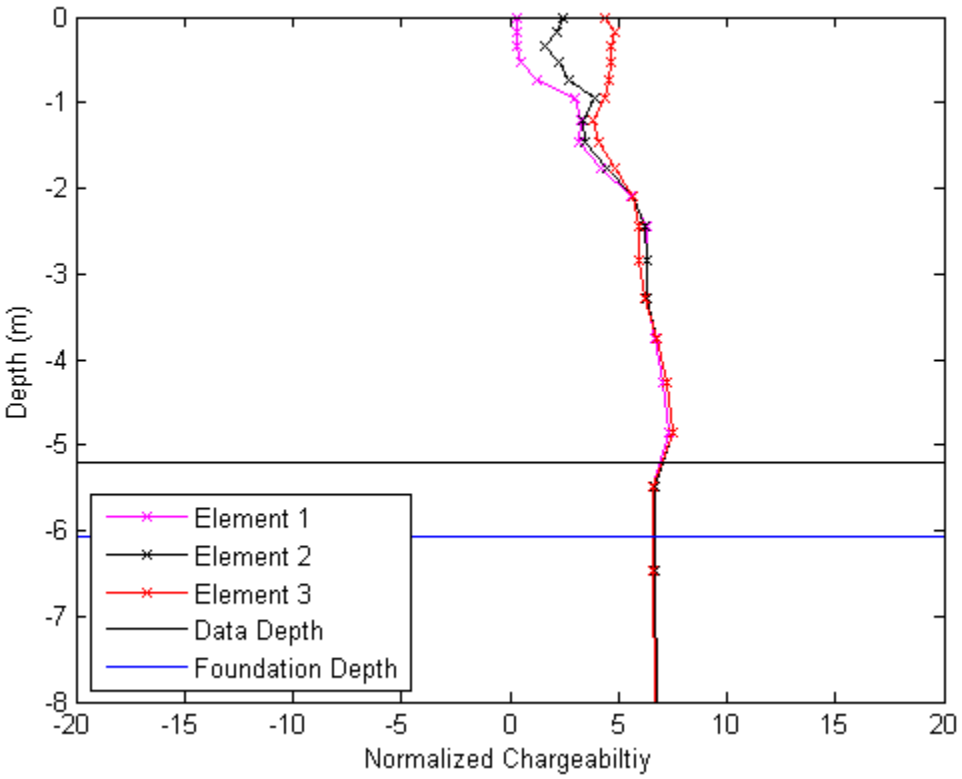

Fig. 4.2. Normalized chargeability for Davidson Creek Bridge 2

Again, the depth where the maximum normalized chargeability occurred for all of the elements combined was the predicted foundation depth, which was −4.85 m for this foundation. Ultimately, the predicted foundation depth was the maximum of the two criterion or −4.85 m for this foundation. Note that the actual foundation depth for Davidson Creek Bridge pile two was −6.08 m, thus the pile was under predicted by 1.23 m.

The number of elements that cover the foundation was dependent on the size of each element. In Fig. 4.1 and Fig. 4.2 the element mesh division was four, meaning that for a 1 m wide electrode spacing, each element was 0.25 m wide. The effect of mesh refinement was also investigated. The maximum refinement was eight. Increasing the mesh refinement to six and eight increased computational time and yielded more conservative predictions using the criteria described. Using the default of two for the mesh refinement yielded a blocky inversion that was not as clear as the mesh division of four. For this reason, a mesh refinement of four was used for all inversions and foundation predictions.

This criterion was used for each of the bridges in Chapter 3 along with the large unknown foundation and control test from the NGES section in Chapter 3. The deep foundations and steel H-piles from the NGES were not used because the RMS values were above the acceptable range to trust the model. While several of the bridges were also above the acceptable RMS (Fig. 3.38, Fig. 3.41, Fig. 3.44, and Fig. 3.51) they were included because they were full scale tests. Also, even though the models were not a good fit for the data, when the stop criteria were used the predictions were less than the foundation. Therefore, if the data quality was low due to uncontrollable factors, such as the soil type, predictions were made for the NBI because they were conservative predictions. Table 4-1 summarizes the predicted depths using this post

processing and the actual depth of the foundations. Appendix B includes all plots for these cases. Note that using these criteria two cases were over predicted, but the errors of these over predictions were both under 0.5 percent.

Table 4-1. Post Processing Results

Name	Fig.	Max chargeability depth (m)	Max normalized chargeability depth (m)	Predicted depth (m)	Actual depth (m)	Error (%)
Control Test	3.08	0.35	0.35	0.35	0.76	−0.54
3 × 3 m^2 foundation	3.19	0.66	1.15	1.15	1.00	0.15
Beason Creek Bridge	3.38	2.09	0.76	2.09	4.88	−0.57
Clear Creek Bridge 1 m spacing	3.40	2.28	4.87	4.87	4.60	0.06
Clear Creek Bridge 0.57 m spacing	3.41	1.45	0.96	1.45	4.60	−0.69
Davidson Creek Bridge pile one	3.44	1.21	1.14	1.43	5.75	−0.75
Davidson Creek Bridge pile two	3.45	4.28	4.85	4.85	6.08	−0.20
Davidson Creek Bridge pile three	3.46	2.79	1.91	2.79	6.19	−0.55
Davidson Creek Bridge pile four	3.47	3.85	3.85	3.85	6.00	−0.36
Davidson Creek Bridge pile five	3.48	1.87	2.24	2.24	6.12	−0.63
Davidson Creek Bridge pile six	3.49	3.60	3.16	3.60	6.27	−0.43
Gum Creek Bridge pile one	3.51	1.36	0.25	1.36	3.03	−0.55
Gum Creek Bridge pile two	3.51	1.36	1.75	1.36	3.03	−0.55

PROBABILITY OF NON-EXCEEDANCE

The results of the post processing predictions were used for creating the probability of non-exceedance curve. The probability of non-exceedance curve was created by fitting a lognormal cumulative distribution function (CDF) to the defined variable ξ:

$$\xi = \frac{D_{\text{actual}}}{D_{\text{predicted}}} \tag{3.2}$$

where D_{actual} is the actual depth of the foundation and $D_{\text{predicted}}$ is the depth predicted by IP using the previously described decision process. To verify that the lognormal distribution was a good

fit for these data over the normal distribution, the normal distribution CDF of ξ and the $\log(\xi)$ were plotted as described by Baecher and Christian (2003). A linear fit indicated that the distribution was a good fit for the data. In Fig. 4.3, p is the probability that a single observation from a normal distribution with a mean, μ, and standard deviation, σ, will fall in the interval $(-\infty\ \mathrm{x}]$ or:

$$p = F(x \mid \mu, \sigma) = \frac{1}{\sigma\sqrt{2\pi}} \int_{-\infty}^{x} \mathrm{e}^{\frac{-(t-\mu)^2}{2\sigma^2}}\, \mathrm{d}t \tag{3.3}$$

where μ and σ have been defined, t is each value of ξ, and x is the interval of the data. The norm of the residuals was used as an estimator of the goodness of fit of the linear fit to the data. The norm is defined as:

$$norm = \sqrt{\sum_{i=1}^{N} d_i^2} \tag{3.4}$$

where d_i is the difference between the i_{th} predicted data and empirical data. For the normal CDF, the linear norm of residual was 0.15. A perfectly linear set of data has a linear norm of residual of 0.

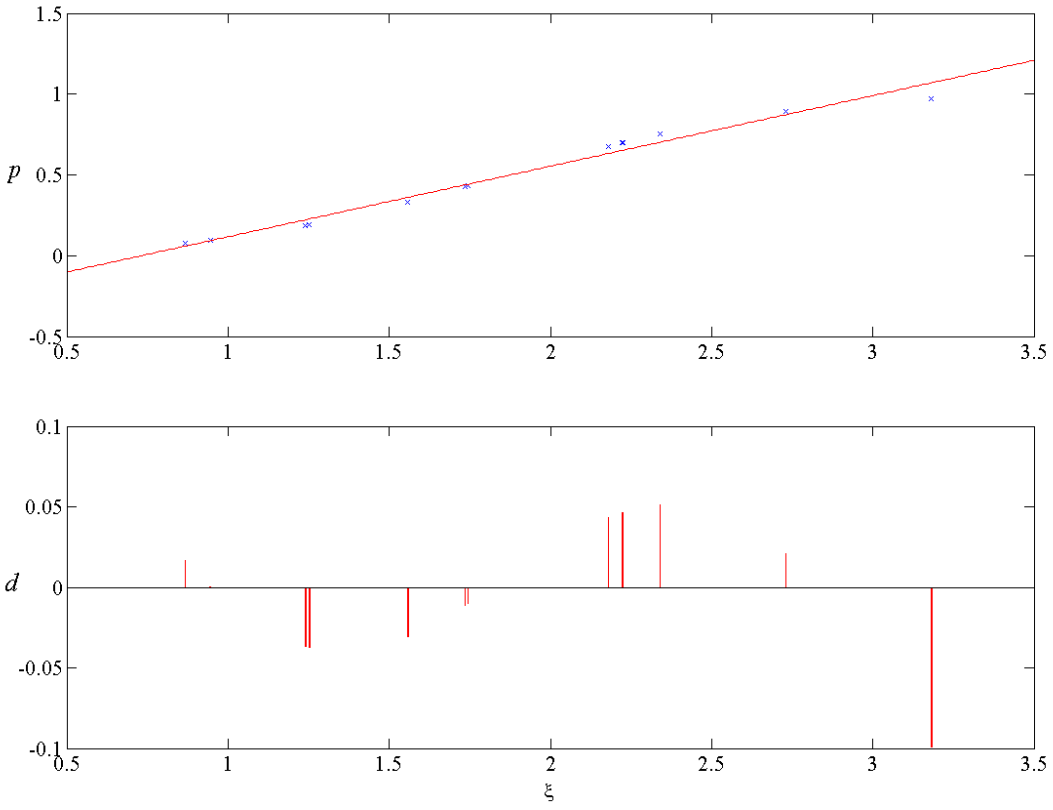

Fig. 4.3. Normal distribution CDF of ξ: probability of ξ from a normal distribution (*top*); residuals of the linear fit (*bottom*)

Fig. 4.4 is the normal distribution of $\log(\xi)$, which is more linear with a norm of 0.01 than Fig. 4.3. Thus, the lognormal distribution was used because it was more linear than the normal distribution, each experiment was independent, and the result could not be a negative number as in the normal distribution.

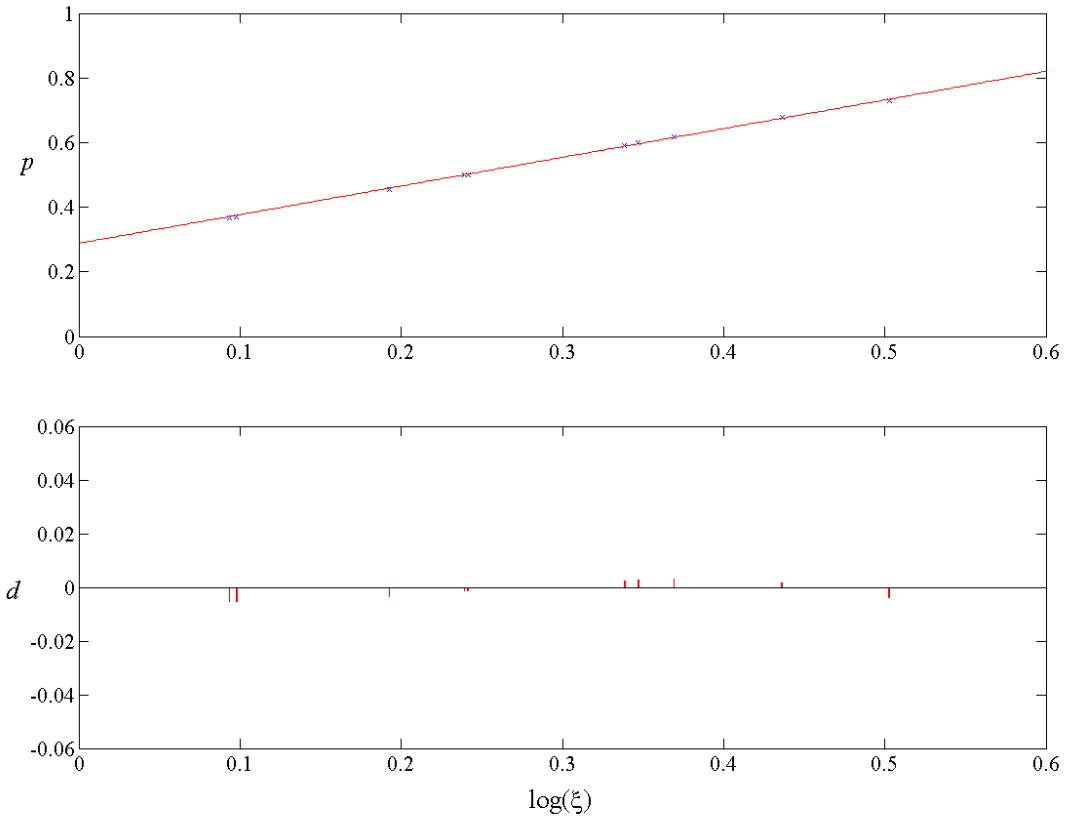

Fig. 4.4. Normal distribution CDF of $\log(\xi)$: probability of ξ from a normal distribution (*top*); residuals of the linear fit (*bottom*)

The lognormal CDF was created by first calculating the mean, μ, and standard deviation, σ, of the $\log(\xi)$. The lognormal distribution with a mean, m, and variance, v, had parameters:

$$\mu = \log(m^2 / \sqrt{v + m^2}) \tag{3.5}$$

$$\sigma = \sqrt{\log(v / m^2 + 1)} \tag{3.6}$$

where μ and σ are the mean and standard deviation. The lognormal CDF was calculated by:

$$p = F(x \mid \mu, \sigma) = \frac{1}{\sigma\sqrt{2\pi}} \int_0^x \frac{e^{\frac{-(\ln(t)-\mu)^2}{2\sigma^2}}}{t} dt \tag{3.7}$$

in which all variables have been defined. Using the parameters that define the data ξ, t is a vector from 0 to 4 because those are the boundaries of the current data set of ξ. The curve fit to

the data and the data are plotted in Fig. 4.5, which shows the probability that the foundation was shallower than the depth predicted by IP as a function of the ratio ξ.

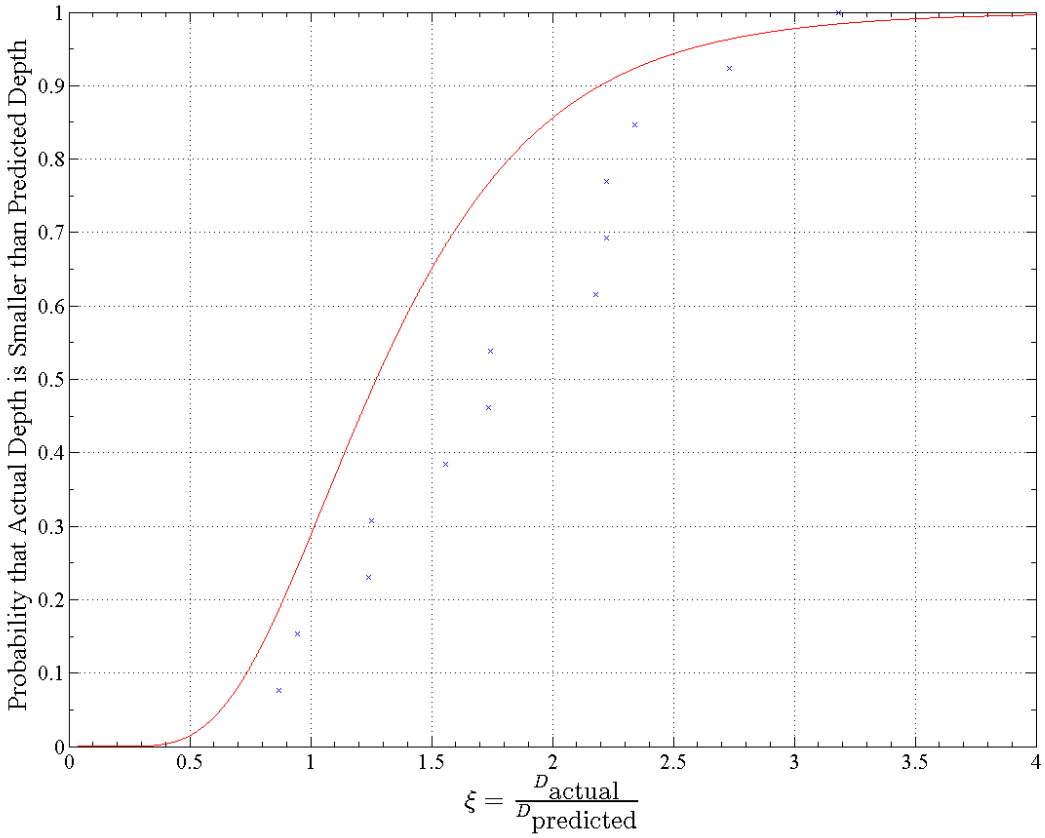

Fig. 4.5. Probability of non-exceedance curve

Fig. 4.5 is used to provide a level of confidence with the inversion output after post processing. For example, if the predicted depth was 8 m from the post processing of the IP data previously described and if 8 m was taken as the actual depth, ξ is 1. Fig. 4.5 indicates that there is 28.73 percent probability that the actual foundation was embedded less than 8 m. This curve was used to adjust the predictions made by IP for an acceptable probability of failure, where failure was over predicting the foundation depth because this was hazardous when accounting for scour. Fig. 4.6 is plotted on a semi-log scale so that smaller probabilities of failure can be seen. A probability of 10^{-6}, for example, was a one in a million chance that the depth predicted by IP was shallower than the actual depth of the foundation. Reducing an IP prediction by this much was necessary on a major interstate with a high daily traffic.

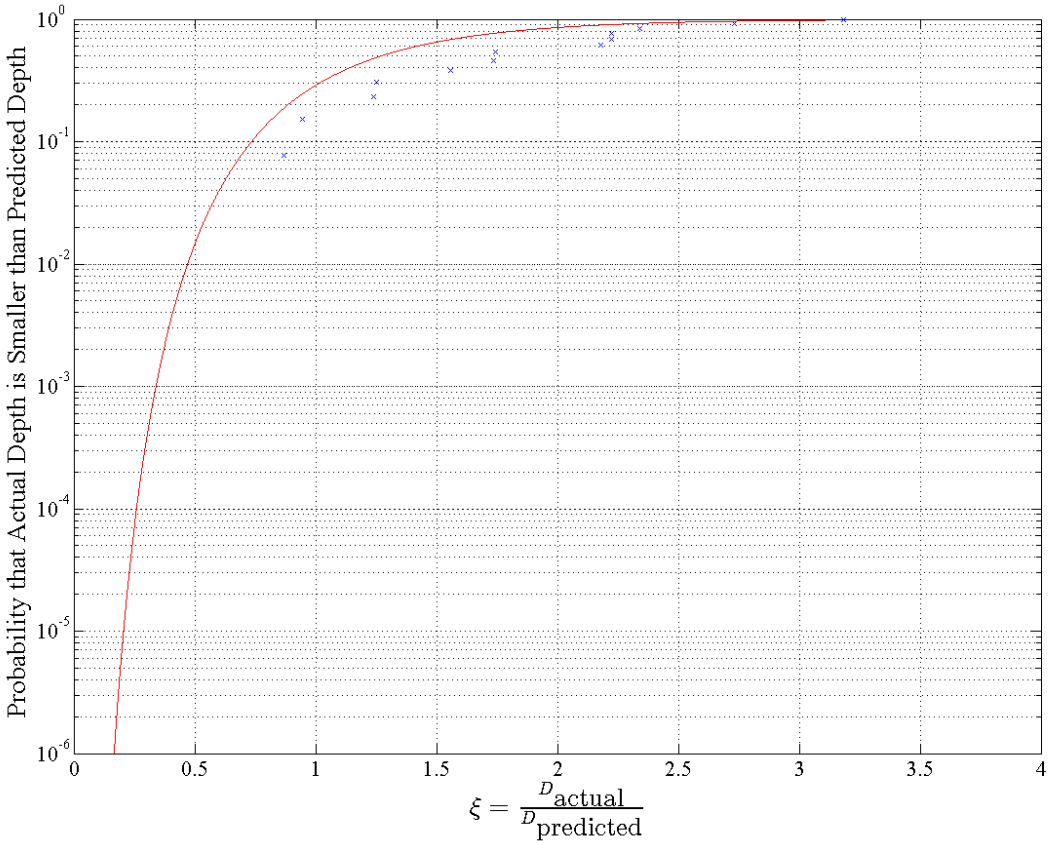

Fig. 4.6. Probability of non-exceedance curve in log scale

RELIABILITY SUMMARY

The post processing analysis that was created for IP surveys on bridge foundations is explained in this chapter and shown to be a reliable decision process for estimating the depth of the foundations. This approach was used for data with RMS above the acceptable range for ERI and IP surveys, but high RMS data was still interpreted with caution as it was a measure of the goodness of fit of the numerical model to the measured data.

These post processing criteria were then used for creating a probability of non-exceedance curve showing the probability that the actual depth of the foundation was less than the depth predicted by IP. Using probability of non-exceedance curve, the depth predicted by IP was reduced or increased depending on the acceptable level of confidence for the bridge that was tested. A major interstate, for example, required a very low probability that the actual depth was less than that predicted by IP, so the predicted depth was reduced by a determined factor. Similarly, for scour critical bridges, the predicted depth needed to be reduced for a lower probability that the actual depth was less than that predicted by IP.

The recommendations for analyzing an unknown foundation are as follows:

1. Conduct an ERI/IP survey and process the data.
2. Estimate D_{pred} using the post processing algorithm.
3. Decide on the target probability of non-exceedance for the infrastructure considered.

4. Read $\xi(p)$ from the probability of non-exceedance curve.
5. Write $D_{\text{actual}} = \xi(p) \times D_{\text{pred}}$.
6. State the results as, "there is a (target probability value) probability that the foundation is at least $\xi(p) \times D_{\text{pred}}$."

5. VALIDATION

INTRODUCTION

All of the experiments in Chapter 3 were conducted on foundations with documented depths of embedment that were known prior to testing. Known foundations were used to validate the use of ERI and IP for identifying bridge foundation depths and to determine the correct procedure for conducting field experiments on bridge foundations. To emphasize the use of ERI and IP for identifying unknown bridge foundation depths, a blind study was conducted.

NAVASOTA RIVER RELIEF BRIDGE

The data were collected at a bridge that was constructed in 2011 on SH 21, 0.83 km southwest of the Brazos/Madison County line (Fig. 5.1). This bridge was labeled as "Unknown Bridge" in Fig. 3.36.

(a) Test site (b) Experimental setup

Fig. 5.1. SH 21 over Navasota River Relief Bridge

The Navasota River Relief Bridge is 515.1 m long with 14 bents spaced every 19.81 m. There are three piles on each bent with 0.762 m diameters. A 1 m electrode spacing was used with 28 SS and 28 NP electrodes. The two lines of electrodes were parallel with a 0.3 m space between. A total station was used to account for the variable ground level, particularly around the pile where some localized scour had occurred.

Fig. 5.2 shows the survey where an isolated zone of resistivity that was higher than the surrounding soil was noted where the pile was located from the superstructure to less than 1 m into the subsurface.

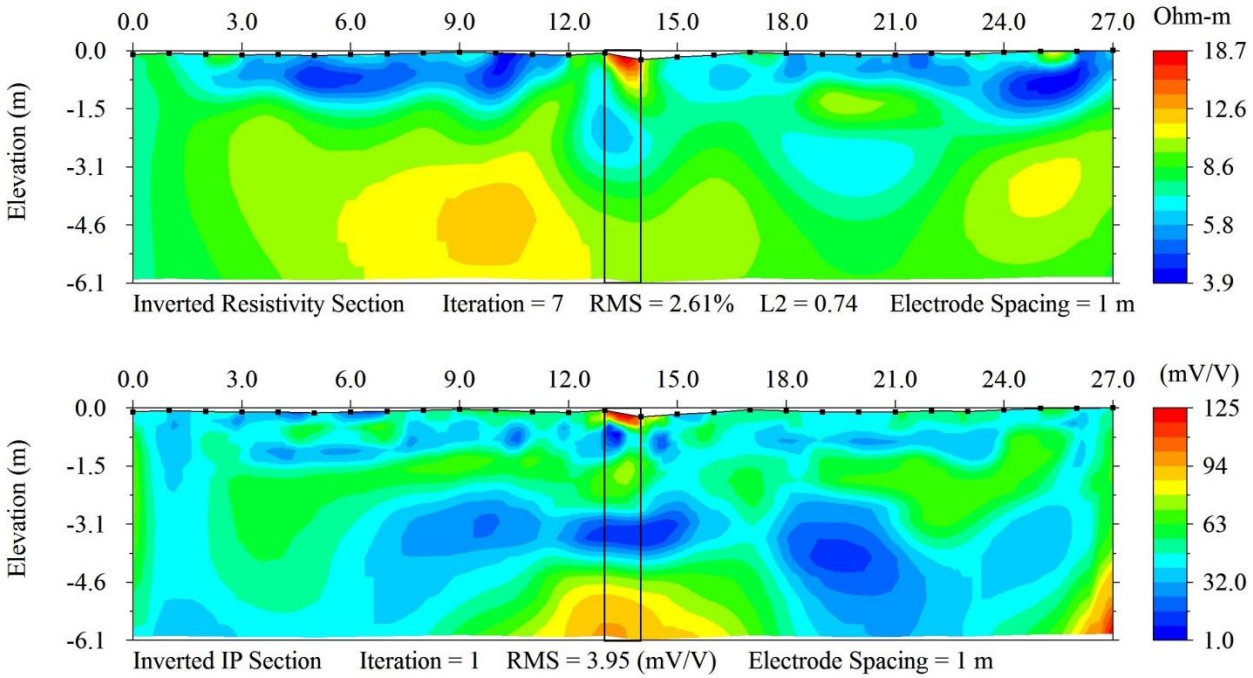

Fig. 5.2. Navasota River Relief Bridge central pile on bent three: inverted resistivity section (*top*); inverted IP section (*bottom*)

The ERI section converged in only seven iterations to an RMS of 2.61 percent. The IP inversion showed a zone of high chargeability directly beneath the pile that expanded radially larger than the diameter of the pile at the surface. Using visual inspection of Fig. 5.2 researchers inferred that the pile was embedded at least 6.1 m.

Fig. 5.2 shows the results of the inversion were post processed using the procedure defined in Chapter 4. Fig. 5.3 is the chargeability divided by the average chargeability of the model versus depth for the elements surrounding the foundation.

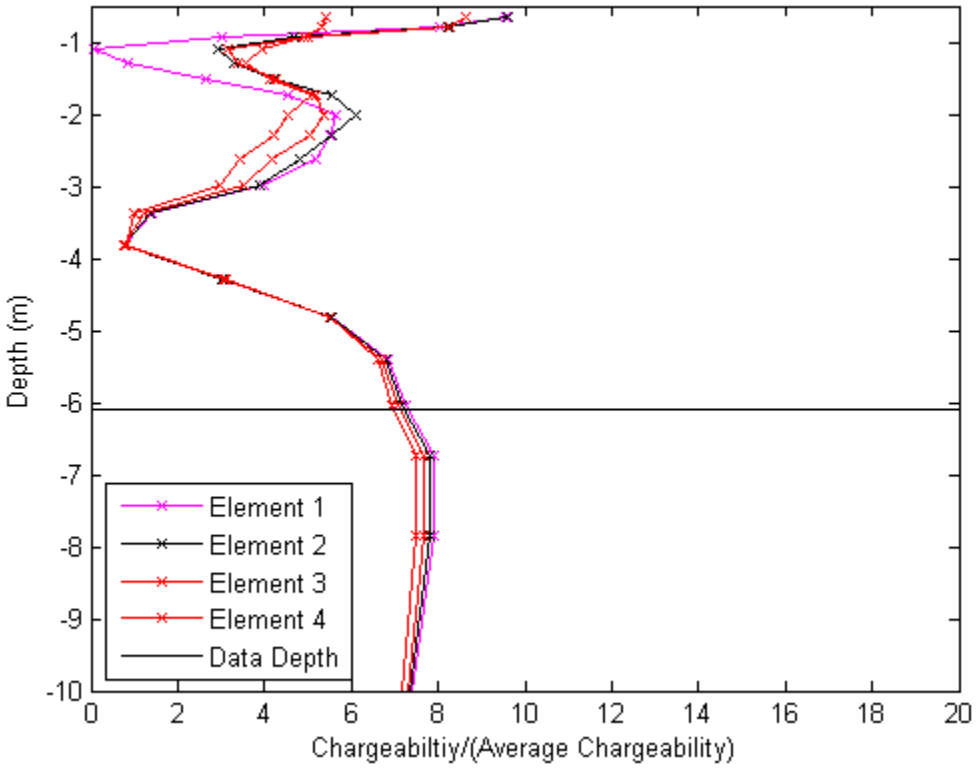

Fig. 5.3. Chargeability for Navasota River Relief

The maximum of all three elements occurred at −7.86 m. The points at the top that appeared to be larger than the elements at the bottom of the plot were excluded after looking at Fig. 5.3. The zone of high chargeability that was typically located around the bottom of the foundation was seen, so this was the zone where the predictions were focused.

Next, the normalized chargeability was plotted versus depth in Fig. 5.4. Again, the depth where the maximum occurs was taken as the depth of the foundation (−7.86 m). Note that the model continued to get larger below this point, but the values were the same as the average apparent chargeability indicating that these values were just the residual model space and not areas close to the depth of penetration.

The predicted foundation depth was −7.86 m, which was the same for both methods. There was a 28.73 percent probability that the actual foundation more shallow than −7.86 m.

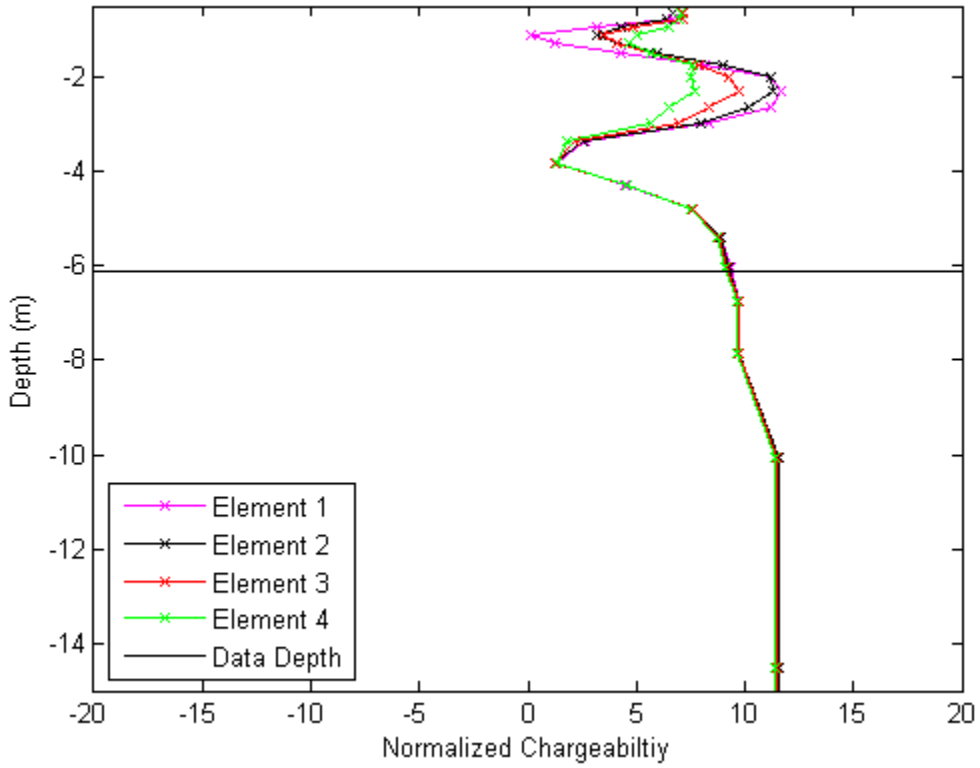

Fig. 5.4. Normalized chargeability for Navasota River Relief

After this prediction was made, the bridge plans were located to determine the prediction error from the blind study. Pile three in Fig. 5.5 was the pile tested. These plans were the drawings for the scour analysis for this bridge. The as-built bridge plans indicated that the foundation is 9.75 m beneath the subsurface; the pile was under predicted by 19.38 percent.

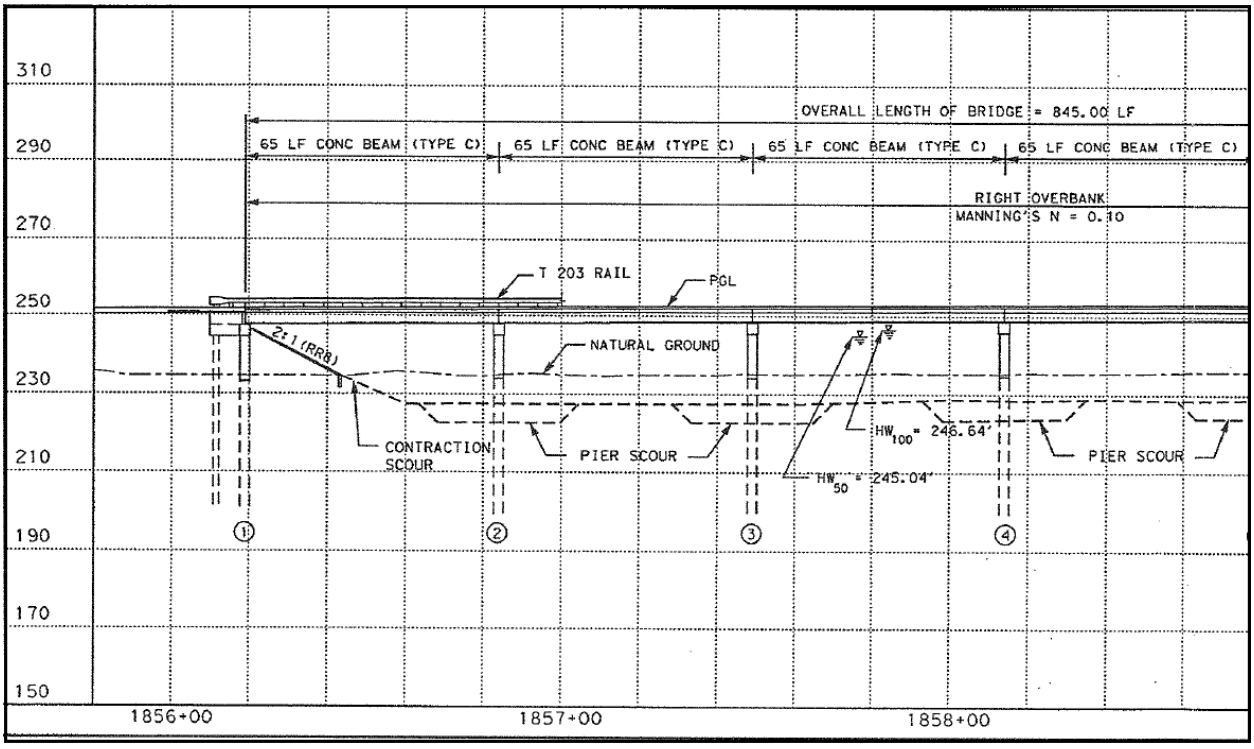

Fig. 5.5**. Navasota River Relief Bridge Plans**

VALIDATION SUMMARY

A newly constructed bridge was tested to increase the likelihood that the plans could be located after the testing and foundation depth estimation were complete. The data were collected and post processed using the procedure defined in Chapter 4 and predicted to be −7.86 m with a 28.73 percent probability that the actual depth was less than predicted. The true depth of embedment for the pile was −9.75 m so the pile length was under predicted by 19.38 percent. Thus the use of the method and corresponding probability of non-exceedance curve for predicting the depth of unknown foundations was validated.

6. UNDERGROUND UTILITY

INTRODUCTION

Near surface geophysical methods were limited in their applications due to a common variable, depth of penetration. The depth of penetration for most methods, including IP and ERI, was limited by available space for testing. When testing bridges, for example, the length of the array was limited by personal property fences on each side of the bridge. The depth of penetration was also related to the signal to noise ratio. In addition to bridge foundations, there were many shallow buried objects that required nondestructive imaging. One example of this is infrastructure mapping of unknown buried gas, water, or sewer lines. Particularly in urban areas, while theoretically the location of these subsurface lines should be known, older maps may not be accurate or as in the case of unknown bridge foundations, the plans may have been lost over time.

In this chapter, a buried gas line was imaged. In most geophysical studies, the influence of man-made objects on an ERI or IP survey was seen as a nuisance (Sumner 1976) but for civil engineering studies these structures were the desired targets. Another objective of testing the gas line was to reduce the size of the imaged anomaly. In Chapter 3 it was shown that IP can successfully image bridge foundations to provide an estimation of the depth. While the depth of the foundation was inferred from these images, the width of the foundation was not. Knowing that all deep foundations in this research were straight shaft piles, the results often appeared much wider than the dimensions of the substructure. In this chapter, a natural gas line on the north side of the TAMU Riverside Campus was imaged using 12 arrays. Each array was centered about the same point and varied by 15° to narrow the apparent width of the pipe.

GAS LINE DESCRIPTION

The natural gas line on the north side of the TAMU Riverside Campus is located between SH 21 and Warehouse Loop (Fig. 6.1). It is owned and operated by Atmos Pipeline and is an in-service gas transmission system. The pipeline is 11.43 cm in diameter and is buried 1.5 m beneath the surface.

Fig. 6.1. Map of the natural gas transmission system

As previously mentioned, the same point over the pipe was tested by rotating the array by 15° from a central point. The central point was located following a preliminary test used as an example for a classroom field trip. Fig. 6.2 shows the field study that initiated further testing of the gas line.

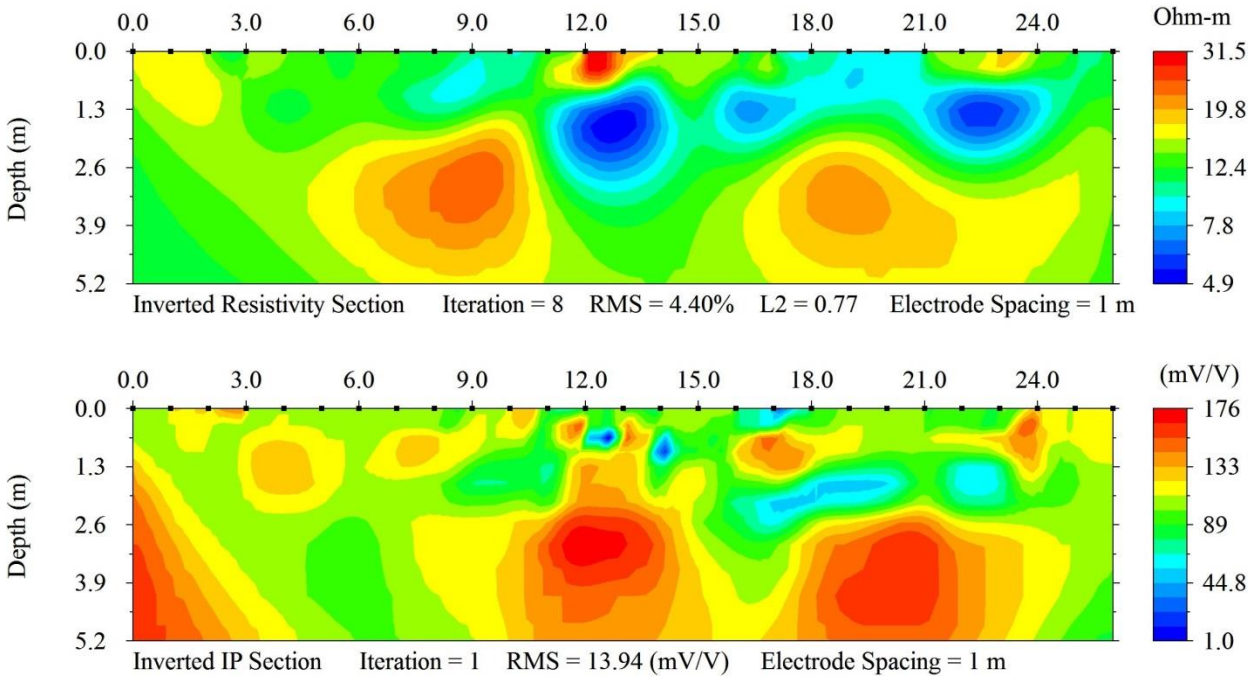

Fig. 6.2. Preliminary field study of the Atmos gas line: inverted resistivity section (*top*); inverted IP section (*bottom*)

The ERI and IP profiles here send conflicting messages. The gas line was located between the 13th and 14th electrodes. The location of the gas line was estimated using the gas line markers, the yellow sign in Fig. 6.3a. The depth of the gas line was approximately 1.5 m, so the depth on the ERI profile was accurate, though much larger than the 11.43 cm diameter galvanized steel pipe. The inverted IP section made the pipe appear to be buried approximately 3 m instead of 1.5 m. The RMS of the IP section was 13.94 mV/V; the model was not a good fit for the inversion.

This experiment full of poor IP curves and negative apparent resistivity measurements. To improve the data quality, holes were dug and filled with a bentonite slurry for the rotating arrays. The bentonite slurry allowed for better contact with both the SS and NP electrodes, allowing more current to be injected in the ground and higher quality decay curves. The bentonite was necessary because the ground was so stiff that when holes were dug for the NP electrodes there were large voids surrounding the NP electrodes leading to a loss of signal.

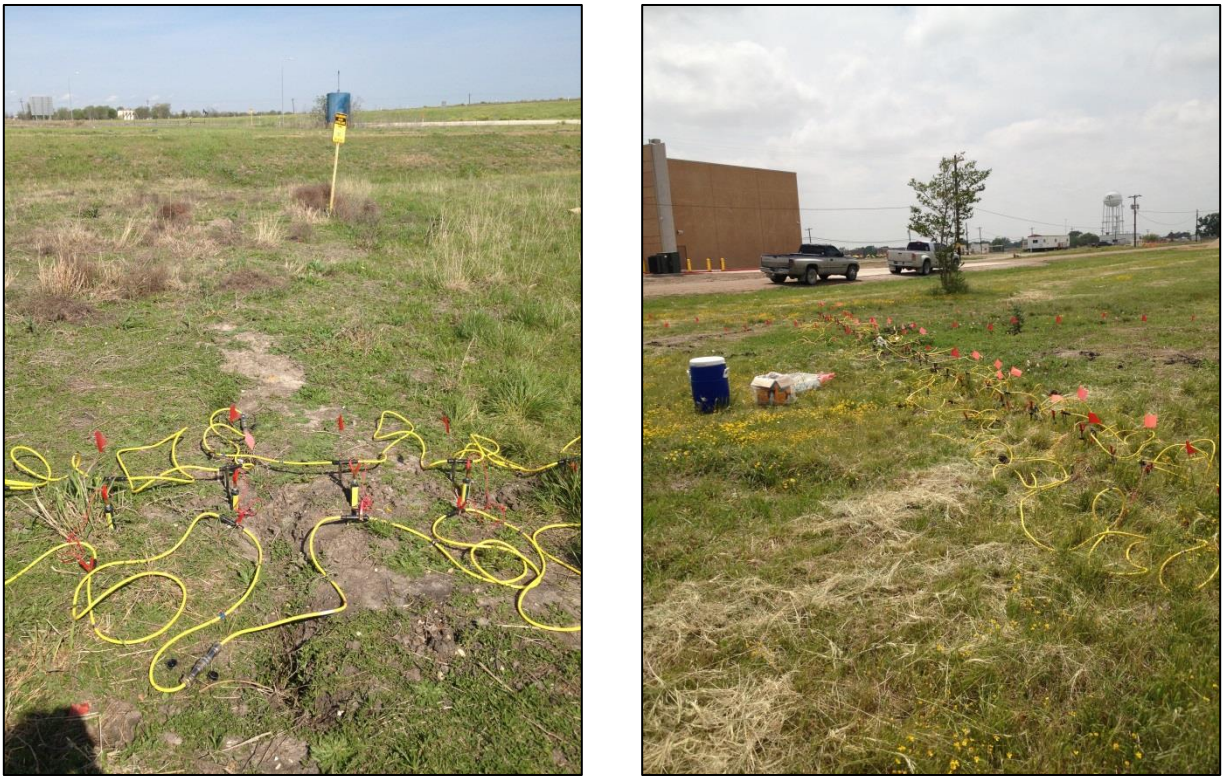

(a) Experimental setup (b) Test site

Fig. 6.3. Gas line test at Riverside Campus

EXPERIMENTAL SETUP AND RESULTS

The results of the preliminary study were used to plan the survey. The center of the resistivity anomaly was taken as the center point for the field set up. From this point, lines were rotated by 15° and stretched radially out by 6.75 m. This kept the total length of the array at 13.5 m (28 NP and 28 SS electrodes spaced every 0.5 m) and the exact center point the same. A diagram of the field set up for all 12 lines is shown in Fig. 6.4.

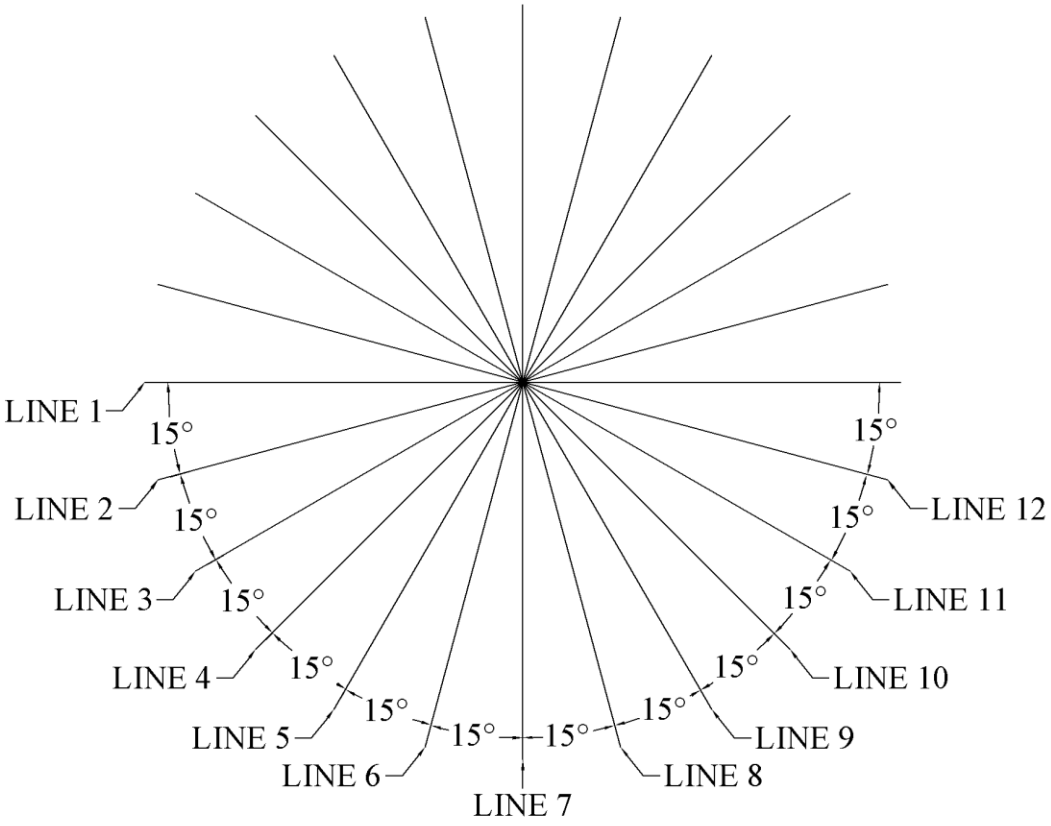

Fig. 6.4. Aerial layout of array setup

The pipe was not successfully imaged by IP in most of the inversions. This was most likely due to the small size of the pipe and the numerous poor decay curves despite the improvement from the bentonite slurry. The ERI and IP inversion of each of the 12 lines are included in Appendix C along with the rotated image relative to Line 1. Because the IP images did not successfully image the pipe, they were not included in the 3D model. Fig. 6.5 shows all of the results of the 12 lines combine.

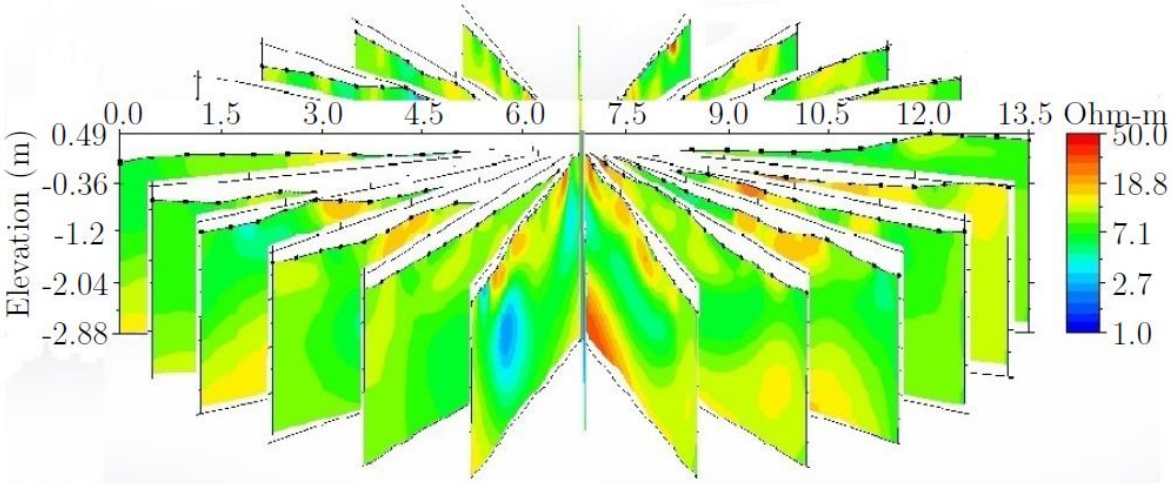

Fig. 6.5. Combined ERI inversions for a 3D model

The line with the elevation labeled and the apparent resistivity values is Line 1 from Fig. 6.4. The scale of apparent resistivity was maintained the same for all 12 inversions. Because the arrays were centered on the same point, the model of all 12 lines did not show the images clearly. Line 1 is kept in all figures and each subsequent line is shown relative to Line 1 so the pipe can be seen.

In order to show the increasing angle from Line 1, each slice was placed on its respective rotated plane relative to Line 1 in Solid Works. Overlaying these images obscured some of the first line so it is shown in Fig. 6.6 alone.

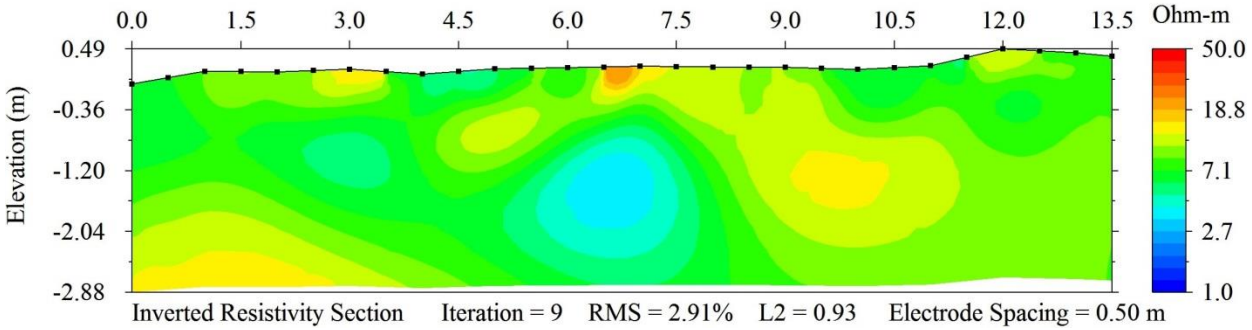

Fig. 6.6. ERI Inversion of Line 1 in the gas line survey

The pipe can be seen as a circular zone of low resistivity between 6 m and 7.5 m centered approximately 1.6 m beneath the surface. This anomaly was buried near the known depth of the gas line (1.5 m) but it appeared much larger than the documented 11.43 cm diameter gas line. An objective of this study was to reduce the side of ERI response of the pipe by changing the angle of the array respective to the gas line. The 45° and 90° are included in this chapter.

The 45° line, Line 4, shows the reduced diameter of the gas line compared to Fig. 6.6 in Fig. 6.7. There was a small, circular zone of low resistivity beginning at 2 m to approximately 3 m. This is a mathematical anomaly, because this section of the model was removed because of negative apparent resistivity values.

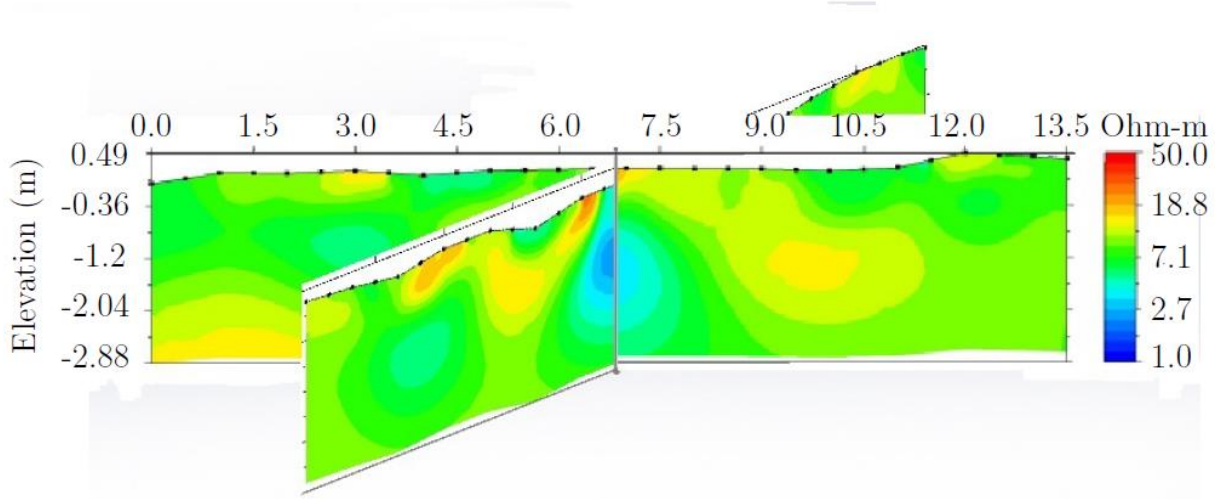

Fig. 6.7. 3D model of the 45° line in the gas line survey

The RMS for this inversion was 11.03 percent despite having removed some of the negative values. Despite this, a localized circular zone of high conductivity was seen over the location of the pipe in Fig. 6.8. The conductivity of the pipe was higher at 45° and the diameter of the pipe was smaller.

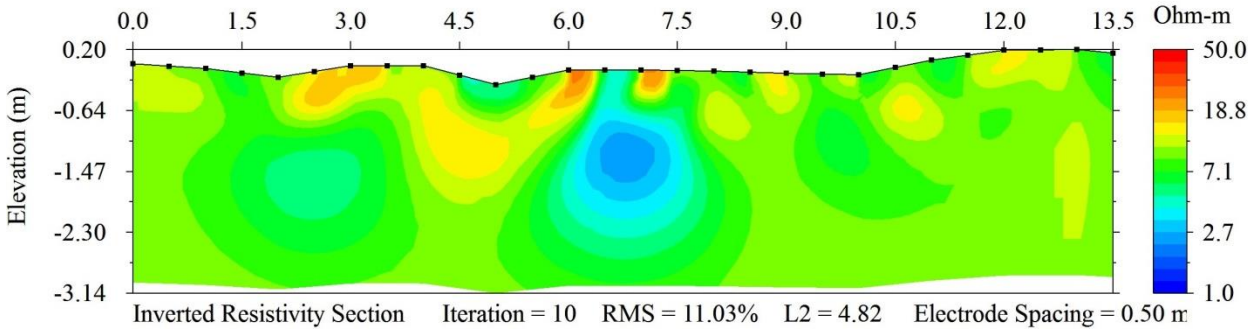

Fig. 6.8. ERI inversion of Line 4 in the gas line survey

Line 7, which is rotated 90° from Line 1, had an RMS of 7.51 percent and again a region of low resistivity was seen around 3 m from the front of the line in Fig. 6.9. The zone of high conductivity around the pipe was the smallest in Line 7, appearing around 20 cm, nearly twice the diameter of the pipe.

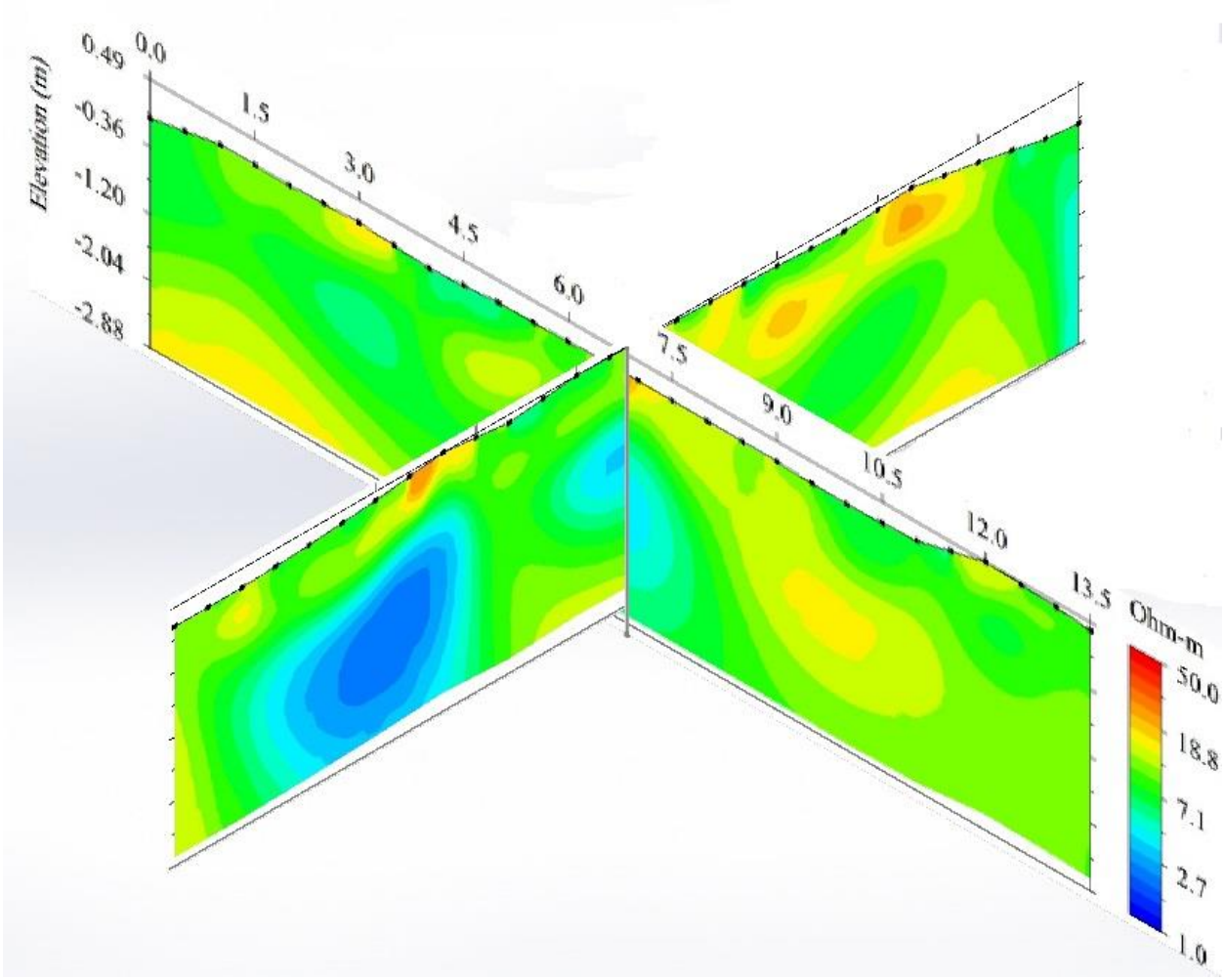

Fig. 6.9. 3D model of the 90° line in the gas line survey

Researchers expected that there was a zone of low resistivity all along this profile around 1.5 m because Line 7 should have been directly over the pipe. The significantly reduced diameter of the pipe, along with the lack of a layer of low resistivity indicated that this line was not directly over the pipe. The line appeared to run perpendicular to Warehouse Loop in Fig. 6.3, but Line 1 may have not been exactly parallel to Warehouse Loop during testing.

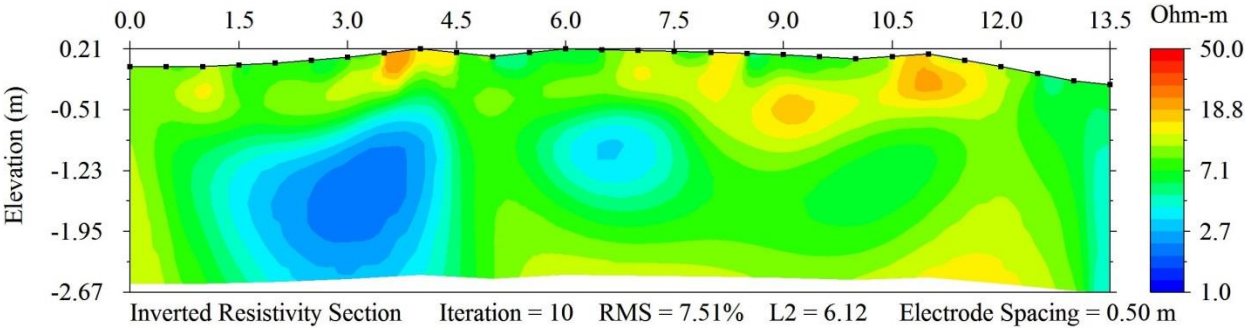

Fig. 6.10. ERI Inversion of Line 7 in the gas line survey

A slight error in the original layout of Line 1 led to error propagation around the circle so that inside of testing directly on top of the pipe for Fig. 6.10, only a small section of the pipe was tested at the middle. This may also be the cause of the response of the pipe appearing larger in diameter than in reality because of the close proximity of a highly conductive material along the line instead of an isolated section of the pipe. Unfortunately, because of the slight skew of the lines the response of the gas line did not appear symmetric on the other half of the circle. When comparing the 45° line and the 135° line, for example, the 135° appeared much more spread out than Fig. 6.8 and shifted slightly to under 6 m.

UNDERGROUND UTILITY SUMMARY

An objective of this research was to show that ERI and IP can be applied to other subsurface infrastructure. IP was not successful at imaging the galvanized steel gas line due to low quality IP decay curves and possibly due to the small diameter of the pipe. ERI, however, was successful at imaging the pipe. By rotating the array by 15° the diameter of the pipe in the inversion was successfully reduced. Unfortunately, the original line was not exactly perpendicular to the gas line so these images were not symmetric through the inversions. Also, the exact depth of the gas line was not consistently achieved in this study. Despite this another possible application of ERI for civil engineering investigations was proved.

7. CONCLUSIONS

This final report presented an experimental study that established the feasibility of using ERI and IP for estimating the final depth of bridge foundations where this pertinent information is no longer available. Foundations made of reinforced concrete and steel H-piles were successfully imaged to estimate the depth of the foundation where it is unknown. This was demonstrated using foundations at a NGES and four bridges in the Bryan TxDOT District that are both shallow and deep, in different soil conditions, and in one case, through the presence of water. The experimentally determined setup for using ERI and IP for determining the depth of bridge foundations are:

1. Arrange the array so that the foundation is in the middle of the electrode line.
2. The central electrodes (14th and 15th in a 28 electrode line) should be placed on either side of the foundation.
3. SS electrodes should be next to the foundation and NP electrodes offset by less than 0.3 m for a side scan survey.
4. The IP cycle time should be 2 s.
5. The dipole-dipole array should be used.
6. For concrete structures, the foundation must contain reinforcement.

If it is determined after an initial survey that the foundation is deeper than the depth to which data are collected, the length of the array should be increased. There is a tradeoff between the depth of penetration and image quality when the electrode spacing is increased to lengthen the survey line. If deeper data are needed, additional electrodes should be used so that the electrode spacing remains equal to or less than the width of the foundation.

The two limitations of the method are related to the soil type. If the soil is very loose, like a loose sand, the interconnected pore space will allow the signal to dissipate lowering the quality of the data collected and the resulting inversion. Data can be improved by using a bentonite slurry around the electrodes to increase the amount of current that is injected into the subsurface, but if the soil profile remains a loose sand to the depth of penetration of the survey the results will not be significantly increased. Also, little can be seen in an inversion if the response of the soil is similar to the response of the reinforced structure, lowering the contrast between the two materials. Table 7-1 summarizes the conditions under which different foundations in different soils will yield a very good, fair, or poor result. This table should be used as a general guideline when considering using IP for predicting the depth of an unknown foundation. Note that timber piles were never tested, but because steel is necessary to gather a measurable IP response, the data quality of a timber pile test is assumed to be poor.

Table 7-1. In Situ Parameter Guidelines

Foundation	Clay	Clayey Sand	Silty Sand	Well Graded Sand	Poorly Graded Sand
Spread footing $L \leq 5$ m	Very good	Very good	Very good	Fair	Fair
Reinforced concrete pile $0 \leq L \leq 10$ m $d \leq 1$ m	Very good	Very good	Fair	Fair	Poor
Reinforced concrete pile $0 \leq L \leq 10$ m $d \geq 1$ m	Very good	Very good	Very good	Fair	Poor
Reinforced concrete pile $L \geq 10$ m $d \leq 1$ m	Very good	Fair	Fair	Fair	Poor
Reinforced concrete pile $L \geq 10$ m $d \geq 1$ m	Very good	Very good	Very good	Fair	Poor
Unreinforced concrete foundation	Poor	Poor	Poor	Poor	Poor
Steel pile $0 \leq L \leq 10$ m	Fair	Fair	Fair	Poor	Poor
Steel pile $L \geq 10$ m	Fair	Fair	Fair	Poor	Poor
Time pile	Poor	Poor	Poor	Poor	Poor

A quantitative post processing algorithm is created to remove the qualitative uncertainty of interpreting the inversions from each experiment. This algorithm can be used for high and low quality data, but surveys with resulting high RMS models should still be interpreted with caution as it is a measure of the goodness of fit of the numerical model to the measured data. After all tested bridges and two shallow foundations at the NGES have been post processed the predicted depths and known foundation depths are used to create a probability of non-exceedance curve showing the probability that the actual depth of the foundation is less than the depth predicted by IP. Using this curve the depth predicted by IP can be reduced or increased depending on the acceptable level of confidence for the bridge that is being tested. This curve should be used to provide an acceptable level of certainty depending on the situation of the inversions when used in practice. The steps for data reduction and probability failure of the foundation prediction are as follows:

1. Conduct an ERI/IP survey with the experimentally determined setup above.
2. Process the data and visually interpret the inverted IP section.
3. Estimate D_{pred} using the post processing algorithm for the inverted IP model.
4. Decide on the target probability of non-exceedance for the infrastructure considered.
5. Read $\xi(p)$ from the probability of non-exceedance curve.

6. Write $D_{\text{actual}} = \xi(p) \times D_{\text{pred}}$.
7. State the results as, "there is a (target probability value) probability that the foundation is at least $\xi(p) \times D_{\text{pred}}$."

Finally, a bridge with foundation details unknown to the researcher was successfully tested to validate the use of ERI and IP for truly unknown foundations. The data were collected and post processed using the procedure defined in Chapter 4 and predicted to be 7.86 m with a 28.73 percent probability that the actual depth was shallower than predicted. The actual depth of embedment for the pile was 9.75 m so the pile length was under predicted by 19.38 percent. Researchers also showed that the method can be used for imaging other subsurface structures. An 11.43 cm gas line was imaged. More testing of buried lines with varying diameters, varying depths of embedment, and in different soil conditions is still required to evaluate the full potential of ERI and IP for locating buried lines.

REFERENCES

AGI (2007). *EarthImager 2D Resistivity and IP Inversion Software Instruction Manual*. 2121 Geoscience Drive, Austin, Texas 78726, version 2.4.0 edition.

Arjwech, R. (2011). "Electrical Resistivity Imaging for Unknown Bridge Foundation Depth Determination." Ph.D. thesis, Texas A&M University, Texas A&M University.

Baecher, G. and Christian, J. (2003). *Reliability and Statistics in Geotechnical Engineering*. John Wiley & Sons.

Ballouz, M., Nasr, G., and Briaud, J.-L. (1991). "Dynamic and Static Testing of Nine Drilled Shafts at Texas A&M University Geotechnical Research Sites." *Report No. 1*, Research Report to FHWA, Civil Engineering, Texas A&M University.

Bavusi, M., Rizzo, E., and Lapenna, V. (2006). "Electromagnetic Methods to Characterize the Savoia di Lucania Waste Dump (Southern Italy)." *Environmental Geology*, 51, 201-308.

Bernstone, C., Dhalin, T., Ohlsson, T., and Hogland, W. (2000). "DC Resistivity Mapping of Internal Landfill Structures: Two Pre-Excavation Surveys." *Environmental Geology*, 36, 360-371.

Bosscher, P., Menclova, E., Russell, J., and Wahl, R. (1998). "Estimating Bearing Capacity of Piles Installed with Vibratory Drivers." *Report No. 1*, US Army Corps of Engineers.

Briaud, J., Medina-Cetina, Z., Hurlebaus, S., Everett, M., Tucker, S., Yousefpour, N., and Arjwech, R. (2012). "Unknown Foundation Determination for Scour." Report No. 6604-1. Austin, TX: Texas Department of Transportation (TxDOT).

Deceuster, J. and Kaufmann, O. (2012). "Improving the Delineation of Hydrocarbon Impacted Soils and Water through Induced Polarization (IP) Tomographies: A Field Study at an Industrial Waste Land." *Journal of Contaminant Hydrology*, 136-137, 25-42.

Dolan, W. and McLaughlin, G. (1967). "Considerations Concerning Measurement Standards and Design of Pulsed IP Equipment, Part I." *Symposium on Induced Electrical Polarization*, University of California, Berkeley, 2-31.

Dunn, P. (2010). "Comparison of Cone Model and Measured Dynamic Impedance Functions of Shallow Foundations." Ph.D. thesis, University of Florida, University of Florida.

Edwards, L. (1977). "A Modified Pseudosection for Resistivity and IP." *Geophysics*, 42(5), 1020-1036.

FHWA (1988). "Interim Procedures for Evaluating Scour at Bridges." *Report No. 1*, Federal Highway Administration.

FHWA (2008). "Technical Guidance for Bridges over Waterways with Unknown Foundations." *Report No. 1*, Federal Highway Administration.

FHWA (2012). "Evaluating Scour at Bridges." *Report No. 5*, Federal Highway Administration.

Gibbens, R. (1995). "Load Tests on Five Large Spread Footings on Sand and Evaluation of Prediction Methods." Masters of Science Thesis, Texas A&M University, Texas A&M University.

Groves, P., Cascante, G., Dundas, D., and Chatterji, P. (2011). "Use of Geophysical Methods for Soil Profile Evaluation." *Canadian Geotechnical Journal*, 48(9), 1364-1377.

Hiltunen, D. and Roth, M. (2003). "Investigation of Bridge Foundation Sites in Karst Terrane via Multi-Electrode Electrical Resistivity." *3rd International Conference on Applied Geophysics*. Geophysics 2003: Orlando, Fl.

Holt, J. and Douglas, R. (1994). "Determining Length of Installed Timber Piles by Dispersive Wave Propagation." *Technical report 9516*, Federal Highway Administration (March).

Hossain, M., Khan, M., Hossain, J., Kibria, G., and Taufiq, T. (2011). "Evaluation of Unknown Foundation Depth Using Different NDT Method." *Journal of Performance of Constructed Facilities*, 27, 209-214.

Hubbard, S., Zang, J., Monteiro, P., Peterson, J., and Rubin, Y. (2003). "Experimental Detection of Reinforcing Bar Corrosion using Nondestructive Geophysical Techniques." *Materials Journal*, 100, 501-510.

Leroux, V., Torleif, D., and Svensson, M. (2007). "Dense Resistivity and Induced Polarization Profiling for a Landfill Restoration Project at Härlöv, Southern Sweden." *Waste Management & Research*, 25, 49-60.

Lowrie, W. (2007). *Fundamentals of Geophysics*. Cambridge University Press.

Maser, K., Sanqeui, M., Lichtenstein, A., and Chase, S. (1998). "Determination of Bridge Foundation Type from Structural Response Measurements." *Nondestructive Evaluation Techniques for Aging Infrastructure and Manufacturing*, 55-67.

McKinney, F. (2012). "25 years ago, the bridge was gone." Times Union archive, <http://www.timesunion.com/local/article/25-years-ago-the-bridge-was-gone-3460076.php#photo-2780116> (April).

Melville, B. and Coleman, S. (2000). *Bridge Scour*. Water Resources Publications, LLC.

Mercado, E. and O'Neil, M. (2003). "Methods to Measure Scour Depth and the Depth of Unknown Foundations." *3rd International Conference on Applied Geophysics*. Geophysics 2003: Orlando, Fl.

Meyer, C., Burkard, U., and Barlieb, C. (2007). "Archaeological Questions and Geophysical Solutions: Ground-Penetrating Radar and Induced Polarization Investigations in Menigua, Spain." *Archaeological Prospection*, 14, 202-211.

National Transportation Safety Board (1988). "Collapse of New York Throughway (I-90) Bridge over the Schoharie Creek, near Amsterdam, New York, April 5, 1987." *Report No. 1*, Highway Accident Report: NTSB/HAR-88/02, Washington, D.C.

Olson, L. (2005). "Dynamic Bridge Substructure Evaluation and Monitoring." Report No. FHWA-RD-03-089. Federal Highway Administration (FHWA).

Olson, L., Jalinoos, F., and Aouad, M. (1998). "Determination of Unknown Subsurface Bridge Foundations" A summary of the NCHRP 21-5 Interim Report. USDOT Geotechnical Engineering Botebook Guideline No. 16, Federal Highway Administration (FHWA).

Parola, A., Hagerty, D., Mueller, D., Melville, B., Parker, G., and Usher, J. (1997). "The Need for Research on Scour at Bridge Crossings." *Managing Water: Coping with Scarcity and Abundance*, ASCE, ed., ASCE.

Pellerin, L. (2002). "Applications of Electrical and Electromagnetic Methods for Environmental and Geotechnical Investigations." *Surveys in Geophysics*, 23, 101-132.

Robinson, B. and Webster, S. (2008). "Successful Testing Methods for Unknown Bridge Foundations." *Proceedings of the Fifth Highway Geophysics - NDE Conference*: Charlotte, NC, 101-110.

Schlumberger, C. (1920). *Etude Sur la Prospection Electrique du Sous-Sol*. Paris: Gautheir-Villars.

Scott, W. and West, G. (1969). "Induced Polarization of Synthetic High-Resistivity Rocks Containing Disseminated Sulfides." *Geophysics*, 34(1), 87-100.

Seigel, H. (1959). "Mathematical Formulation and Type Curves for Induced Polarization." *Geophysics*, 24(3), 547-565.

Slater, L. and Lesmes, D. (2002). "IP Interpretation in Environmental Investigations." *Geophysics*, 67(1), 77-88.

Sogade, J., Scira-Scappuzzo, F., Vichabian, Y., Shi, W., Rodi, W., Lesmes, D., and Morgan, F. (2006). "Induced-Polarization Detection and Mapping of Contaminant Plumes." *Geophysics*, 71, B75-B84.

Su, J., Yang, C., Wu, W., and Huang, R. (2002). "Effect of Moisture Content on Concrete Resistivity Measurements." *Journal of Chinese Institute of Engineers*, 25, 117-122.

Sumner, J. (1976). *Principles of Induced Polarization for Geophysical Exploration*. Elsevier Scientific Publishing Company.

Suzuki, O., Shimarmuram, M., and Matsunuma, M. (2007). "A Health Monitoring System for Railway Bridge Piers." *Third International Conference on Structural Health Monitoring of Intelligent Infrastructure*: Vancouver, Canada.

Tuuti, K. (2001). "Corrosion of Steel in Concrete." *Construction and Building Materials*, 15, 125-131.

Wisen, R., Auken, E., and Dhalin, T. (2005). "Combination of 1D Laterally Constrained Inversion and 2D Smooth Inversion of Resistivity Data with a Priori Data from Boreholes." *Near Surface Geophysics*, 3, 71-79.

APPENDIX A. POST PROCESSING RESULTS

A.1 CONTROL TEST

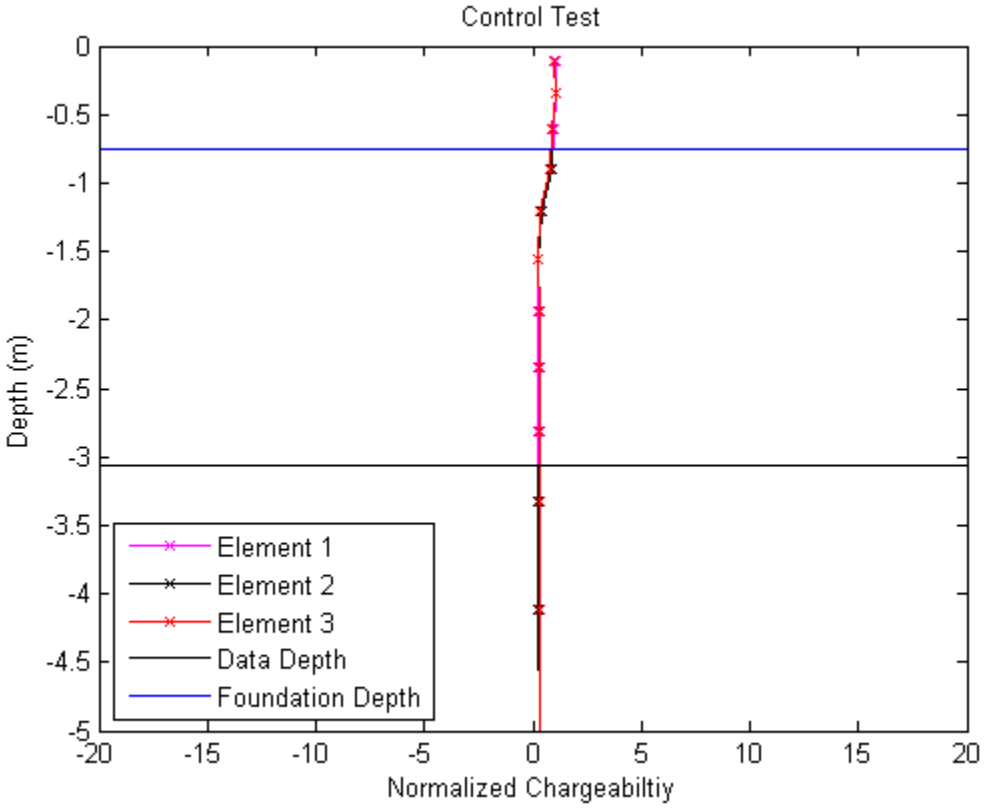

Fig. A.1. Normalized chargeability for control test

A.2 3 × 3 M^2 UNKNOWN DEPTH

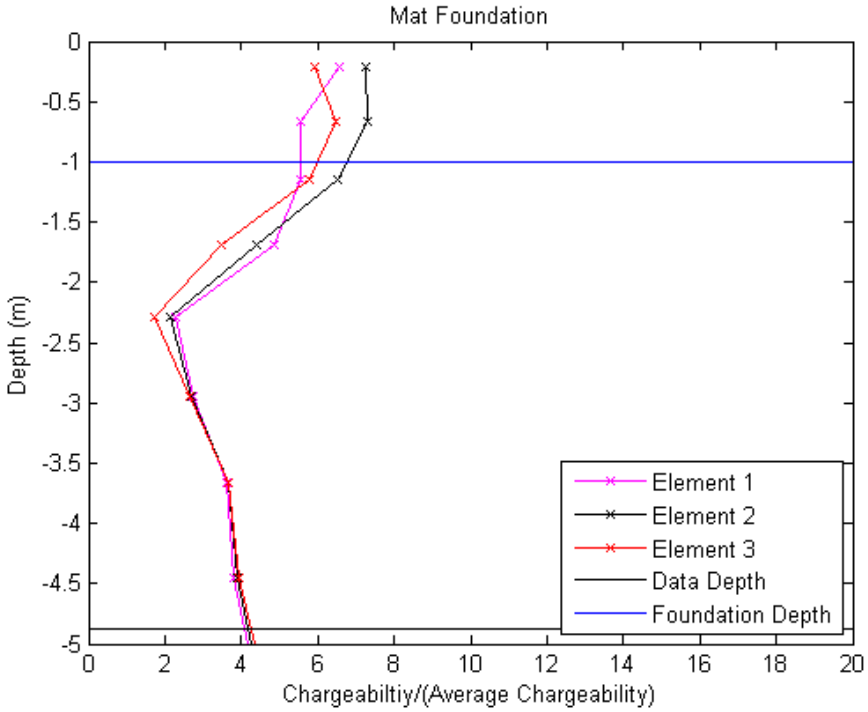

Fig. A.2. 3 × 3 m^2 mat chargeability around the foundation

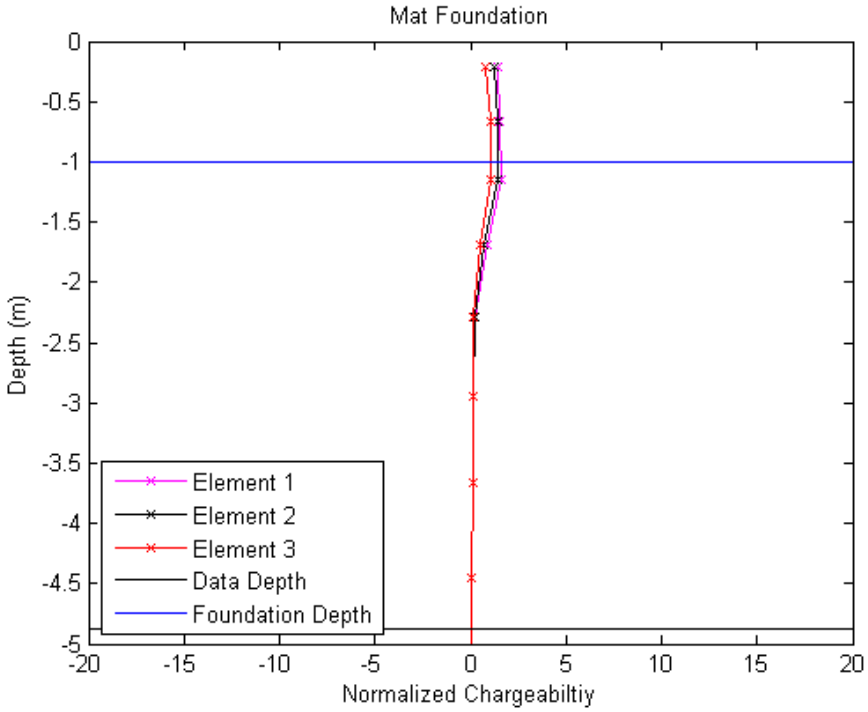

Fig. A.3. Normalized chargeability around the 3 × 3 m^2 mat foundation

A.3 BEASON CREEK BRIDGE

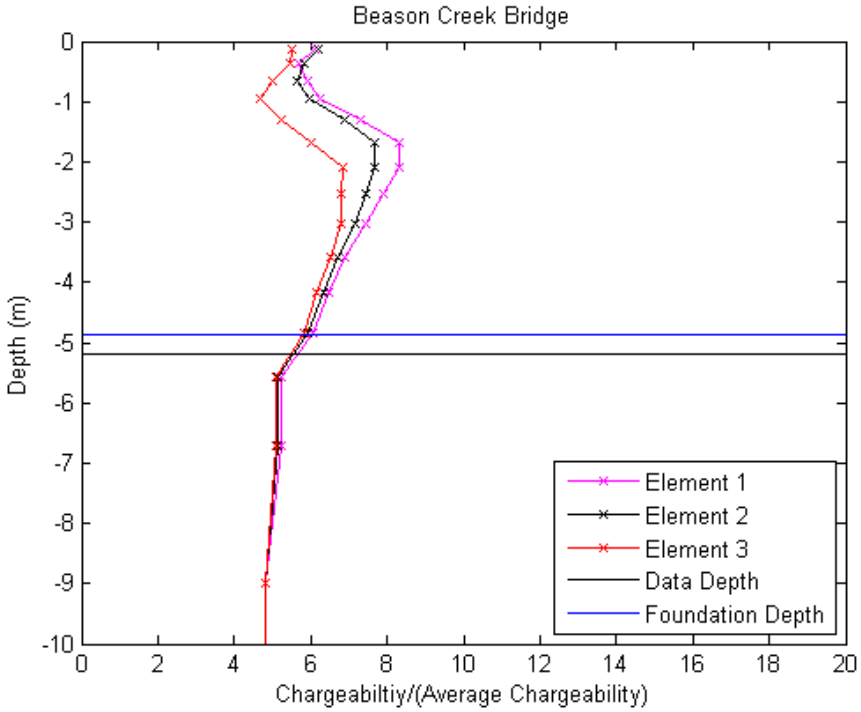

Fig. A.4. Beason Creek Bridge chargeability around the foundation

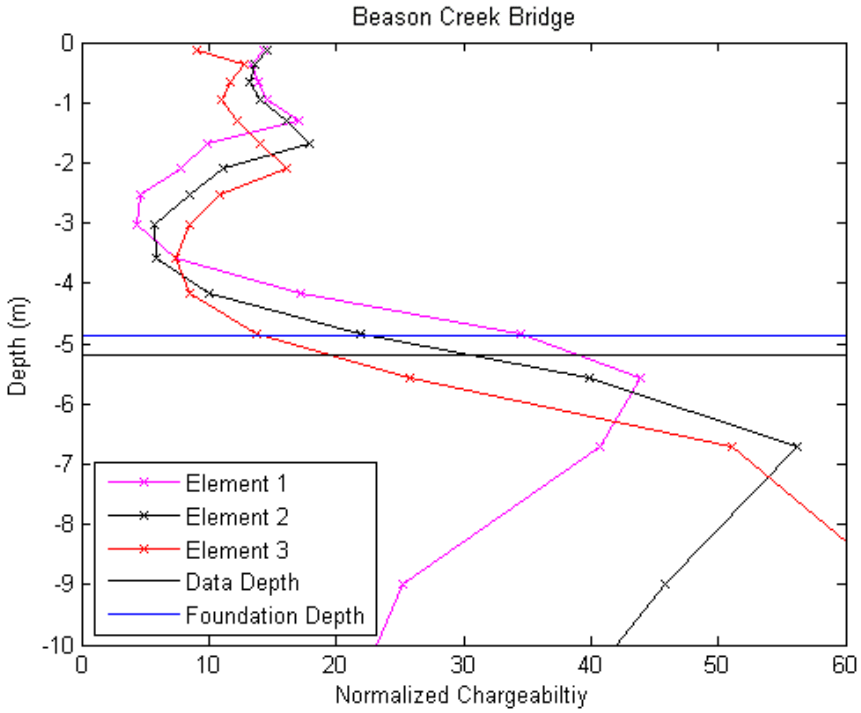

Fig. A.5. Normalized chargeability around the Beason Creek Bridge foundation

A.4 CLEAR CREEK BRIDGE 1 M SPACING

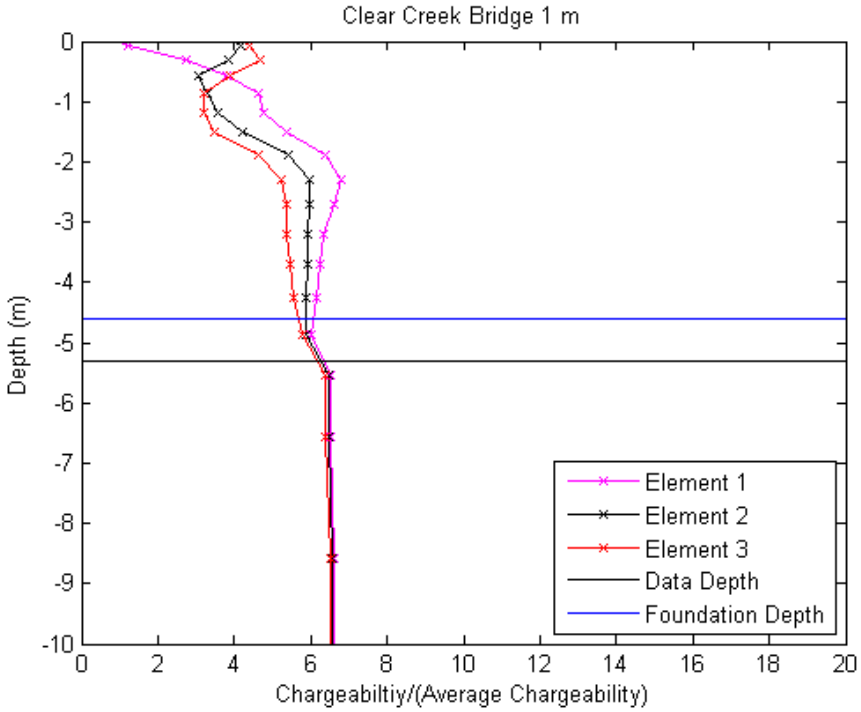

Fig. A.6. Clear Creek Bridge 1 m spacing chargeability around the foundation

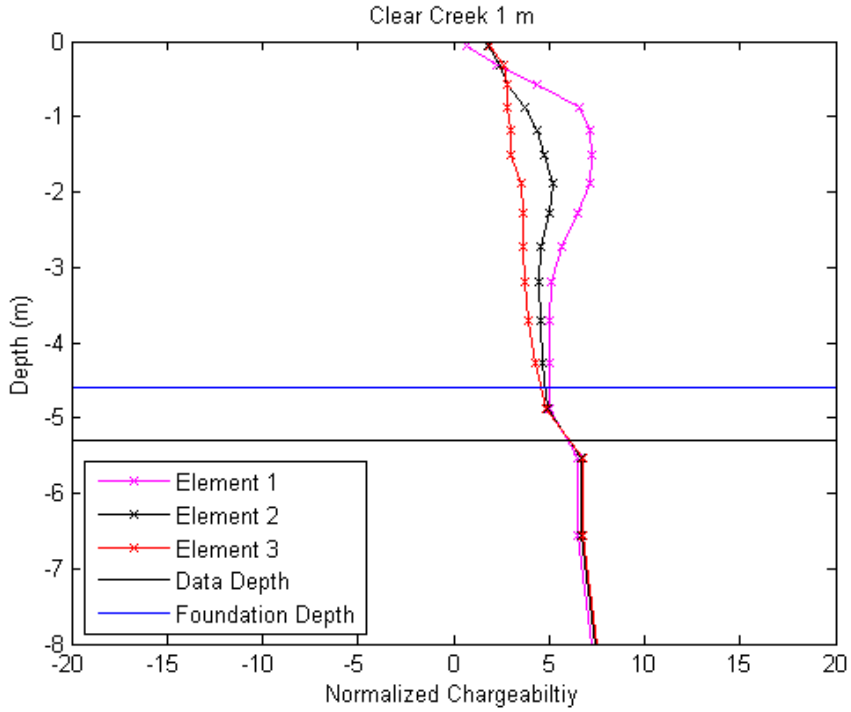

Fig. A.7. Normalized chargeability around the Clear Creek Bridge 1 m spacing foundation

A.5 CLEAR CREEK BRIDGE WITH 0.57 M SPACING

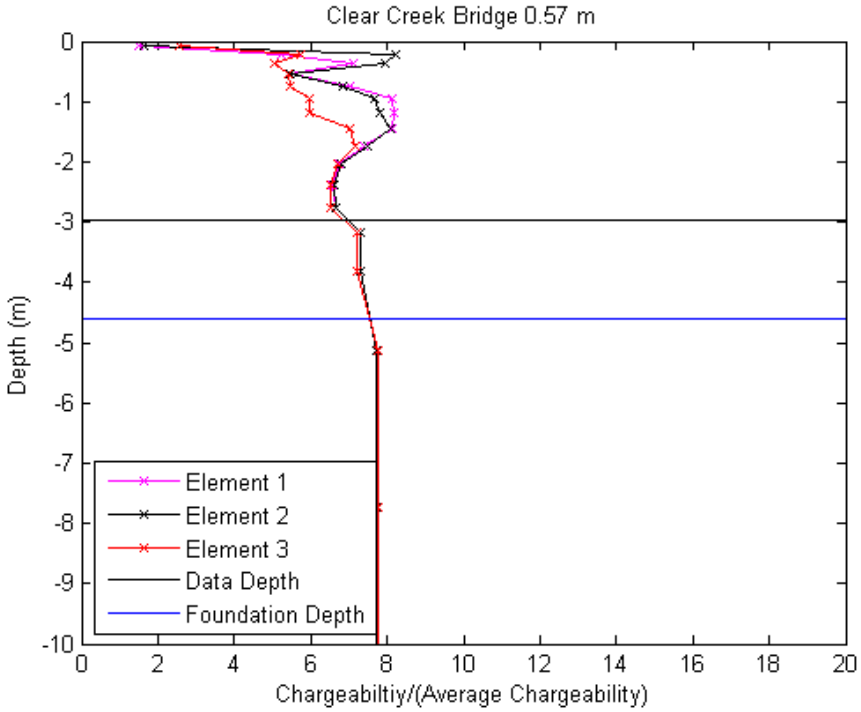

Fig. A.8. Clear Creek Bridge 0.57 m spacing chargeability around the foundation

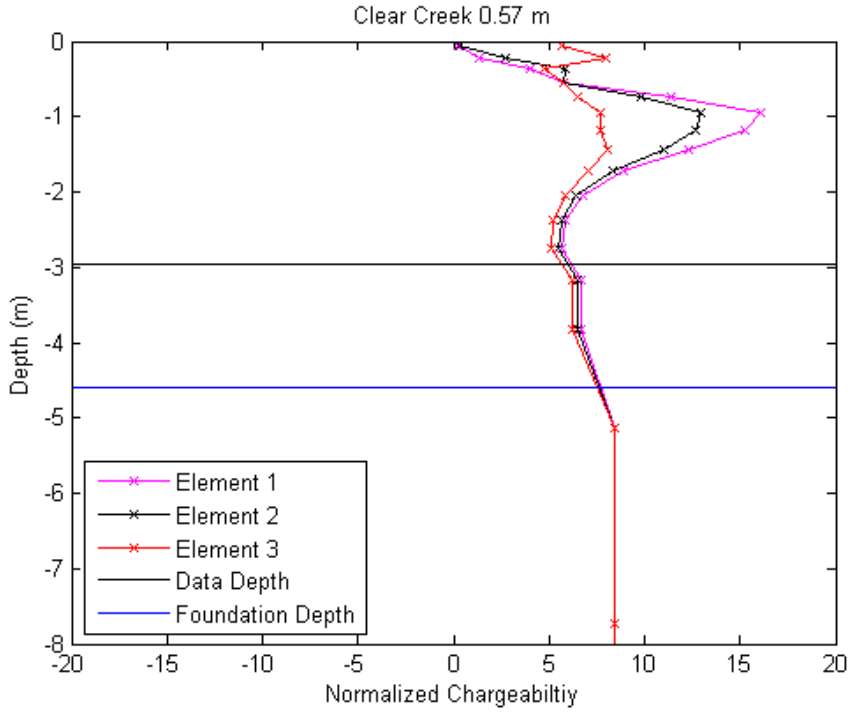

Fig. A.9. Normalized chargeability around the Clear Creek Bridge 0.57 m spacing foundation

A.6 DAVIDSON CREEK BRIDGE 1

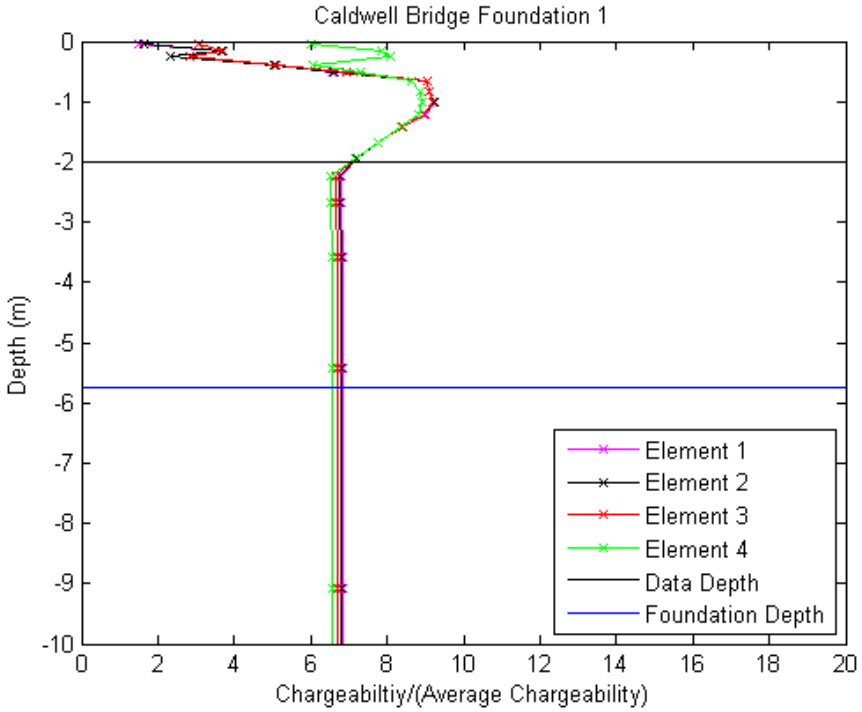

Fig. A.10. Davidson Creek Bridge 1 chargeability around the foundation

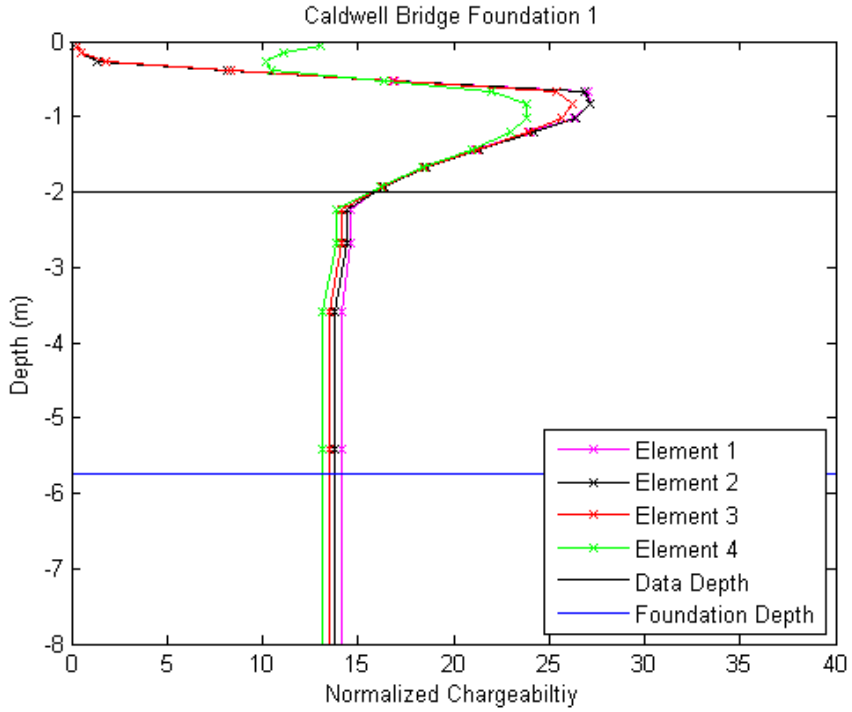

Fig. A.11. Normalized chargeability for the Davidson Creek Bridge 1

A.7 DAVIDSON CREEK BRIDGE 2

Results are included in Chapter 4.

A.8 DAVIDSON CREEK BRIDGE 3

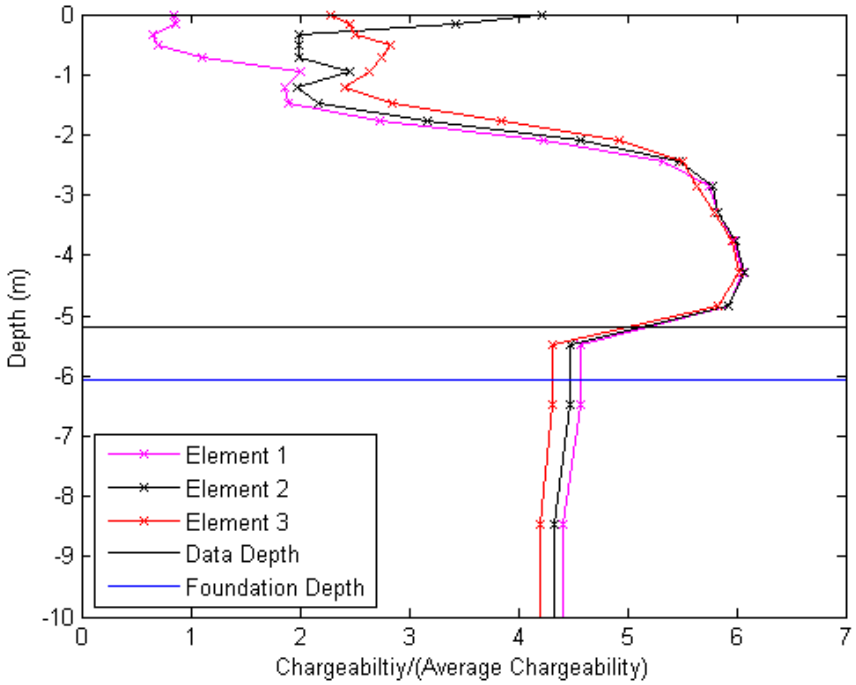

Fig. A.12. Davidson Creek Bridge 3 chargeability around the foundation

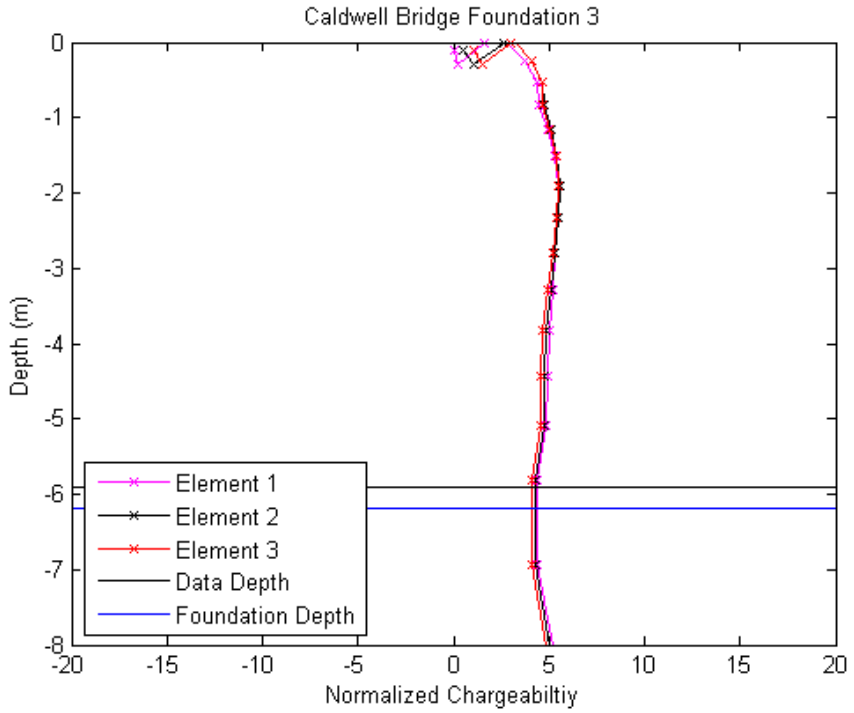

Fig. A.13. Normalized chargeability for the Davidson Creek Bridge 3

A.9 DAVIDSON CREEK BRIDGE 4

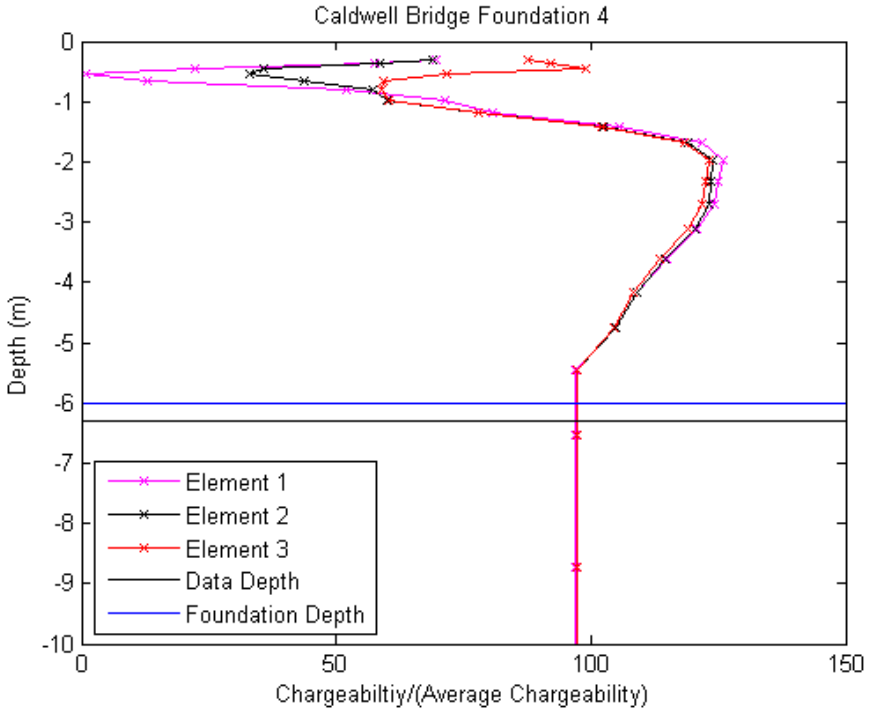

Fig. A.14. Davidson Creek Bridge 4 chargeability around the foundation

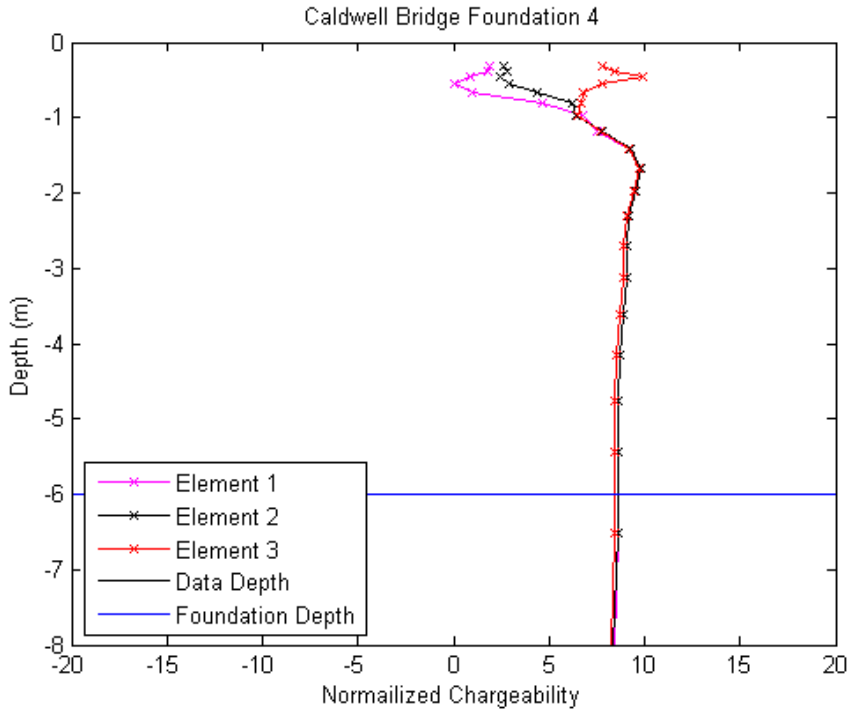

Fig. A.15. Normalized chargeability for the Davidson Creek Bridge 4

A.10 DAVIDSON CREEK BRIDGE 5

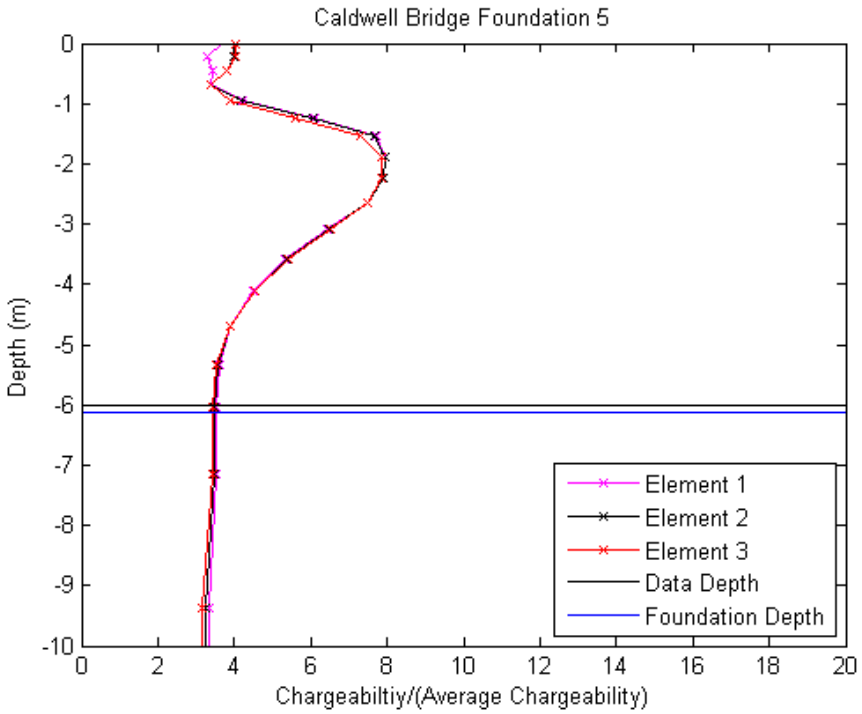

Fig. A.16 Davidson Creek Bridge 5 chargeability around the foundation

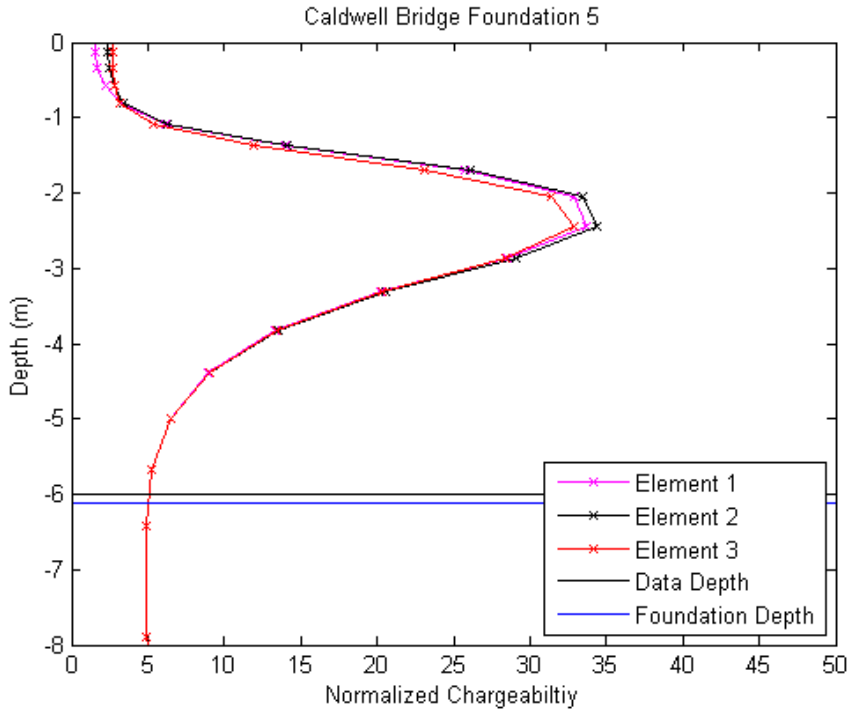

Fig. A.17. Normalized chargeability for the Davidson Creek Bridge 5

A.11 DAVIDSON CREEK BRIDGE 6

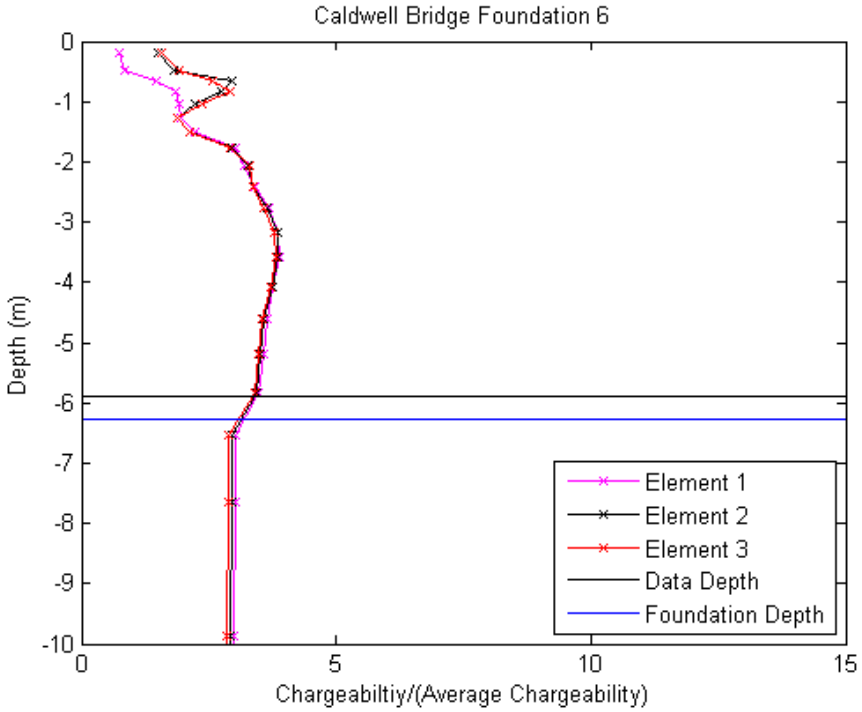

Fig. A.18 Davidson Creek Bridge 6 chargeability around the foundation

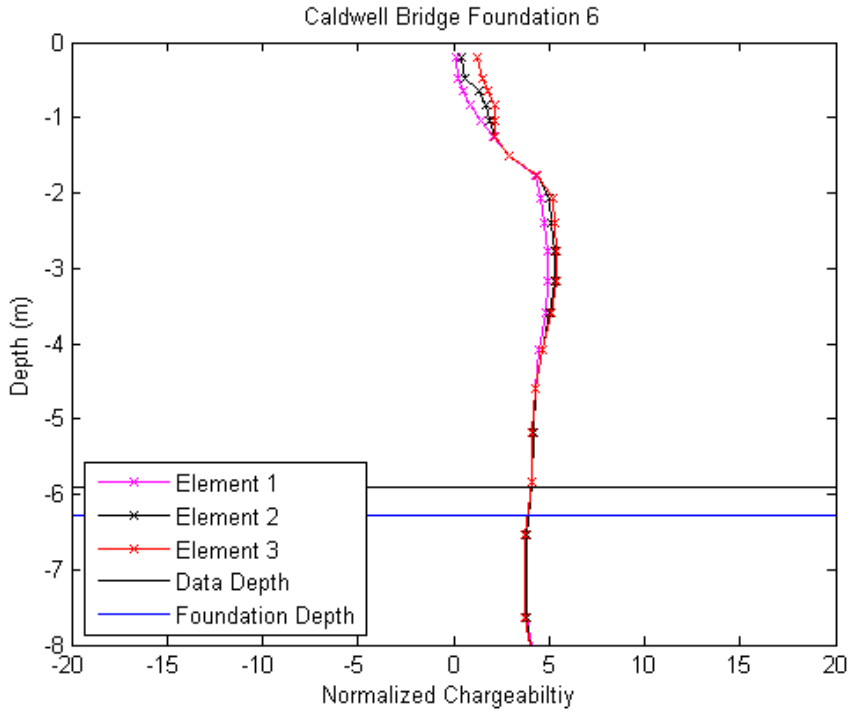

Fig. A.19. Normalized chargeability for the Davidson Creek Bridge 6

A.12 GUM CREEK BRIDGE PILE 1

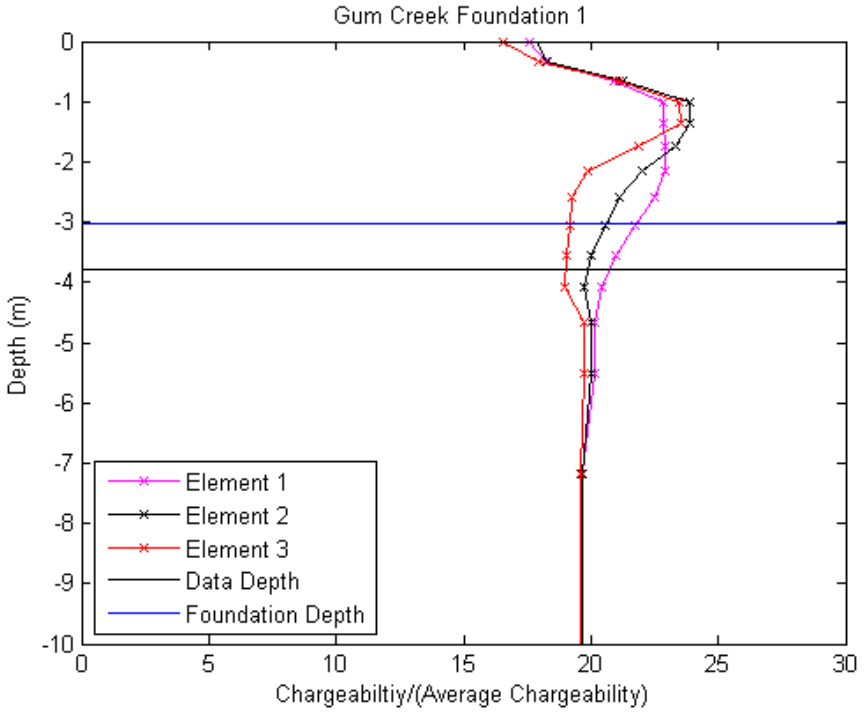

Fig. A.20. Gum Creek Bridge pile 1 chargeability around the foundation

A.13 GUM CREEK BRIDGE PILE 2

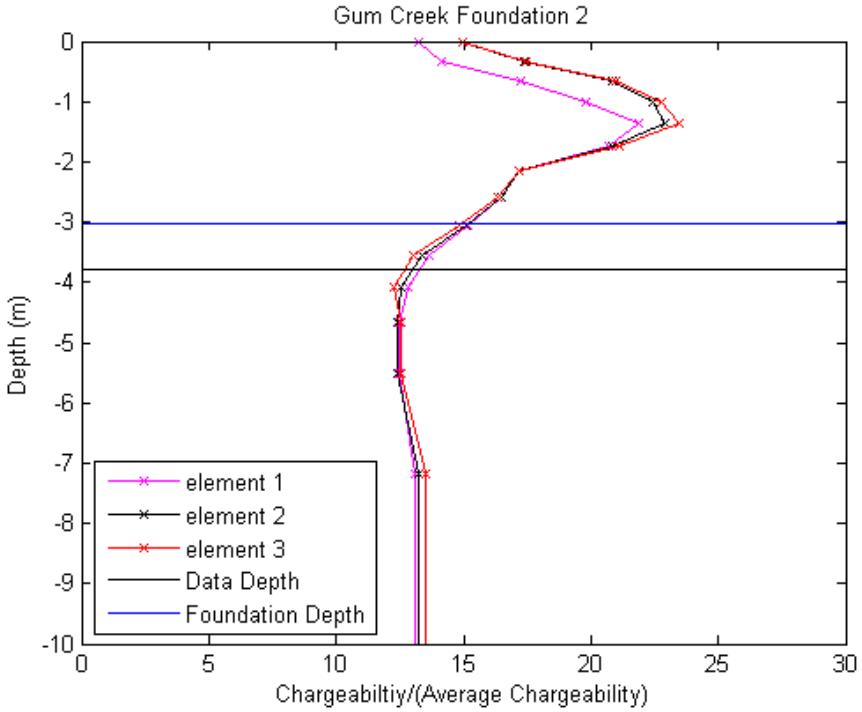

Fig. A.21. Gum Creek Bridge pile 2 chargeability around the foundation

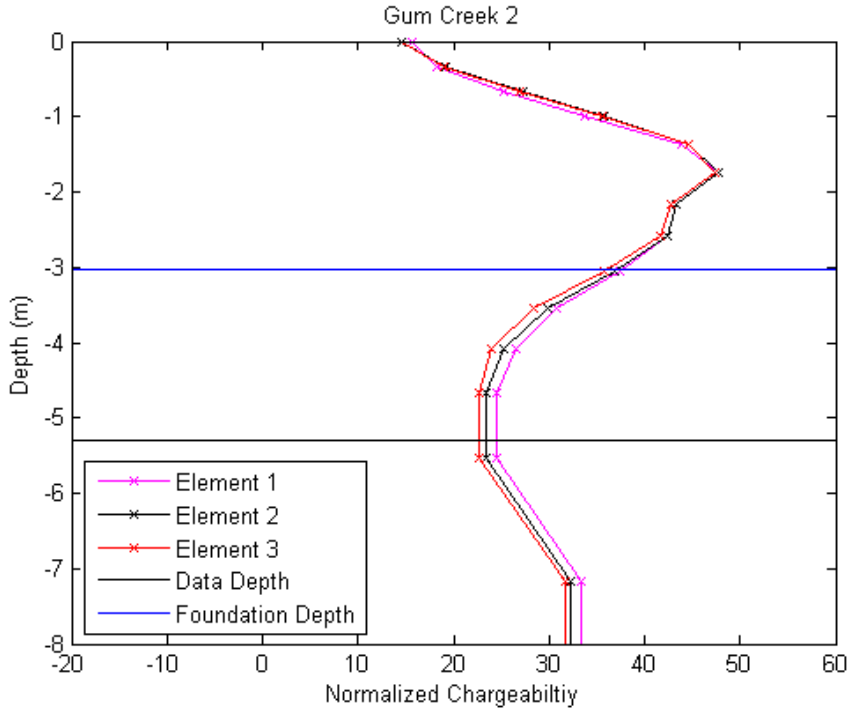

Fig. A.22. Normalized chargeability for Gum Creek Bridge pile 2

APPENDIX B. ELECTRICAL RESISTIVITY IMAGING AND INDUCED POLARIZATION UNKNOWN FOUNDATION PREDICTION PROTOCOL

INTRODUCTION

This manual guides users for optimal setup and use of a survey using electrical resistivity imaging and induced polarization for predicting the depth of unknown bridge foundations. The ERI/IP Unknown Foundation Prediction Protocol can be used as a guide for investigating other subsurface infrastructure, but it is specifically tailored to bridge foundations.

EQUIPMENT

The equipment used for this research and described is an Advanced Geosciences, Inc. SuperSting R8/IP™ system. The SuperSting R8/IP™ is capable of simultaneously measuring voltage potentials over eight channels allowing for faster data acquisition in the field. The other necessary pieces of equipment are at least one 12 V deep cycle marine battery, a minimum of two sets of passive land cables with electrode take-outs at a minimum of 1 m spacing, SS electrode stakes for one cable, and NP electrodes for the second cable.

The SuperSting R8/IP™ can also be powered using a 12 V generator. If a battery is used, two batteries can be connected in parallel to reduce the draw down on the battery or they can be connected by an AGI produced boost cable that switches between the two batteries internally (Fig. B.1a). The boost cable is recommended over connecting the batteries in parallel to prevent the operator from accidentally connecting the batteries in series. Connecting the batteries in series can potentially damage the SuperSting R8/IP™. For optimal data collection (particularly for IP data collection) the external power should remain above 11.75 V. Below 11.75 V the SuperSting R8/IP™ will switch to power saving mode and will reduce the maximum possible injected current, potentially lowering the data quality. The SuperSting R8/IP™ will shut down below 11.5 V. The current battery level can be constantly monitored on the SuperSting R8/IP™ in the bottom right corner of the screen on the top face of the box during surveys.

The current injecting SS electrodes are 45 cm long, 1 cm diameter stainless steel rods that connect directly to the cable take-outs. The NP electrodes have a porous tip with a plastic casing that contains a copper rod surrounded by a copper sulfate solution in contact with the porous stone. The NP electrode is depicted in Fig. B.1b; the copper sulfate solution is the blue liquid inside the chamber. The NP electrodes are used because polarization voltages at the contact between the SS electrodes and the ground can cause debilitating noise to the survey. IP is a phenomenon captured during resistivity surveys, so the NP electrodes are not required. It was shown in Chapter 3 that NP electrodes are necessary to collect data that are able to be numerically modeled for predicting the depth of bridge foundations.

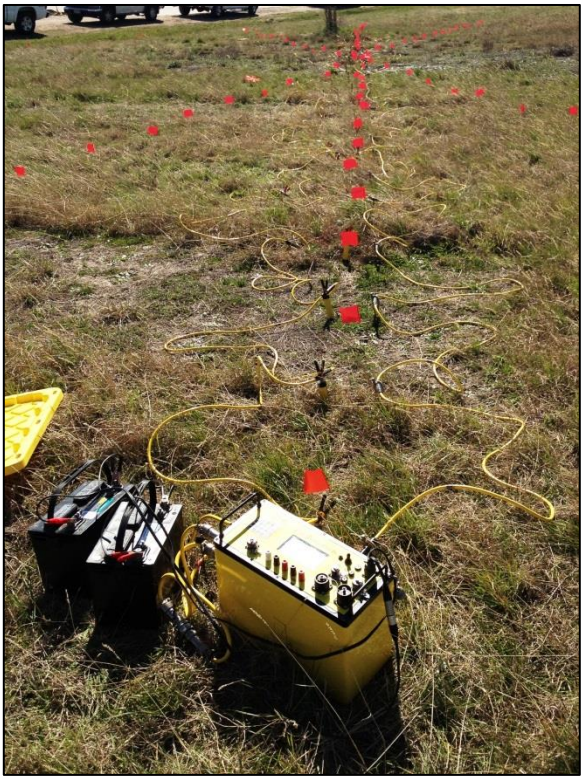

(a) SuperSting R8/IP™

(b) Non-polarizable electrode

Fig. B.1. Field Equipment

Field Setup

To collect quality ERI and IP data simultaneously two sets of electrodes are necessary. The SS electrodes should be pushed or driven straight into the ground until the cross bar is approximately 2 cm above the ground surface in a straight line at set intervals. If the soil is very loose, such as a loose sand, see the section on Troubleshooting. The NP electrodes should be buried approximately 0.3 m from each stainless steel electrode so that the full porous stone tip is in the ground. The stone must also have good contact with the ground. If the ground is soft, the soil can be slightly loosened and the NP electrode pushed into the soil. If the ground is very stiff, a hole is dug deep enough so the stone can be buried, and the soil is mixed with distilled water and back filled so the stone can be pushed in without damaging it. If the porous stone does not have good contact with the soil (i.e., there are voids around the stone caused by soil clumping after the hole is dug) the IP decay curves will appear jagged and will be removed from the data set.

The electrode cables are numbered for each electrode take-out where an electrode is connected. Each NP electrode is connected to the cable take-out using alligator clips so that the copper rod exposed above the chamber is in contact with the takeout or using alligator to alligator cables (Fig. B.2a). The SS electrode crossbars must be in contact with the cable take-out during a survey. Each electrode has a spring attached to it so that the cable is held in place on the crossbar during the survey. The spring over the cable holding it in place is seen in Fig. B.2b along with the minimum depth of installation for each electrode.

(a) Non-polarizable electrode connection (b) Electrode installation

Fig. B.2. Electrode Connections

The TAMU system is four cables, with electrode take-outs spaced every 2 m. Two cables are numbered 1–14 and two are numbered 15–28. For a typical ERI/IP data set, one of each cable section is connected to another so that two long cable sections are made numbered 1–28. For bridge foundations, the electrodes should be spaced equal to or less than the width of the foundation tested. The electrodes should be installed so that the SS electrodes are on one side of the foundation, and the NP electrodes are on the other side of the foundation for a pile, column with a spread footing, or column with an embedded pile cap, with the pile/column in the center of the array (Fig. B.3). If an abutment is tested or a foundation that is larger than the take-out spacing above the ground, the line of SS electrodes should be as close to the abutment as possible and straight along the side of the abutment. The line of NP electrodes should be offset from the SS line with approximately 0.3 m space between the two lines.

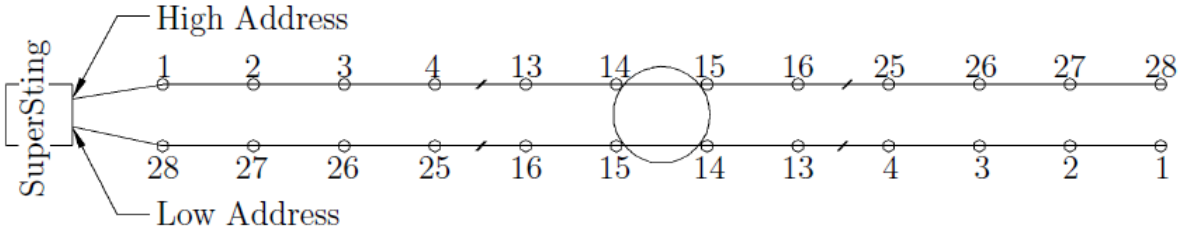

Fig. B.3. Field setup of SuperSting R8/IP™ with 28 take-outs

A schematic of the field set up is below in Fig. B.3 including the cable layout. Note that sections of the cables are removed for space in the schematic but the continuous string of electrodes is necessary in the field. The 28th takeout with the NP electrodes must be connected to the low address port and the 1st takeout with the SS electrodes must be connected to the high address port. The free ends of the cables away from the test box should *not* be connected. The cable sections must be installed exactly as shown to use the command file described in the following section.

File Writing

Prior to field testing, a command file should be written in the office and loaded on the SuperSting R8/IP™ for later use. The SuperSting R8/IP™ comes with software to write command files and to add/remove files to the system. AGI SuperSting Administrator automatically creates data collection files for the Wenner, Schlumberger, dipole-dipole, pole-dipole, pole-pole, and inverse Schlumberger arrays. For bridge foundations the dipole-dipole array is preferred as it yields the highest quality data for foundations.

From the Command Creator interface in the Administrator program, type 28 in the number of electrodes section and select "Dip-Dip" as the array type when using a field setup with 28 NP and 28 SS electrodes (Fig. B.3). Beneath the number of electrodes is the option for "Extended data coverage." Checking this will force the command file to be written so that all eight channels are used to measure potentials for each measurement instead of only those necessary for the dipole-dipole array. Extended data coverage will allow the user to gather more data without adding time to the survey. Because some data from the basic dipole-dipole array may not meet the criteria to be used in the model, collecting more data around these points increases the number of usable data in the model and the overall quality of the model.

The other two options, "Create reverse array" and "Include reverse array," can be used if proving data quality is necessary. Theoretically, if an array is run from left to right or right to left the results should be the same. These options allow the researcher to show that the data are in fact the same forward and back, but they are not necessary for determining the depth of a bridge foundation. The electrode spacing units must also be specified. The best way to ensure an acceptable signal to noise ratio for the dipole-dipole array is to keep the "Max n" less than or equal to eight. If an *n* of eight is used with the electrodes spaced every 1 m the maximum distance between the current sink and current source is 8 m. The "Max Dipole"' should be less than or equal to six for this array. The dipole is the factor that the spacing is multiplied by between the current and potential reading electrodes. If a max dipole of six is used with the electrodes spaced every 1 m the maximum distance between the set of current electrodes and potential electrodes is 6 m.

The last step before creating a command file is to select "Use IP." This changes the measurement times from the shorter ERI only survey times to the longer IP measurement times. The options for an IP survey are 0.5, 1.0, 2.0, 4.0, and 8.0 s. For bridge foundations, 2 s is recommended. Any shorter period yields lower quality results but longer time windows only add to the length of time for the survey to run without improving results. This is proved in Chapter 3.

Once all of these options are selected, name the program in Prog. ID. It is recommended to name the file something that informs the user in the field what the file is designed for. The Prog. ID will be the name shown on the SuperSting. The SuperSting can hold several files so to avoid confusion, for example, the name "28ddNP" tells the user how many electrodes should be installed, to use NP electrodes as well as SS (all surveys require SS electrodes), and that this file uses the dipole-dipole array. After the command file is named, click "Save Cmd File."

The command file is now ready to be used in the field if only SS electrodes are used. Note that it is possible to collect ERI and IP data using only SS electrodes. For optimal results, NP electrodes should be used as well. In order to use NP electrodes the command file must be altered. Command files have three required sections, ":header," ":geometry," and ":commands." After automatically creating a command file, the :header section should not be altered, this section gives the SuperSting R8/IP™ and the data processing system information about the

survey such as the name of the file and the array type. The ":geometry" section is the first section that must be altered.

The three numbers in the geometry section refer to the electrode ID, the location in the *x*-direction, and the location in the *y*-direction. The electrode ID is correlated to the ID numbers on the cable sections; this is why it is important to set up the cables as shown in Fig. B.3. The current geometry in the file is the geometry for the NP electrodes so another 28 electrodes need to be added for the SS electrodes. Even though the two cables connected to the stainless steel electrodes are also labeled 1–14 and 15–28, the electrode ID for the stainless steel electrodes should be numbered 29–56. The *x*-location, on the other hand, must correspond to the *x*-location in the field. This means that the 29th electrode ID corresponds to an *x*-location of 27 m away from the switch box. Table B.1 includes the sections of the geometry section for a 28 electrode survey with NP electrodes.

Table B.1. Geometry of a Command File with NP Electrodes

:geometry		
1,	0.00,	0.00
2,	1.00,	0.00
3,	2.00,	0.00
…	…	…
26,	25.00,	0.00
27,	26.00,	0.00
28,	27.00,	0.00
29,	26.00,	0.00
…	…	…
55,	1.00,	0.00
56,	0.00,	0.00

After adding the extra cable sections to the ":geometry" section of the command file the :commands section must also be updated. The geometry section has been updated for the 29–56 electrode IDs as the SS electrodes. The SS electrodes inject the current into the ground, therefore the electrode IDs corresponding to 29–56 should inject the current in the command file. A and B indicate current electrodes, and P1 through P9 indicate potential measuring electrodes. So, all the A and B electrode IDs must be updated to the current electrode IDs that correspond to the same x--location as the initial NP electrode. For example, this first command line:

;A,B,P1,P2,P3,P4,P5,P6,P7,P8,P9,channels
2,1,3,4,5,6,7,8,9,10,11,12345678

should be updated to:

;A,B,P1,P2,P3,P4,P5,P6,P7,P8,P9,channels
55,*56*,3,4,5,6,7,8,9,10,11,12345678

This can be done one line at a time or easily calculated and made into a string in a program such as Microsoft® Excel. After these updates are made, the command file is complete for a 28 electrode array using stainless steel and NP electrodes.

SuperSting Settings

One the equipment is setup and powered on, there is a series of settings that must be addressed before running a test. An image of each screen is included for ease of use. From the home screen in Fig. B.4, press 1 on the keypad to select the Automatic mode. Automatic mode indicates that the SuperSting R8/IP™ will automatically switch between the electrodes following a previously written command file. This screen can also be used to run tests of the equipment to check that it is working and to adjust the display settings.

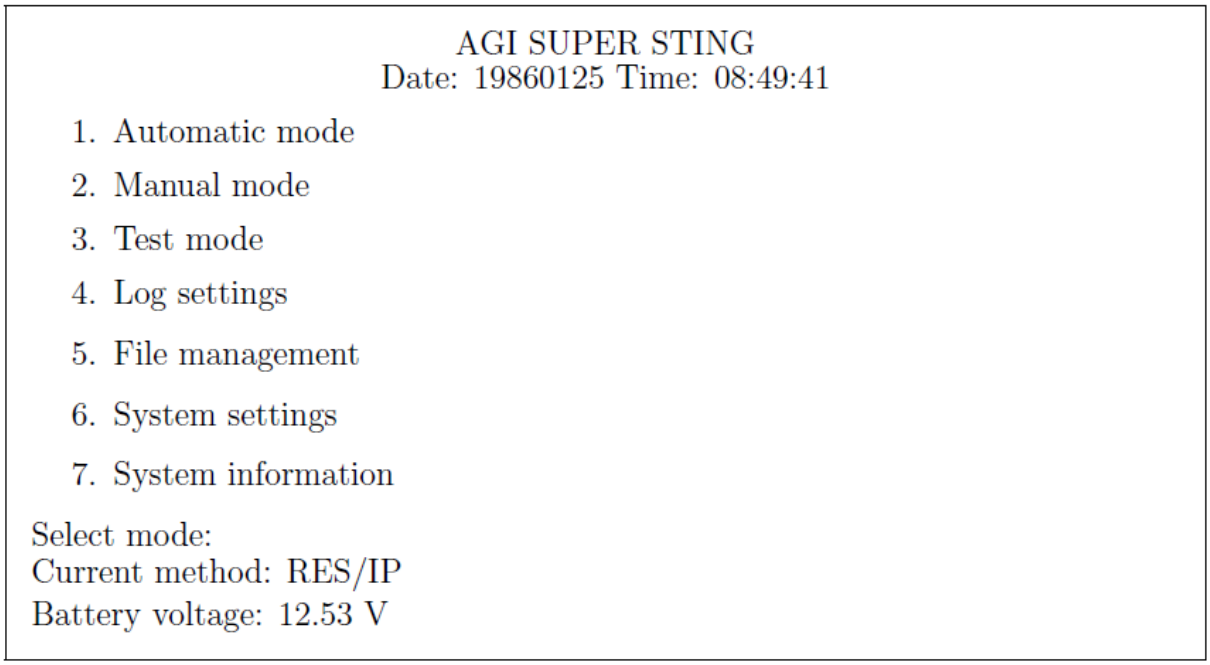

Fig. B.4. SuperSting home screen

The next screen, Fig. B.5, allows the user to open an existing file if a survey has already been started or to create a new file for a new survey. This screen contains all the information pertaining the current survey that is open. If no data file is open, the screen will look like Fig. B.5. To create a new survey, press 2 on the keypad. Upon selecting create data file the current survey must be named. Once a name is typed into the SuperSting R8/IP™ press ENTER to continue the setup.

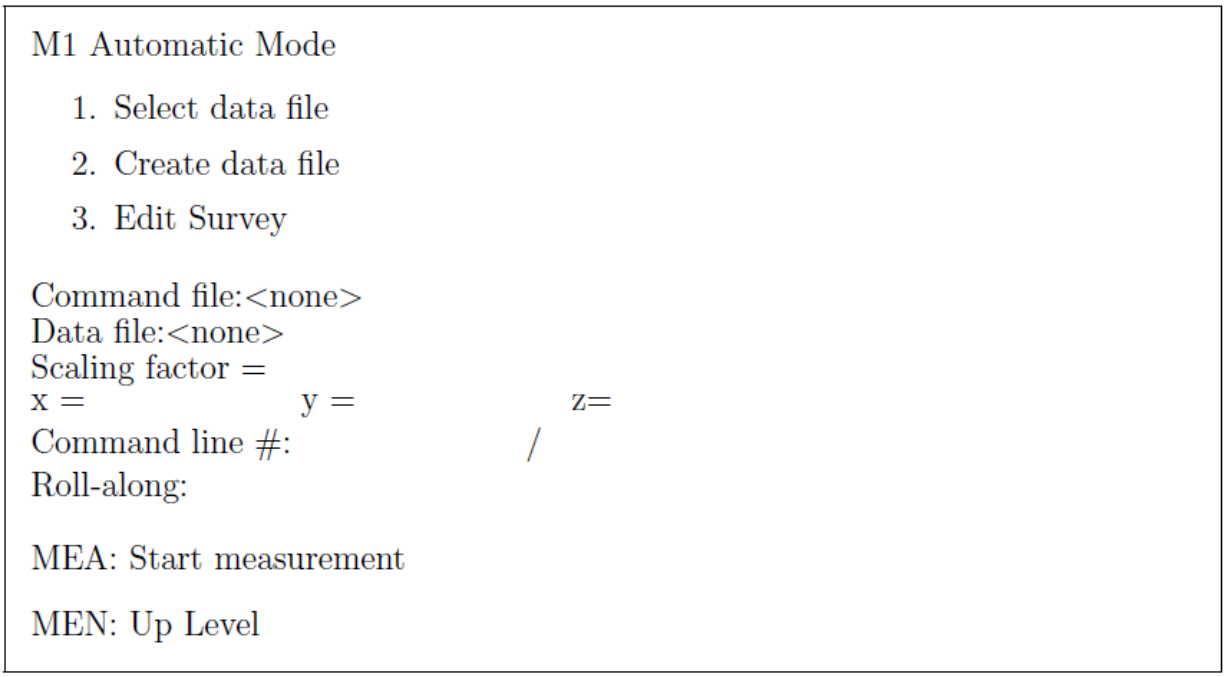

Fig. B.5. Automatic mode settings

Fig. B.6 is what the command file selection screen looks like. The command files shown in Fig. B.6 have already been loaded on the SuperSting R8/IP™ using the AGI Administrator program and a cable to connect the equipment to a laptop or computer. The "+/−" keys are on the keypad. The command file "28ddNP" is used for most of this research, describing a dipole-dipole, 28 NP electrode array.

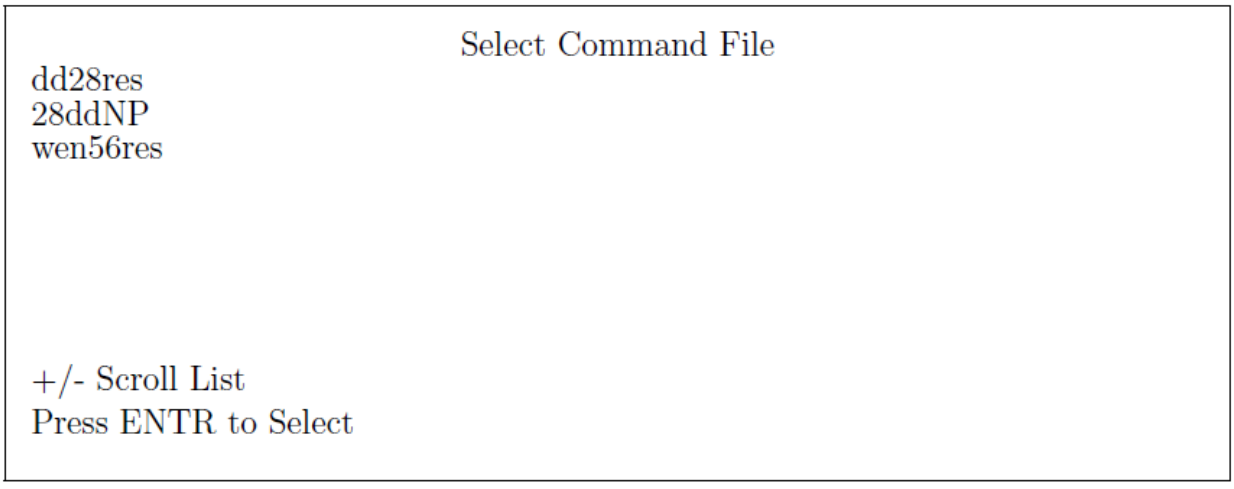

Fig. B.6. Select command file screen

Fig. B.7 includes the geometry of the field. Each option will blink; once the desired quantity is selected press enter to move to the next option. If, for example, feet are used instead of meters, press the + key to change the option to feet, then press enter and feet will be used.

Now the scaling factor will be blinking. Enter the electrode spacing in the field; a 0.85 m spacing was used for this survey. All other options should look like Fig. B.7.

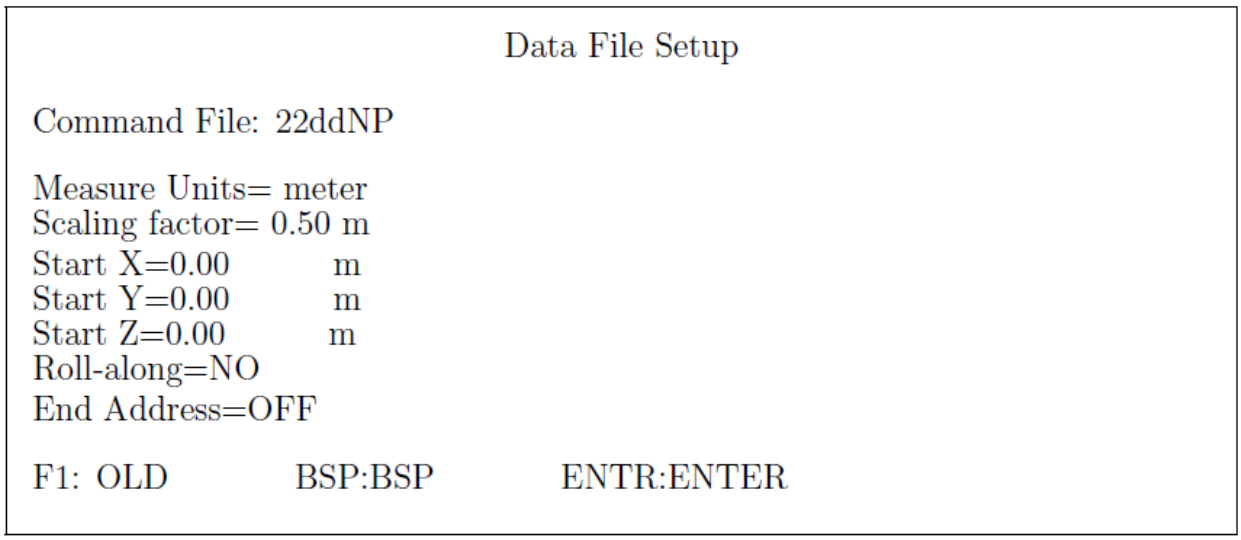

Fig. B.7. Data file setup

The SuperSting allows the user to exit the setup with the screen shown in Fig. B.8. Press ENTR to continue to setup this survey.

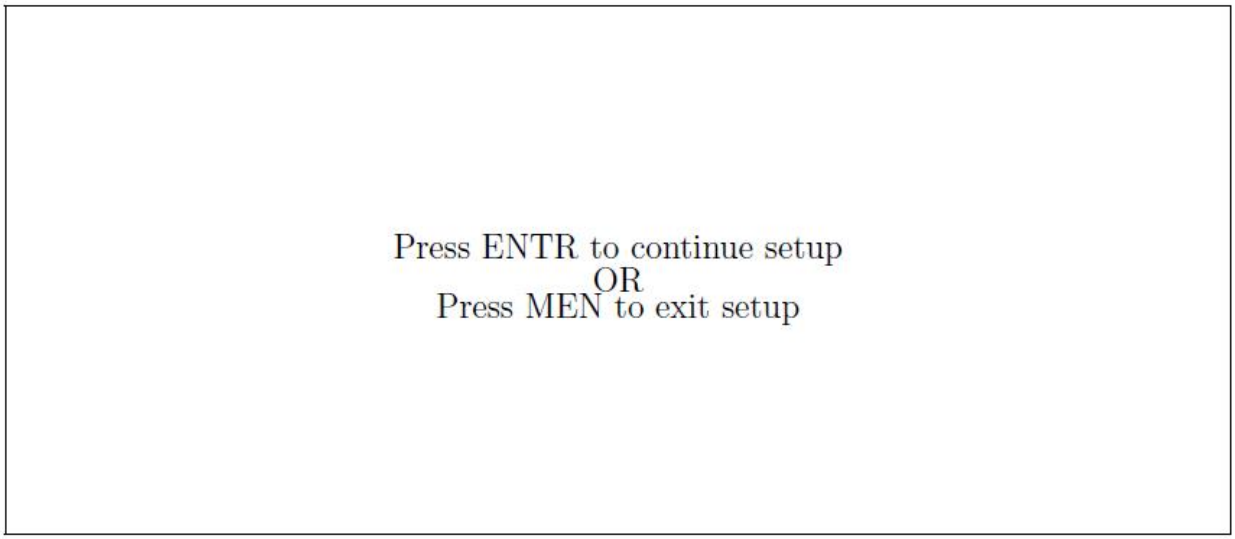

Fig. B.8. Continue setup screen

For surveys that use both NP and SS electrodes, the distributed switch system must be used. Press 2 when the screen looks like Fig. B.9.

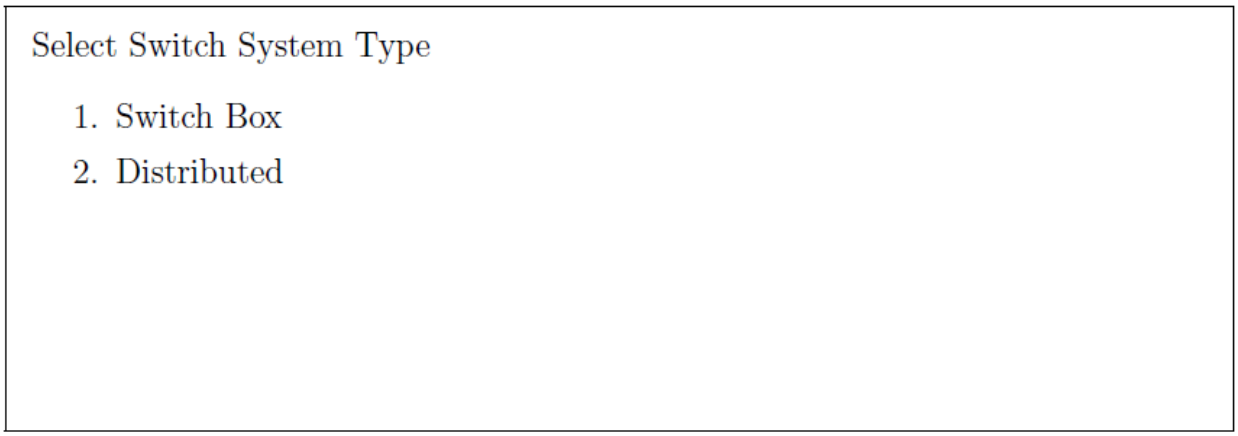

Fig. B.9. Switch system type

The SuperSting R8/IP™ has the term "R8" in its name because it is an eight channel instrument. This means that it can measure the voltage potentials over eight channels simultaneously, reducing the time for each survey. Press 2 to use all eight channels as shown in Fig. B.10.

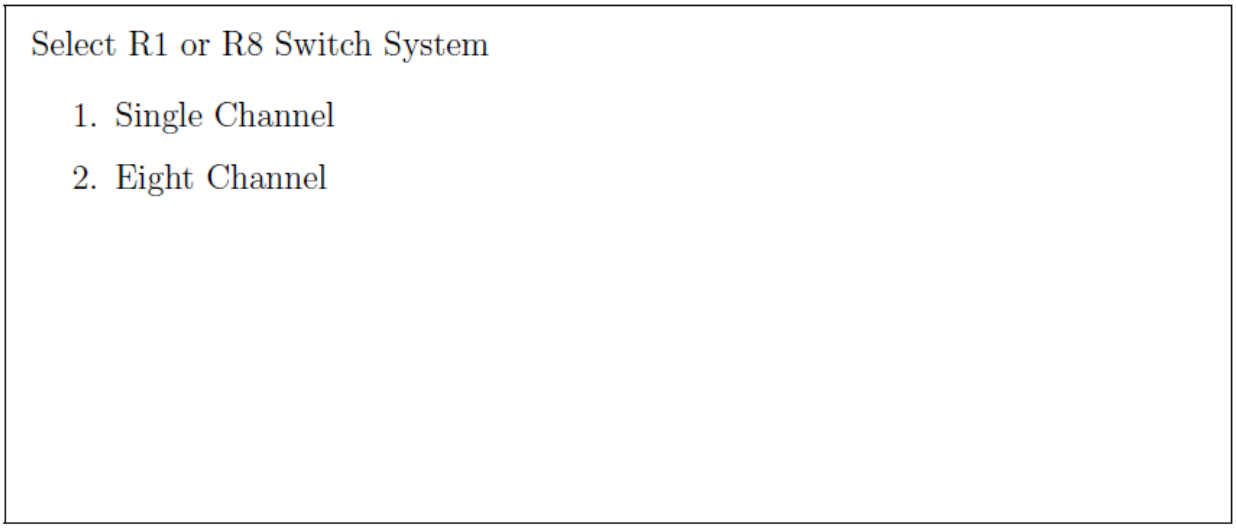

Fig. B.10. Switch system channels

Fig. B.11 is the screen that allows the user to setup the cable sections. The TAMU system has four cable sections that should be connected as shown in *Field Setup*. To use 28 NP and 28 SS electrodes the cable address screen must look like Fig. B.3 so the two sets of two cables can be used.

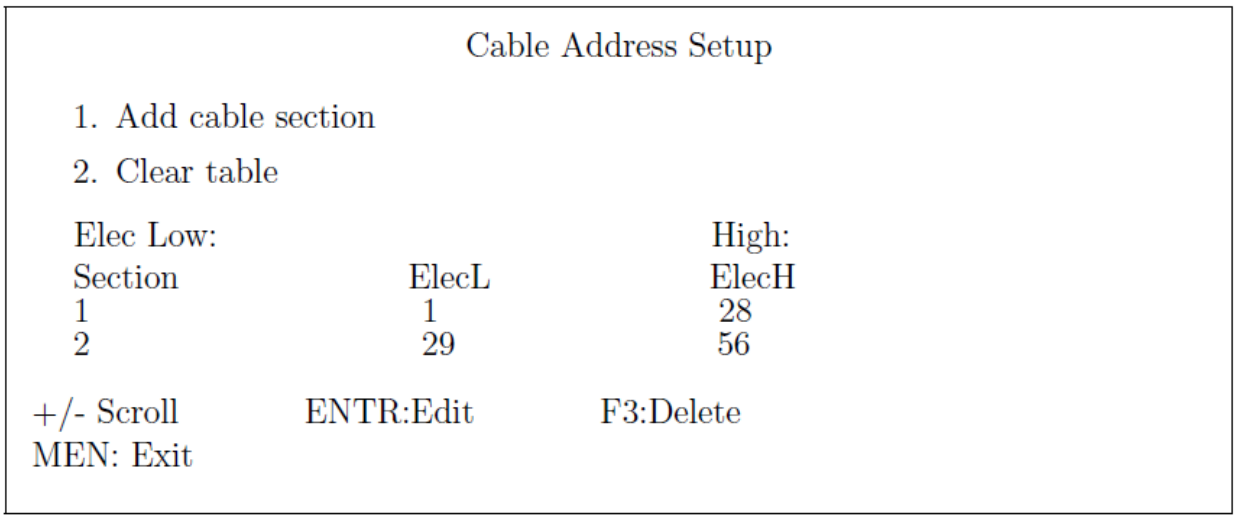

Fig. B.11. Cable address setup

The measurement settings should be set to look like Fig. B.12. Press the number on the keypad that corresponds to the field that needs to be changed in order that activate the setting. The measure time of 2 s is the proven ideal time for surveys of unknown bridge foundations.

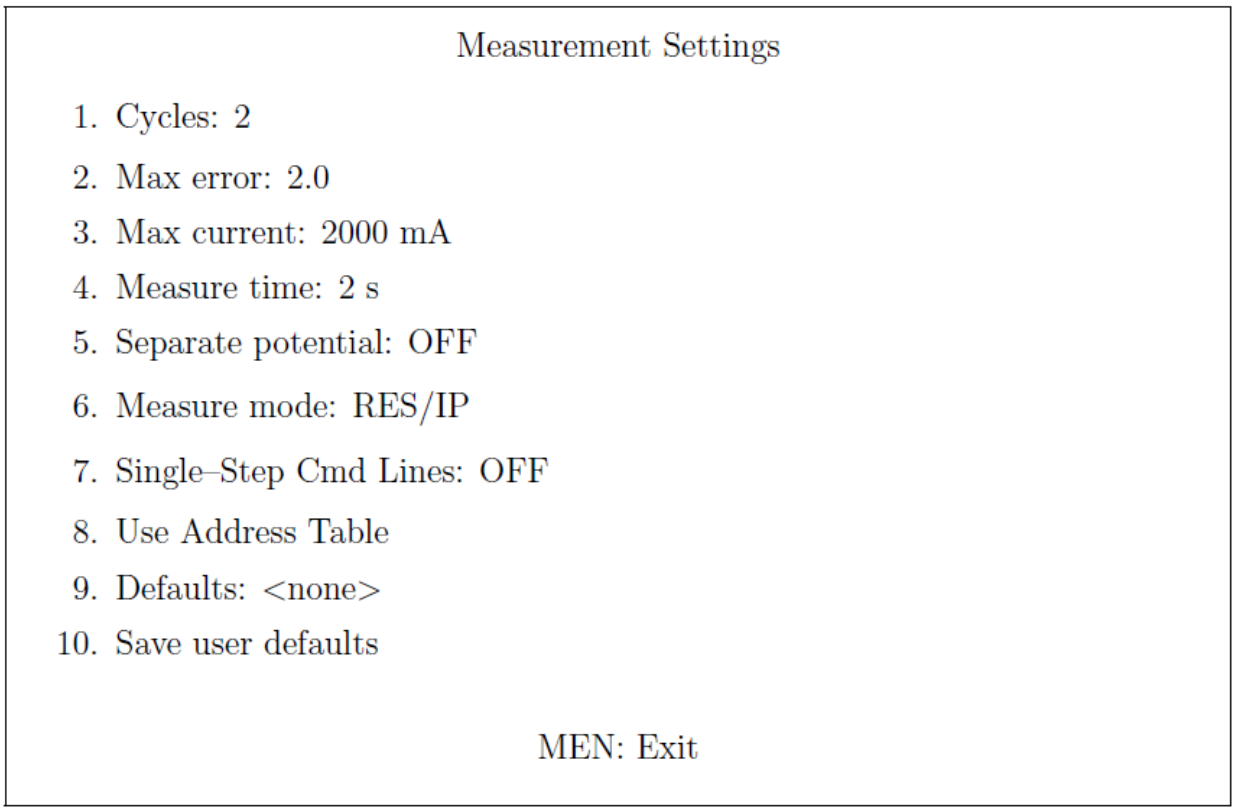

Fig. B.12. Measurement settings

The survey is now ready to be run with the current settings. Before returning to the screen from Fig. B.7, the SuperSting R8/IP™ forces the user to consider running a contact

resistance test (Fig. B.13). This test will alert the user if there is an installation problem with an electrode before a survey is conducted.

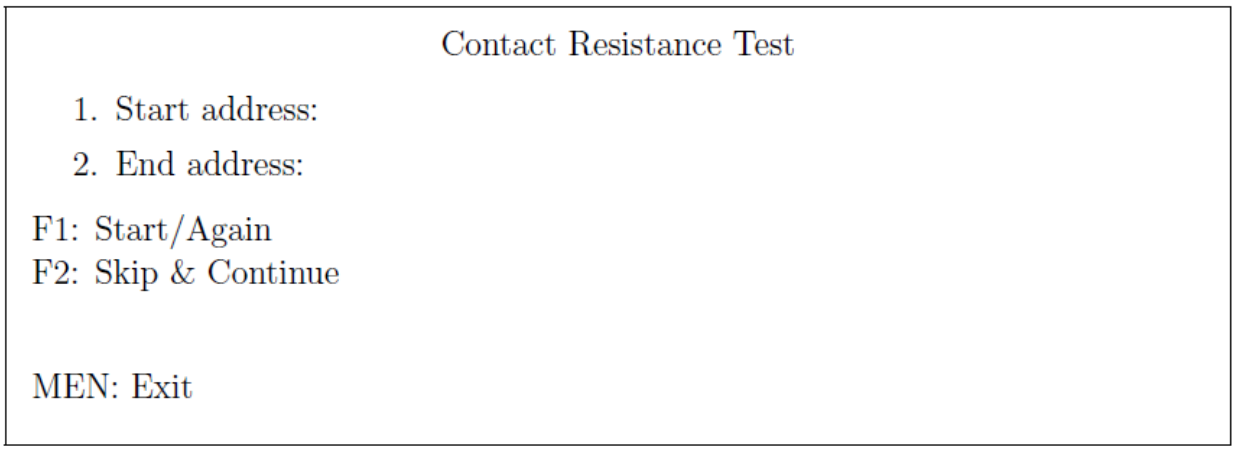

Fig. B.13. Contact resistance test

First, the start address and end address must be entered to only check the SS electrodes. The start address must be 29 and the end address 56 to match the command file that has been described and the cable setup shown. After these are entered, press F1 to start the test. If the electrodes are connecting properly, the test will inject current in the A electrode and measure the resistance on the next electrode in the line (the B electrode). The results will be shown below the start and end addresses as shown in Fig. B.14.

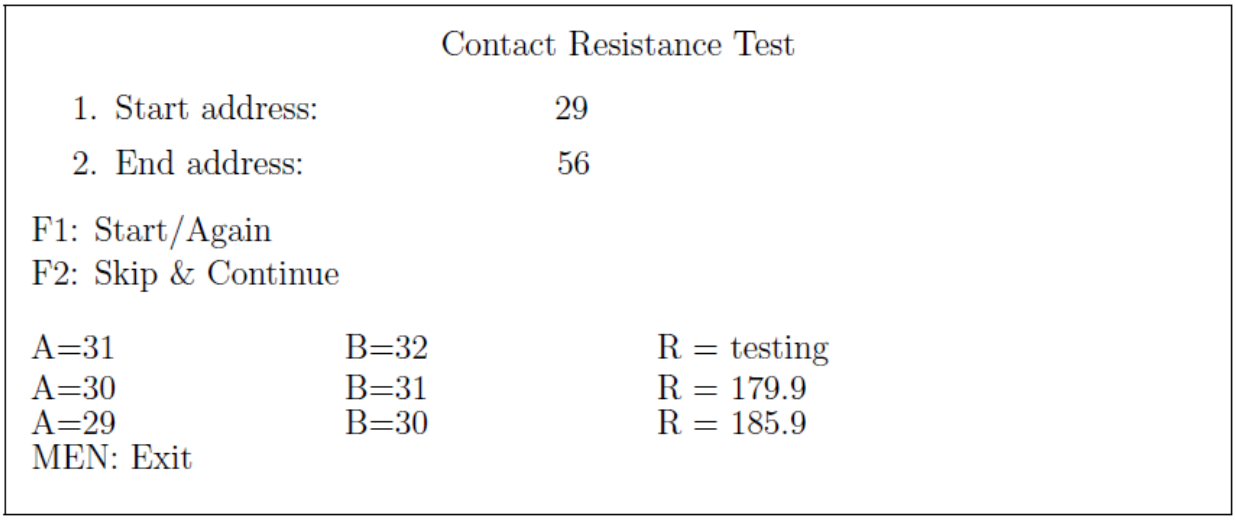

Fig. B.14. Contact resistance test settings

For surveys with NP electrodes, a contact resistance below 300 Ω is ideal. If the contact resistance is over 2,000 Ω, refer to the Troubleshooting section because above 2,000 Ω resistance the maximum current injected will automatically be below 2,000 mA. If the contact resistance test stops and reads high voltage overload (HVOVL) this means that the stake is not properly connected. Check the electrode pair and restart the test to ensure that all electrodes are installed

correctly. HVOVL will also appear if the electrodes are installed incorrectly and the current injecting electrodes are the NP electrodes instead of the SS electrodes.

Once the contact resistance test is complete, press MEN to exit the test. This will return the user to the screen with the survey information now loaded as shown in Fig. B.15. Note that the information shows the user what command file is being used, what the data file is named, the electrode spacing, and the command line that the survey is currently on. If the survey is stopped at any time this screen will tell the user on which command line the survey will restart.

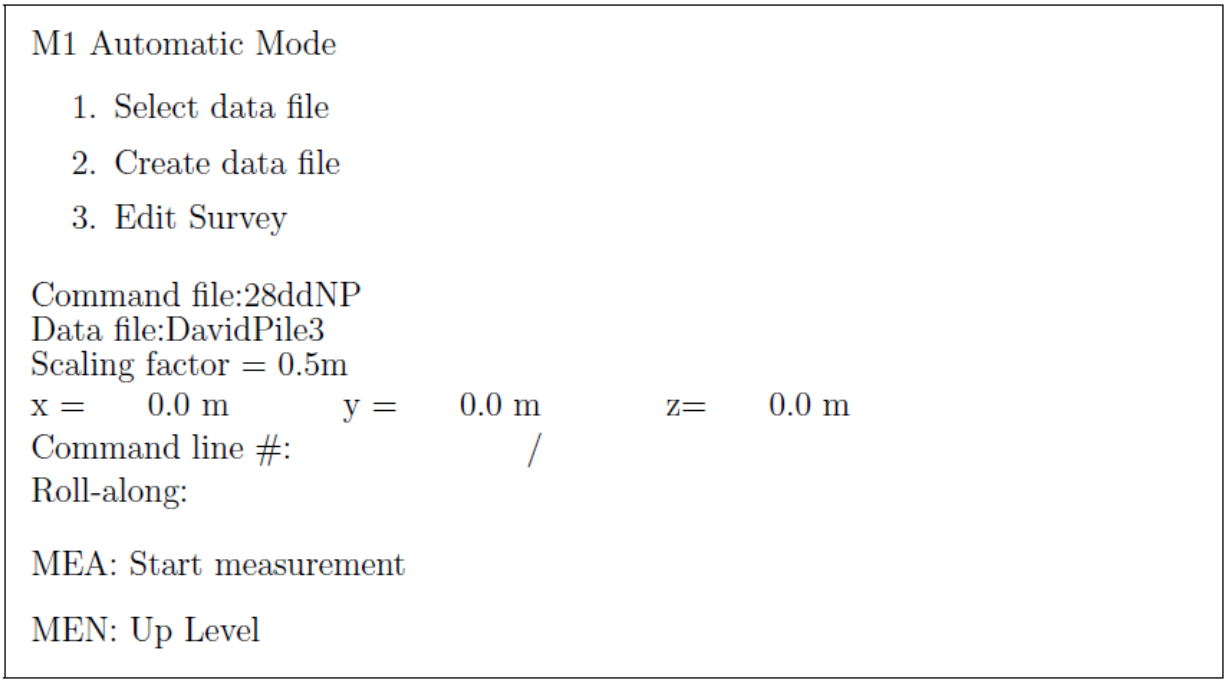

Fig. B.15. Final screen before starting a survey

Once the user is satisfied with the installation of the electrodes press MEA to start the survey.

Troubleshooting

If the instructions for field installation, writing a command file, and equipment setup are followed exactly, the SuperSting R8/IP™ will collect a field survey. The quality of the survey is related to the soil type and the amount of current that can be injected into the subsurface. If the contact resistance of a stake is over 1,000 Ω the value can be lowered using different methods. First, wet the ground around the stake with some water, if the water contains some salt the contact with the ground will be improved. If watering the stake does not lower the contact resistance, multiple stakes can be driven around the initial stake and attached to each other to create a cluster of electrodes. This can easily and quickly be done for one or two electrodes, but is not advisable if all 28 electrodes have contact resistances that are too high. The final remediation for electrodes is to dig a hole where the electrode is located and fill the hole with a mixture of water and bentonite or water and local mud. Bentonite holes are useful if the site consists of sand and gravel and will reduce contact resistances by over half of the original value.

If the contact resistance is less than 300 Ω but the IP decay curves do not match the calculated IP curves the NP electrodes need to be adjusted. First, ensure that all electrodes are connected to the cable take-outs and that there is copper sulfate and distilled water in each electrode. The tips of the electrodes should always be moist. If they are stored for long periods of time, the porous stones should be stored in distilled water. If they are being used on a regular basis, insert damp sponges into the caps covering the stones so they do not dry out.

Once it is ensured that the electrodes are properly maintained and in contact with the cable take-outs, the soil around the NP electrodes can also be wet with water to increase the contact with the stone. If the ground is too stiff to push the electrode into the ground, dig a hole and break up the removed soil. Mix this soil with water and back fill the hole so the electrodes can be pushed into the soil. If the soil is loose sand or gravel the hole can be filled with bentonite and water or local mud before the electrodes are pushed into the hole. This will ensure that the small signal does not dissipate while measurements are being taken.

Data Processing

The data processing described here uses the commercial software EarthImager™ created by Advanced Sciences, Inc. EarthImager™ is designed to specifically process the data files output by the SuperSting R8/IP™. Before loading a command file, the user must specify the settings for the forward modeling, the inversion method, and the inversion of the resistivity and IP data. A good starting point for changing these settings is to first set the defaults by using the drop-down arrow in the bottom of the pop up and selecting "Surface" as the setting. Next, select "Robust Inversion" as the inversion method on the Initial Settings tab. The mesh refinement on the Forward Modeling tab needs to be set to four instead of two. Next click the Resistivity Inversion tab and remove the option for Error Reduction by un-checking the box. Make sure that the Starting Model is Average Apparent Resistivity. On the IP Inversion tab, select Linear IP Inversion as the IP Inversion Method and check the box for Positivity. Finally, change the Start to two on the IP Window Range. Typically, for bridge foundations, the first IP window is very noisy; this will improve the calculated decay curves.

Open the data file using the Read Data option from the File drop-down menu or the folder with a green arrow. Next, if survey data are available, load the terrain file from the File drop-down menu. A terrain file is simply a list of the electrode ID with its associated elevation. It is easiest to open an example terrain file (*.trn) and to change the relative elevations and add or remove electrodes if necessary. EarthImager™ will alert the user of any data that will be removed prior to inverting the data if over 10 percent is marked for removal due to the user settings. Click the green arrow to start the inversion. Once the inversion is complete, consider where the foundation is located relative to the survey line and check the RMS value for the inverted resistivity section and the inverted IP section. If no large anomaly is seen on the IP inversion where the foundation is located or if the RMS values are above 5 percent, on the View drop-down menu open the Data Misfit Histogram from the Convergence and Data Misfit option (Fig. B.16).

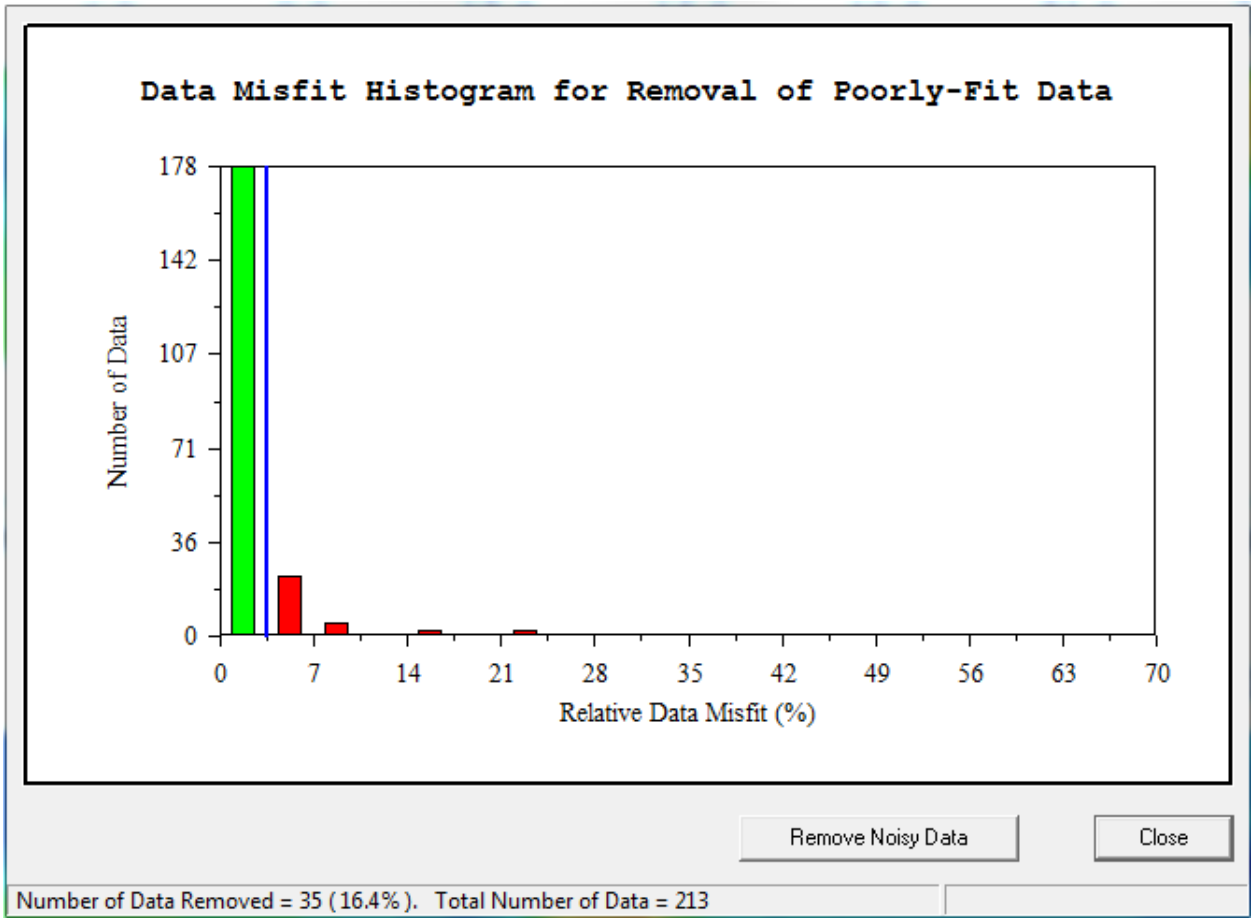

Fig. B.16. Data misfit histogram

Removing these data will reduce the number of poorly-fit data in the forward model and will decrease the RMS of the inversions to an acceptable level. Engineering judgment must be used to determine the amount of data that can be removed and still be a good representation of the subsurface. As a rule of thumb, removing more than 20 percent of the data is extreme and indicates that a new survey of the foundation needs to be carried out.

After the noisy data are removed, rerun the inversion and both RMS values should now be reduced. The final results of a foundation with no topographic data are shown in Fig. B.17.

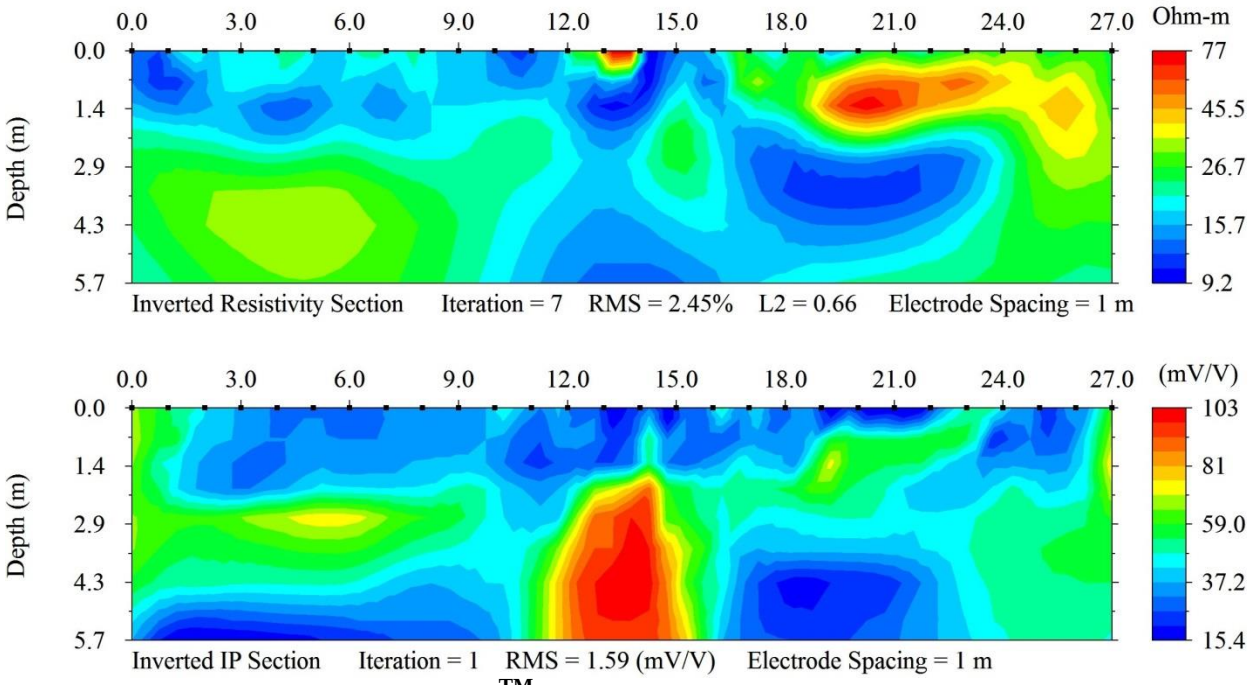

Fig. B.17. Output of EarthImager™ of a bridge foundation survey: inverted resistivity section (*top*); inverted IP section (*bottom*)

The foundation of this bridge is located 13 m along the line and is seen as a large highly chargeable zone in the Inverted IP section. The inverted resistivity section has a zone of high resistivity at the top of the pile, but nothing is seen below this point. The actual depth of this foundation is 6.08 m. It is difficult to estimate the depth of the foundation using the IP section because the highest zone of chargeability stops around 5 m, yet a zone that is more chargeable than the surrounding soil penetrates through the inversion window. For this reason, the post processing algorithm is used.

After each inversion three files are automatically saved in the folder where the data file is opened from. These files are the configuration settings (the command file), the inversion output file, and the data file. Each of these can be manually inspected by opening them in a text editor like the open source Programmer's Notepad. When EarthImager™ calculates and inverts the apparent resistivity and apparent chargeability pseudosections, the calculated data and inverted data are saved in an output text file that EarthImager™ uses to visually display the results. This text file includes the following information in the order listed below:

1. Headings.
2. Summary of data and electrodes.
3. Initial settings.
4. Surface electrode locations.
5. Commands, raw V/I, geometric factor, apparent resistivity, IP (V/V), correlation.
6. Mesh size.
7. Node location in X (m).
8. Node location in Y (m).
9. Timing.
10. Convergence.

11. IP Convergence.
12. Output of data and model of all iterations.

The inputs necessary for the post processing code are Item 6, Item 7, Item 8, and Item 12. These are copied and pasted into the MATLAB® m-file in the labeled sections. The following inputs are necessary from the user for the code to run: number of elements, number of elements in the *x* direction, number of elements in the *y* direction, and the range of *x*-nodes where the foundation is located. The last item is found using the known horizontal distance of the foundation at the time of testing. For example, if the foundation is located 6.5 m from the start of the line and is 1 m wide, the nodes corresponding to a horizontal distance from 6.5–7.5 m in the *x*-node section are used. The node number is first, followed by the distance in the *x* direction in m. If node 35 is at 6.5 m and node 39 is at 7.5 m 35:39 should be used as the input for the foundation. No other inputs are necessary for the code to run.

The MATLAB® code has four main sections: loading the data, organizing the elements into a numerical pseudosection, isolating the elements around the bridge foundation, and calculating the chargeability divided by the average chargeability and the normalized chargeability. The chargeability divided by the average chargeability data are used instead of the inverted chargeability values because chargeability is not an intrinsic value. The current delay time and IP measurement time are the same for all tests, so by dividing by the average chargeability the different tests may be loosely compared. The chargeability data are divided by the average chargeability of the model (19 mV/V) for the foundation shown above. Only the elements that coincide with the location of the foundation are plotted. The chargeability plot for Fig. B.17 is shown in Fig. B.18.

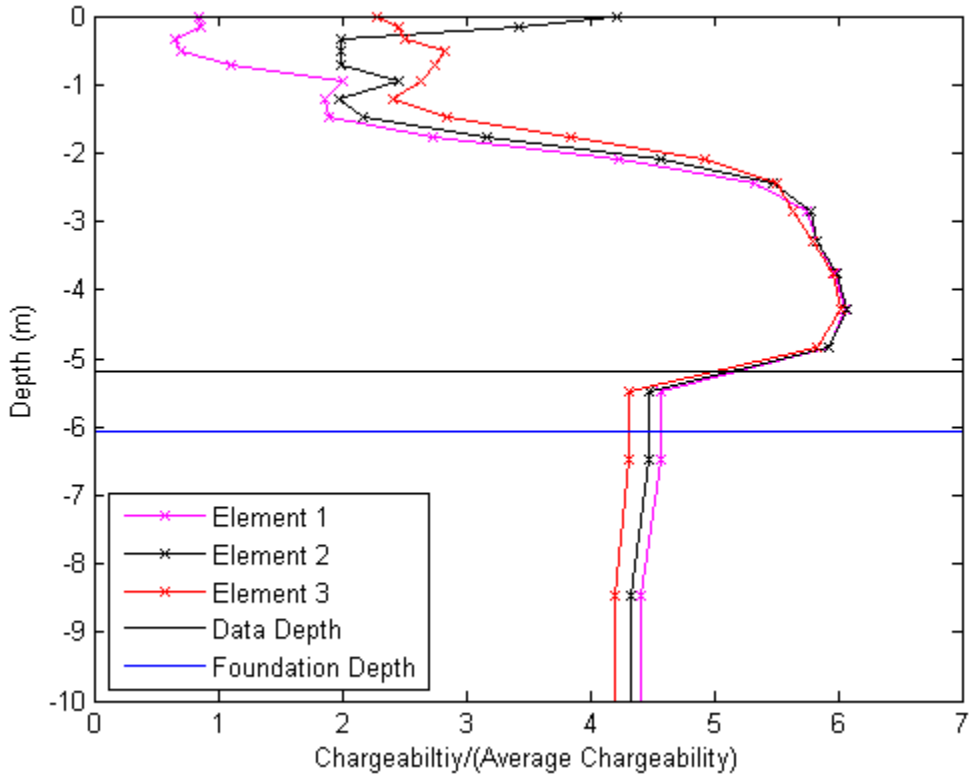

Fig. B.18. Bridge foundation chargeability around the foundation

The first criterion for estimating the foundation depth is the depth where the maximum ratio of the chargeability divided by the average chargeability of the model occurs, which is −4.27 m. Next, the normalized chargeability is calculated. Normalized chargeability is:

$$MN = \sigma'_{\text{rock}} M \tag{B.1}$$

where MN is the normalized chargeability, σ'_{rock} is the conductivity of the subsurface or the inverse of resistivity, and M is the chargeability. Again, only the data surrounding the foundation are plotted with depth in Fig. B.19.

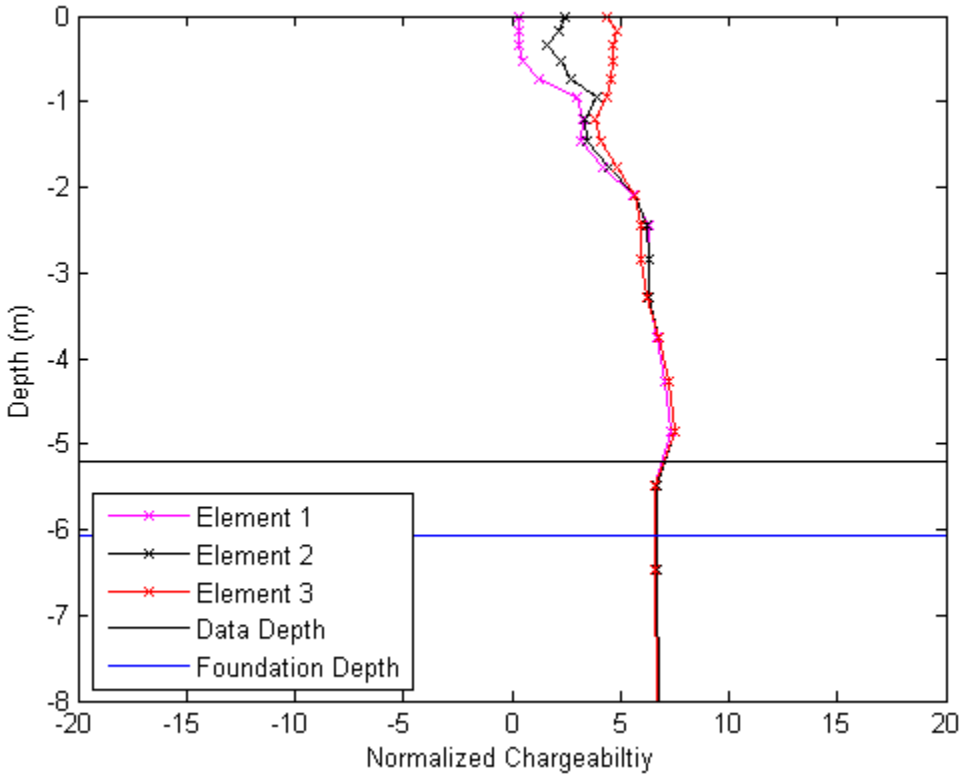

Fig. B.19. Normalized chargeability for foundation

Again, the depth where the maximum normalized chargeability occurs for all of the elements combined is the predicted foundation depth; −4.85 m for this foundation. Ultimately, the predicted foundation depth is the maximum of the two criterion or −4.85 m for this foundation. Note that the actual foundation depth is −6.08 m, thus the pile is under predicted by 1.23 m.

If this foundation was a truly unknown foundation the results of the post processing algorithm may be adjusted based on an acceptable level of risk. A probability of non-exceedance curve has been created to account for the uncertainties in these predictions. The curve is shown in Fig. B.20.

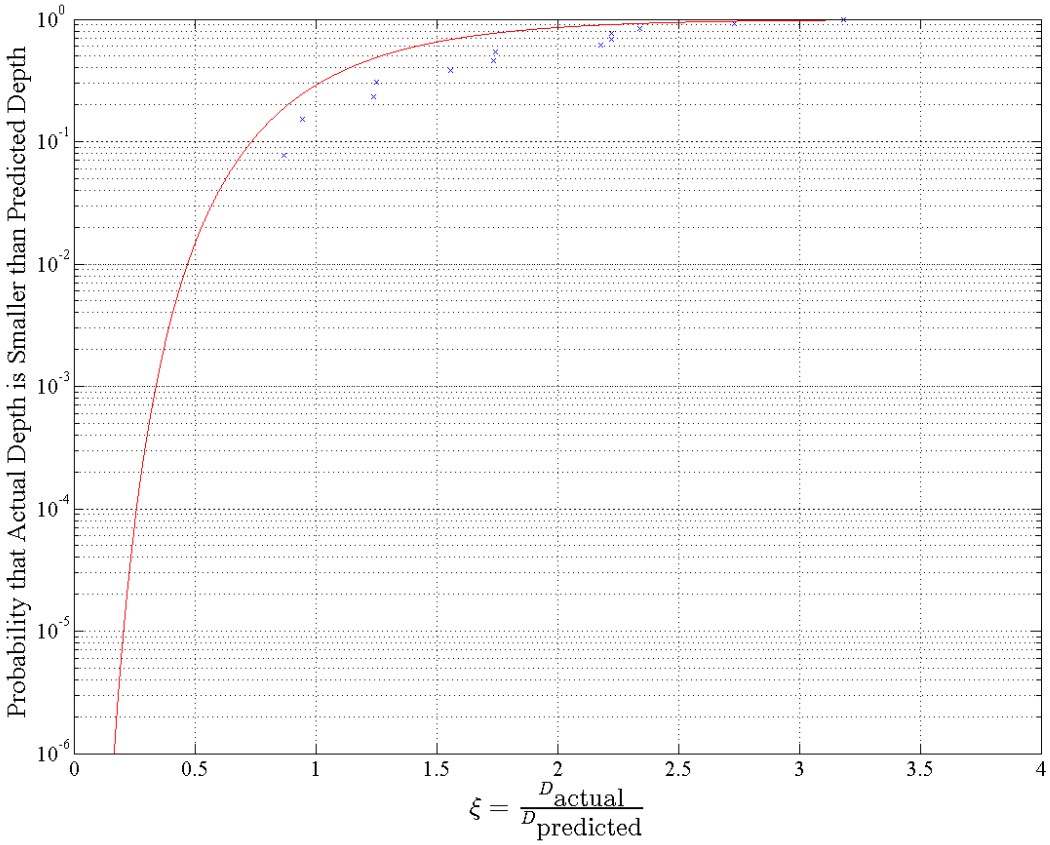

Fig. B.20. Probability of non-exceedance curve

This curve has been created using experimentally predicted foundations and the actual foundation depths. The variable ξ is the ratio of the actual depth of the foundation to the predicted depth of the foundation. The probability that the actual depth is shallower than the predicted depth depends on the variable ξ; the goal is to minimize this probability for a sensible design. If $\xi \times D_{\text{pred}}$ is larger than the actual foundation depth, the foundation is overestimated and what would be thought of as an allowable depth of scour may potentially fail the foundation. On the other hand, when ξ is 0, the prediction would have a probability of failure of 0, yet this information would not be very useful. Therefore, if the −4.85 m predicted depth from Fig. B. 19 is assumed correct then ξ is one. Using Fig. B.20 there is a 28.73 percent probability that the actual foundation is shallower than −4.85 m. If a probability of 28.73 percent is too high for the level of confidence needed in the foundation prediction, ξ may be reduced. For example, if ξ is 0.21, the probability that the actual foundation depth is less than the predicted is 0.000001 percent. The appropriate value of ξ should be selected based on the acceptable risk level determined by the engineer estimating the unknown bridge foundation.

CONCLUSIONS

This manual is intended for assisting engineers using ERI and IP for predicting the depths of unknown bridge foundations. It is written under the assumption that users are using the AGI SuperSting R8/IP™ system and the accompanying commercial software EarthImager™. The

post processing code is an open source code that can be altered if other equipment or software is used.

APPENDIX C. PIPE IMAGES

C.1 PIPE FIGURES

The inverted electrical resistivity images and IP images are included in this appendix. They are in order of the increasing angle of rotation of the line. First the inverted ERI section and IP sections are shown, followed by the rotated inverted ERI section relative to the first line.

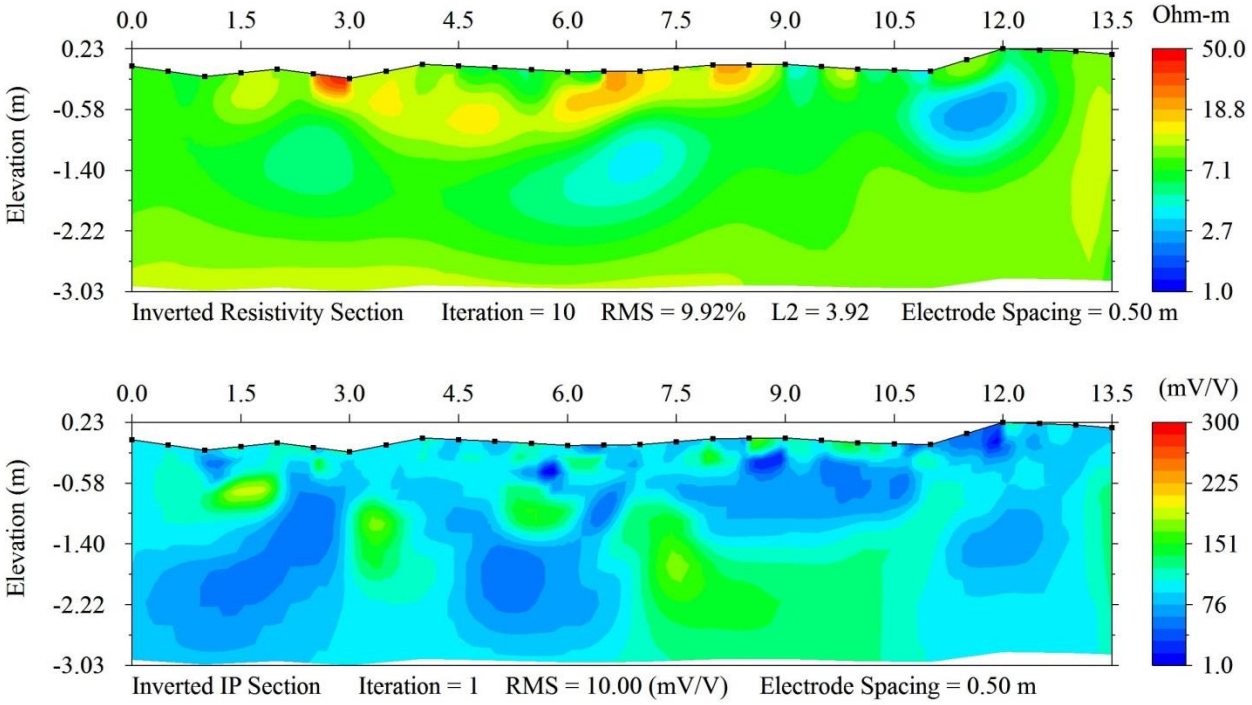

Fig. C.1. Pipe line rotated 15°: inverted resistivity section (*top*); inverted IP section (*bottom*)

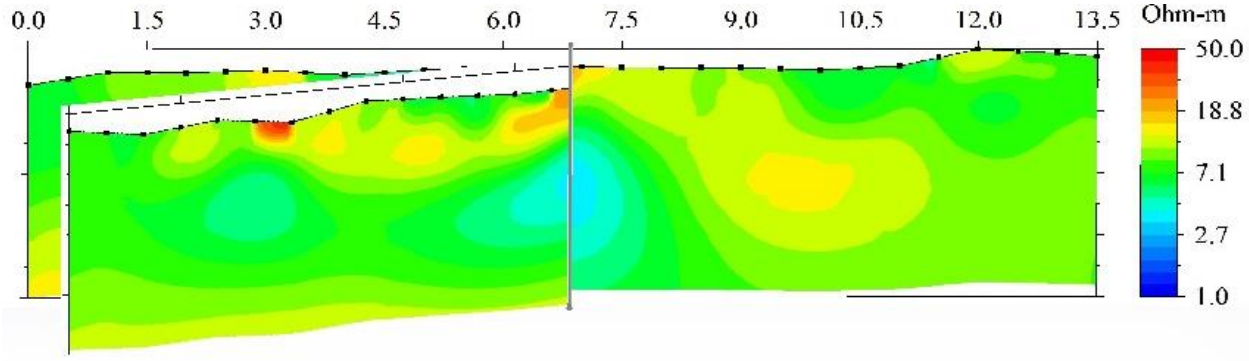

Fig. C.2. Pipe line rotated 15° relative to line one

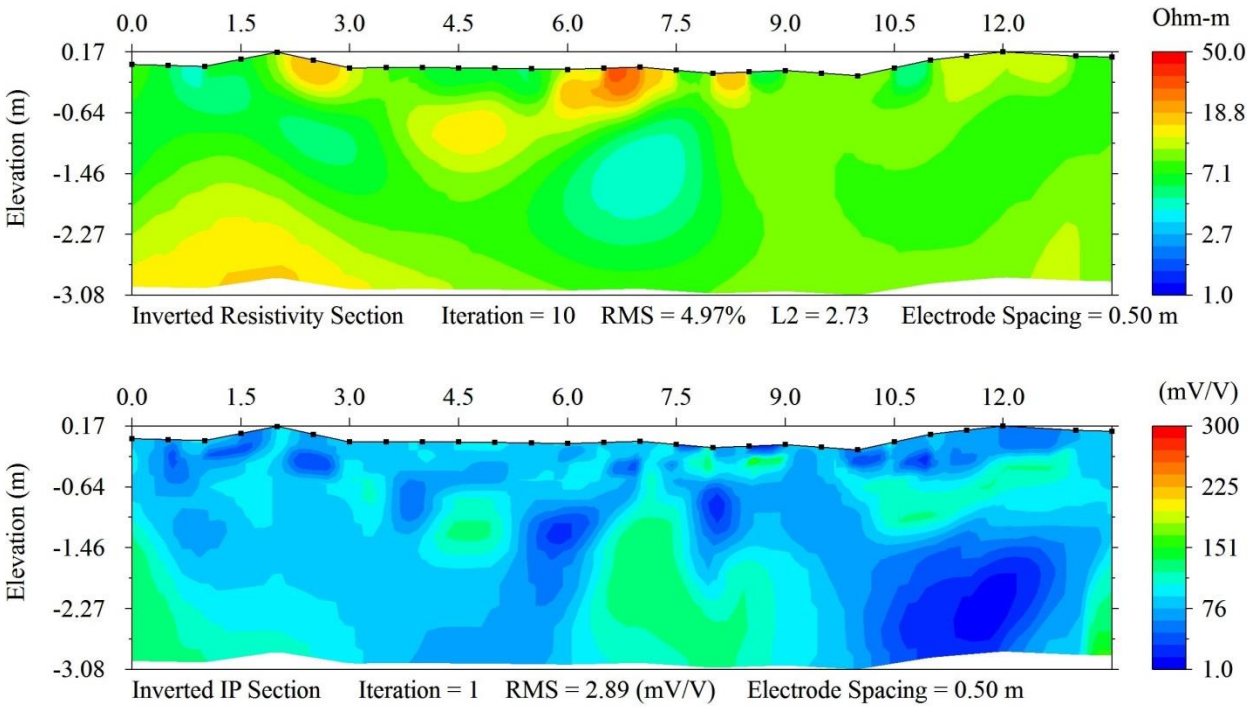

Fig. C.3. Pipe line rotated 30°: inverted resistivity section (*top*); inverted IP section (*bottom*)

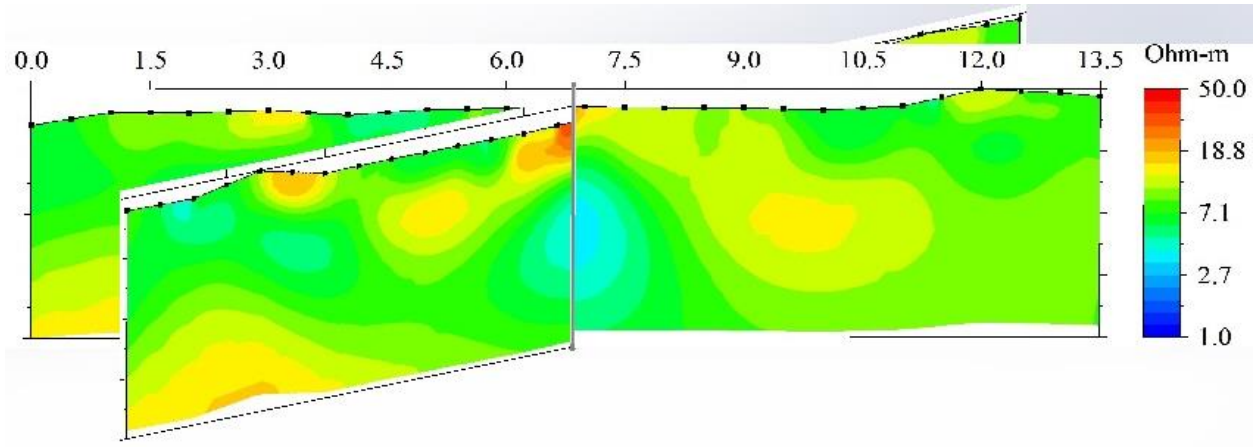

Fig. C.4. Pipe line rotated 30° relative to line one

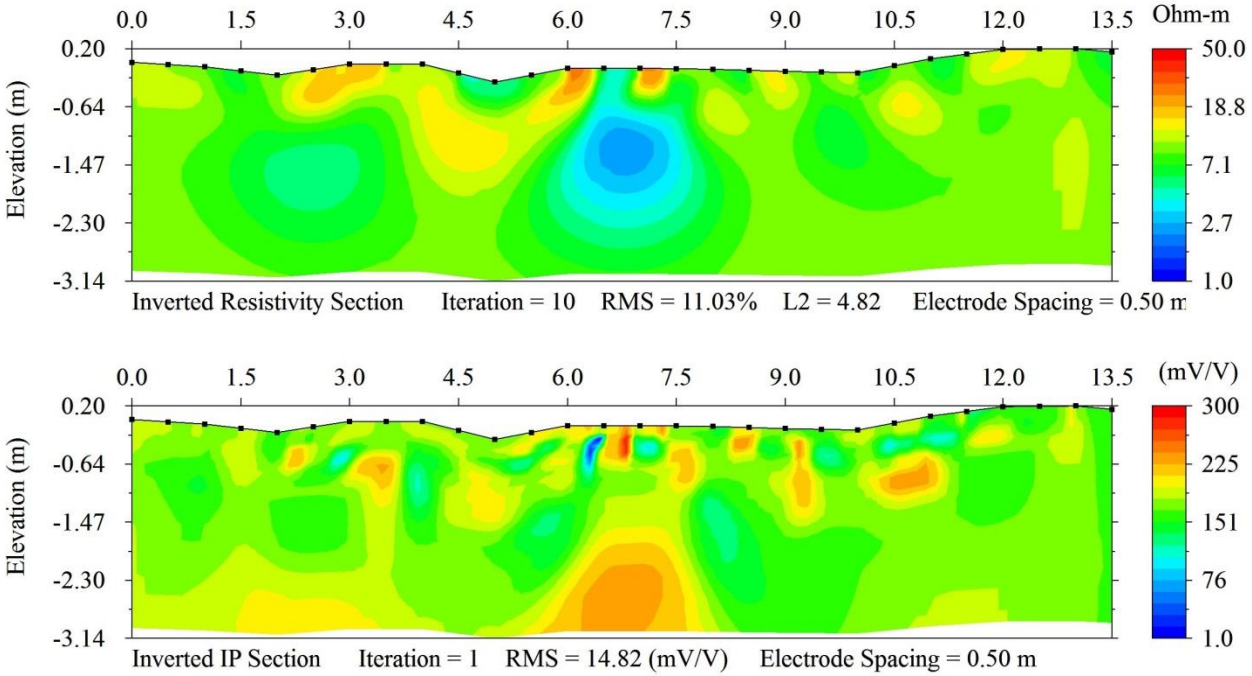

Fig. C.5. Pipe line rotated 45°: inverted resistivity section (*top*); inverted IP section (*bottom*)

The rotated line for the 45° is included in Chapter 6.

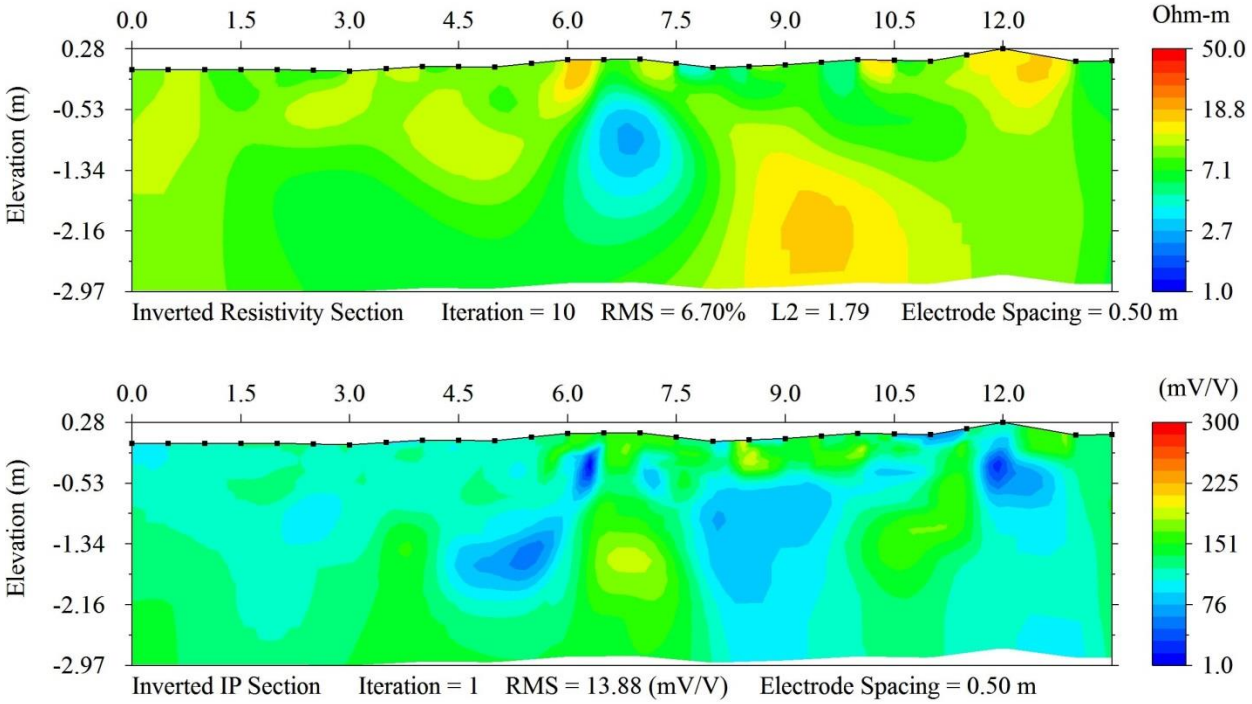

Fig. C.6. Pipe line rotated 60°: inverted resistivity section (*top*); inverted IP section (*bottom*)

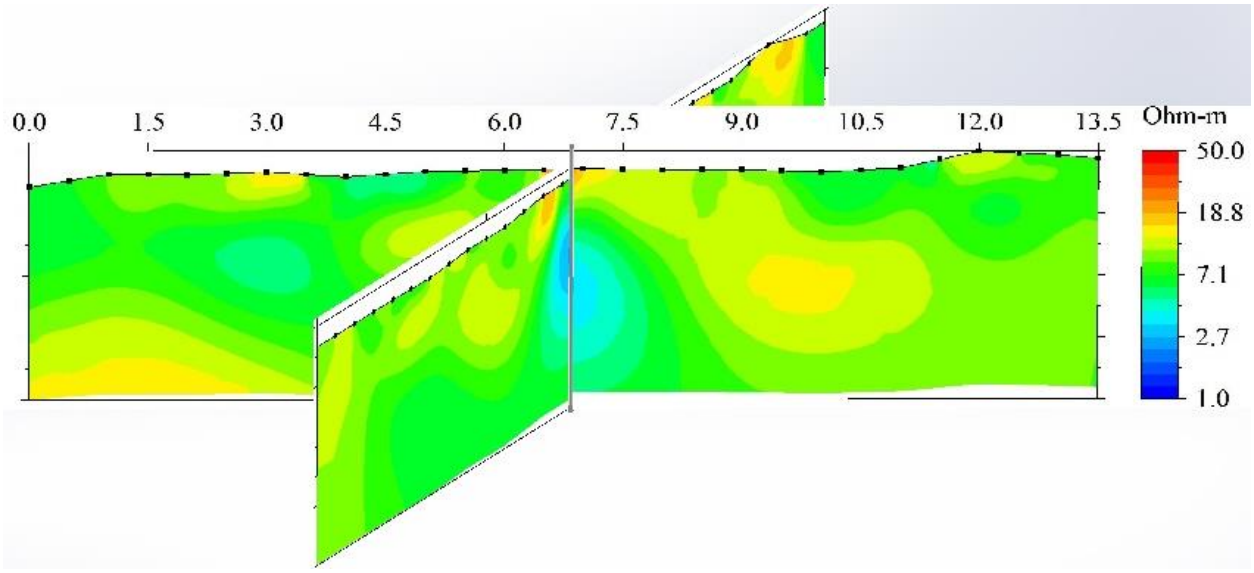

Fig. C.7. Pipe line rotated 60° relative to line one

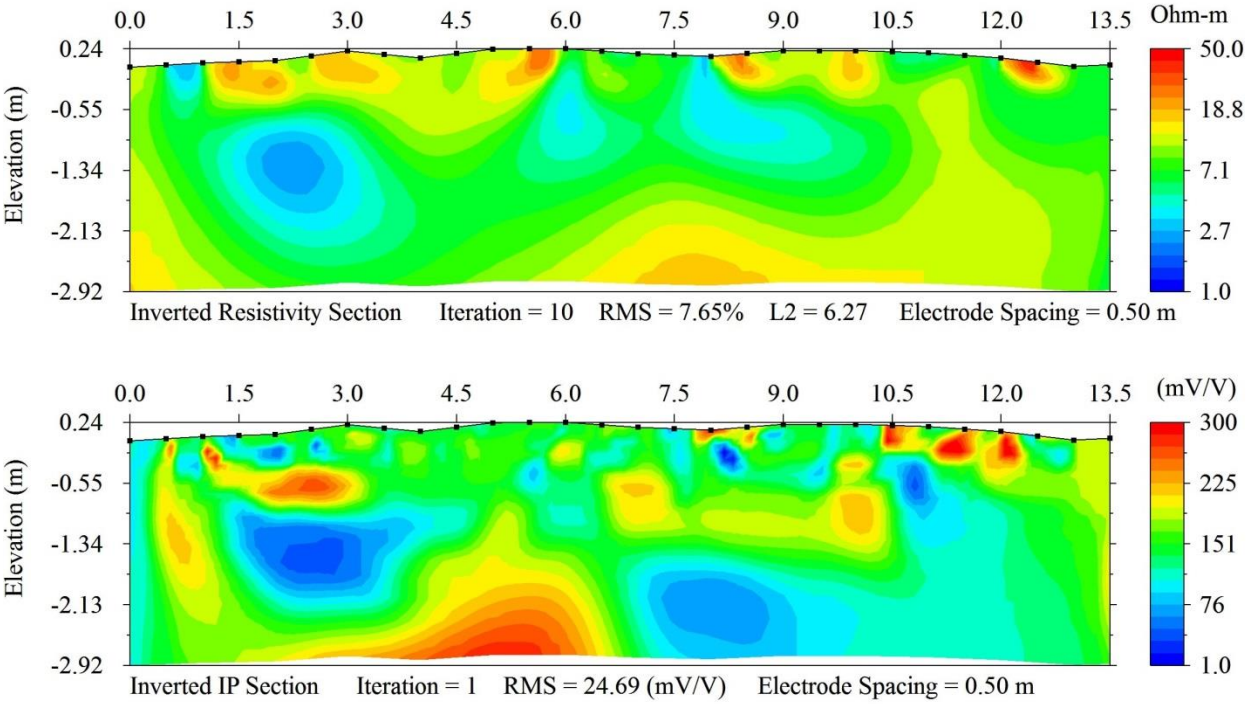

Fig. C.8. Pipe line rotated 75°: inverted resistivity section (*top*); inverted IP section (*bottom*)

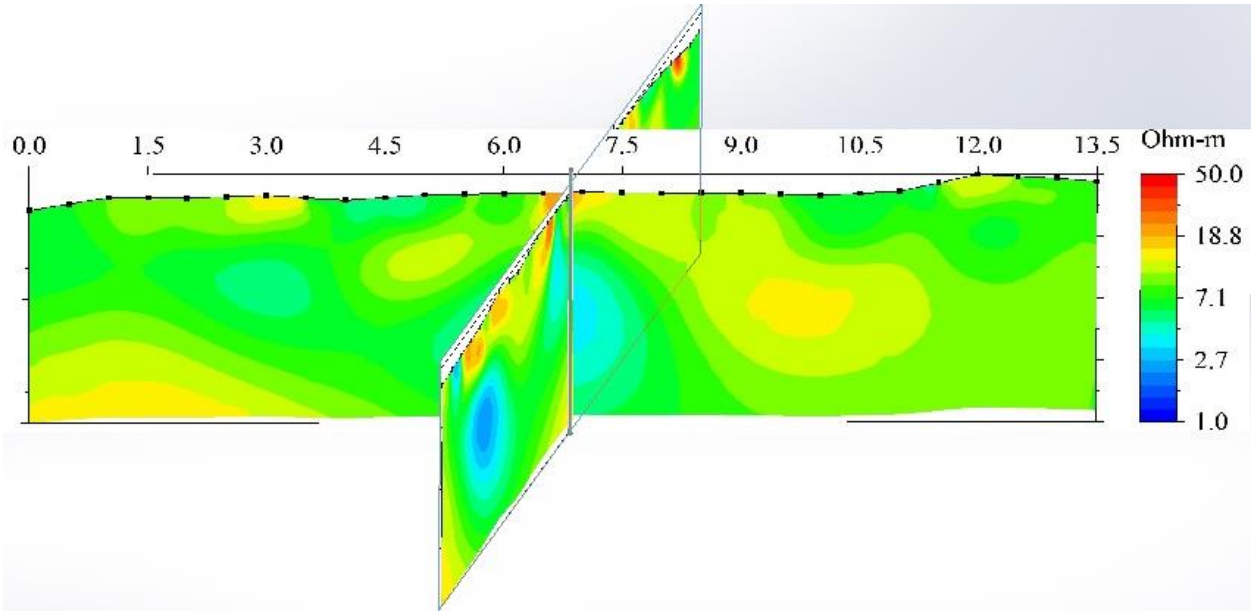

Fig. C.9. Pipe line rotated 75° relative to line one

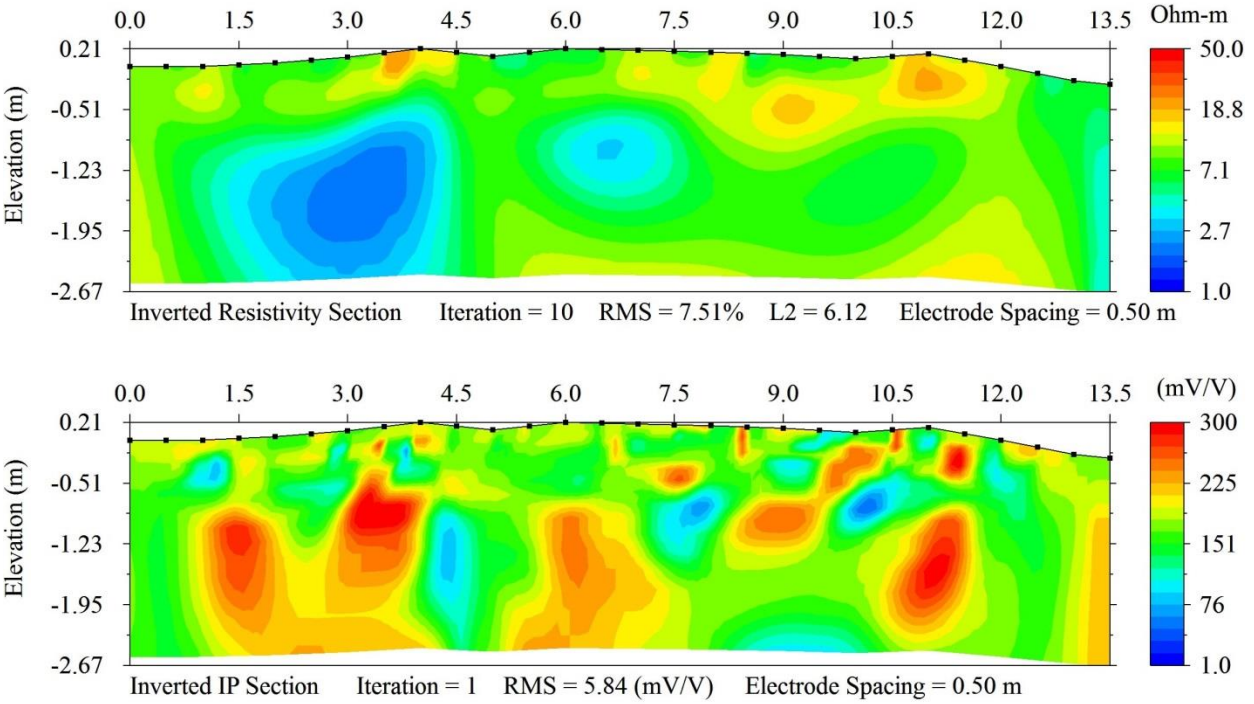

Fig. C.10. Pipe line rotated 90°: inverted resistivity section (*top*); inverted IP section (*bottom*)

The rotated image for the 90 line is included in Chapter 6.

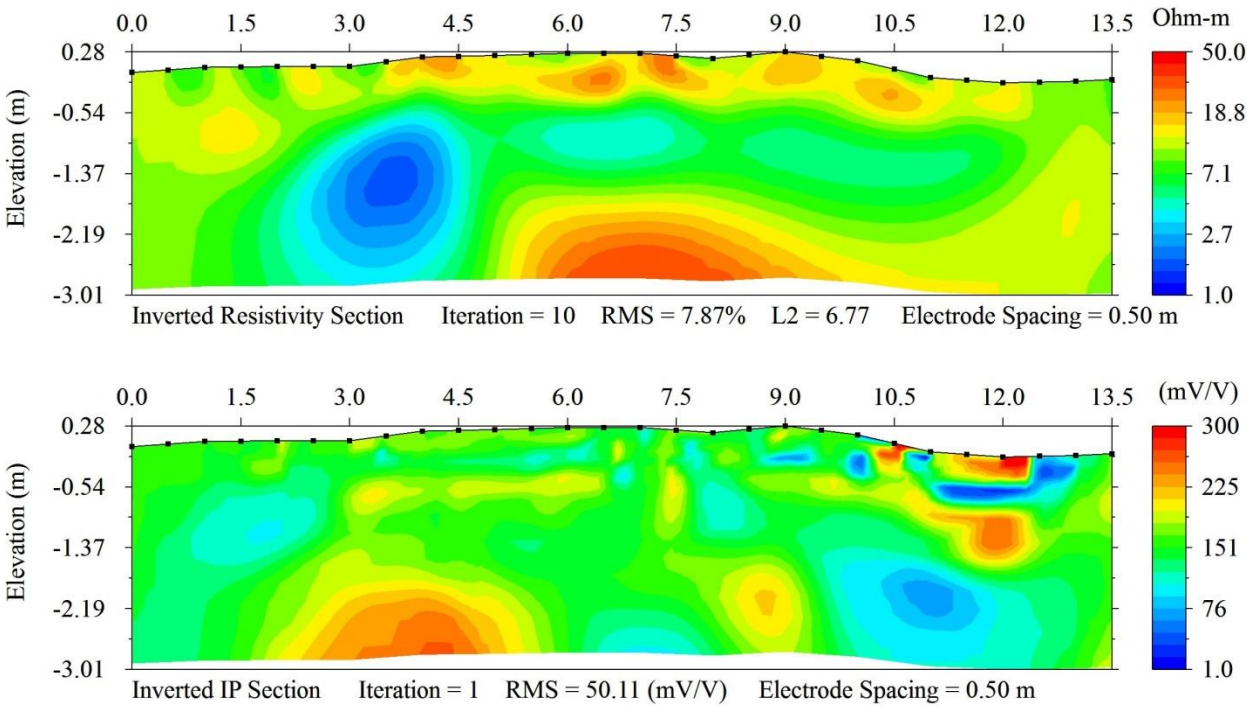

Fig. C.11. Pipe line rotated 105°: inverted resistivity section (*top*); inverted IP section (*bottom*)

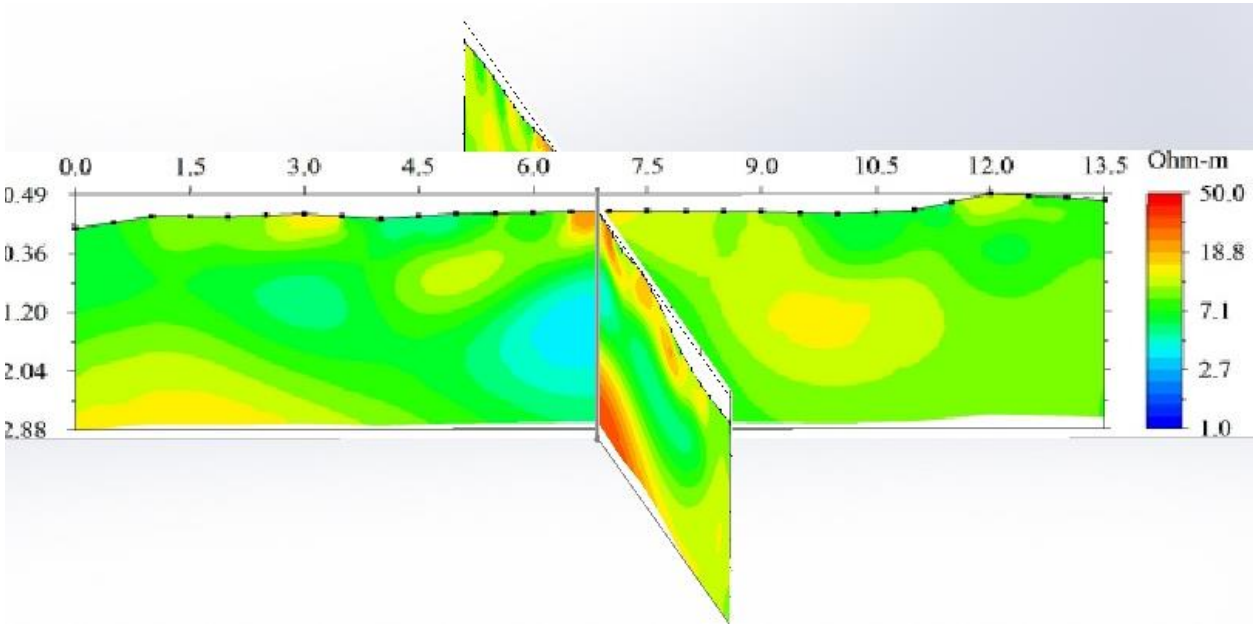

Fig. C.12. Pipe line rotated 105° relative to line one

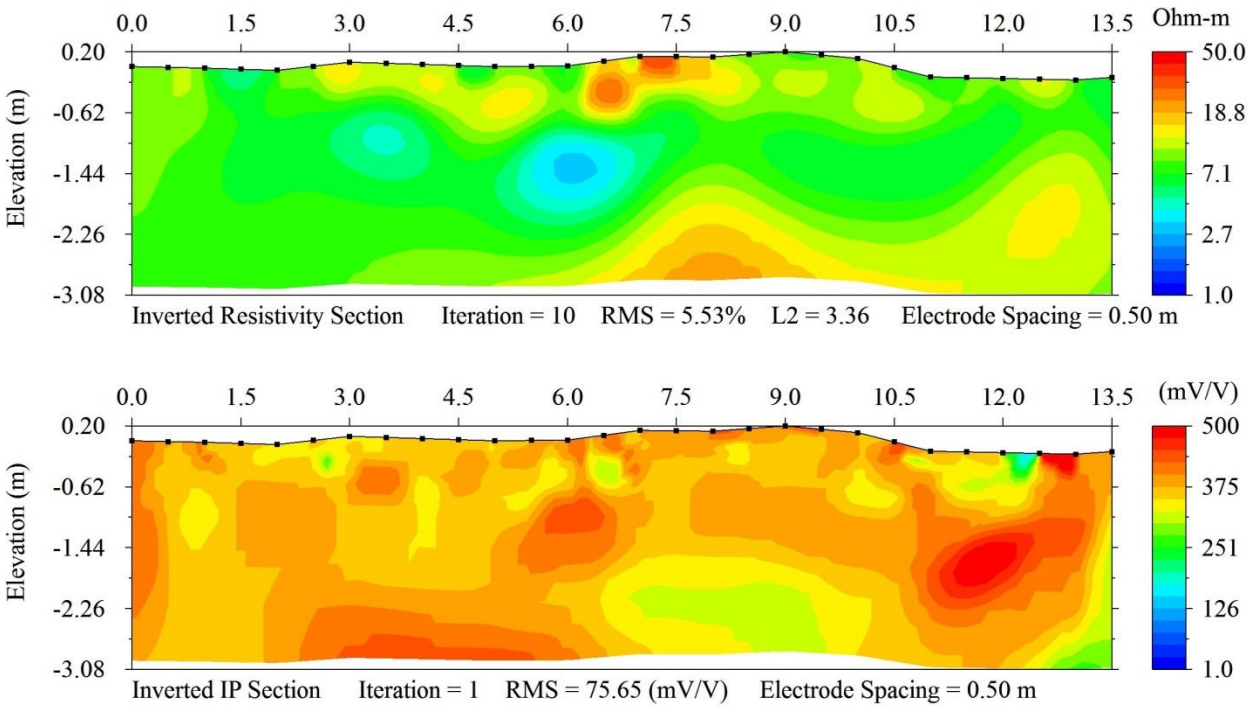

Fig. C.13. Pipe line rotated 120°: inverted resistivity section (*top*); inverted IP section (*bottom*)

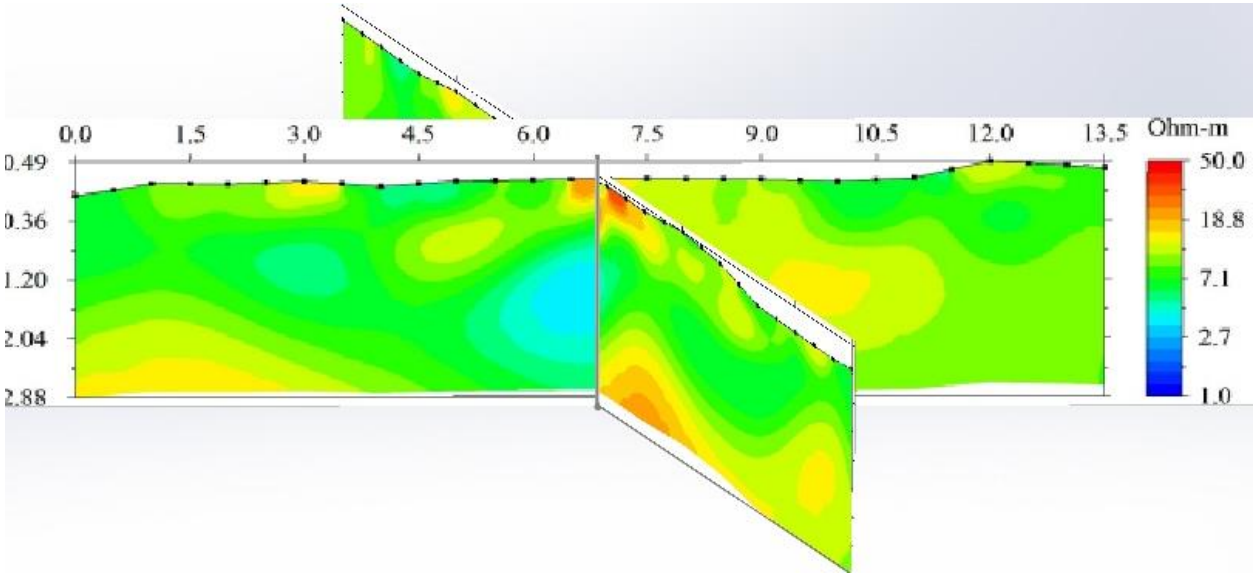

Fig. C.14. Pipe line rotated 120° relative to line one

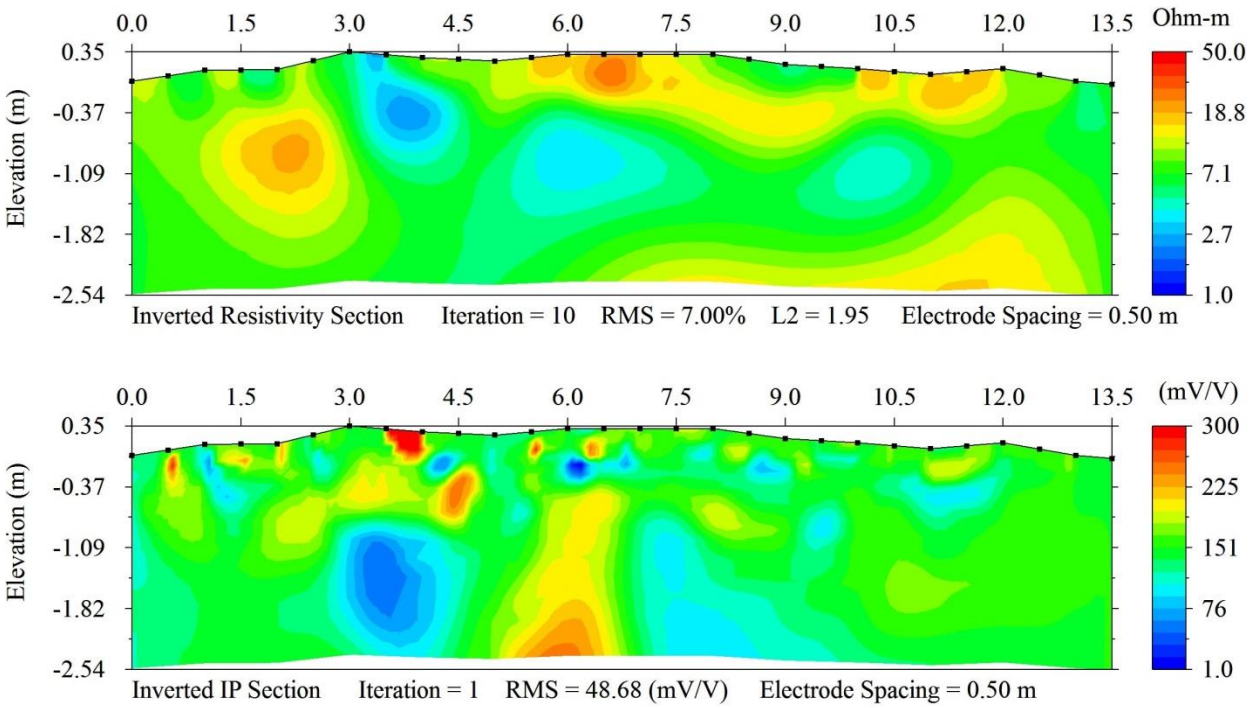

Fig. C.15. Pipe line rotated 135°: inverted resistivity section (*top*); inverted IP section (*bottom*)

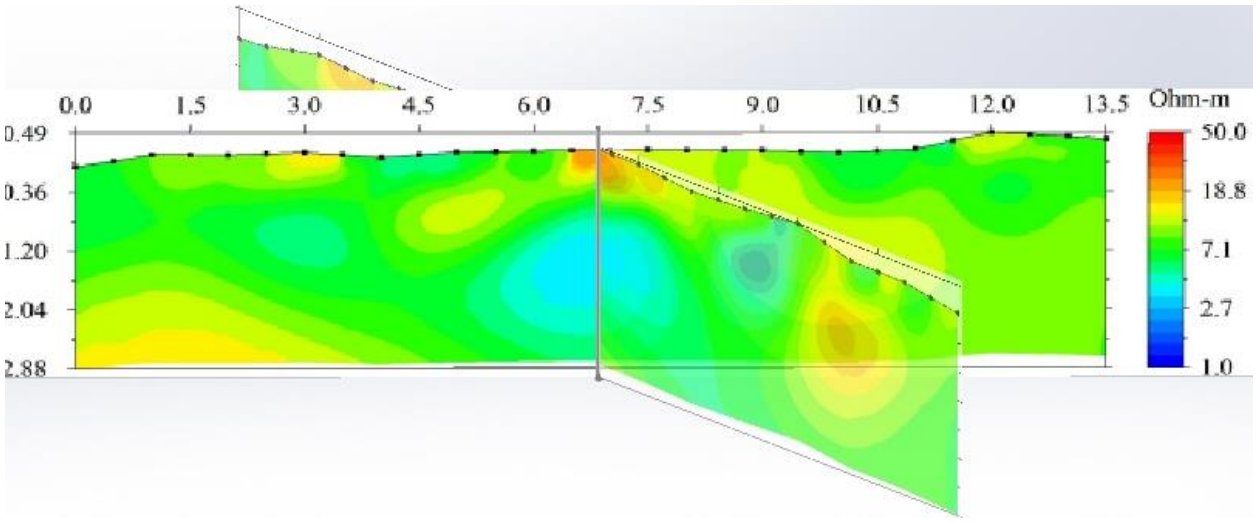

Fig. C.16. Pipe line rotated 135° relative to line one

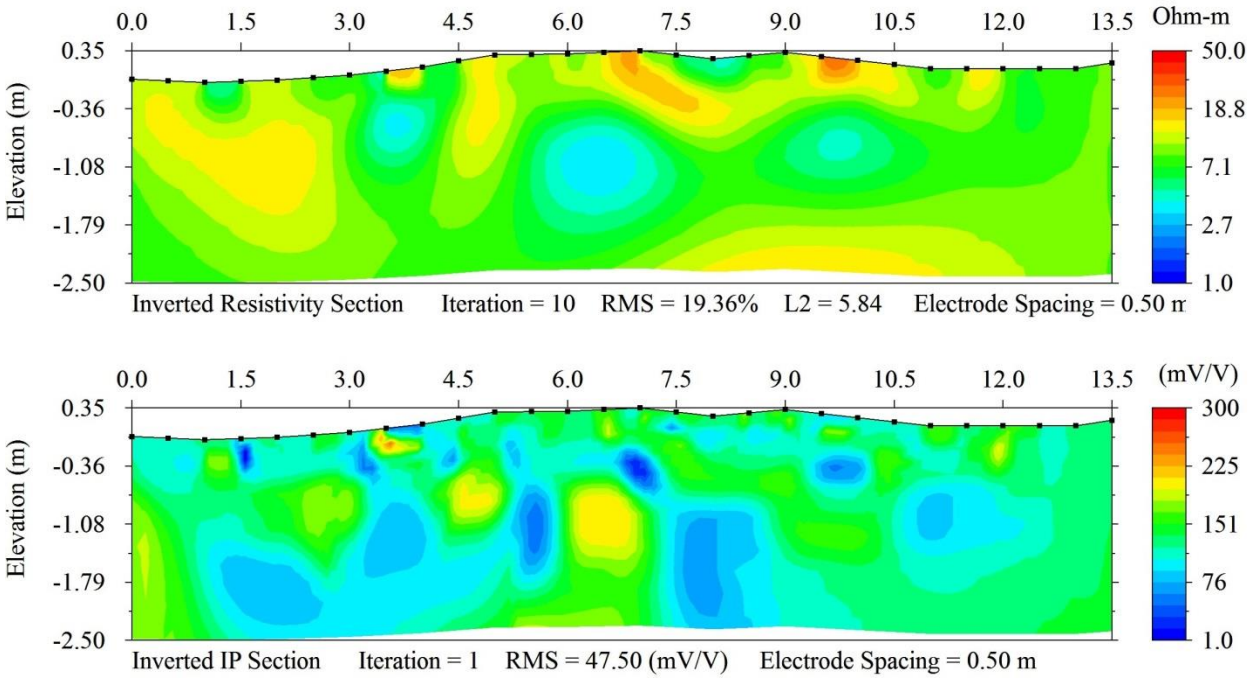

Fig. C.17. Pipe line rotated 150°: inverted resistivity section (*top*); inverted IP section (*bottom*)

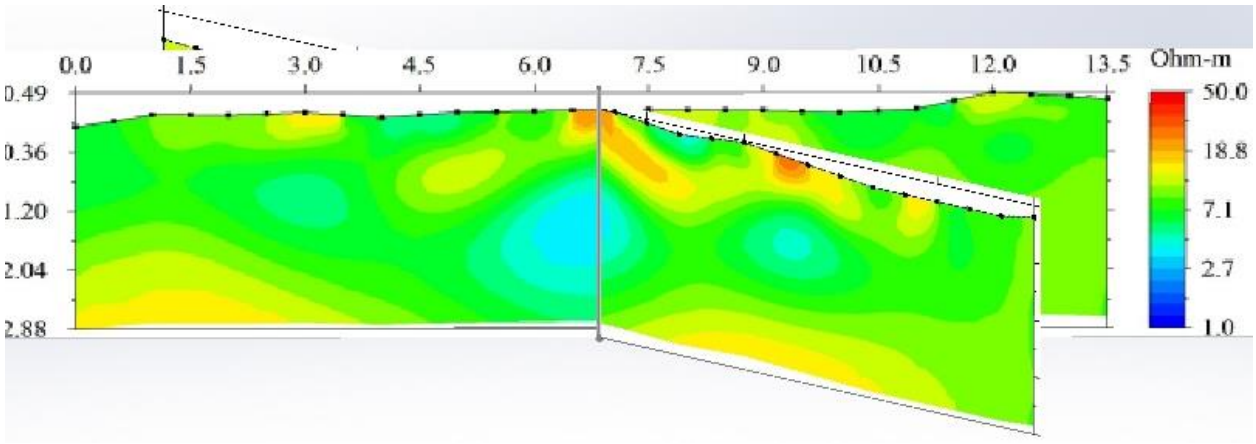

Fig. C.18. Pipe line rotated 150° relative to line one

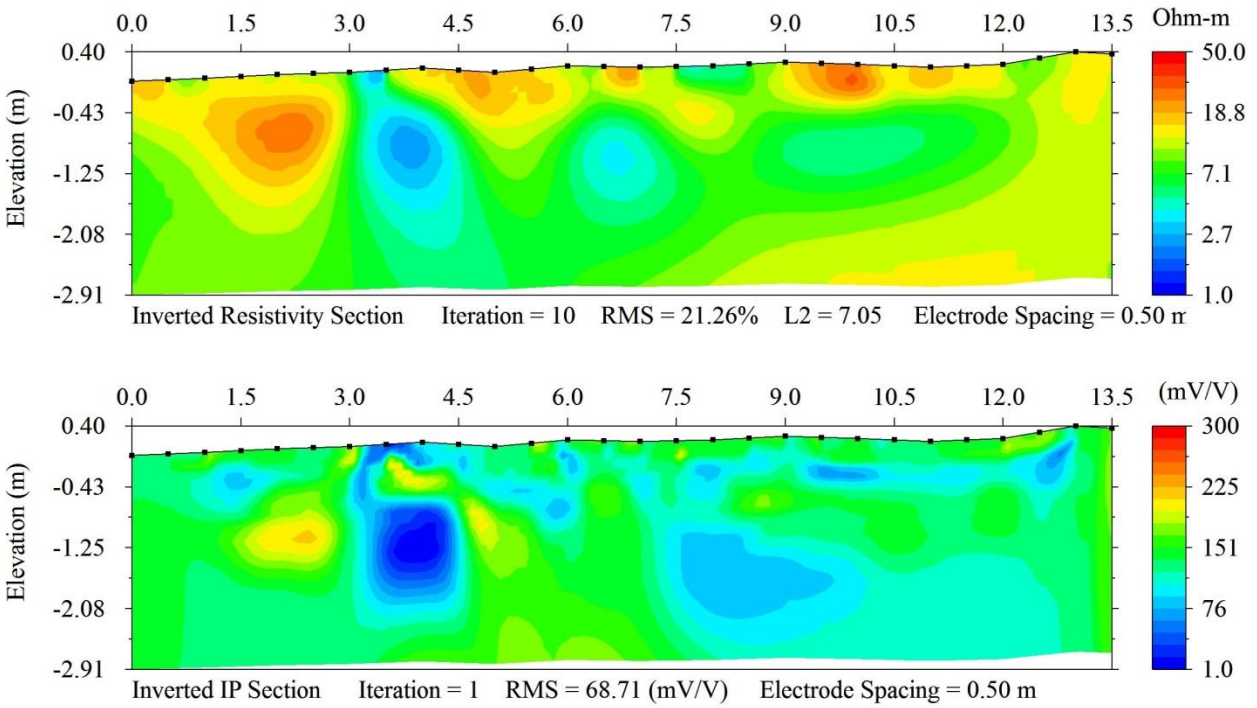

Fig. C.19. Pipe line rotated 165°: inverted resistivity section (*top*); inverted IP section (*bottom*)

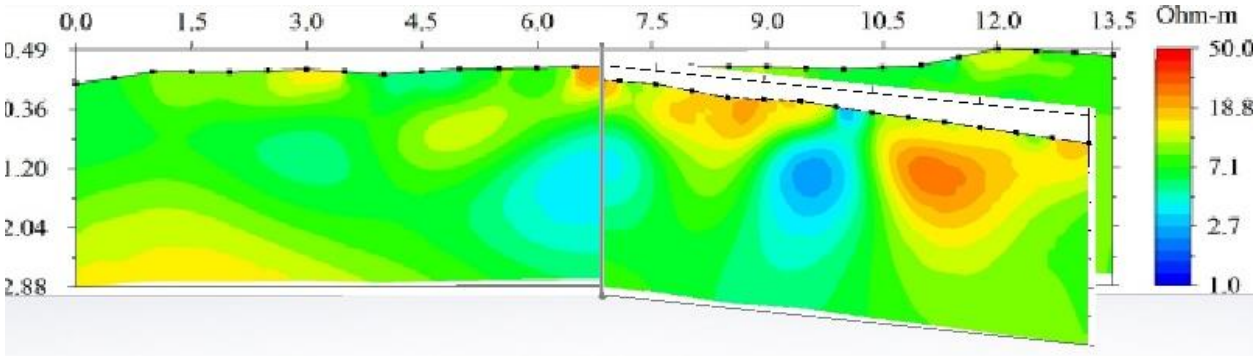

Fig. C.20. Pipe line rotated 165° relative to line one

APPENDIX D. MATLAB POST PROCESSING CODE

D.1 MATLAB CODE

```
clear all
close all
clc

%Mesh Size%
% Number of nodes           = 3125
% Number of nodes in X      = 125
% Number of nodes in Y      = 25
% Number of elements        = 2976
% Number of elements in X   = 124
% Number of elements in Y   = 24
% Number of parameters      = 2016
% Number of parameters in X = 112
% Number of parameters in Y = 18
% Number of left elements   = 8
% Number of right elements  = 8
% Number of top elements    = 0
% Number of bottom elements = 8

nelm = 2976;
elmx = 124;
elmy = 24;
%Load node data
xnode = [];
ynode = [ ];

%Foundation information and relative node info
d = -6.08;
yplot = -10;
ynodeplot = 21;

%Load IP DATA from Output
Charge = [ ];

%Arrange data into a single array
array = zeros(nelm,1);
org = ceil(nelm/5)
for i = 1:org
  array(1+5*(i-1):5+5*(i-1),1)=Charge(i,:);
end
array = array(:,:).*1000;

pseud = zeros(elmy,elmx);

%Organize data into pseudosection
for i = 1:elmx
pseud(:,i) = array(((1+(elmy)*(i-1)):((elmy)+(elmy)*(i-1))),1);
end

%Pull chargeability from around foundation
```

```
foundation = pseud(:,63:65);
%Vertical ratio
curve = zeros(elmy,3);
for j=1:3
for i = 1:elmy-1
curve(i,j) = foundation(i,j)./foundation(i+1,j);
end
end

%Foundation Depth
A = [0, 2];
B = [d, d];
C = [yplot 0];
D = [1 1];
E = [1.2 1.2];
datadepth = [-5.2,-5.2];

xplot = zeros(124,1);
for i = 1:124
    xplot(i) = (xnode(i,2) + xnode(i+1,2))/2
end

yplot = zeros(24,1);
for i = 1:24
    yplot(i) = (ynode(i,2) + ynode(i+1,2))/2
end

norm = zeros(24,3);
for i = 1:3
    for j = 1:24
        norm(j,i) = foundation(j,i)/19;
    end
end

figure(1)
plot(norm(1:ynodeplot,1),yplot(1:ynodeplot,1),'-mx')
hold on
plot(norm(1:ynodeplot,2),yplot(1:ynodeplot,1),'-kx')
hold on
plot(norm(1:ynodeplot,3),yplot(1:ynodeplot,1),'-rx')
hold on
line(A,datadepth,'Color','k');
hold on
line(A,B)
legend('Element 1', 'Element 2', 'Element 3','Data Depth', 'Foundation
Depth','location','southwest')
xlabel('Chargeabiltiy/(Average Chargeability)')
ylabel('Depth (m)')
title('Caldwell Bridge Foundation 2')
axis([0 7 -10 0])

 res = [ ];

%Arrange data into a single array
arrayres = zeros(nelm,1);
```

```
orgres = ceil(nelm/5);
for i = 1:orgres
  arrayres(1+5*(i-1):5+5*(i-1),1)=res(i,:);
end

pseudres = zeros(elmy,elmx);

%Organize data into pseudosection
for i = 1:elmx
pseudres(:,i) = arrayres(((1+(elmy)*(i-1)):((elmy)+(elmy)*(i-1))),1);
end

%Pull chargeability from around foundation
foundationres = pseudres(:,63:65);
%Normalized
for j=1:3
for i = 1:elmy
normalized(i,j) = foundation(i,j)./foundationres(i,j);
end
end

normalized(:,4) = (normalized(:,1) + normalized(:,2) + normalized(:,3))/3;

%Normalized Foundation Depth
A = [-100, 100];
B = [d, d];
figure(2)
plot(normalized(1:ynodeplot,1),yplot(1:ynodeplot,1),'-mx')
hold on
plot(normalized(1:ynodeplot,2),yplot(1:ynodeplot,1),'-kx')
hold on
plot(normalized(1:ynodeplot,3),yplot(1:ynodeplot,1),'-rx')
hold on
line(A,datadepth,'Color','k');
hold on
line(A,B);
legend('Element 1', 'Element 2', 'Element 3','Data Depth', 'Foundation
Depth','location','southwest')
ylabel('Depth (m)')
xlabel('Normalized Chargeabiltiy')
title('Caldwell Bridge Foundation 2')
axis([-20 20 -8 0])
```